Elucidating the biological role of neuronal dystonin isoforms in the hereditary sensory neuropathy *dystonia musculorum*

Andrew Ferrier

Thesis submitted to the Faculty of Graduate and Postdoctoral Studies in partial fulfillment of the requirements for the Ph.D. degree in Cellular and Molecular Medicine

Department of Cellular and Molecular Medicine

Faculty of Medicine

University of Ottawa

Abstract

Dystonin is a cytoskeletal linker protein whose loss-of-function in *dystonia musculorum* (*dt*) mice results in a hereditary sensory neuropathy with profound sensory ataxia. The dystonin gene (*Dst*) is exceptionally large (~400 kb) producing three giant neuronal dystonin isoforms (>600 kDa) through alternative splicing, namely dystonin-a1, -a2, and -a3. Although loss of expression of dystonin-a1 and -a2 is sufficient to cause *dt* pathogenesis, the causal dystonin-a variant and the pathological mechanisms activated upon their individual loss remains unclear. Moreover, while the primary pathology lies in the sensory neurons of *dt* mice, the overt movement disorder coupled with dystonin's expression in motor neurons, suggests the motor system may also be affected. Here we report that *dt* mice exhibit motor neuron defects, including, but not limited to, aberrant phosphorylation of neurofilaments, axonal swellings, reduced axon branching and immature neuromuscular junctions. Furthermore, we find that various pathologies (*e.g.*, Ca^{2+} dyshomeostasis, unfolded protein response (UPR) induction, caspase activation, and apoptosis) within *dt* sensory neurons are attributable to the specific loss of dystonin-a2. Coupled with this, transgenic mice exogenously expressing dystonin-a2 within the nervous system of *dt* mice attenuated the degeneration of sensory neuron subtypes, and was sufficient to ameliorate the phenotype and increase life span. Despite these improvements, however, both dystonin-a2 and dystonin-a1 appear necessary for complete amelioration of *dt* pathogenesis. Finally, pertubations in autophagic activity underlie the degeneration of *dt* sensory neurons. Restoring dystonin-a2 expression in *dt* sensory neurons rescues this autophagic defect. Taken together, our work reveals that dystonin-a loss-of-function imparts defects on the neuromuscular system that likely contribute to the

dt phenotype. Moreover, although loss of dystonin-a2 expression impedes key biological processes, such as autophagy, endoplasmic reticulum (ER) dynamics and intracellular trafficking, and elicits numerous pathological mechanisms, this work suggests the *dt* disorder to be a multi-isoform disease.

TABLE OF CONTENTS

LIST OF TABLES

LIST OF FIGURES

LIST OF ABBREVIATIONS

ABD: actin-binding domain
Ac: Acetylated
Acf7: microtubule actin crosslinker factor 7
AChRs: acetylcholine receptors
BiP: binding protein
BPAG1: bullous pemphigoid antigen 1 gene
Bpag1e: Bpag1 epithelial isoform
BTX: alpha-bungarotoxin
CA1-CA3: cornu ammonis area 1-3
Ca^{2+}: calcium
CC: coiled-coil domain
CH1/CH2: calponin homology domains 1 and 2
CHOP: CCAAT/-enhancer- binding protein
CLIP-170: cytoplasmic linker proteins
CLTB: clathrin, light chain B
DAPI: 3,3′-diaminobenzidine
DIC: differential interference contrast
D.I.V.: days *in vitro*
DMC: dynein motor complex
DMEM: Dulbecco's minimum essential medium
DRG: dorsal root ganglion
Dst: murine dystonin gene
dt: dystonia musculorum
dynein-IC1: dynein intermediate chain 1
dystonin-a: neuronal dystonin isoform
dystonin-b: muscle dystonin isoform
dystonin-e: epithelial dystonin isoform
EB1: end-binding protein 1
EDL: extensor digitorum longus
EF: helix-loop-helix structural domain
eIF2α: eukaryotic initiation factor-alpha
ER: endoplasmic reticulum
FD: familial dysautonomia
FLICA: fluorescence-labeled inhibitor of caspase activity
FLuc: RFP-firefly luciferase
GAPDH: glyceraldehyde-3-phosphate dehydrogenase
GAR: growth arrest protein-related region
GAS2: growth arrest-specific 2
GFAP: glial fibrillary acidic protein

GFP: green fluorescent protein
GLuc: YFP-Gaussia luciferase
GM58K: Golgi marker 58K
GO: Gene Ontology
HDAC: histone deacetylase
HRP: horseradish peroxidase
HSAN-VI: hereditary sensory and autonomic neuropathy type 6
HTT: Huntingtin
ICC: immunocytochemistry
IF: intermediate filament
IFBD: intermediate filament binding domain
IHC: immunohistochemistry
KO: knock out
L1: lumbar vertebral level
LC3: microtubule associated protein light chain 3
MACF: microtubule–actin cross-linking factor
MAP1B: microtubule associated protein-1B
MAP2: microtubule associated protein 2
MAPT: microtubule associated protein tau
MF: actin microfilament
MTBD: microtubule-binding domain
NE: nuclear envelope
NF: neurofilament
NLS: nuclear localization signal
NMJ: neuromuscular junction
PD: plakin domain
PERK: protein kinase R–like ER kinase
PFA: paraformaldehyde
PM: plasma membrane
PNS: peripheral nervous system
PRD: plakin-repeat domain
PrP: prion protein promoter
MT: microtubules
MTOC: microtubule organizing centre
Myr: myristoylation
RT: room temperature
RT-PCR: reverse-transcriptase polymerase chain reaction
SCG10: superior cervical ganglion-10
SERCA: sarco/endoplasmic reticulum Ca^{2+}-ATPase
SH3: Src-homology-3

siRNA: small interfering ribonucleic acid
SMART: Simple Modular Architecture Research Tool
SPAST: spastin
SQSTM: sequestosome
SR: spectrin-repeat
SV2: synaptic vesicle
TA: tibialis anterior
+TIP: microtubule plus-end tracking proteins
TM: transmembrane
TPPP: tubulin polymerization promoting protein
TSA: trichostatin A
TUNEL: terminal deoxynucleotidyl transferase dUTP nick end labeling
UPR : unfolded protein response
VSVG: YFP tagged VSV-Gts0-45
WT: wild type
YFP: yellow fluorescent protein

ACKNOWLEDGEMENTS

First and Foremost I thank my parents, Audrey and Terry Ferrier, and my brothers, Jonathan and Taylor, for their constant support and love, and banter during this and previous endeavors. This accomplishment means little to me without you guys.

This work would not have been completed without the profound influence and expert guidance of my supervisor, Dr. Rashmi Kothary. Furthermore, I must thank Dr. Kothary for his career and life advice, and for the patience he has shown me while dealing with an ongoing medical issue. I truly could not have asked for a better supervisor. I also wish to thank my undergraduate supervisors, Dr. Pliny Smith and Dr. Shubhik DebBurman. While at my alma mater (Lake Forest College) both supervisors provided me opportunities to engage in scientific research and, most importantly, instilled in me the confidence that I could be a researcher. I am deeply indebted to you both.

The experience about which I write has been accumulated over a period of about five years while in the Kothary lab. I am grateful to my colleagues, especially members of the Kothary lab: Yves De Repentigny, Dr. Lyndsay Murray, Dr. Melissa Bowerman Dr. James Knight, Carrie Anderson, Ariane Beauvais, Sabrina Gibeault, Samantha Kornfeld, Armin Yazdani, Dr. Hong Liu, Dr. Scott Ryan, Dr. Tadasu Sato, and *The Core*: Justin Boyer, Kunal Bhanot, John-Paul Michalski, and Ryan O'Meara. I am equally grateful for scientific conversations had with Dr. Maggie Thomson, Dr. Kevin Young, Dr. Scott Ryan, and *The Core*. Our dialogues have helped me see the big picture, thank you! Finally, I am very happy for the support of my girlfriend, Eloise Aubin, during my thesis dissertation! Thank you.

I wish to thank members of my thesis advisory committee, Drs. Chris Kennedy, Antonio Colavita, and John Copeland, for their valuable commentary and recommendations.

I am grateful to the following funding agencies for supporting me during my graduate studies: Ontario Graduate Scholarship in Science, National Aboriginal Achievement Foundation.

Chapter 1
General Introduction

1. Introduction to the Cytoskeleton and Cytoskeletal Linking Proteins

Cell shape and function are highly reliant upon an intricate inner scaffolding of cytoplasmic networks and their associating proteins. The mammalian cytoskeleton is composed of three well-defined filamentous structures: microtubules (MTs, 25 nm diameter), actin microfilaments (MFs, 7–10 nm diameter), and intermediate filaments (IFs, 10–12 nm diameter). Together, these filaments form an elaborate supportive meshwork. MTs, which consist of heterodimer polypeptide chains designated α- and β-tubulin, are exceptionally dynamic, capable of polymerizing, depolymerizing, and moving within the cytoplasm in seconds to minutes (Howard and Hyman, 2003). MTs provide the cell with rigidity and shape, anchor organelles, act as a track for organelle (*e.g.* autophagosome) movement, and are involved in axonal and dendritic growth.

MFs are composed of actin monomers that, similar to MTs, can also undergo polymerization and depolymerization. With the assistance of assembly factors (*e.g.* Arp2/3 complex), these filaments can be further assembled into a variety of higher order structures ranging from lamellipodia to microvilli, each of which has a distinct cellular function (Chhabra and Higgs, 2007). MFs are also involved in structural support of the cell and cellular organelles, and provide trafficking routes throughout the cytoplasm to support signal transduction. Furthermore, they assist in both endo- and exocytosis as well as in muscle contractions, and collaborate with MTs in axon and dendrite extension (Michelot and Drubin, 2011).

Unlike MTs and MFs, IFs do not undergo assembly and disassembly. In neurons nine IF proteins exist many of which have temporal and cell/tissue-specific expression patterns (Lee and Cleveland, 1996). IFs primarily play a structural role throughout the

soma, axon, and nucleus, and are abundant in tissues that undergo mechanical stress, for example, the epidermis, muscle tissues and peripheral nerves (Leung et al., 2002).

Although individual cytoskeletal networks have inherently distinct roles, it has been evident for some time that interactions between these seemingly distinct filament systems exist (Fuchs and Karakesisoglou, 2001; Rodriguez et al., 2003; Suozzi et al., 2012a). Indeed, these interactions underlie many fundamental cellular processes, including cell motility, growth cone guidance, cellular division and chromosomal separation, and wound healing. In order to achieve these disparate functions, the cytoskeleton relies upon numerous cyto-linking proteins, including one family of proteins named the *plakins*. In mammalian cells, there exist seven protein members within this family including dystonin/bullous pemphigoid antigen 1 (BPAG1, hereafter referred to as dystonin), desmoplakin, plectin, microtubule–actin cross-linking factor (MACF), envoplakin, periplakin, and epiplakin. The proteins within this family are exceptionally large (200–800 kDa) and all share a common plakin domain with the exception of epiplakin (Sonnenberg and Liem, 2007). Furthermore, plakins are also endowed with different combinations of structural domains (*e.g.* actin-binding domain (ABD), spectrin-repeat (SR)-containing rod domain, and microtubule-binding domain (MTBD); Leung et al., 2002). This amalgam of domains enables plakins to have dual capacities, such as simultaneously cross-linking cytoskeletal filaments or linking filaments to junctional complexes and organelles.

Plakin family members are commonly found in tissues that undergo mechanical stress, such as epithelial and muscle tissues, and peripheral nerves (Leung et al., 2002). Within epithelial cells, some plakins (*e.g.* dystonin-e or desmoplakin) can localize to both

IFs and filament attachment sites (*e.g.* desmosomes and hemidesmosomes), which are situated at the plasma membrane, and in turn provide the cell structural stability (Ruhrberg and Watt, 1997). Furthermore, certain plakins (*e.g.* dystonin or plectin) are capable of modulating the dynamics of all three cytoskeletal filaments (Leung et al., 2001a, 2002). It is therefore not surprising that deficiencies in plakin proteins can have grave complications, not only at the cellular level but also at an organism level. Indeed, pathological change to most plakin proteins results in development of human disease. These human disorders involve tissue fragility, skin blistering, and muscular dystrophies, and are the consequence of autoimmune disorders or are inherited through mutations in plakin genes (Sonnenberg and Liem, 2007). Moreover, plakin proteins, such as dystonin and MACF, are critical in the development and survival of neurons in both mice and humans (Brown et al., 1995; Sanchez-Soriano et al., 2009; Goryunov et al., 2010; Edvardson et al., 2012).

Dystonin is also considered a member of the spectraplakin family of proteins (Roper et al., 2002). Similar to plakins, spectraplakins are giant (>500 kDa) evolutionary conserved multifunctional cytoskeletal proteins that can modulate different cytoskeletal elements simultaneously (Suozzi et al., 2012a). The dystonin gene (*Dst*) is characterized as having tissue-specific promoters and an abundance of exons that are alternatively spliced yielding differentially expressed protein isoforms that localize to distinct cellular regions where they perform unique cellular functions (Fig. 1).

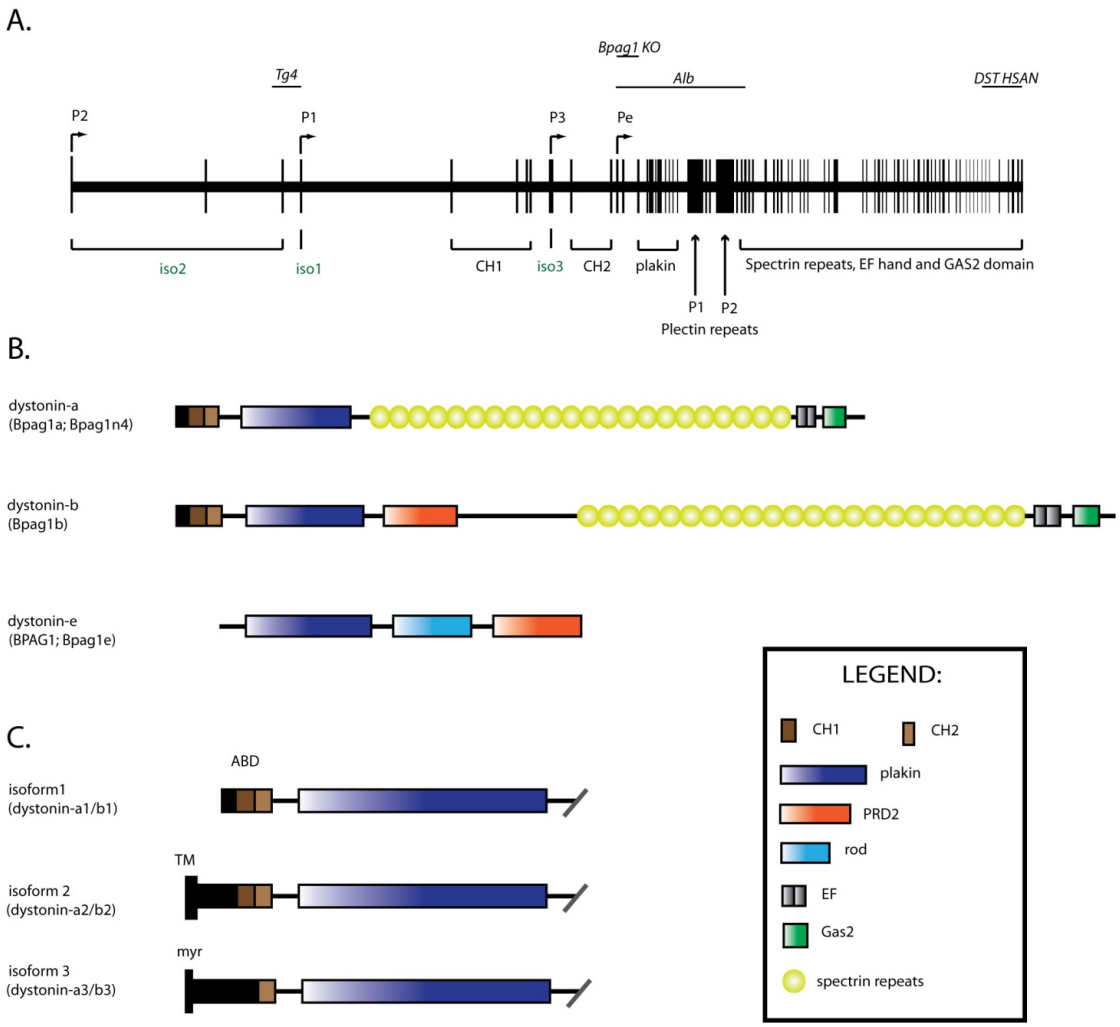

Figure 1. Schematic diagram of the dystonin gene, tissue-specific dystonin isoforms, and the unique N-termini of the dystonin-a/b isoforms. (A) The *Dst* locus in mice and humans spans 400 kb and 500 kb, respectively, and comprises >100 exons in both. Alternative splicing of the first 5′ exons yields three distinct dystonin-a/b isoforms (iso1, iso2, and iso3), and dictates domain structure of each isoform. The 5′ region of the gene also contains coding regions for the calponin homology domains (CH1 and CH2) and a plakin domain. The middle region of the gene contains exons that encode plectin repeats and spectrin repeats (SRs), while the 3′ region of the gene also harbors SRs, a pair of EF

hands, and a GAS2 domain. Putative promoters (P1, P2, P3) and known promoters (Pe) drive the tissue-specific expression of dystonin-a/b/e isoforms. Known mutations in the mouse and human dystonin locus include the $dt^{Tg4/Tg4}$ mutation, caused by a 45 kb transgene insertion and deletion of exons unique to dystonin-1 and -2 (iso1 and iso2). The dt^{Alb} lesion results from a deletion-insertion eliminating exons 12 through 46 and disrupts all known major dystonin transcripts. The dt^{tm1efu} (Bpag1 knockout [KO]) was generated through homologous recombination and affects all known dystonin-a isoforms. The homozygous recessive human dystonin mutation results in hereditary sensory and autonomic neuropathy type 6 (HSANVI). HSANVI is caused by a frame-shift mutation in the 3′ region of the gene. (Adapted fromYoung and Kothary (2007).) (B) The *Dst* locus produces three major tissue-specific dystonin isoforms, including a neuronal isoform (dystonin-a), a muscle isoform (dystonin-b), and an epithelial isoform (dystonin-e), each of which comprises different domains. (C) Isoforms of dystonin-a and -b. Dystonin-a/b1 contain a unique N-terminal region followed by CH1 and CH2 domains in tandem. Dystonin-a/b2 contains a highly conserved N-terminal transmembrane (TM) domain followed by a CH1 and CH2 domain in tandem. Dystonin-a/b3 harbor a conserved myristoylation motif (myr) followed by a single CH2 domain. Figure was adapted from (Ferrier et al., 2013)

2. Dystonin Gene Organization and Isoform Diversity

2.1. The Dystonin Gene

Our understanding of the *Dst* gene and its tissue-specific transcripts has greatly increased over the years 1991–2010. The murine *Dst* gene is located on chromosome 1 and is approximately 400 kb in length, whereas the human gene is located on chromosome 6p12 and is 500 kb in length (Leung et al., 2001a; Pool et al., 2005). In both rodents and humans, the gene encompasses >100 exons. In rodents, *Dst* has four tissue-specific promoters expressing dystonin in the epidermis, central and peripheral nervous systems, and muscle (Fig. 1A). Furthermore, alternative splicing of the gene yields three tissue-specific isoforms in neurons and muscle, each of which carries out unique cellular functions (Fig. 1B,C).

The initial impetus to understand the *Dst* gene arose half a century ago, in 1963, when researchers identified the spontaneous mouse mutant, which they named *dystonia musculorum* (*dt*) (Duchen et al., 1964). When the *dt* mutation was present in the homozygous state, mice displayed pronounced sensory neuron degeneration and severe ataxia at approximately 2 weeks postnatal development (Duchen et al., 1964; Duchen, 1976). In future, several other *dt* alleles would arise and lead to a better biological understanding of movement disorders (Schlager and Dickie, 1967; Janota, 1972; Thornburg and Hanker, 1975; Messer and Strominger, 1980a; Sotelo and Guenet, 1988). While a great deal of knowledge was gained on the *dt* disorder, the gene responsible for *dt* remained unknown.

The epithelial isoform (Bpag1e) was the first characterized protein encoded by the *Dst* gene. It is a major autoantigen in patients suffering from bullous pemphigoid, the

most frequent autoimmune subepidermal blistering disease in humans (Stanley, 1993; Di Zenzo et al., 2012). In keratinocytes, the outermost and most predominant cell type of the epidermis, Bpag1e, localizes to hemidesmosomes and binds keratin IFs, serving as an intracellular bridge and providing cellular integrity (Stanley, 1993).

In 1995, two separate lines of research led to the discovery of the neuronal isoforms of the *Dst* gene responsible for the *dt* phenotype (Brown et al., 1995; Guo et al., 1995). In an effort to understand both the biological function and the role of Bpag1e in the human autoimmune skin blistering disorder bullous pemphigoid, Guo et al. generated *Bpag1* null mice. In this approach, Guo et al. targeted the 5′ end of the coding region of the epithelial protein by homologous recombination. Ablation of this region of the gene led not only to skin blistering in the mice but also to a movement disorder and sensory nerve degeneration indistinguishable from that of *dt* mice. Complementation analysis between the knockout mice and *dt* mice would prove that these mice were allelic. This work suggested that in addition to the Bpag1e isoform, the *Dst* locus likely encoded a neuronal isoform (or isoforms).

In the second study, this question of the *dt* causative gene was addressed simultaneously by following up on a previously identified *dt* allele, $dt^{Tg4/Tg4}$. The dystonin-deficient $dt^{Tg4/Tg4}$ line was created in 1988 when researchers generated a mouse hsp68 promoter-lacZ transgenic mouse (*Tg4*) for the purposes of studying heat-shock protein gene regulation (Kothary et al., 1988). Unexpectedly, homozygous mice belonging to the *Tg4* line of transgenic animals displayed a limb in coordination phenotype similar to that previously reported by Duchen in the 1960s for the *dt* mice. Breeding of heterozygous mice from the *Tg4* line with those of a *dt* line from the Jackson

Laboratory revealed that the *Tg4* mutation was allelic to *dt*. By sequencing the 5′ region encompassing the transgene insertion, Brown et al. determined the affected gene, termed dystonin, was part of the same transcriptional unit as Bpag1e (Brown et al., 1995a). It was also demonstrated that the *Dst* gene encoded two novel neuronal transcripts. These novel transcripts were derived from distinct neuronal transcription start sites and encoded exons 5′ to an ABD (Fig. 1A) (Brown et al., 1995; Yang et al., 1996).

2.2. Dystonin Isoform Diversity

Through multiple tissue-specific promoters, three major spectraplakin isoforms were defined including the neuronal isoform [dystonin-a (17.2 kb transcript, 615 kDa)], the muscle isoform [dystonin-b (22.2 kb transcript, 834 kDa)], and the original Bpag1 epithelial isoform [(dystonin-e, (8.6 kb transcript, 302 kDa)] (Fig. 1B) (Leung et al., 2001a). The predominant neuronal and muscle transcripts identified in this study shared a similar coding sequence, including an N-terminal ABD domain and plakin domain, SR-containing rod domain, and a C-terminal pair of EF hand calcium-binding motifs and an MTBD composed of a GAS2 homology domain. However, the dystonin-b transcript differed from the dystonin-a transcript in that it contained a 6 kb region composed of four additional exons in the middle of the molecule encoding a putative IF-binding domain (IFBD). (For detailed description of the structural and molecular properties of dystonin see Appendix 1.1)

Subsequent detailed analyses of the 5′ portion of the *Dst* gene demonstrated that alternative splicing of 5′ exons gives rise to three unique neuronal and muscle isoforms, namely dystonin-a1/b1, dystonin-a2/b2, and dystonin-a3/b3 (Fig. 1C) (Jefferson et al.,

2006; Young et al., 2006). Upstream of the ABD, dystonin-a1/b1 and dystonin-a3/b3 are composed of a single 5′ exon, whereas the dystonin-a2/b2 comprised five 5′ exons (Jefferson et al., 2006; Young et al., 2006). These alternatively spliced 5′ exons of the dystonin-a/b isoforms are highly conserved among human and mouse. Moreover, these unique 5′ exons encode different domains in each isoform. For instance, dystonin-a1 contains 30 unique amino acid residues followed by a CH1 and CH2 domain in tandem, whereas dystonin-a2 contains a conserved N-terminal transmembrane domain upstream of the CH1 and CH2 domains. Dystonin-a3 encodes a putative myristoylation motif upstream of a single CH2 domain. These unique N-terminal regions preceding the ABD domain of dystonin-a1-3 impart cell-specific localization and function (Jefferson et al., 2006; Young and Kothary, 2008; Ryan et al., 2012b). Taken together, alternative splicing of distinct 5′ exons within the *Dst* gene provides the cell a repertoire of unique dystonin-a isoforms.

2.3 Isoform-Specific Domains — the transmembrane and myristoylation domains

Their three unique amino-terminal regions further characterize the dystonin-a/b isoforms (Fig. 1C). Evidence suggests that these unique N-terminal sequences dictate the biological functions of dystonin isoforms by influencing the subcellular localization of each isoform (Young et al., 2003a, 2006; Jefferson et al., 2006). Within the N-terminal regions of dystonin isoforms, a transmembrane domain and a myristoylation motif have been identified thus far. The transmembrane (TM) region is unique to dystonin-a2 and -b2 and is not found in other plakin family members (Young et al., 2006; Young and Kothary, 2007). The addition or removal of the TM domain in dystonin-a2 fusion

constructs either directs these proteins to or away from membranes of the perinuclear region. On the basis of the body of evidence demonstrating the perinuclear localization of dystonin-a2 and its interaction with the MF and MT cytoskeleton, it has been suggested that dystonin-a2 may regulate organelle integrity such as the nucleus, endoplasmic reticulum (ER), and Golgi complex (Young et al., 2006; Young and Kothary, 2008). Loss of dystonin-a2 function may in turn lead to impaired structural organization, organelle dysfunction, and precipitate the demise of *dt* sensory neurons.

Unlike dystonin isoforms 1 and 2, the dystonin isoform-3 does not harbor a full ABD and was not observed to colocalize with actin stress fibers. Rather, the N-terminal isoform-3 displayed a cortical localization, which is likely attributed to the presence of a unique myristoylation motif. The myristoylation signal promotes membrane binding and is found upstream of the N-terminal CH2 domain (Jefferson et al., 2006)

3**. Expression and Subcellular Localization**

3.1. Temporal and Spatial Expression of Dystonin-a in the Nervous System

Dystonin-a is expressed in the spinal cord and brain at various embryonic and postnatal time points, including embryonic (E9.5–E16.5), postnatal (P3 and P42) and adult stages. Dystonin-a expression is highest at sexual maturity (P42) (Bernier et al., 1995). The presence of dystonin-a as early as E9.5 is interesting since the *dt* phenotype is only overtly obvious at approximately 2 weeks postnatal development. This suggests that dystonin-a expression is perhaps dispensable or redundant during early development but clearly indispensible during postnatal development.

In both postnatal sensory and motor neurons, immunohistochemical analyses revealed dystonin-a expression throughout the perikarya, axons, and in preterminal branches in the peripheral and central nervous system (Yang et al., 1996; Dalpé et al., 1998). The DRG contains distinct cell populations including large-, medium- (muscle sensory), and small-caliber (skin and visceral sensory) sensory neurons, each of which has specific physiological properties. Dystonin-a is expressed throughout the DRG, and not restricted to single subgroup (Bernier et al., 1995). Interestingly, however, while dystonin-a is expressed throughout all sensory neuron populations, large- and medium-sized sensory neurons are most affected in the *dt* disorder (al-Ali and al-Zuhair, 1989; Carlsten et al., 2001). Why specific subpopulations of *dt* sensory neurons are more vulnerable to disease is undetermined. Moreover, which dystonin-a isoforms are important in the viability of large- and medium-sized sensory neurons is also unresolved.

Another interesting feature is the significant expression of dystonin-a in the ventral horn during embryogenesis (*i.e.* site of developing motor neurons). Indeed, between E9.5 and E15.5, dystonin-a expression in embryonic motor neurons is equivalent to that of the DRG neurons. At E17.5, however, dystonin-a expression undergoes a substantial decline in embryonic motor neurons compared to the DRG. This transition in expression within embryonic motor neurons is likely why robust degeneration, as seen in DRGs, is not observed. Albeit dystonin-a expression does persist in postnatal motor neurons, and its loss accounts for the *dt* motor neuron pathologies observed later in the disease (Duchen, 1976; Dowling et al., 1997; De Repentigny et al., 2011). Whether these pathologies extend to the distal region of motor neurons (*i.e.*, neuromuscular junctions) is unknown. Dysfunctional neuromuscular junctions are well documented to underlie

movement abnormalities and may be a pathological feature contributing to the ataxia seen in *dt* mice.

In 2001, Leung et al. provided a more comprehensive picture of the *Dst* locus and its major neuronal and muscle isoforms (dystonin-a and dystonin-b, respectively). Transcript expression analyses of these major isoforms described dystonin-a as being highly expressed in the brain and spinal cord, whereas dystonin-b was predominantly expressed in heart and skeletal muscle (Leung et al., 2001a). While dystonin-a1 and -a2 isoforms were highly expressed in the brain, the dystonin-a2 isoform was the major isoform in DRGs. (For further discussion on the temporal and spatial expression of dystonin-a see Appendix 2.1).

3.2 Subcellular Localization and Interactions of Dystonin-a Isoforms

Dystonin-a isoforms are large in size—exceeding 600 kDa—and have limited distinctiveness in amino acid sequence, qualities that have made reagent development (*e.g.* antibodies for specific isoforms) arduous. As such, progress in elucidating the endogenous localization and function of dystonin-a isoforms has been challenging. Nevertheless, by conducting cell transfection experiments using truncated N-terminal (N-terminal region followed by the ABD and/or a plakin domain) or full-length fusion proteins of dystonin-a1, a-2, and a-3, it was determined that the divergent N-termini impart isoform-specific localization and function (Fig. 2) (Young et al., 2003a, 2006; Jefferson et al., 2006).

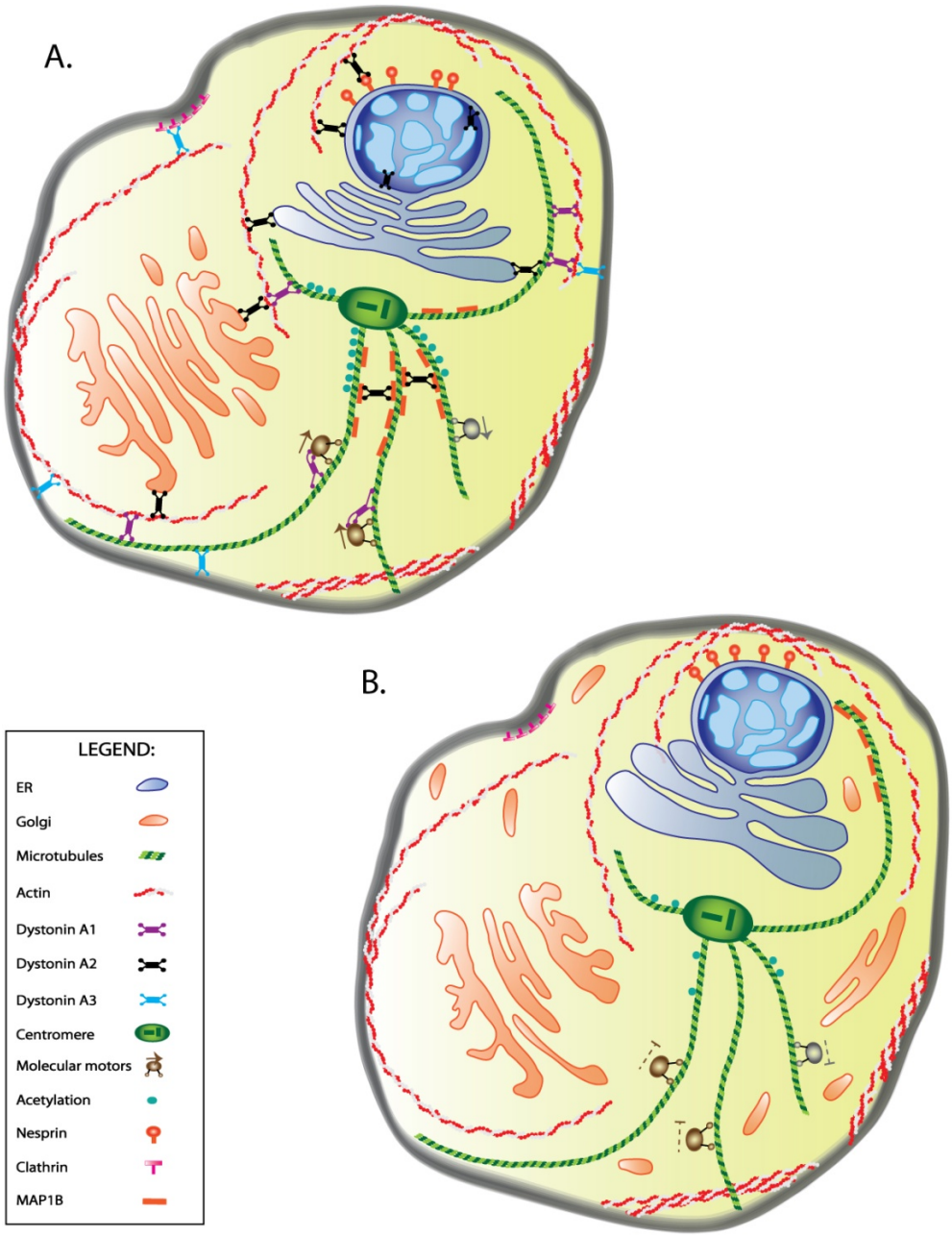

Figure 2. A schematic illustration of the localization of dystonin-a isoforms and their putative functions in the cell. A, B. All three dystonin-a isoforms exhibit distinct cellular localizations and functions. Dystonin-a1 displays a diffuse cytoplasmic and cortical localization pattern, interacting and coaligning with actin MFs and MTs (A).

Dystonin-a1 also interacts with a core component of the retrograde dynein motor complex, dynactin p150Glued (A). Loss of this interaction perturbs neuronal retrograde transport (B). As well, dystonin-a1 tethers endosomal vesicles to the dynein/dynactin motor complex through an interaction with retrolinkin, and loss of this interaction affects retrograde trafficking of endosomes in neurons (not shown). Dystonin-a2 localizes to the intranuclear space and nuclear envelope (NE) where it can associate with the outer NE protein nesprin-3α. Dystonin-a2 also maintains the organization of ER membranes presumably through interactions with cytoskeletal filaments (A). Absence of dystonin-a2 at the ER leads to disorganized ER membranes and ER dyshomeostasis in neurons (B). Dystonin-a2 also associates with the Golgi apparatus and actin MFs, and interacts with MAP1B within the centrosomal region (A). Loss of the dystonin-a2/MAP1B interaction displaces MAP1B from the centrosomal region and disrupts tubulin acetylation, Golgi organization, and anterograde trafficking (B). Dystonin-a3 localizes to the cell membrane and interacts with cytoskeletal filaments. A putative interaction between dystonin-a3 and clathrin is depicted at the cell membrane (A). Figure was adapted from (Ferrier et al., 2013)

3.2.1. Dystonin-a1

Full-length dystonin-a1 protein constructs express throughout the cytoplasm and at the plasma membrane where they predominantly colocalize with bundled MTs and to a lesser extent with actin MFs, actin stress fibers and focal contact sites (Young et al., 2006). The bundling of MTs is mediated through the C-terminal MTBD of dystonin-a1. Full-length dystonin-a1 also coaligns with actin MFs and MTs, suggesting dystonin-a1 can cross-link actin MFs and MTs. Outside of its interactions with cytoskeletal filaments dystonin-a1 was also shown to interact with p150Glued, the largest subunit of the dynactin retrograde motor complex (J. J. Liu et al., 2003). In addition to this study, dystonin-a1 was also found to interact with the neuronal-specific endosomal vesicle protein retrolinkin (J.-J. Liu et al., 2007). In neurons, retrolinkin functions as a receptor tethering endosomal vesicles to dynein/dynactin through dystonin-a.

3.2.2. Dystonin-a2

In contrast to dystonin-a1, full-length dystonin-a2 fusion proteins do not localize freely throughout the cytoplasm, nor to the cortical regions. Instead, dystonin-a2 interacts with nuclear and perinuclear membranes (*i.e.* ER and Golgi membranes) through its N-terminal transmembrane domain in neuronal and nonneuronal cells. At the NE, dystonin-a2 interacts with the outer NE protein nesprin-3α, where it may serve a role in nuclear positioning. Given that dystonin-a2 is known to recruit actin filaments to the NE, it seems plausible that the perturbation of the cytoskeleton-NE link via loss of dystonin-a2 could result in the eccentric (*i.e.*, displaced) nuclei observed in *dt* sensory neurons (Duchen et al., 1964; Messer and Strominger, 1980b; Sotelo and Guenet, 1988).

The NE is contiguous with the ER, another site of dystonin-a2 localization (Young and Kothary, 2008). Specifically, dystonin-a2 localizes with markers of rough ER sheets within the soma of neuronal and nonneuronal cell types. Ectopic expression of full-length dystonin-a2 fusion proteins in immortalized kidney cells reorganizes rough ER structures through interactions with actin MFs. This would indicate that dystonin-a2 serves a role in organization at the ER. As rough ER sheets are involved in protein synthesis, trafficking, quality control, and posttranslational modifications (Renvoise and Blackstone, 2010), loss of dystonin-a2 could conceivably impede ER functions through aberrant ER organization.

Full-length dystonin-a2 fusion proteins also localize with Golgi membranes, where they accumulate actin MFs around the organelle. Recently, through work outside this thesis, we ascribed a novel role for dystonin-a2 in the structural organization of the Golgi and flux through the secretory pathway (Ryan et al., 2012a) (for further information, see Appendix 4.0.). Dystonin-a2 appears to mediate Golgi organization through its association with MTs near the centrosome. This is in keeping with the long-held consensus that MTs are essential for Golgi complex organization (Rogalski and Singer, 1984; Ho et al., 1989; Minin, 1997; Thyberg and Moskalewski, 1999). In regards to dystonin-a2 and the Golgi, MACF1B, which shares structural similarities to dystonin, also localizes to the Golgi apparatus where it too imparts a structural organization (Lin et al., 2005). The fact that both proteins are involved in Golgi organization is intriguing, and may represent an evolutionary conserved role among spectraplakins. (Alternative subcellular localizations and interactions of dystonin-a2 and dystonin-a3 isoforms are discussed in the Appendix 2.1.).

In summary, the unique N-terminal regions of each dystonin-a isoform dictate subcellular localization and function. In addition to their role in binding cytoskeletal elements, dystonin-a isoforms can interact with motor protein complexes and transport vesicles, and are endowed with the ability to link membranes and membrane-bound organelles to various cytoskeletal systems.

4. Dystonin Deficiency in Mice and Cell Culture Models

4.1. *dt* Mice

It has been 49 years since the *dt* mouse, an autosomal-recessive mutant of the *Dst* gene, was first observed at the Institute of Animal Genetics in Edinburgh (Duchen et al., 1964). Since then, several other mutant *dt* alleles have been uncovered both at the Jackson Laboratories and laboratories worldwide (Schlager and Dickie, 1967; Messer and Strominger, 1980b; Sotelo and Guenet, 1988). The high frequency of the occurrence of spontaneous *dt* alleles is thought to relate to the large size of the *Dst* gene. Indeed, the *Dst* gene in mice spans 400 kb and is composed of 107 exons (Pool et al., 2005). Pool *et al*. make note of several *dt* alleles including spontaneous mutants (*e.g.* dt^{27J}, dt^{24J}, dt^{Alb}, and dt^{Frk}), two chemically induced mutants, one targeted allele (dt^{tm1Efu}), and one transgene insertion mutant ($dt^{Tg4/Tg4}$). Of these *dt* alleles, only three *dt* mutations ($dt^{Tg4/Tg4}$, dt^{tm1Efu}, and dt^{Alb}) have been characterized at the genomic level (Pool et al., 2005). Work in this thesis has focused on two *dt* strains: $dt^{Tg4/Tg4}$ and dt^{27}.

The $dt^{Tg4/Tg4}$ mutation, which arose through a transgene insertion–deletion, deletes a portion of the 5′ end of the gene, including the exons encoding the ABD (Fig. 1A) (Brown et al., 1995). Loss of this region prevents the expression of both dystonin-a1/b1

and dystonin-a2/b2, but not dystonin-a3/b3 (Young and Kothary, 2007). This suggests that dystonin-a1 and dystonin-a2, but not dystonin-a3, are the chief mediators of *dt* pathogenesis. In contrast, the dt^{27} strain arose through a spontaneous mutation that disrupts the expression of all three dystonin-a isoforms. (For further information *dt* mice see Appendix 3.0.).

As discussed, deficiency in dystonin expression within the nervous system results in the *dt* phenotype. The *dt* phenotype is characterized as a loss of limb coordination beginning at 7–10 days postnatal development (Duchen et al., 1964; Duchen, 1976). As the disease progresses, which it does rapidly, limb movement becomes more uncoordinated, while writhing and twisting of the trunk become increasingly prominent features. Hyperflexion and pronation of foot paws are other documented signs. Although diseased sensory neurons do degenerate, some sensory modalities remain intact including vision and hearing (Dowling et al., 1997). Ultimately, affected mice will die between 2 and 3 weeks of age of causes that have yet to be defined.

4.2. Affected Cell Types of dt Mice

Among the pathological features displayed by *dt* mice, degeneration is most apparent in primary sensory nerves of the DRG and cranial nerves (Duchen et al., 1964; Duchen, 1976; al-Ali and al-Zuhair, 1989). Sensory neuron pathologies are evident as early as E15.5, suggesting that disease progression is gradual, commencing at embryogenesis and continuing through postnatal development (Bernier and Kothary, 1998). As the mice age, the number of axons within sensory roots decreases and sensory receptors (*e.g.* muscle

spindles, Pacinian corpuscles, and Golgi tendon organs) lose their innervation (Duchen, 1976; Dowling et al., 1997).

Outside of sensory neuron degeneration, other cell types are affected in the *dt* disorder. For instance, axonal swellings, indistinguishable from those of *dt* sensory axons, are present in both ventral root and some ventral horn processes at the phenotypic stage (Dowling et al., 1997). Whether these defects extend distally to the neuromuscular junction is not known. As dystonin-a is expressed in the distal region of motor neurons and the fact that *dt* muscles exhibit disorganized cytoskeletal filaments within skeletal muscle and muscle atrophy, the motor unit (*i.e.*, NMJ) becomes a viable contributor to the *dt* disorder (Boyer, Bernstein, & Boudreau-Lariviere, 2009; Dalpe et al., 1999).

Taken together, dystonin-a expression is critical for sensory neuron viability in mice, and serves a function in other cell types of the nervous system. It is conceivable that if *dt* mice were to survive longer, defects in other cell types would be more apparent.

4.3. Hallmark Pathologies of dt Sensory Neurons

Axonal swellings within peripheral and central nerve fibers are a cardinal feature of *dt* pathology (Duchen et al., 1964; Duchen, 1976; al-Ali and al-Zuhair, 1989; Bernier and Kothary, 1998; Saulnier et al., 2002). The axonal swellings are highlighted by accumulations of neurofilaments and disorganized MT networks, and as such, lead to the accumulation of organelles (*e.g.* mitochondria) and smooth vesicles or dense-membrane-bound bodies throughout the axoplasm (Janota, 1972; al-Ali and al-Zuhair, 1989). Neurofilament aggregates were thought to be causative of the *dt* disorder (Leung et al., n.d.; Yang et al., 1996; Dalpé et al., 1998; Tseng et al., 2006). However, when

phenotypically normal transgenic mice that were devoid of axonal neurofilaments were bred onto the *dt* homozygous background, they displayed a normal progression of *dt* pathology (Eyer et al., 1998). Hence, a lack or presence of neurofilaments within the axon does not influence *dt* pathogenesis.

Outside of *dt* axon pathologies, there also exist defects within the sensory neuron perikaryon. Studies have described the *dt* sensory neuron perikarya as containing abnormal accumulations of neurofilaments, F-actin punctae, eccentric nuclei (displacement of the nucleus toward the periphery of the perikaryon) and chromatolysis (a decrease in chromophilic material surrounding the nucleus, caused by rough ER dispersion and expansion of the perikarya) (Duchen et al., 1964; Messer and Strominger, 1980b; Sotelo and Guenet, 1988; Campbell and Peterson, 1992; Young and Kothary, 2008). Taken together, *dt* sensory neuron pathologies extend from the soma through to the axon. The vast majority of these pathologies are likely brought forth as a direct result of deficiencies in cytoskeletal-mediated processes. As cytoskeletal elements are involved in many key biological processes, elucidating the mechanism(s) underlying *dt* pathogenesis is clearly challenging. Moreover, determining which dystonin-a isoform is responsible for the *dt* disorder has also proven difficult. Finally, as the *dt* mouse model shares similar pathological features to human neurodegenerative diseases, a better understating of *dt* pathogenesis will help provide needed insight into the etiology of human neurological disease, particularly hereditary sensory and autonomic neuropathy (HSAN) disorders.

5. Dystonin and Human Disease

In humans, conditions arising through disruptions of the *DST* locus affecting neuronal and muscle isoforms are rarely reported. Although the *DST* gene is relatively large at 500 kb in humans—likely increasing susceptibility to mutations and chromosomal translocations—we presume that any mutation in the *DST* gene is incompatible with human life. Recently, however, deleterious homozygous mutations in *DST* were found to impart a frame-shift mutation resulting in a previously undescribed hereditary autonomic sensory neuropathy in four infants (Edvardson et al., 2012). The frame-shift mutation, which reduces dystonin-a transcript expression, starts at Glu4955 and is thought to lead to a loss of the C-terminus (502 amino acids), which harbors the MTBD. The patients' clinical features are reminiscent of familial dysautonomia (FD), albeit the course and outcome of disease are more severe, and it is ultimately fatal. This newly reported dystonin-related neuropathy was termed hereditary sensory and autonomic neuropathy type 6 (HSAN-VI), and shares clinical features reminiscent of those seen in *dt* mice. Dystonin expression is significantly increased in cultured fibroblasts of two FD patients (Edvardson et al., 2012). In neurons of FD patients, MT disorganization is a common pathological feature (Dalpé et al., 1998; Cheishvili et al., 2011). This disorganization of MT networks is caused by the increased expression of the MT-destabilizing protein called superior cervical ganglion-10 (SCG10). As dystonin-a plays an important role in maintaining MT network integrity within neurons (Dalpe et al., 1998; Yang et al., 1999; Ryan et al., 2012a), the authors of the Edvardson *et al*. study surmise that increased dystonin expression is playing a compensatory role in FD patient's fibroblasts. Taken together, these findings are the first to report an inherited mutation in the neuronal

isoform of dystonin in humans, and suggest dystonin's MT organization activity could be playing a compensatory role in FD.

In other studies, a case report has described an individual with a chromosomal translocation at t(6; 7)(p11–p12; q22) that interrupts the dystonin-a/b transcript (Vincent et al., 2008). The patient's clinical features were characterized by encephalopathy, severe motor and mental retardation and delayed visual maturity. As well, altered splicing of the *DST* gene has been identified in a cohort of patients suffering from Parkinson's disease (Elliott et al., 2012).

6.0. *dt* Sensory Neuron Degeneration: a multi-isoform disease?

The loss of dystonin-a1 and dystonin-a2 is causal of the *dt* disorder. How these isoforms mediate disease and which dystonin-a isoform is more important to disease pathogenesis is unclear. Dystonin-a2 was found to be the more unique isoform and least likely to be compensated for by any related protein (*e.g.*, microtubule actin cross linking factor (MACF) and plectin) (Young and Kothary, 2007). Moreover, dystonin-a2 expression predominated in sensory ganglia, the most severely affected tissue of *dt* mice, and poorly expressed in non-neuronal tissues (Bernier et al., 1995). These initial descriptions of the dystonin-a2 variant suggested it might be the principle mediator of *dt* pathogenesis (Young and Kothary, 2007, 2008). As dystonin-a2 localizes to multiple organelles (*i.e.*, nucleus, ER, Golgi), and is capable of manipulating organelle morphology; it was believed that loss of dystonin-a2 may perturb organelle structure, and as such, organelle function. In support of this notion, $dt^{Tg4/Tg4}$ sensory neurons display perikaryal defects and show altered expression of ER-related proteins (Kevin G Young &

Kothary, 2008). Dystonin-a1, on the other hand, is also involved in fundamental neuronal processes, including anterograde and retrograde trafficking (Liu et al., 2003a, 2007b). Past studies have observed a bidirectional impairment in transport in *dt* neurons (De Repentigny et al., 2003; Liu et al., 2003b, 2007a)**.** As disturbance of these processes are well-known to underlie many neurological diseases (Perlson et al., 2010), including HSANs (Rottier, Annelies; Baets, Jonathan; Timmerman, Vincent; Janssens, 2012), dystonin-a1 remains a potential contributor in *dt* pathogenesis.

6.2. Autophagy and Neurodegeneration

Macroautophagy (hereafter referred to as autophagy) in neurons is a constitutive process that degrades long-lived organelles and protein aggregates via the degradative compartments of the endosomal-lysosomal system (Yang and Klionsky, 2010). This process is essential in the maintenance of neuronal homeostasis (Hara et al., 2006)(Komatsu et al., 2006), and is implicated in various neurodegenerative diseases (Wong and Cuervo, 2010). Within peripheral nerves the transport of autophagosomes is highly reliant upon the neuronal cytoskeleton and it's constituent parts, particularly motor proteins (Jahreiss et al., 2008; Kimura et al., 2008; Monastyrska et al., 2009). Indeed, perturbing the stability of MTs or motor protein function disrupts autophagic flux (Aplin et al., 1992; Ravikumar et al., 2005; Köchl et al., 2006), which in turn can lead to the demise of the cell. Autophagic flux is defined by the formation and trafficking of a mature autophagosomes that ultimately fuse with and are degraded by lysosomes and/or endosomes. A number of studies indicate that dystonin-a isoforms have the potential to negatively influence aspects of the autophagic pathway (through impaired MT stability or

motor protein activity, for instance) (Liu et al., 2003b, 2007a; Bhanot et al., 2011; Ryan et al., 2012a), which would conceivably contribute to the demise of *dt* sensory neurons.

7.0. Objective and Specific Aims:

The causal dystonin-a isoform(s) and the pathological mechanisms activated upon their loss remain unknown in *dt* sensory neurons. The $dt^{Tg4/Tg4}$ mouse is devoid of both dystonin-a1 and -a2, but not dystonin-a3, indicating these isoforms to be the principle mediators of *dt* pathogenesis. Which dystonin-a isoform(s) is/are most important to the *dt* disorder is unknown. Furthermore, as multiple biological functions of dystonin-a isoforms (maintaining MT and organelle stability, and intracellular trafficking) coincide with the autophagic pathway, it is undetermined whether autophagic homeostasis is preserved in *dt* sensory neurons. Finally, while degenerating sensory neurons are the critical determinant driving the overt movement disorder in *dt* mice, expression of dystonin in both motor neurons and muscle tissues, suggests dystonin-a/b loss-of-function may impart defects on the *dt* motor unit. Our hypothesis is therefore threefold:

Hypotheses:

1) Loss-of function of dystonin-a/b isoforms imparts cytoskeletal defects in both motor neurons and muscle cells, thus leading to NMJ pathologies.

2) Dystonin-a2 loss-of-function leads to ER dysfunction and subsequent degeneration of *dt* sensory neurons by altering ER structure.

3) Dystonin-a loss-function impairs both MT stability and motor protein activity, which in turn disrupts autophagic flux and contributes to the demise of *dt* sensory neurons.

To address our hypotheses, we have established the following aims:

Aim 1: Explore the impact dystonin-a/b lose-of-function imparts on pre-synaptic motor neurons and muscle endplates in *dt* mice.

Aim 2: Elucidate the roles dystonin-a isoforms (dystonin-a1/-a2) play in mediating *dt* sensory neuron degeneration through isoform-specific loss-of-function analyses.

Aim 3: Determine if exogenous expression of dystonin-a2 rescues the *dt* phenotype.

Aim 4: Characterize the role of dystonin-a as a mediator of protein aggregate and organelle degradation in neurons.

These aims will provide insight into the causal dystonin-a isoforms and the pathological mechanisms underling *dt* pathogenesis. Furthermore, as *dt* mice share myriad pathological features with that of other neurodegenerative diseases, work in this thesis will aid in the future design of more targeted therapies to delay the onset of disease onset in various neurodegenerative diseases.

Chapter 2

Motor Unit Abnormalities in *Dystonia musculorum* Mice

Motor unit abnormalities in *Dystonia musculorum* mice

Yves De Repentigny[1•], Andrew Ferrier[1,2•], Scott D. Ryan[1], Tadasu Sato[1], Rashmi Kothary[1,2*]

1 Ottawa Hospital Research Institute, Ottawa, Ontario, Canada, 2 Department of Cellular and Molecular Medicine and the Department of Medicine, University of Ottawa, Ottawa, Ontario, Canada

Citation: De Repentigny Y, Ferrier A, Ryan SD, Sato T, Kothary R (2011) Motor Unit Abnormalities in Dystonia musculorum Mice. PLoS ONE 6(6): e21093. doi:10.1371/journal.pone.0021093

Editor: Mel B. Feany, Brigham and Women's Hospital, Harvard Medical School, United States of America

Received March 17, 2011; Accepted May 18, 2011; Published June 15, 2011

Funding: This work was funded by the Canadian Institute of Health Research (CIHR). The funders had no role in study design, data collection and analysis, decision to publish, or preparation of the manuscript.

• These authors contributed equally to this work.

Author Contributions

Conceived and designed the experiments: YDR AF SDR RK. Performed the experiments: YDR, AF (figures 1, 7, 8, 10) and SDR. Analyzed the data: YDR AF SDR TS. Contributed reagents/materials/analysis tools: YDR AF SDR TS RK. Wrote the paper: AF YDR RK.

Abstract

Dystonia musculorum (*dt*) is a mouse inherited sensory neuropathy caused by mutations in the dystonin gene. While the primary pathology lies in the sensory neurons of *dt* mice, the overt movement disorder suggests motor neurons may also be affected. Here, we report on the contribution of motor neurons to the pathology in dt^{27J} mice. Phenotypic dt^{27J} mice display reduced alpha motor neuron cell number and eccentric alpha motor nuclei in the ventral horn of the lumbar L1 spinal cord region. A dramatic reduction in the total number of motor axons in the ventral root of postnatal day 15 dt^{27J} mice was also evident. Moreover, analysis of the trigeminal nerve of the brainstem showed a 2.4 fold increase in number of degenerating neurons coupled with a decrease in motor neuron number relative to wild type. Aberrant phosphorylation of neurofilaments in the perikaryon region and axonal swellings within the pre-synaptic terminal region of motor neurons were observed. Furthermore, neuromuscular junction staining of dt^{27J} mouse extensor digitorum longus and tibialis anterior muscle fibers showed immature endplates and a significant decrease in axon branching compared to wild type littermates. Muscle atrophy was also observed in dt^{27J} muscle. Ultrastructure analysis revealed amyelinated motor axons in the ventral root of the spinal nerve, suggesting a possible defect in Schwann cells. Finally, behavioral analysis identified defective motor function in dt^{27J} mice. This study reveals neuromuscular defects that likely contribute to the dt^{27J} pathology and identifies a critical role for dystonin outside of sensory neurons.

Introduction

The cytoskeleton is a critical intracellular determinant of cellular morphology and is required for fundamental processes during cell differentiation and function (Howard and Hyman, 2003; Chhabra and Higgs, 2007). The Plakin protein family comprises high-molecular weight multi-domain molecules, which include desmoplakin, plectin, envoplakin, periplakin, Microtubule Actin Crosslinker Factor 7 (Acf7/MACF) and dystonin/bullous pemphigoid antigen 1 (dystonin/Bpag1). These proteins all share the plakin domain and various other cytoskeletal domains, allowing for simultaneous cross-linking and modulation of cytoskeletal elements (Sonnenberg and Liem, 2007). Mutations in genes encoding plakin proteins lead to axonal outgrowth defects, neuronal degeneration, and tissue fragility (Leung et al., 2002).

The importance of dystonin/Bpag1 is highlighted in the *dystonia musculorum* (*dt*) mouse. The *dt* mice were originally described as a spontaneously arising mutant with a severe movement disorder (Duchen et al., 1964). To date, several *dt* mouse models exist including numerous spontaneous mutants (e.g. dt^{24J}, dt^{27J}, and dt^{Alb}), 4 chemically induced mutants, 1 targeted allele (dt^{tm1Efu}), and 1 transgene insertion (dt^{Tg4}) (Pool et al., 2005). In only three *dt* mutations (dt^{Tg4}, dt^{tm1Efu}, and dt^{Alb}) have the mutations been characterized (Kothary et al., 1988; Guo et al., 1995) (Fig. 1).

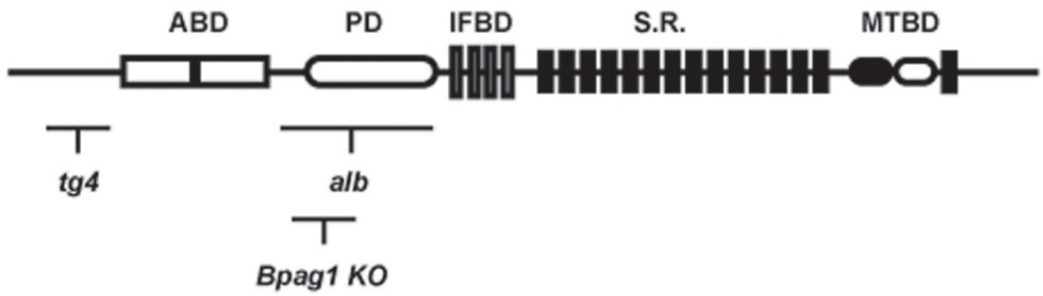

Figure 1: Schematic representation of domains within the dystonin protein and the relative location of mutations for some *dt* alleles.

The dt^{tg4} mutant line has a 45-kb transgene insertion at the 5′ region of the gene, resulting in deletion of coding regions upstream of the actin binding domain (ABD). The dt^{Alb} allele is a spontaneous mutant line resulting in a deletion within the central region of the gene (plakin domain [PD] and intermediate filament binding domain [IFBD]). The dt^{tm1efu} (Bpag1 knock out [KO]) was generated through homologous recombination. All three *dt* alleles affect all known neuronal and muscle dystonin transcripts and are effectively null mutations. The *Dst* gene includes coding sequences for an ABD, PD, IFBD, Spectrin Repeats (S.R.), and Microtubule Binding Domain (MTBD).

The *dt* phenotype, manifesting at ~2 weeks postnatal, is characterized by loss of limb coordination and abnormal posturing of limbs and trunk. The disease progresses rapidly and *dt* mice die in the third week of life of unknown causes. *Dystonin/Bpag1* encodes alternatively spliced epithelial, neuronal and muscle isoforms (Brown, Bernier, Mathieu, Rossant, & Kothary, 1995; Brown, Dalpe, Mathieu, & Kothary, 1995; Leung, Zheng, Prater, & Liem, 2001; Okumura, Yamakawa, Ohara, & Owaribe, 2002; Stanley, 1993). While the epithelial isoform dystonin-e/Bpag1e acts as an autoantigen in the human skin blistering disease bullous pemphigoid, the loss of function of dystonin neuronal and muscle dystonin/Bpag1 isoforms are associated with the *dt* phenotype and underlying pathology in the mouse mutant. The domain architecture of neuronal isoforms can be divided into several parts: an N-terminal actin binding domain, a plakin domain, a central rod region consisting of spectrin-like repeats, a C-terminal region harboring a pair of EF-hand calcium binding motifs and a microtubule binding domain consisting of a GAS2 homology domain as well as a Gly-Ser-Arg repeat region (Leung et al., 2001b; Young and Kothary, 2007) (Fig. 1). Dystonin/Bpag1 is expressed throughout mouse development predominating in neurons of cranial and spinal sensory ganglia (Bernier et al., 1995). As well, dystonin/Bpag1 is expressed in the extrapyramidal motor system, cerebellum and motor neurons (Bernier et al., 1995).

Among the pathological features of various *dt* mouse alleles, sensory neuron degeneration is most apparent. Although the mechanisms mediating degeneration are unclear, much is known about *dt* pathology. Early studies reported the presence of neurofilament (NF) axonal swellings along nerve fibers and a gradual loss of sensory nerve fibers in both the central and peripheral nervous system (Duchen et al., 1964;

Janota, 1972; Duchen, 1976; Sotelo and Guenet, 1988). In addition, eccentricity of nuclei and dispersement of the rough endoplasmic reticulum have been reported in neurons from mice expressing various *dt* alleles (Duchen et al., 1964; Messer and Strominger, 1980a; Sotelo and Guenet, 1988; Young and Kothary, 2008). Moreover, ultrastructure analysis demonstrated the accumulation of organelles within axonal swellings and disorganization of NF and microtubule networks (Janota, 1972; Dalpe et al., 1998). Indeed, the disorganization of cytoskeletal networks likely contributes to the bidirectional impairment of axonal transport in *dt* sciatic nerves (De Repentigny et al., 2003).

In addition to the sensory neuron pathology, some motor neuron defects have also been reported in *dt* mice although the importance to pathology has not been elucidated (Dowling et al., 1997). Improper placement of nuclei and axonal swellings were detected in the ventral root and in the spinal ventral horn at 13 days postnatal (Sotelo and Guenet, 1988; Dowling et al., 1997). Moreover, an abnormal accumulation of hyperphosphorylated intermediate filaments is evident in the perikarya and proximal regions of axons of spinal motor neurons in *dt* mice (Dowling et al., 1997). Examination of *dt* motor neurons revealed accumulation of alpha-internexin, peripherin and NF proteins in axonal swellings and aberrant translocation of alpha-internexin (Tseng et al., 2008). Finally, motor tests have indicated functional impairment in motor activity, exploration, motor coordination, limb coordination, and postural reflexes (Lalonde et al., 2005). Despite these observations, the previous studies fall short of evaluating the impact of motor neuron abnormalities on neuromuscular/NMJ function/pathology in *dt* mice.

In the present study, we have performed a systematic investigation of motor neuron pathology in the spontaneous mouse mutant dt^{27J}. We provide evidence for

neuromuscular defects in the dt^{27J} mouse mutant that likely contribute to the overall neurological phenotype.

Materials and Methods

Mice

dt^{27J} mice have a mutation within the dystonia musculorum locus which occurred in the congenic strain B10.PL(73N)/Sn. These mice were originally identified at The Jackson Laboratory (Bar Harbor, ME) and breeding pairs were obtained from them. The dt^{27J} allele was subsequently maintained in our vivarium facility by mating heterozygous mice. At 1–2 weeks of age, homozygous dt^{27J} mice have difficulty in walking, mainly due to their limb incoordination phenotype. By the third week of life, dt^{27J} mice succumb to the disease and die. Mice were genotyped by polymerase chain reaction amplification of genomic tail DNA using the oligonucleotides (RAS520) sense 5′ GGA TCT GCC CGA CTT TCT GGG 3′ and (RAS521) antisense 5′ CCA AGG TTC ATT GCC TCC GTC 3′. These primers amplify a 400 nucleotide fragment on the wild type allele and a 450 nucleotide polymorphic fragment on the dt^{27J} allele.

Ethics Statement

All experimental protocols on mice were approved by the Animal Care Committee of the University of Ottawa. Care and use of experimental mice followed the guidelines of the Canadian Council on Animal Care.

Spinal motor neuron quantification

Wild type (n = 5) and *dt*^{27J} (n = 5) pups at postnatal day (P)15 were anesthetized with tribromoethanol (Avertin) and perfused transcardially with 3 ml of phosphate buffered saline (PBS) followed by 10 ml of 4% paraformaldehyde (PFA) in PBS. The lumbar L1 spinal cord region was collected and embedded into paraffin, cut in totality in serial sections of 6 μm thickness, deparaffinized in toluene and rehydrated in an alcohol gradient followed by deionized water. Sections were stained with Pyronine Y, washed with water, dehydrated in an alcohol gradient, and finally cleared with toluene and mounted with a coverslip using Permount (Fisher). Sections were examined by light microscopy using a Zeiss Axioplan microscope equipped with a digital camera. Alpha motor neurons were identified based on their location in the gray matter that forms the ventral horn and their large size (nuclear diameter >9–10 μm; cell body diameter >20 μm). Gamma motor neurons (nuclear diameter 7–9 μm) and interneurons (nuclear diameter <6 μm) were identified by their respective nuclear diameters (REXED, 1952; McHanwell and Biscoe, 1981; Lance-Jones, 1982). Alpha motor neurons, gamma motor neurons, and interneurons were counted in every 10th section in the ventral horn of the L1 spinal cord. For the quantification of eccentric alpha-motor nuclei, only L1 ventral horn alpha-motor neurons with distinct nuclei (diameter >9–10 μm) and nucleoli were included.

Antibodies

Eleven primary antibodies were used for immunohistochemistry (IHC) in this study (for details, see Table 1). Secondary antibodies used have been summarized in Table 2.

Table 1: Primary antibodies

Antiserum	Immunogen	Source (cat. no.)	Working dilution	Specificity
Rabbit polyclonal anti-internexin, alpha	Full-length recombinant rat alpha-internexin fused to E. Coli Trp E.	Chemicon International, Temecula, CA (AB5354)	1:250 (I) 1:1000 (W)	Alpha internexin (66 KDa)
Rabbit polyclonal anti-laminin	Protein purified from the basement membrane of Englebreth Holm-swarm (EHS) sarcoma (mouse)	Abcam (ab11575)	1:800 (I)	Laminin is composed of one A chain (400 KDa), one B1 chain (215 KDa),
Anti-myosine Heavy chain Type 1	MyHC (Human) partially purified, pyrophosphate extracted (22 year quadriceps)	Developmental Studies Hybridoma Bank (A4.840)	ud (I)	Adult myosin (200 KDa)
Anti-myosine Heavy chain Type 2A	Purified myosin origin from bovine subcutaneous muscle	Developmental Studies Hybridoma Bank (SC-71)	ud (I)	Immunoblotting (2A myosi heavy chain)
Anti-myosine Heavy chain Type 2B	Purified myosin bovine skeletal muscle (fetal, 3 months)	Developmental Studies Hybridoma Bank (BF-F3)	ud (I)	Recognized 2B myosin heavy chain
Anti-myosine Heavy chain Type 2X	Myosin co-absorbed with an adjuvant peptide to gold particles rabbit retractor bulbi muscle	Developmental Studies Hybridoma Bank (6H1)	ud (I)	Immunoblotting (2X myosin heavy chain) from rat and rabbit limb muscle (200 KDa)
Mouse monoclonal anti-neuron-specific nuclear protein (NeuN)	Purified cell nuclei from mouse brain	Chemicon International, Temecula, CA (MAB377B)	1:100 (I) 1:200 (W)	It recognizes 2-3 bands in the 46–48 KDa range (manufacturer's technical information).
Mouse monoclonal anti-neurofilament RT-97 specific for phosphorylated NF-H	Wistar rat neurofilaments	Developmental Studies Hybridoma Bank (RT-97)	1:3 (I)	It recognizes a band at 200 KDa corresponding to NF-H protein (manufacturer's technical information).
Mouse Monoclonal anti-synaptic vesicle 2 (SV2)	Synaptic vesicle Protein 2	Developmental Studies Hybridoma Bank (SV2)	1:100 (I)	It recognizes a band at ~95 KDa (manufacturer's technical information)
Mouse Monoclonal anti-dystrophin (C-terminus, clone Dy8/6C5)	Synthetic polypeptide re-presenting the last 17 amino acids at the car-Boxy terminus of the human dystrophin molecule (SSRGRNTPGKPMREDTM)	Vector Laboratories (VP-D505)	1:20 (I) 1:10–1:25 (W)	Skeletal muscle, single Strong band at ~400 KDa (manuf0acturer's technical information).
Mouse monoclonal anti-pan-axonal neurofilaments	Pan-axonal neurofilament	Covance (SMI-312R)	1:1000 (I) 1:1000 (w)	SMI-312 is a specific marke for axons in tissue sections and cultures.

(I), Immunohistochemistry, (W), Western blot, ud (undiluted).
doi:10.1371/journal.pone.0021093.t001

Table 2: Secondary Antibodies:

Secondary antibodies	Company	Dilution
Goat anti-mouse 555	Invitrogen	1:500–1:2000
Goat anti-rabbit 555	Invitrogen	1:200
Donkey anti- rabbit 488	Invitrogen	1:500
Goat anti-mouse 488	Invitrogen	1:200

doi:10.1371/journal.pone.0021093.t002

Immunofluorescence

L1 spinal cord segments were collected from wild type (n = 3) and *dt*^{27J} (n = 3) pups at P15 for cryostat sections of 6µm thickness. Sections were air dried at room temperature (RT) then rinsed in PBS and fixed in 4% PFA. P15 wild type and *dt*^{27J} mice were perfused and fixed in 4% PFA and brain sagitally sectioned at a thickness of 10 µm. Sections were rinsed twice in PBS, followed by incubation in blocking solution (10% goat serum and 0.3% Triton-X100 in PBS) for 45 min at RT. The sections were incubated overnight at 4°C with primary antibody in blocking solution with the exception of anti-alpha internexin which, was administered for 2 h at RT. After incubation, slides were rinsed in PBS three times and then incubated with appropriate secondary antibodies in blocking solution for 1 h at RT. Sections were then rinsed in PBS and incubated for 15 min with 3,3′-diaminobenzidine (DAPI) (1∶10,000) in blocking solution. Finally, slides were rinsed in PBS and slides were mounted with Fluorescent Mounting Medium (Dako) and examined under a fluorescent microscope.

Sample preparation for electron microscopy

Wild type (n = 3) and *dt*^{27J} (n = 3) mice were anesthetized at P15 via intraperitoneal injection of tribromoethanol. Mice were perfused transcardially with 3 ml of PBS followed by 10 ml of Karnovsky's fixative (4% PFA, 2% glutaraldehyde, and 0.1 M cacodylate buffer in PBS, pH 7.4). Ventral and dorsal roots of spinal nerves were collected under a stereomicroscope. Samples were fixed for 4 h in Karnovsky's fixative at 4°C. Samples were subsequently washed 2 times in 0.1 M cacodylate buffer for 1 h and once overnight at RT. After 1 h of post-fixation in 1% osmium tetroxide in 0.1 M

cacodylate buffer at 4°C, all samples were washed twice for 5 min each in distilled water. Samples were dehydrated, infiltrated in spur monomer (Electron Microscopy Sciences) with 3 changes over 24 h at RT and embedded in liquid spur resin at 70°C overnight. Ultrathin sections (70 nm) from ventral and dorsal roots of the spinal nerve were cut in cross-section using an ultramicrotome. Sections were placed on a 300 mesh copper specimen grid and counterstained in 5% uranyl acetate and Reynold's lead citrate, and then observed by transmission electron microscopy. Ventral and dorsal root sections of 0.3 µm were mounted on glass slides and stained with toludine blue, and then examined by light microscopy using a Zeiss Axioplan microscope equipped with a digital camera. Motor axons were compared between wild type and dt^{27J} pups, and quantified.

Quantification of the total number of NMJ endplates in skeletal muscle

Wild type (n = 3) and dt^{27J} (n = 3) mice were analyzed at P15. For each mouse, one leg was dissected to collect the TA and the EDL muscles for cryostat sections (14 µm) and the other leg was used to isolate individual myofibers. Muscle cross-sections were incubated with primary antibody to dystrophin 10% goat serum and 0.3% Triton-X100 in PBS for 1 h at 25°C. Sections were then washed three times in the same buffer, incubated with the secondary FITC conjugated antibody for 1 h at 25°C, and then washed three times in buffer. Sections were then incubated with alpha-bungarotoxin (Alexa Fluor 488 conjugate, 1:500, Invitrogen) in PBS at room temperature for 30 min, rinsed twice in PBS, and mounted with Fluorescent Mounting Medium (Dako). NMJs were examined under a fluorescent microscope. The total number of myofibers by cross-section area in the middle of each muscle was multiplied by the number of NMJs by individual myofiber

observed. By this approach we have quantified the total number of NMJs for each muscle analyzed.

Single mouse myofiber isolation

Entire EDL and TA muscles including tendons were collected from wild type (n = 6) and *dt*^{27J} (n = 6) mice at P15. Each muscle was digested for a period of 1 h or more in 0.2% collagenase 1 in Dulbecco's minimum essential medium (DMEM) (supplemented with antibiotics [pen/strep]) at 35°C with agitation to ensure that myofibers were loosened from the muscle bulk. After digestion, each muscle was transferred in a Petri dish coated with horse serum containing DMEM medium with 10% horse serum. Single mouse myofiber isolation was performed by trituration using sterile Pasteur pipettes. A set of pipettes with bore diameter of 1 to 2.5 mm was made with a diamond knife and the sharp ends were fire polished. All pipettes were coated with 10% horse serum in DMEM medium (Bekoff and Betz, 1977; Rosenblatt et al., 1995; Keire et al., 2013). All single myofibers from each muscle were fixed in 4% PFA for 10 min followed by a single wash in PBS and a single wash in 0.1 M glycine/PBS. Single myofibers were incubated with alpha-bungarotoxin in PBS (1:2500) and DAPI (1:10,000) for 1 to 4 h with agitation, then washed 3 times for 10 min each. Slides with single myofibers were mounted with fluorescent mounting medium. Fifty myofibers from each muscle were examined under a fluorescent microscope and NMJ endplate quantification was performed. The NMJ endplate morphology was examined in 25 individual wild type myofibers/muscle and also in 25 individual *dt*^{27J} myofibers/muscle.

Immunohistochemistry and evaluation of NMJ endplates from groups of myofibers

EDL and TA muscles were isolated from P15 wild type (n = 5) and dt^{27J} (n = 5) pups and fixed for 30 min in 2% PFA. After fixation all muscles were washed in 0.75% glycine in PBS at RT and then in PBS. Groups of myofibers were isolated from EDL and TA muscles under a stereomicroscope, then blocked with 10% goat serum in 0.4% Triton X-100/PBS for 30 min at RT, and incubated overnight at 4°C with primary antibodies. Incubation with the secondary antibodies was performed the following day at RT for 1 h. Groups of myofibers were also incubated with alpha-bungarotoxin Alexa Fluor 555 conjugate (1∶10, Invitrogen) for 20 min at RT. Finally, three to four stained myofiber bundles were mounted in Fluorescent Mounting Medium (Dako). Images were taken on a Zeiss LSM 510 confocal microscope with a 40x oil objective, equipped with filters suitable for FITC/Cy3/fluorescence. For the blind quantification analysis, a minimum of 50 NMJs was analyzed for the control and experimental groups. To objectively differentiate between normal and abnormal pre-synapses (axonal swellings) any bulb-like structure exceeding 2 μm in diameter was deemed abnormal. Samples were imaged under identical sample and exposure settings. The number of perforations/endplate defined maturity of the post-synaptic endplate in mice, as previously discussed (Kariya et al., 2008).

Fiber typing

TA muscles were isolated from P15 wild type (n = 3) and dt^{27J} (n = 3) pups. TA muscle cryosections (12 μm) were fixed with 4% PFA and washed with PBS, then with buffer (0.3% Triton-X100 in PBS). Muscle sections were blocked with 5% horse serum in PBS

for 10 min and then incubated overnight with primary antibodies. Sections were then washed 3×10 min in PBS and incubated for 1 hour with secondary antibodies. Sections were rinsed in PBS, and slides mounted with Fluorescent Mounting Medium (DAKO). Sections were examined under a fluorescent microscope to detect any fiber type grouping.

Muscle fiber size quantification

Cross-sections of P15 TA muscles (wild type and dt^{27J}) were stained with hematoxylin and eosin and observed by light microscopy. TA muscle fiber area was measured in μm2 (MIRAX program) for 200 myofibers in the central region of the TA muscle for wild type (n = 6) and dt^{27J} mice (n = 6).

FluoroJade staining

FluoroJade B (Millipore, MA) staining was performed according to the method of (Schmued & Hopkins, 2000). Briefly, 10 μm sagittal brain sections were dried at 50°C, hydrated with descending grades of ethanol, and finally rinsed with deionized water. The sections were dipped in potassium permanganate solution (0.06% weight/vol) for 10 min, washed with deionized water, and further incubated with FluoroJade B (0.0004% vol/vol) and 0.1% vol/vol glacial acetic acid coupled with DAPI counterstained for 20 min in the absence of light. The sections were washed with deionized water, dried at 50°C, dipped in xylene, and coverslipped with Permount. Sections were then visualized under epifluorescence and photomicrographs captured using a Zeiss Axiovert 200M microscope equipped with AxiovisionLE V 4.8.0.0. FluoroJade positive neurons from two replicates

of two independent experiments were quantified by counts of DAPI counterstained nuclei with correction for profile and section thickness according to the method of(Guillery and August, 2002).

Motor neuron quantification in the brainstem

Wild type and dt^{27J} brainstem sections (trigeminal nerve of the pons) were immunostained with anti-NeuN primary and anti-mouse 555 secondary antibodies. Sections were then visualized under epifluorescence and photomicrographs captured using a Zeiss microscope equipped with Axiovision LE V4.8.00. Alpha motor neurons were defined as larger NeuN-positive neurons. Motor neurons from two replicates of two independent experiments were quantified by counts of DAPI counterstained nuclei with correction for profile and section thickness according to the method of [36].

Motor behavior tests at P15

For each motor test, 5 different dt^{27J} pups and 5 different wild type littermates were evaluated. Five attempts per mouse per test were performed. Rod test: Motor performance was evaluated in the mice by measuring their capacity to grasp a flexible rod by their hind legs. Mice were placed at the center of the horizontal rod by their hind legs and the latency to fall was measured. Righting reflex: dt^{27J} and wild type mice were evaluated for the time to right themselves from a supine position. Negative geotaxis: dt^{27J} and wild type mice were placed for 30 sec on a wire grid inclined at 90° to assess negative geotaxis. For methodology, see (Narver et al., 2008).

Results

Motor neurons are not spared in dt^{27J} mice

In the present study, we focused on the spontaneous mutant dt^{27J}. While the dt^{27J} allele does not result in any large genomic rearrangements or deletions at the *dt* locus, it does have a significant impact on neuronal and muscle dystonin transcript expression (Pool et al., 2005). It is believed that small rearrangements or deletions, or point mutations causes either reduced transcription or altered transcript stability. Like all known *dt* mice, dt^{27J} mice are homozygous recessive, heterozygous (dt^{27J} /+) mice fail to manifest a phenotype. Moreover, the dt^{27J} and dt^{Tg4} strains are allelic and failed to genetically complement, indicating that the dt^{27J} mutation is specific to the dystonin gene (Bernier et al., 1998).

Previous work has shown that sensory neuron loss is a primary defect in *dt* mice. Here, we set out to determine whether motor neurons are also affected in the homozygous dt^{27J} mutant mice. Since dt^{27J} mice are smaller than their wild type counterparts, we decided to measure the number of alpha and gamma motor neurons, and interneurons within a defined area. At P15, a moderate loss of alpha motor neurons and gamma motor neurons (29.40% and 23.58%, respectively) was evident in ventral horns of the L1 spinal cord from dt^{27J} mice when compared to age matched control wild type mice (Fig. 2A-B). In contrast, there was no significant difference in the number of interneurons at the L1 level between wild type or dt^{27J} mice (Fig. 2C). Eccentric alpha-motor nuclei in the ventral horn were 2.3 times more abundant at the L1 spinal cord level of dt^{27J} mice compared to wild type mice at P15 (Fig. 3). Thus, defects are readily observed in alpha and gamma motor neurons from dt^{27J} mice.

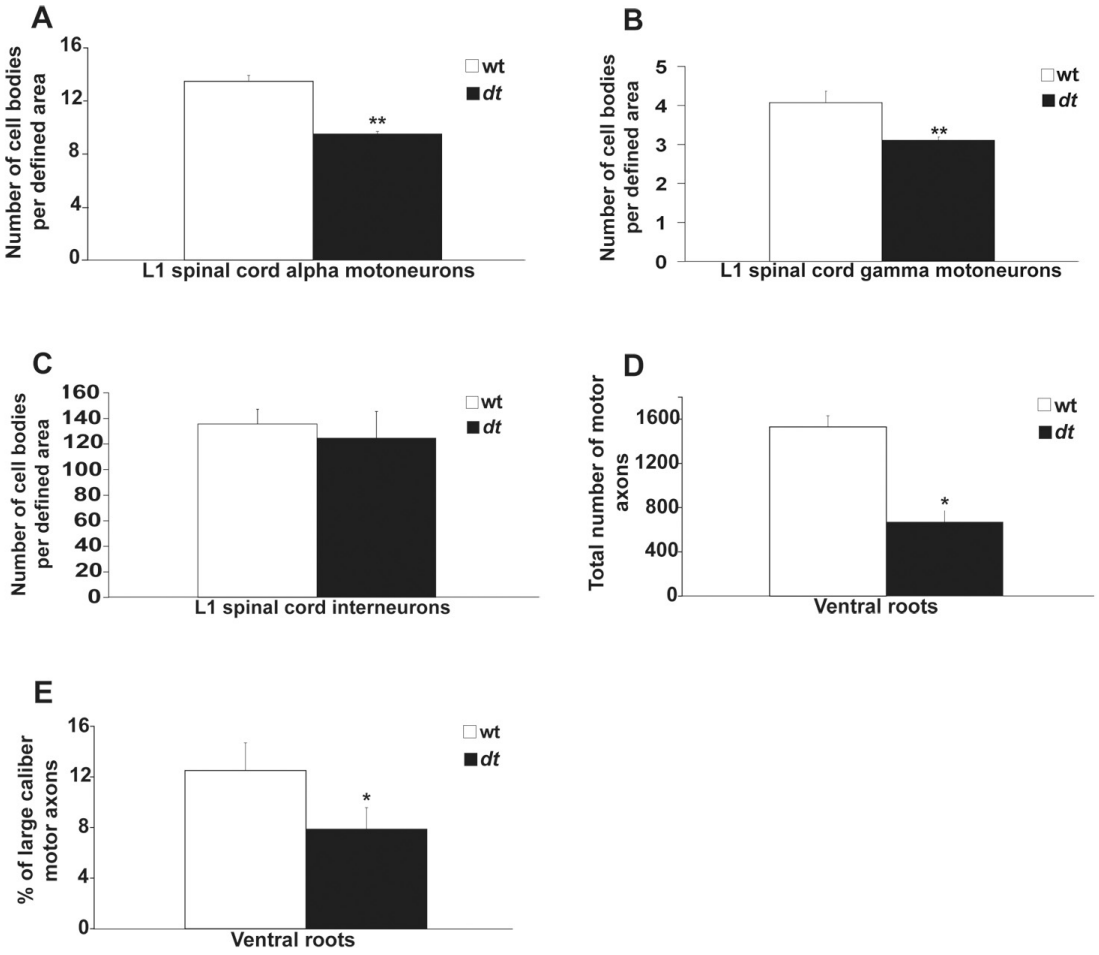

Figure 2. The number of alpha and gamma motor neurons is reduced in *dt*^{27J} L1 spinal cord. A–B. A graphical representation showing the number of neurons per defined area of the ventral horn of the L1 spinal cord from wild type (n = 5) and severely affected *dt*^{27J} (n = 5) mice at P15. There is a significant difference in the number of alpha motor neurons and gamma motor neurons between wild type and *dt*^{27J} mice (**p<0.01, student t-test). C. No significant difference was observed between wild type and *dt*^{27J} mice in the number of interneurons per defined area of the ventral horn of the L1 spinal cord (p>0.05, student t-test). D. The total number of motor axons is significantly reduced in *dt*^{27J} mice (*p<0.05, student t-test). E. The percentage of large caliber motor axons is reduced in *dt*^{27J} ventral roots by comparison to wild type ventral roots (*p<0.05, student t-test).

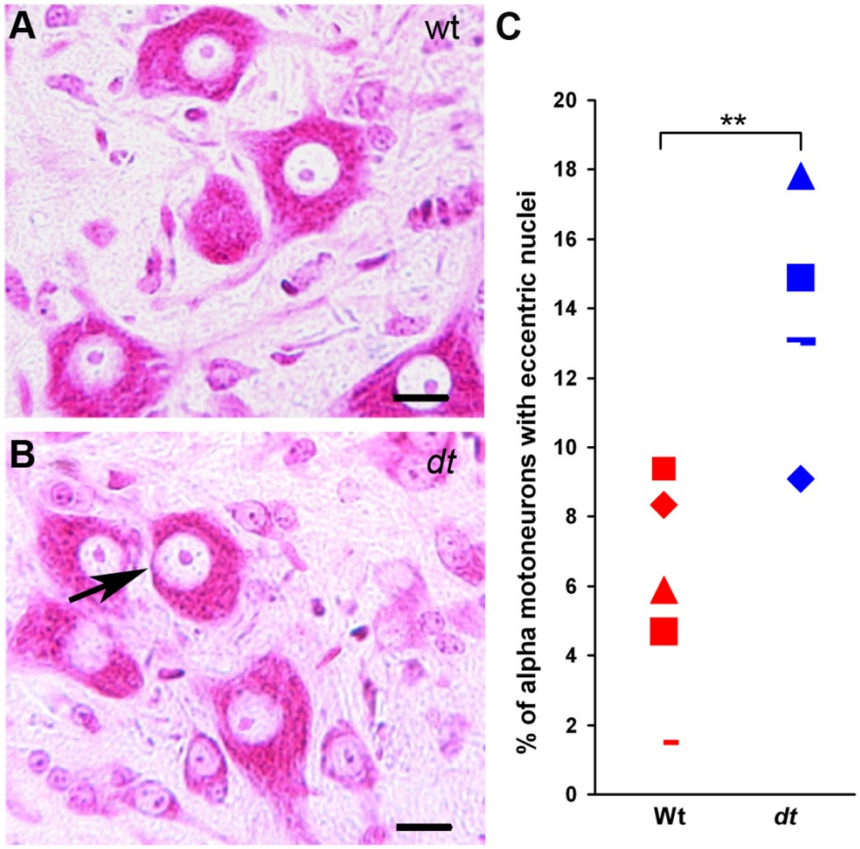

Figure 3. Increase in the number of eccentric alpha motor neuron nuclei in *dt*^{27J} L1 spinal cord compared to wild type L1 spinal cord. A. Normal alpha motor neurons were observed by light microscopy after Pyronine Y staining of the ventral horn of the L1 spinal cord from a wild type mouse. B. Eccentric motor nucleus (black arrow) observed in L1 spinal cord from a *dt*^{27J} mouse. Scale bar, 10 µm (A, B). C. Dot plot graph showing the percentage of eccentric alpha motor neuron nuclei in the L1 spinal cord region as observed in individual wild type (n = 5) and *dt*^{27J} (n = 5) mice (**p<0.01, student t-test).

Neurofilament accumulation in dt^{27J} motor neuron cell bodies

NF accumulation within sensory neurons of *dt* mice is a pathological hallmark of the disease (Sotelo and Guenet, 1988; Dowling et al., 1997; Tseng et al., 2006, 2008). To determine if dt^{27J} sensory as well as motor neurons manifest NF accumulation, we performed immunostaining using anti-alpha-internexin and anti-NF antibodies. Although previous studies have shown that alpha-internexin levels are diminished in DRGs of *dt* mice (Tseng et al., 2006), other work has shown that there is no change in levels (Young et al., 2007). Alpha-internexin staining was observed in P15 wild type DRG perikarya, while only a few cells displayed phosphorylated NF (RT-97) staining (Fig. 4A). Although dt^{27J} DRGs revealed far fewer cell bodies, there were still cells staining for alpha-internexin and a relative increase in the number of cells staining with RT-97 (Fig. 4B). Perikarya of wild type ventral horns were devoid of phosphorylated neurofilament staining (Fig. 4C, white arrows), while alpha-internexin staining was observed in dendrites and axons of ventral horn cells (Fig. 4C). In contrast, dt^{27J} ventral horn staining revealed an abnormal accumulation of phosphorylated NFs within the perikarya of motor neurons (Fig. 4D, white arrows). This staining was also observed in dendrites and axons of neuronal cells (Fig. 4D). Similarly, alpha-internexin staining was observed in ventral horn cells (dendrites and axons; Fig. 4D). To determine whether the pathology described above translated into motor neuron cell death, we conducted TUNEL staining using L1 spinal cord tissue sections of wild type and dt^{27J} mice. This assay did not reveal any TUNEL positive cells in the L1 spinal cords of dt^{27J} mice (Fig. 4E-G). Thus, in addition to sensory neurons, motor neurons from *dt* mice also display abnormal accumulation of NFs.

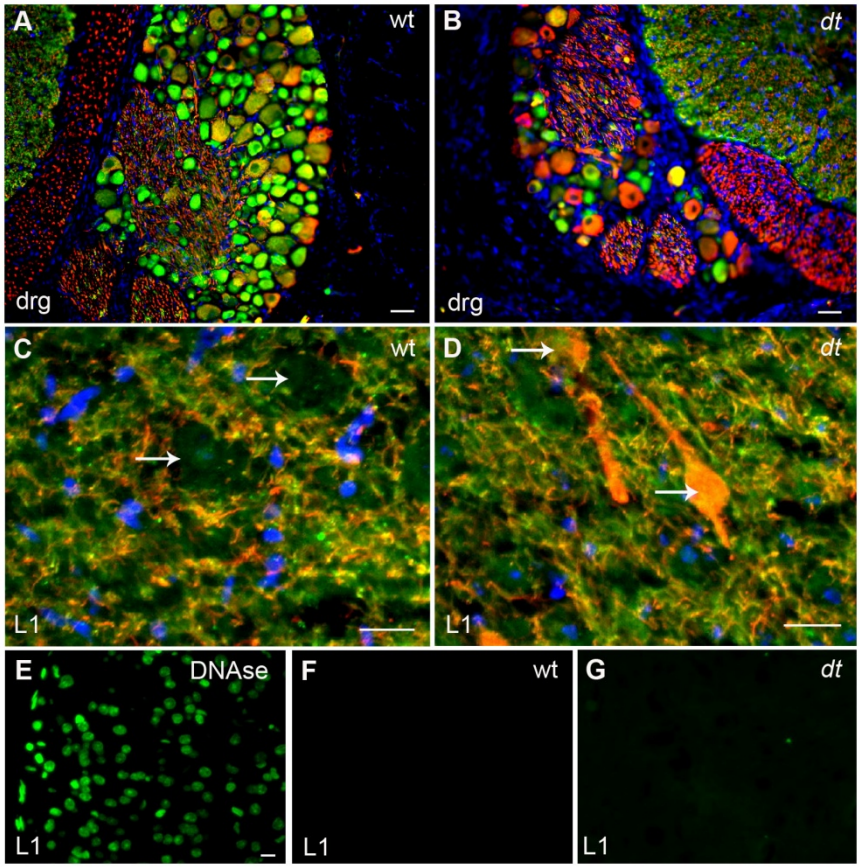

Figure 4. Analysis of neurofilament and alpha-internexin immunostaining in the dorsal root ganglion and ventral horn of the L1 spinal cord of wild type and *dt*^{27J} mice. A. Alpha-internexin staining (green) in cell bodies within the DRG of wild type mice. RT-97 staining of phosphorylated neurofilaments (red) is limited to a few cells. B. The DRG from *dt*^{27J} mice is smaller and has fewer ganglion cells per DRG compared to wild type DRGs. RT-97 staining of phosphorylated neurofilaments (red) can be readily seen within the perikarya of many ganglion cells while alpha-internexin staining (green) is also present in a few cells. Scale bar, 10 μm (A, B). C. Ventral horn region of the L1 spinal cord from a wild type mouse showing no accumulation of phosphorylated neurofilaments within the perikarya of motor neurons (white arrows). Alpha-internexin staining (green) is observed throughout the dendrites and axons of the motor neurons. D.

Ventral horn region of the L1 spinal cord from a *dt*^{27J} mouse showing abnormal accumulation of phosphorylated neurofilaments within the perikarya (white arrows) of motor neurons. In comparison, alpha-internexin staining (green) is observed in dendrites and axons. Scale bar, 20 μm (C, D). E–G. TUNEL assay showed no labeling in cells in the L1 spinal cords of WT and *dt*^{27J} mice (F–G). DNase treated L1 spinal cords were used as a positive control (E). Scale bar 10 μm.

dt^{27J} dorsal and ventral spinal root axons are amyelinated and reduced in number

Previous studies have reported that dt^{27J} peripheral sensory nerves exhibit hypomyelination, reduction in axonal caliber, and amyelinated axons (Bernier et al., 1998). Here, we explored the integrity of L1 dorsal and ventral spinal roots via toludine blue staining. In contrast to wild type controls (Fig. 5A), dt^{27J} spinal roots had fewer sensory axons, and contained axonal swellings (Fig. 5B). Wild type ventral root analysis showed myelinated axons of different calibers (Fig. 5C), while dt^{27J} ventral roots manifested amyelinated intermediate and large caliber axons (Fig. 5D). While normal axonal myelination of different axon calibers was present in dt^{27J} ventral roots, amyelinated axons were evident in different regions of the ventral root. Upon quantification, the total number of motor axons within dt^{27J} ventral roots was significantly lower than that in wild type ventral roots. A total of 1531 axons ±100.02 (SE, n = 3) within wild type ventral root cross-sections were recorded compared to 670 axons ±101.51 (SE, n = 3) within dt^{27J} ventral root cross-sections (p = 0.02, Fig. 2D). Of the motor axon number reduction in dt^{27J} ventral roots, large caliber axons (≥5 μm) were predominantly affected. Wild type ventral roots comprised 12.51% ±2.19 (SE, n = 3) large caliber axons, while dt^{27J} ventral roots had fewer large caliber axons (7.89%±1.68; SE, n = 3, p = 0.03, Fig. 2E).

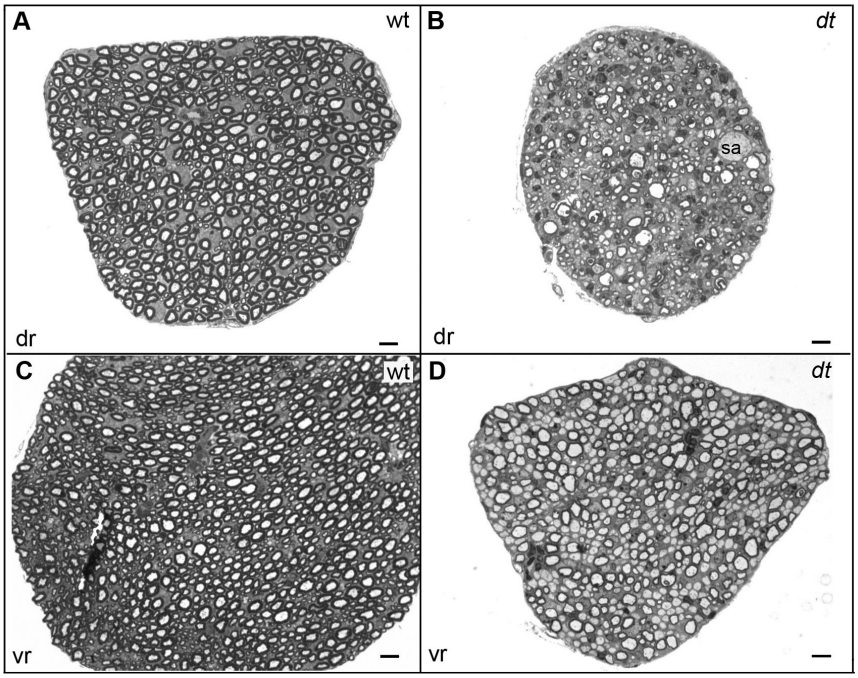

Figure 5. Defects in *dt*^{27J} ventral motor and dorsal sensory spinal roots. Toludine blue staining of transverse sections of dorsal (dr) (A–B) and ventral (vr) roots (C–D). A. Dorsal sensory root from wild type mice showing many myelinated axons. B. Dorsal sensory root from *dt*^{27J} mice showing several abnormalities including fewer axons, axons undergoing degeneration, and axonal swellings (sa). The *dt* dorsal sensory root is also smaller than the wild type counterpart. C. Ventral motor root from wild type mice showing many myelinated axons of different calibers. D. Ventral motor root from *dt*^{27J} mice showing a mixture of myelinated and amyelinated axons of different calibers. Several large and intermediate caliber amyelinated axons are detected. The *dt* ventral motor root is smaller than the wild type counterpart and the axons are more compacted. Scale bar, 5 μm (all panels).

To obtain a better understanding of the myelination defects, P15 wild type and *dt*^{27J} spinal ventral roots were examined via electron microscopy. Other than a few amyelinated small caliber axons, we found that axons of different calibers – large, intermediate and small – manifested normal myelination in the wild type samples (Fig. 6A). In contrast, *dt*^{27J} ventral roots of the L1 spinal nerve displayed numerous amyelinated axons of different calibers (Fig. 6B). Normal myelinated axons of different calibers were also present in the *dt*^{27J} preparation.

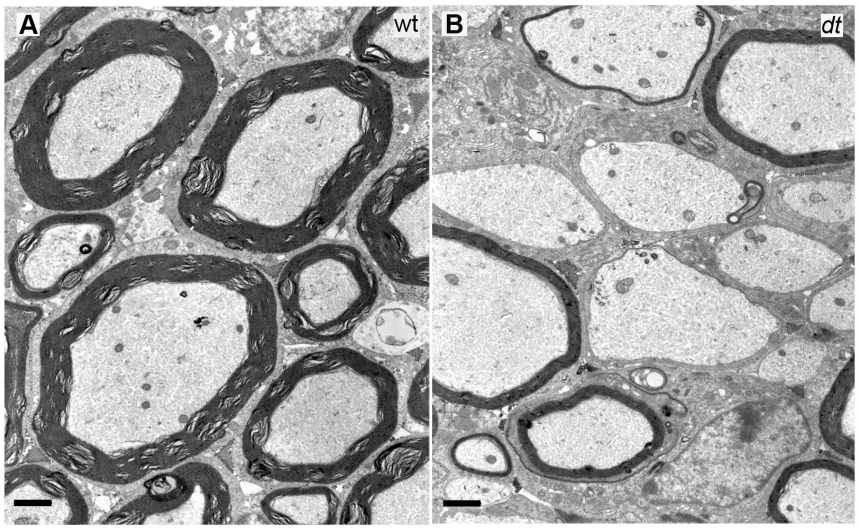

Figure 6. Ultrastructural analysis of ventral motor roots of the L1 spinal nerve of wild type and *dt*^{27J} mice. Transverse sections of ventral motor roots from P15 wild type and *dt*^{27J} mice were prepared for electron microscopy. A. Ventral motor root from wild type mice showing normal myelinated axons of different calibers. B. Ventral motor root from *dt*^{27J} mice showing hypomyelinated and amyelinated axons of large and intermediate caliber. Scale bar, 1 μm.

NMJ endplates from dt^{27J} muscle are reduced in number and appear less mature

Initial observations of *dt* mice reported partial motor denervation of muscle and atrophy of some groups of muscle fibers (Duchen et al., 1964). To determine whether defects located more distally at the NMJ were present, we examined endplates of EDL and TA muscles in P15 mice. We first investigated whether a difference existed between the total number of wild type and dt^{27J} TA and EDL endplates. We found a modest reduction (14.6%, 549±27 endplates, $n = 3$, $p<0.05$) in the total number of dt^{27J} EDL endplates compared to wild type (643±24 endplates, $n = 3$). Consistent with this, the reduction observed in dt^{27J} TA was 7.7% (2875±50 endplates, $n = 3$, $p<0.01$) in comparison to wild type TA muscle (3116±36 NMJs, $n = 3$). No difference in the number of endplates was observed in the dt^{27J} diaphragm in comparison with wild type diaphragm (data not shown). While each EDL and TA dt^{27J} myofiber had an endplate, there were fewer *dt* myofibers when compared to wild type myofibers (data not shown), and this could account for the reduction in endplate number.

The formation of mature NMJ endplates is established at approximately E17 and undergoes further structural and functional change during postnatal development. Maturity is achieved when endplates acquire the characteristic "pretzel-like" pattern with numerous folds (perforations) (Sanes and Lichtman, 2001). Morphological analysis (Fig. 7) of NMJ endplates revealed that 5.22% of endplates were immature (without perforations) in wild type TA muscle and 94.88% began to have one or more perforations. We observed 90% of NMJ endplates manifested two patterns – an elongated pattern and an oval-like pattern (Fig. 7D, E respectively), while the remaining 10% showed various patterns. This patterning was consistent between wild type and dt^{27J} in

TA muscle (Fig. 7D', E'). In contrast however, there was an increase in the percentage of immature endplates in both the TA and EDL muscles from dt^{27J} mice (Fig. 7F). These results indicate an increase in the number of immature endplates (lacking perforations) in dt^{27J} mice.

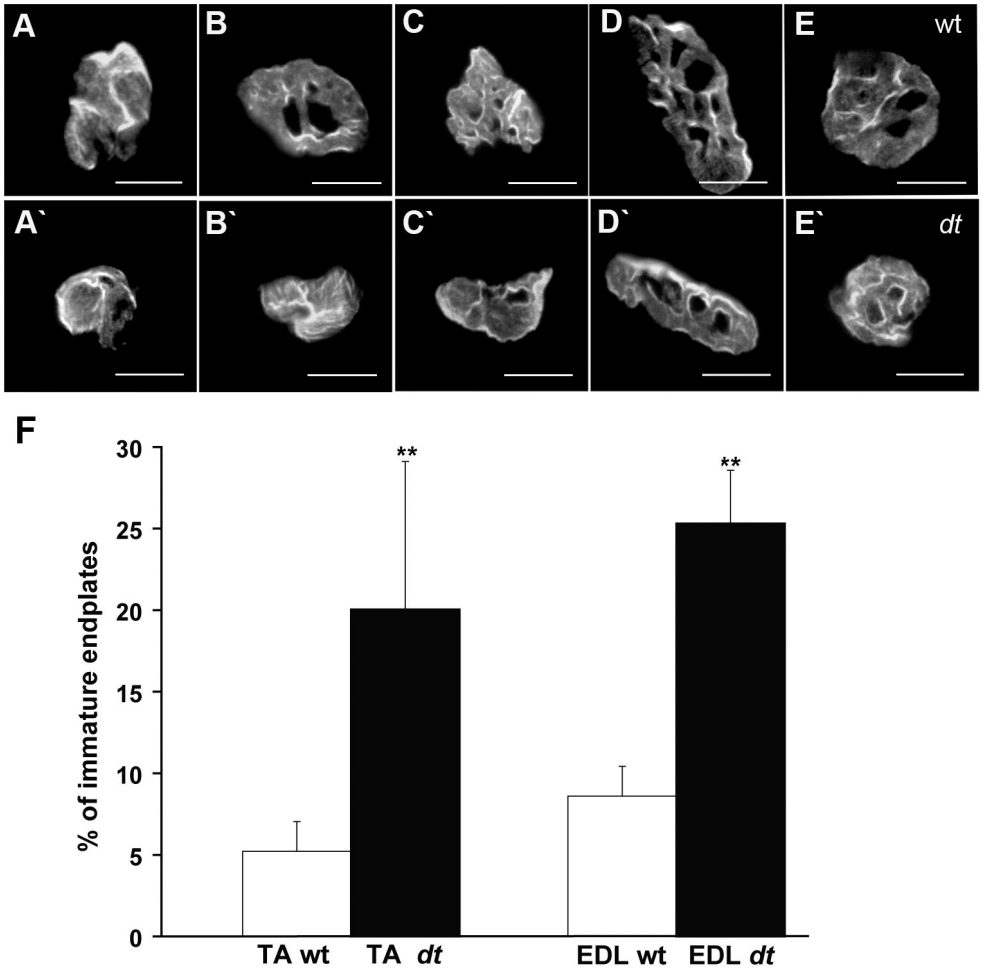

Figure 7. Endplates from *dt*^{27J} mice are poorly developed. Representative photomicrographs showing NMJ endplate morphology in TA muscle at P15 from wild type (A–E) and *dt*^{27J} (A'–E') mice. *dt*^{27J} TA muscles show more immature NMJs (A'–B') when compared to wild type (A–E). The endplate morphology included two different patterns frequently observed – an elongated form with domains (D and D') and oval-like form with domains (E and E'). Scale bar, 15 µm. F. Graphical representation showing the percentage of immature endplates in TA and EDL muscles from wild type (n = 5) and *dt*^{27J} (n = 5) mice at P15 (**p<0.01, student t-test).

Abnormalities at the NMJs in P15 dt^{27J} mice include reduced axonal branching, pre-synaptic swellings, and motor neuron denervation

Based on the defects found at dt^{27J} TA endplates in P15 mice, we decided to examine aspects of P15 TA and EDL NMJs, in particular motor neuron innervation, axonal branching and distal motor neuron integrity. Antibodies against NF protein and synaptic vesicles (SV2) were employed to visualize distal axons and nerve terminals, respectively. Acetylcholine receptors (AChRs) were stained with labeled bungarotoxin. Pre-terminal axons and nerve terminals of TA and EDL muscle from dt^{27J} mice, but not from control littermates were characterized by axonal swellings (Fig. 8F and L). Approximately 40% of TA NMJs and 20% of EDL NMJs from P15 dt^{27J} mice displayed bulb-like accumulation at nerve terminals (Fig. 8M). Motor endplates apposed to these terminals were small and structurally poorly developed (*i.e.*, less perforated) (Fig. 8D and J). Additionally, P15 TA and EDL NMJs from P15 dt^{27J} mice exhibited reduced axonal branching, which accompanied the axonal swellings and the poorly developed endplates (Fig. 8A–L, and N). We did not detect poly-innervated endplates as previously described (Duchen et al., 1964). Collectively, these results suggest that axonal swellings within the distal nerve and poor terminal arborization are previously unappreciated aspects of *dt* pathology.

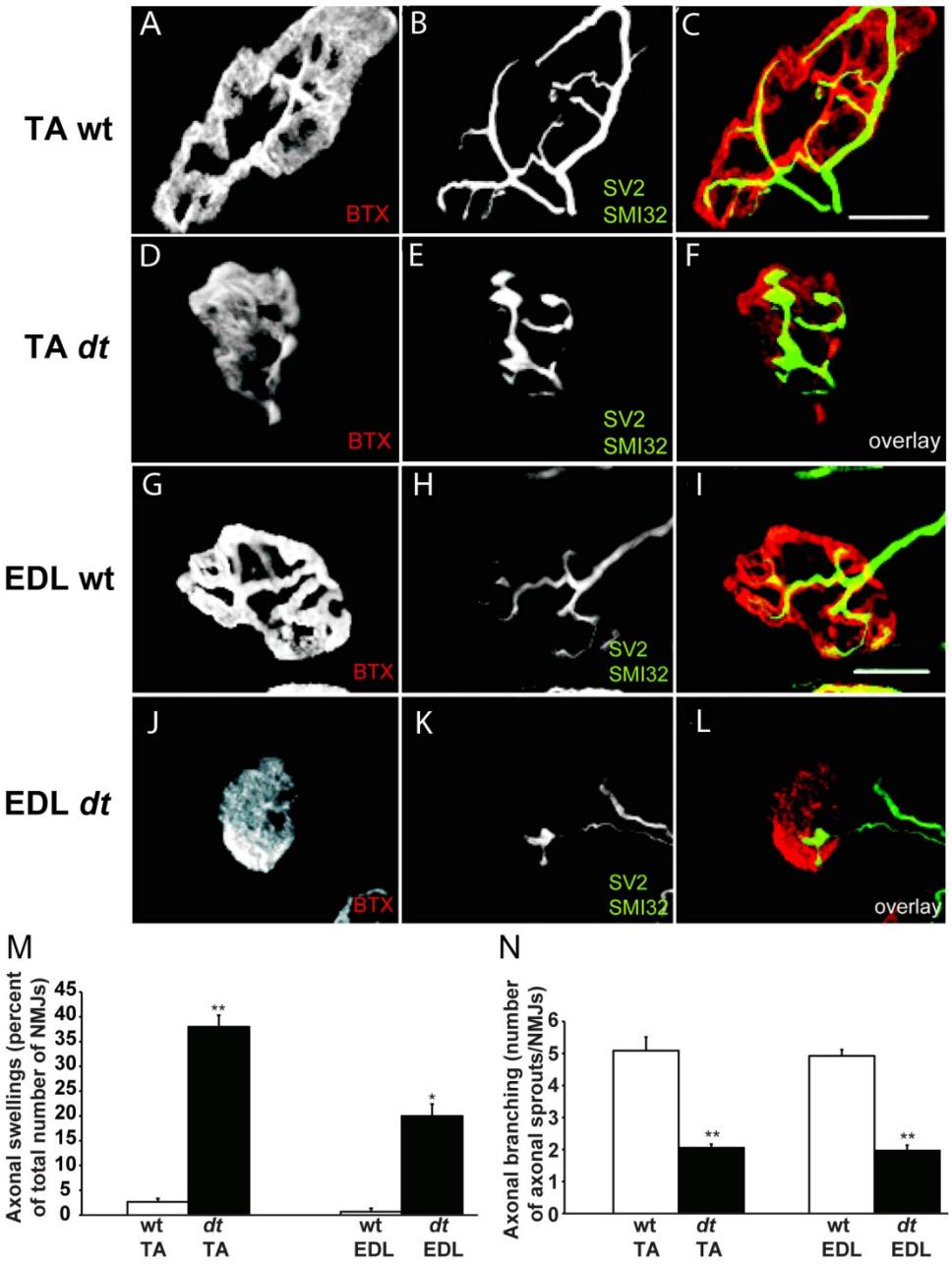

Figure 8. Pre-synaptic axonal swellings and reduced axonal sprouting at TA and EDL NMJs from *dt*^{27J} pre-synaptic terminals. A–L. Representative confocal images of wild type (A–C) and *dt*^{27J} (D–F) TA NMJs and wild type (G–I) and *dt*^{27J} (J–L) EDL NMJs. NMJs are labeled with alpha-bungarotoxin (BTX, red in the merged image), the axons with SMI-312 (green) and the synaptic vesicles with SV2 (green). Scale bar, 50 µm. *dt*^{27J} pre-synaptic terminals display fewer arbors and increased bulb-like swellings (F

and L) whereas wild type pre-synaptic terminals exhibit extensive axon branching with no bulb-like swellings (C and I). *dt*^{27J} endplates (D and J) appear less mature (fewer perforations) in comparison to wild type littermate endplates (A and G). M. The percentage of pre-synaptic swellings at TA/EDL NMJs in wild type (n = 3) and *dt*^{27J} (n = 3) mice (TA NMJ, **p<0.01; EDL NMJ, *p<0.05, student t-test). N. Quantification of axon sprouting between wild type (n = 3) and dt27J (n = 3) at TA and EDL NMJs indicates reduced axon sprouting in *dt*^{27J} NMJs (TA/EDL NMJ, **p<0.01, student t-test).

Atrophy Muscle in dt^{27J} mice

Seeing that P15 dt^{27J} TA and EDL NMJs were morphologically abnormal, we sought to investigate whether these abnormalities would impact the integrity of the muscle. Using hematoxylin and eosin stain we found dt^{27J} TA myofibers to be smaller (Fig. 9A, B). Muscle fiber size quantification revealed muscular atrophy in dt^{27J} mice (Fig. 9C). The myofiber size was significantly reduced in dt^{27J} TA muscle with a mean of 560.79 μm2±97.75 (SD, n = 6) compared to a 380.74 μm2±96.15 (SD, n = 6) in wild type TA muscle (**$p<0.01$). To assess fiber type grouping, immunostaining of mouse TA muscle sections with myosin heavy chain isoforms (type1, 2A, 2B and 2X) was performed. The analysis revealed no fiber type grouping in dt^{27J} TA muscles (Fig. S1).

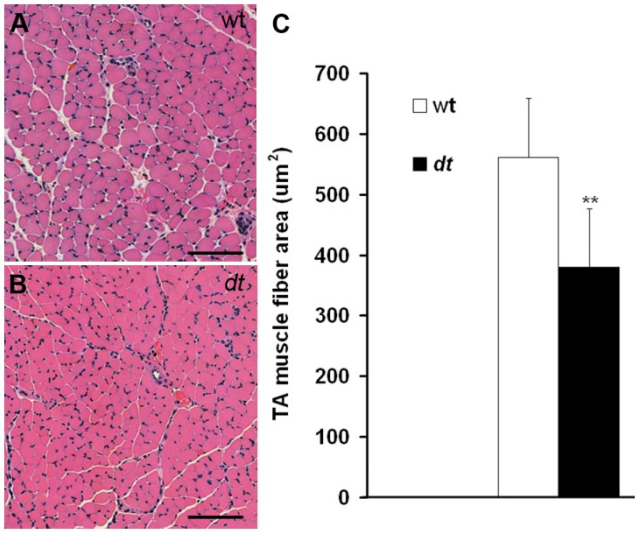

Figure 9. TA myofiber atrophy in *dt*^{27J} mice at P15. TA myofibers in cross-section were stained with hematoxylin and eosin. A. Healthy myofibers from TA wild type muscle were observed under light microscopy. B. Myofiber atrophy in TA *dt*^{27J} muscle is observed. Myofibers are smaller and many more nuclei are visible. C. A graphical representation showing the TA muscle fiber area in µm2 from wild type (n = 6) and *dt*^{27J} (n = 6) mice revealed muscle atrophy in *dt*^{27J} mice (** p<0.01, student t-test). Scale bars (A, B), 100 µm.

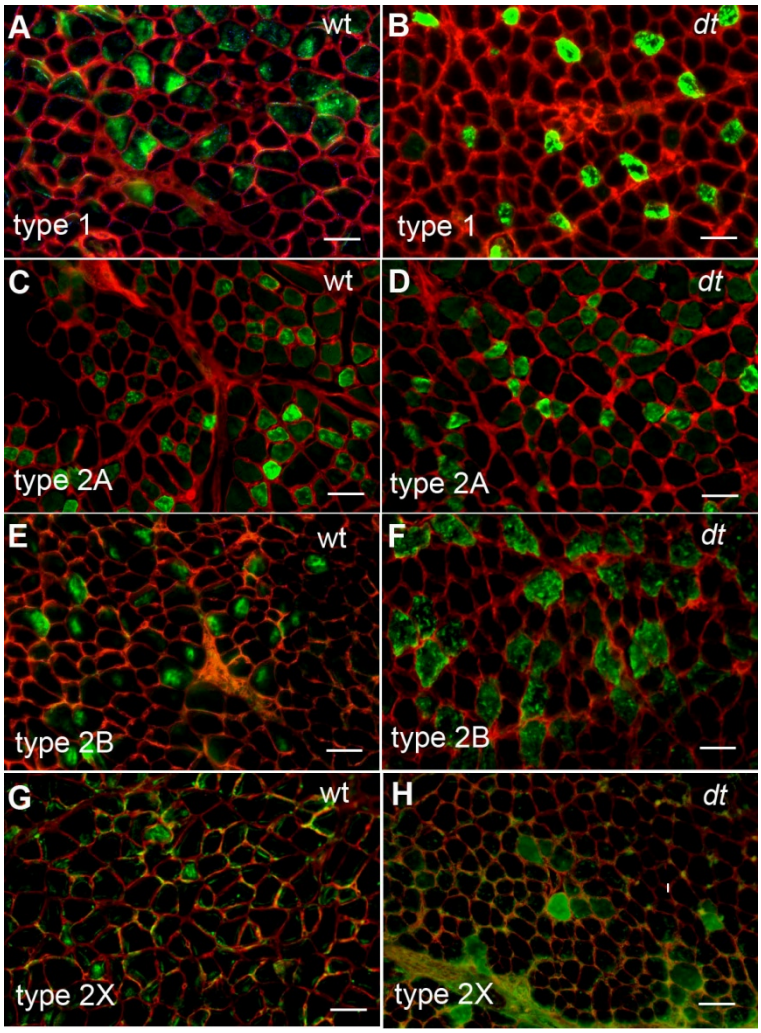

Figure S1: Absence of fiber type grouping in TA muscle of *dt*^{27J} mice. Cryostats sections (12 µm) of TA muscles obtained from wild type (A,C, E and G) and *dt*^{27J} (B, D, F and H) mice at P15 were immunostained with laminin (red) and myosin heavy chain (green) (type 1 (A,B), type 2A (C,D), type 2B (E,F) and type 2X (G,H). No fiber type grouping was observed. Scale bars (A–H), 20 µm.

Loss of alpha motor neurons in the dt^{27J} brainstem

In addition to the spinal cord, alpha motor neurons reside throughout the brainstem where they coordinate motor function via innervations of extrafusal muscle fibers. We thus evaluated the impact of dystonin function on alpha motor neuron survival in the trigeminal nerve of the pons, a region known to express high levels of dystonin (Bernier et al., 1995). FluoroJade staining, that specifically labels degenerating neurons (Schmued & Hopkins, 2000) , showed pronounced degeneration of neurons in the brainstem of dt^{27J} mice (Fig. 10A–D). Quantification of FluoroJade positive neurons (Fig. 10D) yielded a 2.4 fold increase in degeneration in dt^{27J} relative to wild type. To further evaluate whether this degeneration results in a loss of motor neurons, we quantified NeuN staining neurons in the brainstem of wild type and dt^{27J} mice (Fig. 10E–G). Based on morphological analysis of NeuN positive cells, we found a decrease in alpha motor neuron cell number from 13% per 100 μm2 in wild type to 4% per 100 μm2 in dt^{27J} (Fig. 10G) with correction for profile and section thickness according to the method of (Guillery and August, 2002).

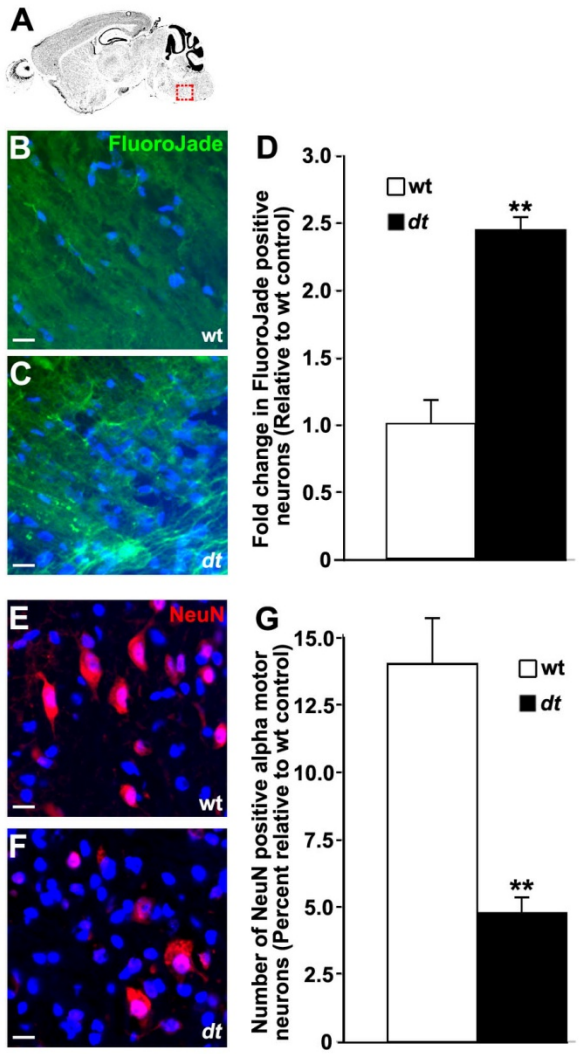

Figure 10. Motor neuron degeneration in the brainstem of *dt*^{27J} mice. Sagittal sections from mouse brainstem (trigeminal nerve of the pons) identified in (A) of P15 wild type (B) and *dt*^{27J} (C) mice were stained for degenerating neurons with Fluorojade B. D. Fold change in neurodegeneration in *dt*^{27J} brainstem relative to wild type littermates is depicted (** $p<0.01$, student t-test). Sagittal sections from mouse brainstem of P15 wild type (E) and *dt*^{27J} (F) mice were antigenically labeled for mature neurons with NeuN. Alpha motor neurons are identifiable by their larger size (greater than 9 µm, arrow) relative to other neuronal cell types (arrowhead). Nuclei were counter stained with DAPI to facilitate quantification. G. Quantification of percent alpha motor neurons

yielded a decrease in neuron number in the trigeminal nerve of dt^{27J} mice relative to wild type littermates (**$p<0.01$, student t-test). Scale bars, 10 μm.

Behavioral analysis reveals defective motor function in dt^{27J} mice

Signs of weakness were observed in the forelimb and in the hind limbs of all dt^{27J} mice and locomotor dysfunction was obvious at P15. Our motor examination revealed that dystonic pups could be affected to different degrees even within the same litter at P15. Severely affected dt^{27J} mice (approximately 70% of all dt^{27J} mice) were not able to grasp a flexible rod by their forelimbs at P15, but less affected dt^{27J} mice (about 30% of all dt^{27J} mice) were able to grasp the rod with their hind limbs for a few seconds. Nevertheless, compared to wild type littermates, the mutant mice had a decreased latency to fall (Table 3).

Table 3. Results from behavioral tests performed on wt and *dt*^{27J} mice at P15.

Rod test				**Righting reflex**				**Negative geotaxis**		
wt		***dt***		**wt**		***dt***		**wt**		***dt***
#	Mean latency to fall (sec±sd)	#	Mean latency to fall (sec±sd)	#	Righting response time	#	Righting response time (sec±sd)	#	+ or –	#
1	15.0±3.8	6	3.4±0.6	11	0	16	6.8±1.3	21	–	26
2	19.0±5.2	7	2.6±0.9	12	0	17	11.2±3.5	22	–	27
3	10.2±2.7	8	3.0±0.7	13	0	18	4.0±1.4	23	–	28
4	22.4±5.3	9	4.2±0.8	14	0	19	8.4±0.5	24	–	29
5	16.6±3.9	10	4.8±0.8	15	0	20	4.4±1.3	25	–	30

= mouse identification, values are expressed as mean ± standard deviation, 0 = righting response occurs immediately, + = positive geotaxis, geotaxis.

doi:10.1371/journal.pone.0021093.t003

We also tested *dt*^{27J} mice in other motor behavior tests. In the righting reflex test, mutant mice had a greater latency to right themselves as compared to wild type littermates when placed in a supine position (Table 3). Similarly, *dt*^{27J} mice did not exhibit negative geotaxis and fell off an inclined grid, whereas wild type littermates were always able to turn themselves around and walk up the grid (Table 3). Collectively our behavioral analysis identified defective motor function in *dt*^{27J} mice.

Discussion

In the present study, we investigated motor neuron pathology in the spontaneous *dt*^{27J} mouse mutant. We have assessed the integrity of L1 motor neurons and the NMJs of *dt*^{27J} mice. Alpha motor neurons of the L1 spinal cord are reduced in number and show eccentric nuclei. Consistent with this, a significant reduction in number of motor axons, most notably large caliber motor axons, was noted. Accumulation of phosphorylated NFs within motor neuron perikarya and axons was also evident. Ultrastructural studies revealed that ventral root spinal axons of different calibers were hypo or amyelinated, implying a defect in Schwann cells. In addition, we show *dt*^{27J} TA and EDL NMJs are poorly developed. Pre-synaptically, the defects are defined by denervated endplates, axonal swellings in the nerve terminals and poor terminal arborization, while post-synaptically poorly developed endplates were noted. The NMJ defects are coupled with TA muscle atrophy, but an absence of fiber type grouping. Finally, brain stem analysis revealed a 2.4 fold increase in degenerating neurons coupled with a decrease in motor neuron number. The observed neuromuscular defects were accompanied by a deficit in motor behavior. Although some of the defects observed may be attributed to the overall smaller size of *dt*^{27J} mice compared to wild type littermates, it is nevertheless clear that

neuromuscular defects likely contribute to the dt^{27J} pathology and our study identifies a critical role for dystonin outside of sensory neurons. It is possible that there is a second mutation within the dt^{27J} mice that is responsible for the observed motor neuron pathology. However, this is unlikely since we have yet to observe a segregation of the sensory and motor neuron defects in dt^{27J} mice. The latter would have been expected if two different genetic loci were involved. Furthermore, motor neuron pathology has been observed in other *dt* mouse strains (Duchen et al., 1964; Dowling et al., 1997).

Structural abnormalities of the NMJ: a new dt pathology

The *dt* pathology has long been defined as a sensory neuropathy. While it has been shown that dystonin mRNA expression levels are equivalent in alpha motor neurons and sensory neurons of the adult spinal cord (Bernier et al., 1995), and that *dt* mice resemble a neuromuscular disorder, it is surprising the NMJ has not been studied in *dt* mice. Here, we sought to fill this gap by studying dt^{27J} NMJs. Our analysis indicates that NMJ defects are present in TA and EDL muscle at the phenotype stage (P15) in these mice. Abnormalities include poor terminal arborization, axonal swellings in nerve terminals and/or pre-terminal axons, and poorly developed, morphologically immature AChR clusters that never attain the complex pretzel-shaped structures seen in wild type animals. The formation of NMJs, which involves nerve-muscle contact, intramuscular nerve branching and neuronal survival, requires reciprocal signals from nerve and muscle (Witzemann, 2006). Indeed, muscle-derived retrograde factors mediate motor neuron survival, remodeling and activity-induced changes at the NMJ (Oppenheim et al., 1992).

Thus it was of interest to observe that muscle endplates are poorly developed in various dt^{27J} muscles.

It should be noted that in addition to the pathological features at the endplates, previous work has shown cytoskeletal disorganization in *dt* skeletal muscle (Dalpe et al., 1999). How or if immature endplates contribute to the motor neuron defects in *dt* mice remains to be determined. Poorly developed endplates described in the present study likely occur via aberrant cytoskeletal organization, hence leading to insufficient crosstalk between dt^{27J} muscle endplates and motor nerve terminals. This is important as crosstalk, mediated by muscle-agrin signaling, initiates axon branching (Ruegg and Bixby, 1998). The motor pathology reported here including denervation and decreased axonal branching could also be brought on via intrinsic mechanisms. Previous studies have noted that motor neurons effectively innervate *dt* muscle. Only later in life at approximately one month of age has denervation been reported in *dt* mice (Duchen et al., 1964). It is safe then to presume that axon path-finding is not perturbed in *dt* motor neurons. Rather, loss of dystonin protein, which results in disorganized cytoskeleton, leads to reduced pre-synaptic arbors and eventual dying-back of motor neurons. Mechanisms mediating reduced axonal sprouting and dying-back are unknown. However, *dt* motor neurons contain focal swellings consisting of disorganized NFs, microtubules and abundant secondary lysosomes, which may impede axonal trafficking (Dowling et al., 1997). In fact, sciatic nerves from dt^{27J} mice have a fast bi-directional transport impairment of acetylcholinesterase (De Repentigny et al., 2003). Impeded transport by NF accumulation or aberrant cytoskeleton organization may be assisting this dying-back event. The NF accumulation within terminal axons likely contributes to the paucity of terminal

arborization. Indeed, similar pathology has been shown in NMJs of spinal muscular atrophy mice. Notably, the loss of survival motor neuron gene leads to pre-synaptic NF accumulation and reduced axonal sprouting and eventual dying-back (Cifuentes-Diaz et al., 2002).

Whether the motor defects shown here are intrinsically caused by the loss of dystonin or, alternatively, are secondary to sensory neuron degeneration, remains unclear. Moreover, whether or not motor neurons are affected through a lack of crosstalk between muscle and motor neurons remains to be established. Interestingly, null mutations within the kakapo gene, the Drosophila ortholog of ACF7/MACF1 which shares high sequence homology with dystonin (Leung, Sun, Zheng, Knowles, & Liem, 1999), results in NMJ abnormalities, notably reduced terminal branches (Prokop et al., 1998). Moreover, rapsyn – a post-synaptic scaffolding protein, which clusters AChRs at the endplate – associates with the actin binding domain of ACF7/MACF1 in skeletal muscle (Antolik et al., 2007). The one detractor of this study was that interactions between rapsyn and ACF7/MACF1 were observed in a non-muscle system. Nevertheless, the fact that a plakin protein family member, ACF7/MACF1, interacts with NMJ proteins and the loss of dystonin expression yields immature endplates leads us to speculate that dystonin may also have a role in the formation and/or maintenance of endplates.

Schwann cell defects: a contributor to dt^{27J} pathology

We show that ventral roots of dt^{27J} mice exhibit hypo- and amyelinated axons. Previous studies have shown that dystonin is an essential component of the Schwann cell cytoskeleton and loss of dystonin expression causes hypo/amyelinated peripheral nerves (Bernier et al., 1998). It is tempting to associate the Schwann cell defects seen here with

the NMJ abnormalities. For instance, Schwann-cell processes are known to cap the nerve terminals, thereby providing insulation and perhaps trophic sustenance. In addition, Schwann cells ensheathe motor axons and pre-terminals allowing proper saltatory conduction along the nerve fiber and signal transmission to the muscle (Sanes and Lichtman, 1999). Mechanisms mediating the defective myelination in dt^{27J} mice are unknown. We hypothesize that because Schwann cells undergo extensive cytoskeletal rearrangements during the myelination process (Mirsky and Jessen, 1999), and dystonin is a cytoskeletal linker protein, it is likely that loss of dystonin perturbs cytoskeletal-driven axon ensheathment. Alternatively, disruption in the composition of *dt* axonal proteins, due to axonal swellings for instance, may impede signaling between the axon and Schwann cell, thus leading to improper myelination. However, it seems unlikely that this latter possibility contributes to defective myelination as Schwann cell defects in *dt* mice are intrinsic (Bernier et al., 1998). Finally, it is important to note that myelination has a profound effect on axon caliber, distal nerve terminals and long-term survival (De Waegh et al., 1992; Martini, 2001; Popko, 2010). The absence of ventral root myelination seen here may account for the reduced number of large caliber axons and distal defects.

The *dt* pathology has classically been described as a sensory neuropathy. Here, we have shown that in addition to the sensory neuron defects, the dt^{27J} mouse displays motor neuron and NMJ pathologies. When considering the fact that *dt* mice die at weaning, the importance of dystonin in various tissues becomes grossly evident.

Chapter 3

Neuronal dystonin isoform 2 is a mediator of endoplasmic reticulum structure and function

Neuronal dystonin isoform 2 is a mediator of endoplasmic reticulum structure and function

Scott D. Ryan,[a,*] Andrew Ferrier,[a,b,*] Tadasu Sato,[a,c] Ryan W. O'Meara,[a,b] Yves De Repentigny,[a] Susan X. Jiang,[d] Sheng T. Hou,[d] and Rashmi Kothary[a,b,e,§]

[a]Ottawa Hospital Research Institute, Ottawa, ON K1H 8L6, Canada

[b]Department of Cellular and Molecular Medicine, University of Ottawa, Ottawa, ON K1H 8M5, Canada

[c]Division of Periodontology and Endodontology, Graduate School of Dentistry, Tohoku University, Sendai 980-8575, Japan

[d]Institute for Biological Sciences, National Research Council Canada, Ottawa, ON K1A 0R6, Canada

[e]Department of Medicine, University of Ottawa, Ottawa, ON K1H 8M5, Canada

*These authors contributed equally to this work.
§Address correspondence to: Rashmi Kothary.

Published in ***Molecular Biology of the Cell***, 2012 February 15; 23(4): 553–566.

Author Contributions

Conceived and designed the experiments: AF SDR RK. Performed the experiments: AF (figures 1, S1, 2, 4, 6, 7, S3, 8, 9) SDR. Analyzed the data: AF SDR TS. Contributed reagents/materials/analysis tools: YDR AF SDR TS RK. Wrote the paper: AF SR RK.

Abstract

Dystonin/Bpag1 is a cytoskeletal linker protein whose loss of function in dystonia musculorum (*dt*) mice results in hereditary sensory neuropathy. Although loss of expression of neuronal dystonin isoforms (dystonin-a1/dystonin-a2) is sufficient to cause *dt* pathogenesis, the diverging function of each isoform and what pathological mechanisms are activated upon their loss remains unclear. Here we show that dt^{27} mice manifest ultrastructural defects at the endoplasmic reticulum (ER) in sensory neurons corresponding to in vivo induction of ER stress proteins. ER stress subsequently leads to sensory neurodegeneration through induction of a proapoptotic caspase cascade. *dt* sensory neurons display neurodegenerative pathologies, including Ca^{2+} dyshomeostasis, unfolded protein response (UPR) induction, caspase activation, and apoptosis. Isoform-specific loss-of-function analysis attributes these neurodegenerative pathologies to specific loss of dystonin-a2. Inhibition of either UPR or caspase signaling promotes the viability of cells deficient in dystonin. This study provides insight into the mechanism of *dt* neuropathology and proposes a role for dystonin-a2 as a mediator of normal ER structure and function.

Introduction

The eukaryotic cytoskeleton comprises three cytoskeletal networks, including microtubules, actin microfilaments, and intermediate filaments. These filaments rely on cytoskeletal cross-linking proteins to facilitate their multifaceted functions, ranging from vesicular transport and maintenance of organelle integrity to mitosis (Fuchs and Karakesisoglou, 2001). As such, loss of cytoskeletal-linking proteins can have grave implications on cellular functioning and viability (Sonnenberg and Liem, 2007). In particular, loss of the neuronal cytoskeletal linking protein dystonin has been attributed to degeneration of both sensory and motor neurons (Brown et al., 1995; Guo et al., 1995; De Repentigny et al., 2011).

Dystonia musculorum (*dt*) is an inherited homozygous recessive sensory neuropathy caused by mutations in the dystonin gene (*Dst*) (Duchen et al., 1964). At approximately 2 wk postnatal development, *dt* mice exhibit loss of control of the fore limbs, hind limbs, and trunk, and they die shortly thereafter of unknown causes (Duchen, 1976). Several *dt* alleles exist through spontaneous mutations (dt^{27}), chemically induced mutations, targeted alleles (dt^{tm1Efu}), and transgenic insertions ($dt^{Tg4/Tg4}$) (Pool et al., 2005). Although only three *dt* mutations ($dt^{Tg4/Tg4}$, dt^{tm1Efu}, and dt^{Alb}) have been characterized at the DNA level, $dt^{Tg4/Tg4}$ and dt^{27} are allelic and do not complement (Kothary et al., 1988; Guo et al., 1995). To date, *dt* pathologies have been recorded in motor neurons, skeletal muscle, and Schwann cells, but degeneration is most prominent in the sensory neurons of the dorsal root ganglia (DRG) (Dowling et al., 1997; Bernier and Kothary, 1998; Dalpe et al., 1999; De Repentigny et al., 2011).

The *Dst* gene is exceptionally large (~400 kb in mice) and gives rise to three tissue-specific dystonin isoforms—dystonin-e (epithelial isoform, ~315 kDa), dystonin-b (muscle isoform, ~834 kDa), and dystonin-a (neuronal isoform, ~615 kDa) (Sawamura et al., 1991; Brown et al., 1995; Okumura et al., 2002). Whereas dystonin-e serves as an autoantigen in the skin blistering disease bullous pemphigoid, loss of function of the dystonin-a isoform or isoforms is causal in the *dt* disorder (Kothary et al., 1988; Sawamura et al., 1991; Brown et al., 1995; Pool et al., 2005). Like muscle, three major neuronal isoforms are derived through alternative splicing, namely dystonin-a1, dystonin-a2, and dystonin-a3 (Young and Kothary, 2007). These isoforms share an N-terminal actin-binding domain, an extensive coiled-coil region, and a C-terminal microtubule-binding domain, allowing for interactions with cytoskeletal filaments (Leung et al., 2001b). Although the dystonin-a isoforms share similar domain architecture, it is the unique N-terminal regions that differentiate them and dictate their subcellular localization. Specifically, dystonin-a1 encodes a short N-terminal domain that includes an actin-binding domain, whereas dystonin-a2 possesses a transmembrane domain and dystonin-a3 possesses a putative myristoylation domain, aiding their membrane localization to the nuclear envelope and perinuclear membranes and to the plasma membrane, respectively (Jefferson et al., 2006; Young et al., 2006). Recently it has been demonstrated that the lack of one copy of the *Dst* gene or the presence of truncated forms of the mutant protein in humans can lead to a partial disorganization of the sensory and motor circuits. Giorda and collaborators described a human subject with a translocation in the *Dst* gene that specifically disrupted neuron- and muscle-specific isoforms and was associated with a profound delay in the acquisition of cognitive and motor skills, as well

as in visual maturation (Giorda et al., 2004). Thus, although no mutations in *Dst* have been identified in humans, haploinsufficiency or altered expression can result in phenotypic abnormalities reminiscent of the inherited disorder in mice.

A common cellular pathology preceding *dt* sensory neuron degeneration is axonal swelling, characterized by the accumulation of organelles and vacuoles within *dt* sensory neurons (Janota, 1972). These accumulations are accompanied by disorganized neurofilament, actin and microtubule networks in *dt* sensory neurons (Leung et al., 2001; Yang et al., 1996, 1999), which in turn lead to bidirectional impairment of fast axonal transport (Dalpé et al., 1998; De Repentigny et al., 2003). Although neurofilament defects do exist in *dt* mice, they are not causal in initiation of *dt* pathology (Bernier and Kothary, 1998; Eyer et al., 1998). Moreover, the microtubule cytoskeleton of *dt* and wild-type (WT) sensory neurons grown in culture displays no ultrastructural defects, and local trafficking of mitochondrial organelles proceeds normally (Pool et al., 2005). Nonetheless, enhanced apoptosis is observed in these cultures (Pool et al., 2005). Consequently, it is plausible that abnormalities aside from axonal cytoskeleton defects may initiate or contribute to *dt* sensory neuron pathology. Some studies suggest that the dystonin-a2 isoform is involved in nuclear envelope structuring, nuclear tethering, and organization of membranous structures surrounding the nucleus (Young et al., 2003b, 2006; Young and Kothary, 2008). Indeed, $dt^{Tg4/Tg4}$ sensory neurons (devoid of dystonin-a1 and dystonin-a2 expression) display perikaryal defects and show altered expression of the microsomal enzyme protein disulfide isomers (Young and Kothary, 2008). Yet the mechanism resulting in perikaryal defects in *dt* remains uncertain. Taken together, the observations make it reasonable to presume that dystonin-a has a role in maintaining

integrity of the ER and nuclear envelope, and subsequently organelle function, but this hypothesis has yet to be empirically validated.

Whereas *dt* pathology has been thoroughly examined, there remains a dearth of evidence to explain the mechanisms mediating *dt* pathogenesis. Moreover, although it is known that the $dt^{Tg4/Tg4}$ mouse strain is devoid of dystonin-a1 and dystonin-a2 expression, it is unresolved as to whether loss of a single isoform or combination of isoforms is responsible for neurodegeneration. The present study therefore aims to elucidate underlying mechanisms of *dt* pathogenesis and to determine the individual roles of dystonin-a1 and dystonin-a2 in *dt* sensory neuronal degeneration. To this extent, we selectively reduced the expression of dystonin-a1 or dystonin-a2 via small interfering RNA (siRNA) in F11 neuronal cells and screened these cells for canonical endoplasmic reticulum (ER) stress proteins and caspase activity and assessed cell viability using various cell death assays. In parallel, dt^{27} DRGs and primary sensory neurons were screened for ER stress, caspase activation, and sensory neuron viability using similar experimental analysis. To assess *dt* ER integrity and function, ultrastructural and ratiometric Ca^{2+} analyses were conducted, respectively. Data presented here provide insight into the mechanisms underlying neuropathology in *dt* mice. Furthermore, this study proposes a novel role for dystonin-a2 as a critical structural component of perinuclear organelles, required for maintenance of ER homeostasis.

Results

Loss of dystonin-a2 leads to activation of a neurodegenerative caspase cascade in *dystonia musculorum* mice

To evaluate the isoform-specific contribution of dystonin loss to neurodegeneration in *dt* mice, we first evaluated the correlation between degeneration of sensory neurons and phenotypic onset in dt^{27} mice, which are null for all three neuronal isoforms of dystonin. At the pre-phenotype stage (P4), DRGs from WT and dt^{27} mice were negative for both Fluoro-Jade B staining and terminal transferase dUTP nick-end labeling (TUNEL; Figure 1, A, B, E, and F), indicating the absence of neurodegeneration. In phenotypic (P15) dt^{27} animals, however, a marked increase in both Fluoro-Jade staining and TUNEL labeling (Figure 1, C, D, G, and H) was observed relative to WT littermates. This result indicates that phenotypic onset correlates closely with severe degeneration of DRG sensory neurons. We then sought to determine which neuronal isoform of dystonin was critical to maintaining cell viability in sensory neurons. dt^{Tg4} transgenic mice are null for dystonin-a1 and dystonin-a2 but express dystonin-a3 (Pool et al., 2005). Labeling of P15 WT and dt^{Tg4} DRGs for TUNEL shows an increase in TUNEL reactivity in dt^{Tg4} DRGs relative to WT (Supplemental Figure S1). This indicates that the neurodegeneration associated with dystonin loss in dt^{Tg4} mice is not due to loss of dystonin-a3 but rather to loss of dystonin-a1 or dystonin-a2 or the combined loss of both.

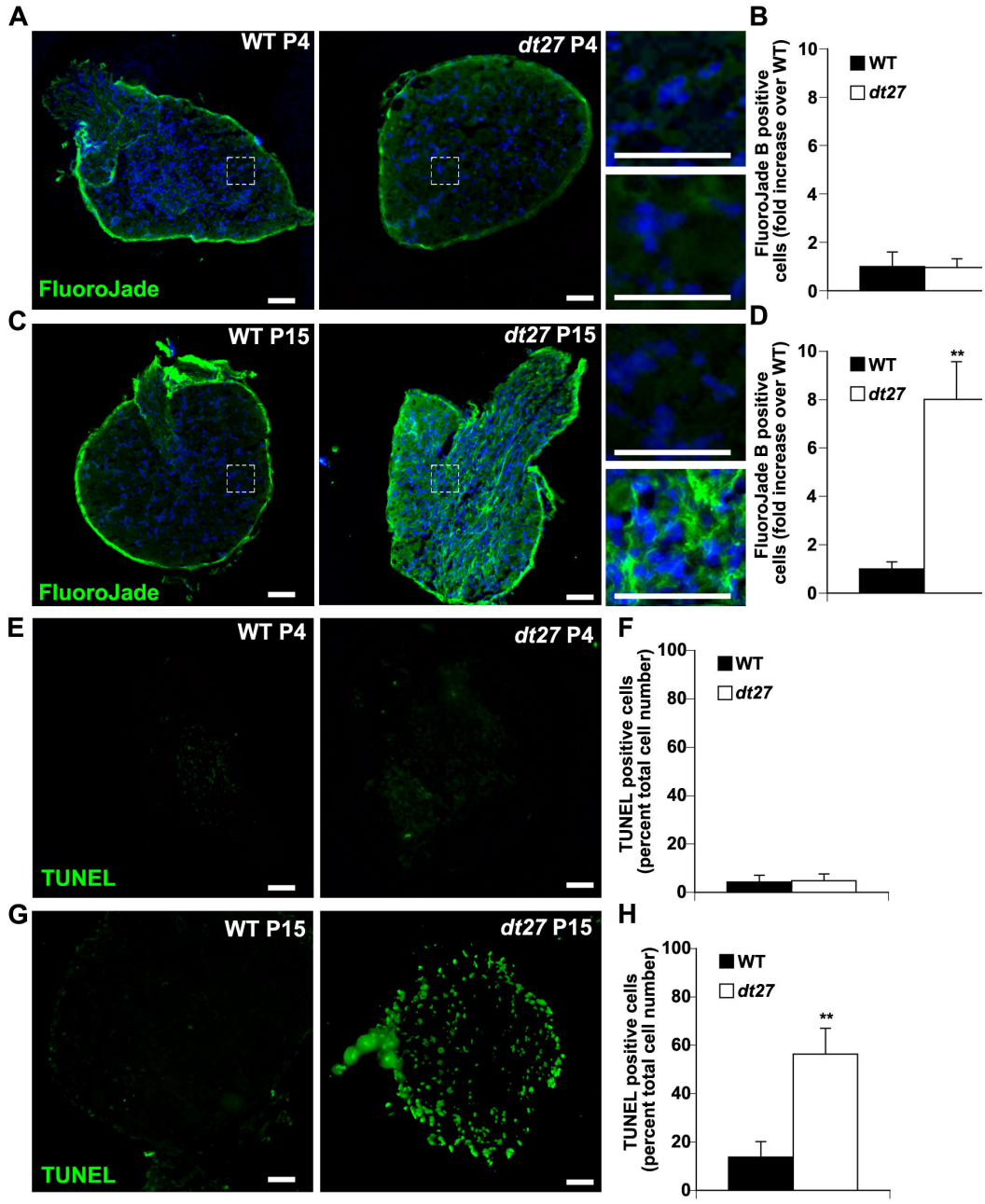

Figure 1: Dystonin deficiency leads to degeneration of sensory neurons in mice.

DRGs from P4 (A, B) and P15 (C, D) WT and *dt*^{27} mice were stained with Fluoro-Jade B to identify degenerating neurons. No degeneration of sensory neurons is evident pre-phenotype (A, B), whereas Fluoro-Jade–positive degenerating neurons were evident at P15 in phenotypic *dt*^{27} animals (C, D). Analysis of TUNEL labeling from P4 (E, F) and

P15 (G, H) WT and dt^{27} DRGs yielded no difference in apoptotic index pre-phenotype (E, F). At P15, a significant increase in percentage TUNEL-positive cells was observed in phenotypic dt^{27} animals relative to WT controls (G, H). Scale bars, 50 μm; Student's *t* test, **p < 0.01, n = 5.

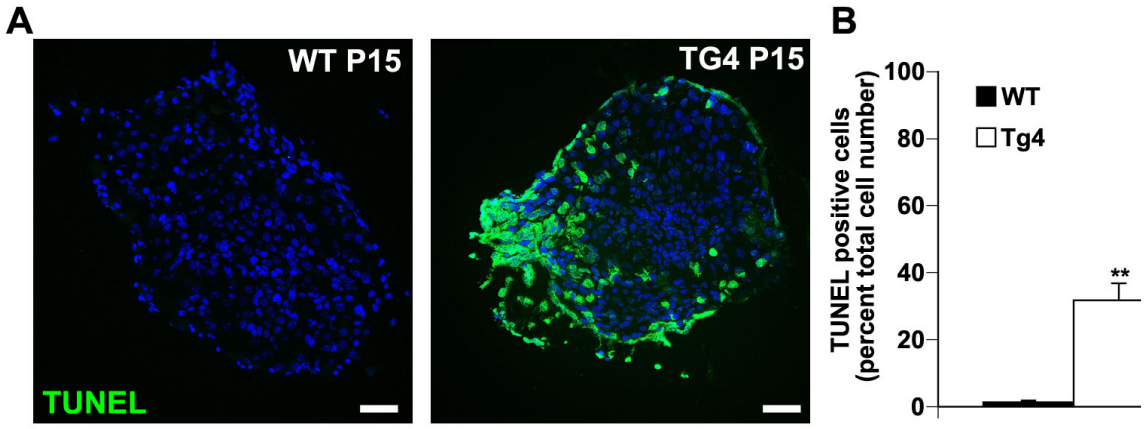

Figure S1. Dystonin-a3 expressing dt^{Tg4} DRGs have an increased apoptotic index relative to WT littermates. dt^{Tg4} transgenic mice are null for dystonin-a1 and dystonin-a2 but express dystonin-a3. Labeling of (A) P15 WT and (B) dt^{Tg4} DRGs for TUNEL show an increase in TUNEL reactivity in dt^{Tg4} DRGs relative to WT. This indicates that the neurodegeneration associated with dystonin loss is not due to loss of dystonin-a3 but rather due to loss of dystonin-a1, dystonin-a2 or the combined loss of both neuronal isoforms. Scale bars = 50 mm (student t-test, **p<0.01, n=5-7).

The diverging cellular localization of dystonin-a1 and dystonin-a2 resulting from the heterogeneity of the N-terminus would implicate distinct organelle-specific dysfunction with their depletion (Young and Kothary, 2008). To determine the functional requirement of both dystonin-a1 and dystonin-a2 to neuronal viability, we performed isoform-specific loss-of-function analysis in immortalized F11 neuronal culture. F11 neuronal cells are a fusion of embryonic rat DRG neurons with mouse neuroblastoma cells. The resulting hybrid exhibits neuronal gangliosides, action potentials, and extensive neurite-like processes (Platika et al., 1985). We first assessed the efficiency of isoform-specific, siRNA-mediated dystonin knockdown. In the absence of isoform-specific dystonin antibodies, we assessed knockdown of exogenously expressed dystonin-a1–green fluorescent protein (GFP) and dystonin-a2–yellow fluorescent protein (YFP) fusion proteins coupled to siRNA-mediated knockdown of endogenously expressed dystonin-a1 and dystonin-a2 mRNA (Figure 2, A and B, and Supplemental Figure S2, A and B). siRNA-mediated targeting of dystonin proved to be isoform specific. Analysis of the effect of dystonin loss on neuronal viability showed that knockdown of dystonin-a2 resulted in an increase in death within 24 h as indicated by ethidium homodimer incorporation (Figure 2C and Supplemental Figure S2C) and an increase in TUNEL labeling within 48 h (Figure 2D) of silencing relative to scrambled control. Loss of dystonin-a1 has no impact on cell death (Figure 2, C and D, and Supplemental Figure S2C). Positive TUNEL labeling in phenotypic DRGs from *dt*^{27} mice coupled with TUNEL labeling following specific depletion of dystonin-a2 in F11 neuronal cells led us to explore the pathway of apoptotic induction in order to trace to the mechanism of pathology.

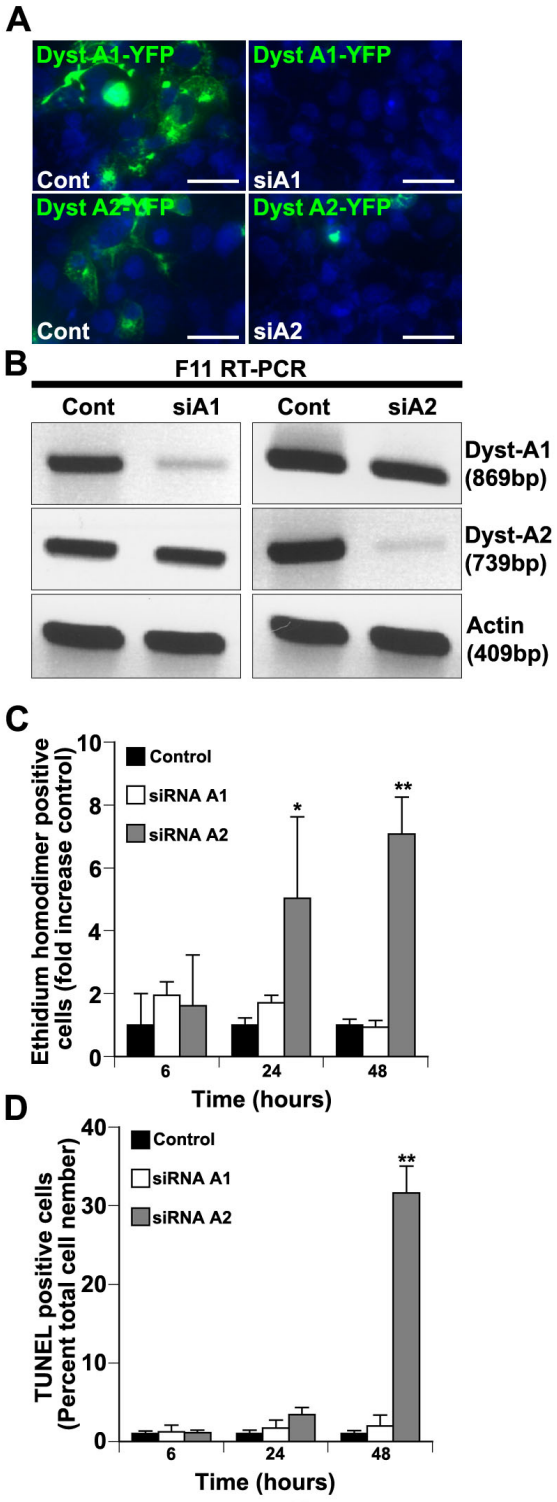

Figure 2: Isoform-specific loss of dystonin-a2 promotes neuronal cell death. (A) Efficiency of siRNA-mediated knockdown of exogenously expressed dyst-a1–YFP and

dyst-a2–YFP protein was evaluated in COS-1 cells by epifluorescence. (B) Efficiency of siRNA-mediated knockdown of endogenously expressed dystonin-a1 and dystonin-a2 mRNA was measured in F11 neuronal cells by RT-PCR. Knockdown of dystonin-a2 resulted in an increase in death as assessed by ethidium homodimer incorporation within 24 h (C) and an increase in TUNEL labeling within 48 h of silencing relative to scrambled control. Loss of dystonin-a1 has no impact on cell death (C, D). Scale bars, 10 μm; ANOVA, post hoc Dunnett's t test, *$p < 0.05$, **$p < 0.01$, $n = 5$.

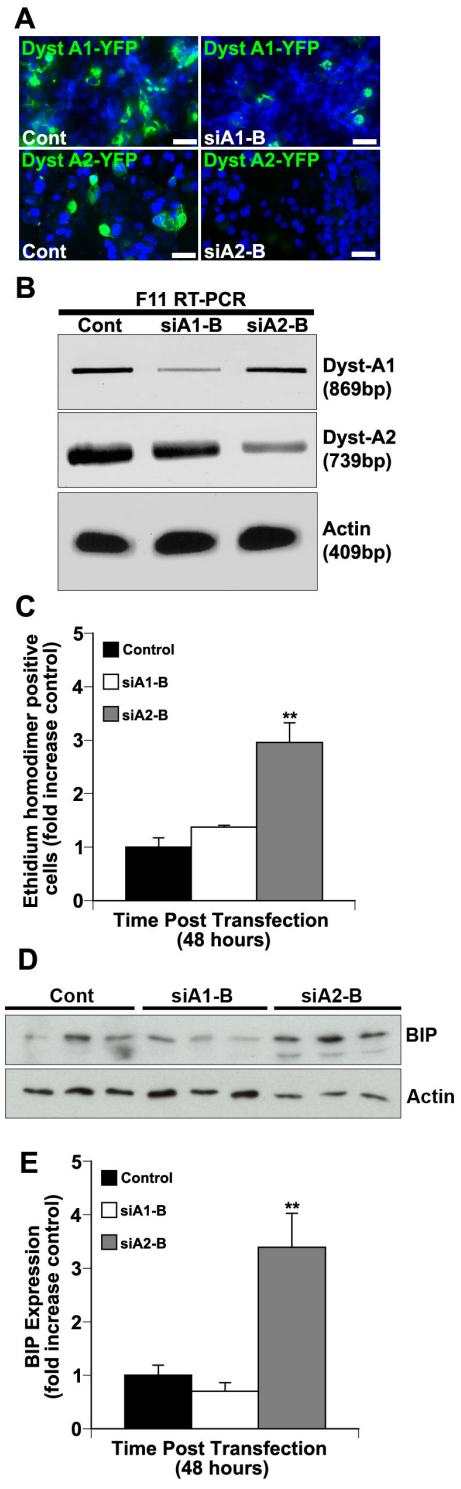

Figure S2. Isoform-specific loss of dystonin-a2 by multiple siRNA sequences induces ER-stress mediated cell death. (A) Efficiency of siRNA-mediated knockdown of

exogenously expressed dyst-a1-YFP and dyst-a2-YFP protein by a second set of siRNA sequences designated B and targeted against dystonin a1 or dystonin a2 was evaluated in COS-1 cells by epi-fluorescence. (B) Efficiency of siRNA-B-mediated knockdown of endogenously expressed dystonin-a1 and dystonin-a2 mRNA was measured in F11 neuronal cells by RT-PCR. (C) siA2-B mediated knockdown of dystonin-a2 specifically resulted in an increase in death as assessed by ethidium homodimer incorporation within 48 h relative to control siRNA treated cells (anova, post-hoc dunnett t-test, **$p<0.01$, n=3-7). (D) Isoform-specific depletion of dystonin was performed in F11 neuronal cells and the impact on BIP induction determined. While western analysis did not revealed a change in BIP expression following dystonin-a1 silencing, (E) a significant increase in BIP expression was detected within 48 h of dystonin-a2 silencing (anova, post-hoc dunnett t-test, **$p<0.01$, n=3).

We thus screened for caspase activation in F11 cells following siRNA-mediated depletion of dystonin isoforms. Using fluorescence-labeled inhibitors of caspase activity, we screened F11 neuronal cells for activation of caspases 2, 12, 8, and 3 at multiple time points following loss of either dystonin-a1 or dystonin-a2 (Figure 3). No induction of death receptor–associated caspase 8 was detected (Figure 3A), thus excluding the extrinsic apoptotic cascade as a potential mediator of death. A pronounced increase in both caspase 2 and caspase 3 activity was observed (Figure 3, C and D) following 24 and 48 h of dystonin-a2 depletion relative to scrambled siRNA control cells, coupled to a modest increase in caspase 12 activation (Figure 3B) following 48 h of dystonin-a2 depletion. Loss of dystonin-a1, however, had no effect on caspase activation. Collectively, these data strongly suggest that specific depletion of dystonin-a2 induces an intrinsic apoptotic cascade that is a likely effector of neurodegeneration in *dt*.

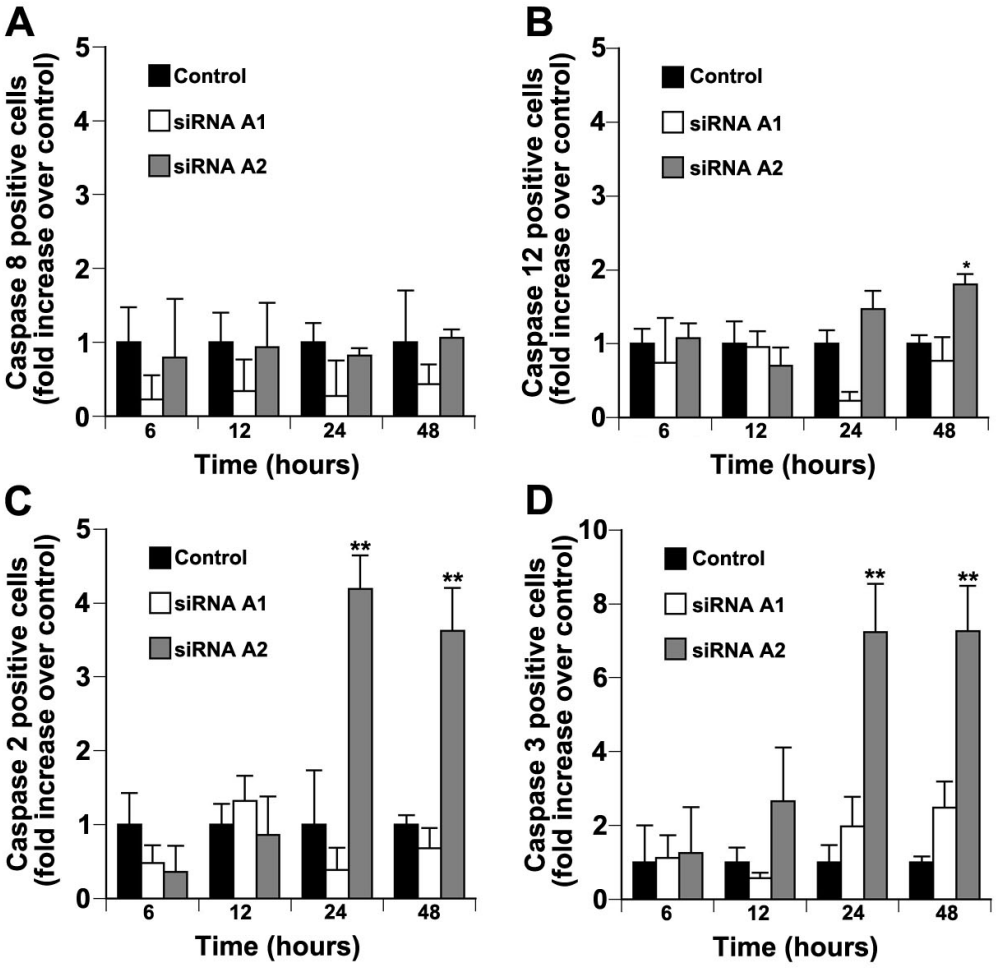

Figure 3: Loss of neuronal dystonin-a2 results in activation of a caspase 2–dependent caspase cascade in F11 cells. F11 neuronal cells were screened for caspase activation using FLICA assays at multiple time points following knockdown of either dystonin-a1 or dystonin-a2. (A) No induction of death receptor–associated caspase 8 was observed at any time point. (B) A modest increase in caspase 12 activation was measured following 48 h of dystonin-a2 depletion. A pronounced increase in both caspase 2 (C) and caspase 3 (D) activity was observed following 24 and 48 h of dystonin-a2 depletion relative to scrambled siRNA control cells. Loss of dystonin-a1 had no effect on caspase activation (A–D). ANOVA, post hoc Dunnett's t test, *$p < 0.05$, **$p < 0.01$, $n = 5$.

Loss of dystonin results in ER stress–mediated induction of the unfolded protein response

To ascertain the cellular stresses evoking the increase in caspase activity in F11 neuronal cells, we first discerned which if any of these caspases contributed to pathology in dt^{27} mice by screening WT and dt^{27} primary sensory neurons for caspase activation. A time course of caspase 3 activation was conducted in DRG sections at P4, P10, and P15 (Figure 4A). These data suggest that caspase 3 activation in DRGs coincides with phenotypic onset in dt^{27} mice. We then established the ability of these neurons to survive in culture. Cultured DRG sensory neurons (DRGNs) from P4 and P15 WT and dt^{27} mice were assessed by TUNEL (Figure 4B). Whereas both WT and dt^{27} cultures were negative for TUNEL labeling at P4 (Figure 4C), we were surprised to see that P15 DRGNs from dt^{27} mice also showed no increase in TUNEL labeling relative to WT controls (Figure 4D). We then screened P15 WT and dt^{27} sensory neurons for caspase activation (Figure 4E). Although we saw no induction of death receptor–associated caspase 8 and no significant increase in ER-associated caspase 12 activity, an increase in activity of executioner caspases 2 and 3 was observed. Activation of caspase 2 in whole DRGs was confirmed by Western analysis of cleaved (active) caspase 2 at P4 (Figure 4, F and G) and P15 (Figure 4, F and H). Caspase activation was only observed in DRGs from phenotypic dt^{27} mice (Figure 4, F and H). In addition, although these results suggest that culturing sensory neurons at a phenotypic stage selects for those neurons that have not yet undergone apoptosis, a caspase 2–dependent signaling cascade has nonetheless been initiated.

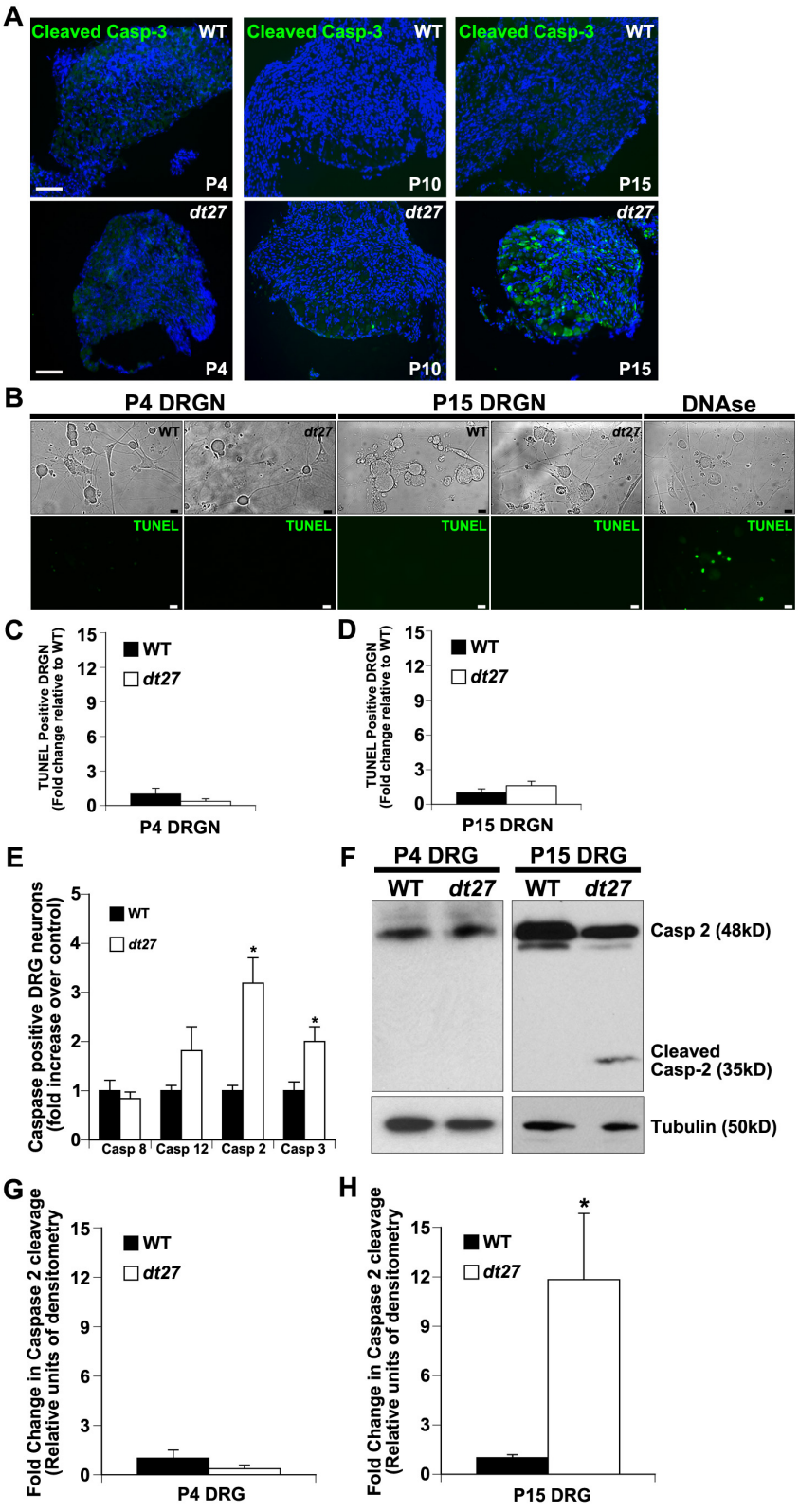
A
Cleaved Casp-3
WT
P4
P10
P15
dt27
B
P4 DRGN
P15 DRGN
DNAse
TUNEL
C
TUNEL Positive DRGN (Fold change relative to WT)
WT
dt27
P4 DRGN
D
P15 DRGN
E
Caspase positive DRG neurons (fold increase over control)
Casp 8
Casp 12
Casp 2
Casp 3
F
P4 DRG
P15 DRG
Casp 2 (48kD)
Cleaved Casp-2 (35kD)
Tubulin (50kD)
G
Fold Change in Caspase 2 cleavage (Relative units of densitometry
H

Figure 4: Loss of dystonin results in activation of an ER-associated caspase cascade in DRGs. (A) A postnatal time course of caspase 3 activity was conducted by immunofluorescence analysis of cleaved caspase 3 expression at P4, P10, and P15 in WT and *dt*^{27} DRG sections; scale bars, 50 μm. (B) Survival of cultured primary sensory neurons was then assessed by TUNEL labeling of WT and *dt*^{27} DRGNs at P4 and P15; scale bars, 10 μm. DNase-treated sensory neurons were processed as a positive control. Fold change in TUNEL reactivity was quantified at (C) P4 and (D) P15. Data are expressed as fold increase in TUNEL-positive *dt*^{27} neurons relative to WT; Student's t test, n = 3–6. (E) WT and *dt*^{27} primary sensory neurons were screened for caspase activation following 48 h in culture using FLICA assays. Although no induction of death receptor–associated caspase 8 was measured, an increase in activity of executioner caspases 2 and 3 was recorded; ANOVA, post hoc Dunnett's t test, *$p < 0.05$, n = 9. (F) Caspase 2 activity was confirmed by Western analysis of pro–caspase 2 cleavage in both P4 and P15 WT and dt27 DRGs. Caspase 2 cleavage in (G) P4 and (H) P15 WT and *dt*^{27} DRGs was quantified by densitometry and normalized to tubulin standard; Student's t test, *$p < 0.05$, n = 5.

In rodents, ER stress leading to neuronal loss is mediated in part by activation of caspase 12 (Nakagawa et al., 2000). Caspase 2, however, has been proposed as a functional orthologue to caspase 12 in some systems, mobilized in response to ER stress to activate downstream caspase 3/7 (Hitomi et al., 2004; Cheung et al., 2006). Caspase 2 localizes to both the Golgi apparatus and ER (Mancini et al., 2000; Ferri and Kroemer, 2001; Cheung et al., 2006). Activation is associated with fatal interruption of protein transport from the ER to the Golgi, triggering cell death (Murakami et al., 2007; Ouasti et al., 2007). To evaluate whether caspase 2 was localized to the ER and functioning as a component of ER stress following dystonin loss, we contrasted caspase 2 localization in F11 neuronal cells between the ER and Golgi and determined whether dystonin-a2 depletion altered this localization (Figure 5). Confocal analysis of caspase 2 with the ER marker calreticulin-YFP showed extensive colocalization (Figure 5A). Furthermore, loss of dystonin-a2 has no effect on the distribution of caspase 2 in the ER (Figure 5, B and E). Assessment of caspase 2 colocalization with Golgi-YFP also showed caspase 2 present in Golgi (Figure 5C). Consistent with our findings in the ER, loss of dystonin-a2 has no effect on Golgi-localized caspase 2 (Figure 5, D and F). Although dystonin-a2 has no effect on overall caspase 2 distribution, we see extensive caspase 2 staining through both the ER and Golgi complex, suggesting that caspase 2 is positioned in F11 neuronal cells to respond to ER stress signals. We thus examined the effect of dystonin-a2 depletion on the macrostructural organization of the ER. It was surprising that staining of endogenous calreticulin in F11 neuronal cells showed no obvious aberrations in ER macrostructure (Figure 5G).

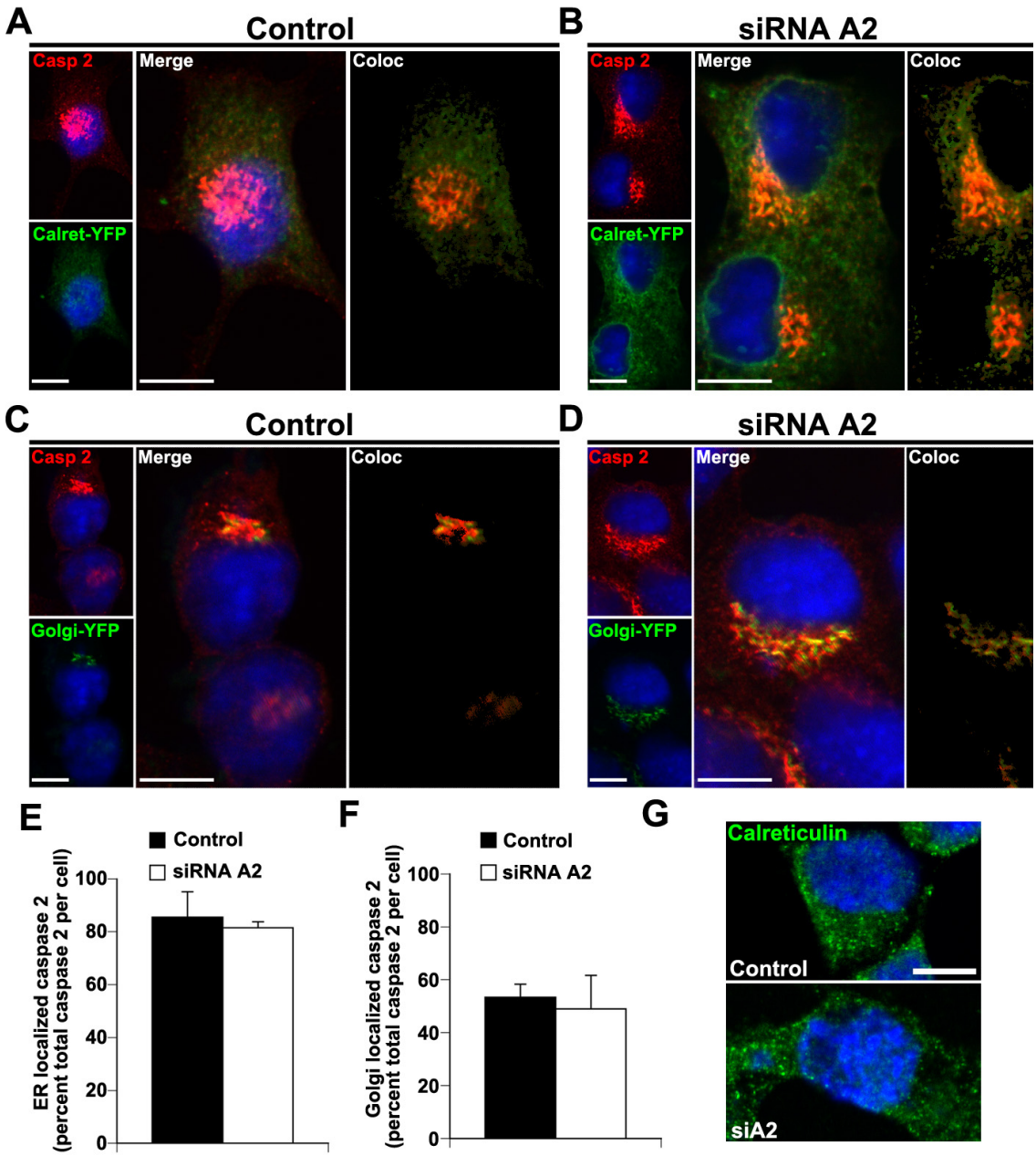

Figure 5: Caspase 2 is ER associated in F11 neuronal cells. F11 cells overexpressing either calreticulin-YFP (A, B) or Golgi-YFP (C, D) were antigenically labeled for caspase 2 following 48-h treatment with either (A, C) control or (B, D) dystonin-a2 siRNAs (scale bars, 10 μm). Colocalization of caspase 2 with either the ER (calreticulin) or Golgi was subsequently determined and colocalization masks generated.

Quantification of the percentage colocalized area between caspase 2 and (E) the ER or caspase 2 and (F) the Golgi was subsequently performed; Student's *t* test, n = 12. Loss of dystonin has no effect on localization. (G) ER macrostructure was visualized by antigenic labeling of endogenous calreticulin (scale bars, 10 μm). Loss of dystonin-a2 had little effect on calreticulin subcellular organization.

Further elucidation of the ER stress mechanism associated with neurodegeneration in *dt*^{27} mice focused on two canonical ER stress signal transduction cascades—mobilization of ER Ca^{2+} stores and the unfolded protein response (UPR). Phenotypic WT and *dt*^{27} DRGs were analyzed by Western blot for induction of chaperones of protein folding—BiP (GRP78) and CHOP (GADD153). Induction of these proteins is an early marker of ER stress (Gülow et al., 2002). Expression of these proteins increases following cessation of translation induced by UPR activation (Munro and Pelham, 1986; Gülow et al., 2002). A significant induction of both BiP and CHOP was observed in DRGs from phenotypic *dt*^{27} mice relative to WT (Figure 6, A–C). Isoform-specific depletion of dystonin was subsequently performed to ascertain which dystonin isoform is critical to ER function. Western and immunofluorescence analysis of F11 neuronal cells revealed an increase in BiP and CHOP expression within 48 h of dystonin-a2 silencing but not following dystonin-a1 silencing (Figure 6, D–I). UPR signal transduction results in the mRNA splicing of XBP1 by IRE1 (Yoshida et al., 2001). Translation of spliced XBP1 mRNA, a potent transcription factor, induces BiP and CHOP expression (Lee et al., 2003). UPR-mediated activation of XBP1 splicing was determined following isoform-specific depletion of dystonin. Although dystonin-a1 depletion resulted in a modest induction of XBP1 splicing, a dramatic increase in splicing was observed following loss of dystonin-a2 (Figure 6, J and K). Collectively, these data demonstrate that dystonin-a2 functional loss is the predominant mediator of neurodegeneration in *dt*^{27} mice through induction of an ER stress–mediated apoptotic cascade.

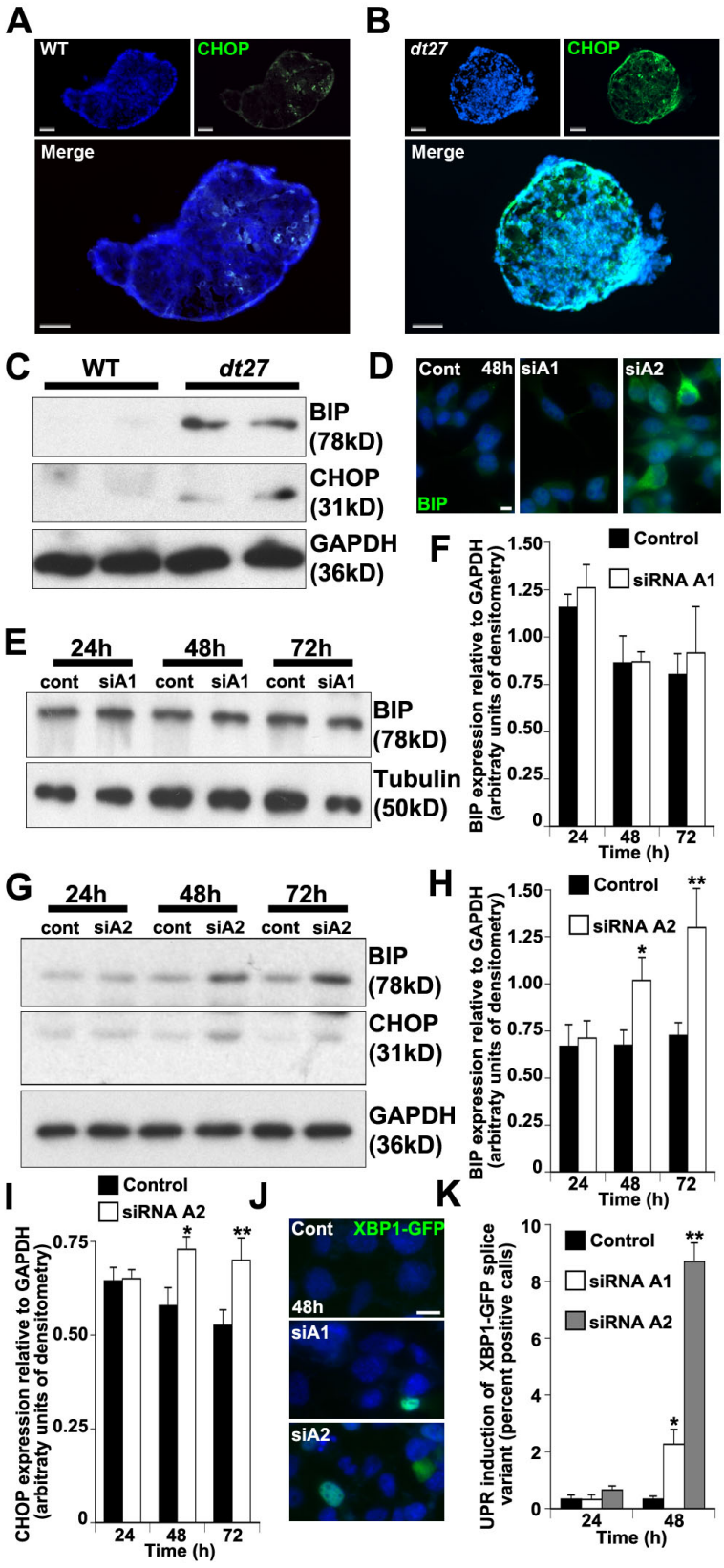
A
WT
CHOP
Merge
B
dt27
CHOP
Merge
C
WT
dt27
BIP (78kD)
CHOP (31kD)
GAPDH (36kD)
D
Cont
48h
siA1
siA2
BIP
E
24h
48h
72h
cont siA1 cont siA1 cont siA1
BIP (78kD)
Tubulin (50kD)
F
Control
siRNA A1
BIP expression relative to GAPDH (arbitraty units of densitometry)
Time (h)
G
24h
48h
72h
cont siA2 cont siA2 cont siA2
BIP (78kD)
CHOP (31kD)
GAPDH (36kD)
H
Control
siRNA A2
BIP expression relative to GAPDH (arbitraty units of densitometry)
Time (h)
I
Control
siRNA A2
CHOP expression relative to GAPDH (arbitraty units of densitometry)
Time (h)
J
Cont
XBP1-GFP
48h
siA1
siA2
K
Control
siRNA A1
siRNA A2
UPR induction of XBP1-GFP splice variant (percent positive cells)
Time (h)

Figure 6: Loss of dystonin results in ER stress–mediated induction of the unfolded protein response. (A, B) Antigenic labeling of CHOP by immunofluorescence confirmed an induction of CHOP expression in whole DRGs from *dt*^{27} animals relative to WT littermate controls (scale bars, 50 μm). (C) Phenotypic WT and *dt*^{27} DRGs were analyzed by Western blot for induction of UPR proteins BiP and CHOP. A significant induction of both BiP and CHOP was observed in P15 *dt*^{27} DRGs (each lane represents pooled DRGs from three animals). (D) Induction of BiP expression following loss of dystonin-a2 was confirmed by immunofluorescence antigenic labeling (scale bars, 10 μm). (E–I) Isoform-specific depletion of dystonin was performed in F11 neuronal cells and the effect on UPR induction determined. (E, F) Although Western analysis did not reveal a change in BiP expression following dystonin-a1 silencing, an increase in (G, H) BiP and (G, I) CHOP expression was detected within 48 h of dystonin-a2 silencing; ANOVA, post hoc Dunnett's t test, *$p < 0.05$, **$p < 0.01$, $n = 3–7$). (J, K) UPR-mediated activation of XBP1 splicing was then determined by total cell counts of XBP1-GFP expression. A 48-h dystonin-a1 depletion resulted in a modest induction of XBP1 splicing, whereas a dramatic increase in splicing was observed following loss of dystonin-a2 (scale bars, 10 μm); ANOVA, post hoc Dunnett's t test, *$p < 0.05$, **$p < 0.01$, $n = 3–7$.

ER structural integrity and calcium homeostasis are perturbed in dt^{27} mice

We previously reported that the N-terminal transmembrane domain of dystonin-a2 localizes the protein to the ER and that overexpression of dystonin-a2 results in reorganization of ER membranes (Young and Kothary, 2008). We thus postulated that ER stress induced by loss of the dystonin-a2 isoform might manifest as a result of perturbed cytoarchitecture within the ER and/or the impaired anchoring of ER membrane to the cytoskeleton. To test these possibilities further, we performed a time course of electron microscopy on WT and dt^{27} DRGs and evaluated ER morphology within sensory neurons (Figure 7, A–C). Normal striated patterning of ER can be identified in WT and dt^{27} DRGs at P4; however, by P10 the ER of dt^{27} DRGs appear dilated. This pathology increases in severity by P15, and in some instances the ER appears vacuolated, suggesting impaired ER cytoskeletal dynamics (Figure 7D). This ER pathology precedes phenotypic onset in dt^{27} mice.

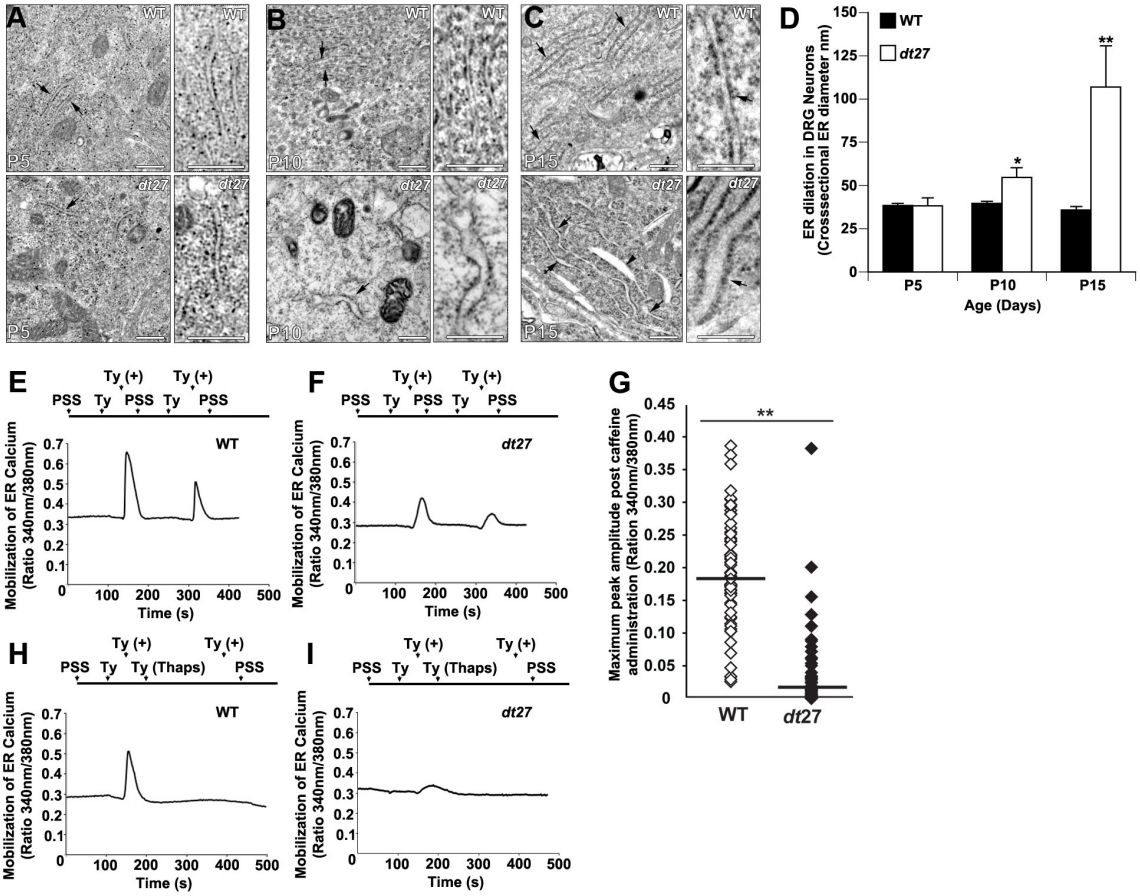

Figure 7: ER Ca^{2+} homeostasis is perturbed in the sensory neurons of *dt*^{27} mice.

Electron microscopy of WT and *dt*^{27} DRGs at (A) P5, (B) P10, and (C) P15. Normal striated patterning of ER can be observed in WT DRGs (A–C top, arrows). In contrast, the ER in *dt*^{27} DRGs is dilated (A–C, bottom arrows), leading to vacuole formation in some instances (C, bottom, arrowhead; scale bars, 500 nm). (D) Quantification of ER dilation shows a significant increase in ER dilation at P10 and P15 in *dt*^{27} DRGs relative to WT; one-way Student's t test, *$p < 0.05$, **$p < 0.01$, $n = 3$. Ca^{2+} mobilization from the ER of (E) P15 WT and (F) *dt*^{27} primary sensory neurons was visualized and recorded using Fura-2AM dye, and a representative graph is depicted. Neurons were perfused with PSS for 100 s prior to Ca^{2+} depletion in tyrode (Ty) buffer for 30 s. Caffeine was then administered for 30 s in tyrode buffer [Ty(+)] to stimulate Ca^{2+} efflux from the ER.

Following Ca^{2+} efflux, neurons were then reperfused in PSS to replenish Ca^{2+} stores and the sequence was repeated. Ca^{2+} efflux from the ER is indicated by a shift in the 340/380-nm ratio of Fura-2 fluorescence emittance. (F, G) *dt*^{27} sensory neurons showed reduced ER calcium efflux relative to WT sensory neurons as indicated by a reduction in maximum peak amplitude following caffeine administration; Student's t test, **$p < 0.01$, $n = 61–63$. Ca^{2+} reuptake was normal in both WT and *dt*^{27} sensory neurons as indicated by the second peak response. The experimental paradigm in E was repeated in (H) WT and (I) *dt*^{27} sensory neurons, with the exception that between the first and second sequences the neurons were perfused with thapsigargin (Thaps) for 180 s to block Ca^{2+} reuptake by SERCA pumps. Following SERCA inhibition, caffeine stimulation did not result in Ca^{2+} mobilization, confirming that caffeine was indeed stimulating efflux from ER stores alone and that all Ca^{2+} in the ER was effluxed following stimulation with caffeine.

We then evaluated whether a defect in ER morphology correlates with aberrant Ca^{2+} homeostasis, thus initiating ER stress signal transduction. WT and *dt*^{27} primary sensory neurons were visualized and recorded using the Ca^{2+}-sensitive dye Fura-2AM. Neurons were depleted of Ca^{2+} by perfusion in Ca^{2+}-free tyrode solution. Cells were then stimulated with caffeine to promote ryanodine receptor–mediated Ca^{2+} efflux from the ER (Ehrlich et al., 1994). *dt*^{27} sensory neurons showed reduced ER calcium efflux relative to WT sensory neurons as indicated by a reduction in maximum peak amplitude following caffeine administration (Figure 7, E–G). Ca^{2+} reuptake was normal in both WT and *dt*^{27} sensory neurons as indicated by the second peak response following caffeine administration. To confirm that the observed peak response was indeed a result of Ca^{2+} efflux from the ER, following caffeine administration, neurons were perfused for 3 min with thapsigargin to block Ca^{2+} reuptake by sarco/endoplasmic reticulum Ca2+-ATPase (SERCA) pumps (Lytton et al., 1991). Following SERCA inhibition, caffeine stimulation did not result in Ca^{2+} mobilization, confirming that caffeine was indeed stimulating efflux from ER stores alone and that all Ca^{2+} in the ER was effluxed following stimulation with caffeine (Figure 7, H and I). We then further evaluated which dystonin isoform was primarily responsible for maintaining ER Ca^{2+} homeostasis. Mobilization of ER Ca^{2+} stores was measured following isoform-specific dystonin silencing in F11 neuronal cells (Supplemental Figure S3). Isoform-specific loss of dystonin-a2 resulted in a decrease in maximum peak amplitude relative to control siRNA-treated cells, whereas dystonin-a1 depletion had no effect on ER Ca^{2+} efflux (Supplemental Figure S3, A–D). Taken together, these data suggest that impaired cytoarchitecture at the ER results in ER dilation

and a reduction in the steady-state levels of ER Ca^{2+}. This in turn would promote the observed ER stress–mediated apoptotic signaling cascade.

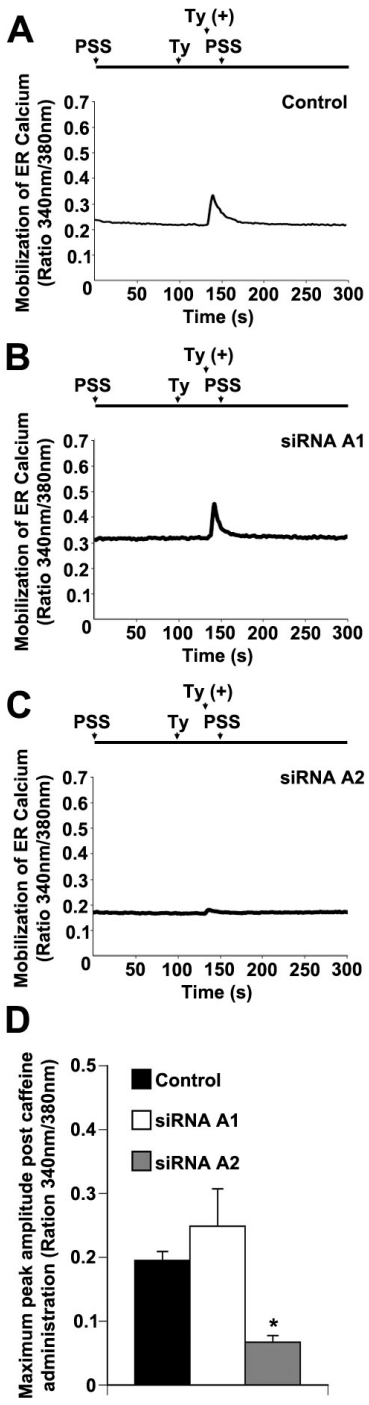

Figure S3. Dystonin-a2 loss perturbs ER calcium homeostasis. Ca^{2+} mobilization from the ER of F11 neuronal cells treated with (A) scrambled control siRNA, (B) siRNA to dystonin-a1 or (C) siRNA to dystonin-a2 was visualized and recorded using Fura-2AM dye, and a representative graph depicted. Neurons were perfused with PSS for 100 s

prior to Ca^{2+} depletion in tyrode (Ty) buffer for 30 s. Caffeine was then administered for 30 s in tyrode buffer [Ty(+)] to stimulate Ca^{2+} efflux from the ER. Following Ca^{2+} efflux, neurons were then re-perfused in PSS to replenish Ca^{2+} stores. Ca^{2+} efflux from the ER is indicated by a shift in the 340 nm/380 nm ratio of Fura-2 fluorescent emittance. (D) Depletion of dystonin-a2 specifically resulted in reduced ER Ca^{2+} efflux relative to control cells as indicated by a reduction in maximum peak amplitude following caffeine administration. Depletion of dystonin-a1 did not have a significant impact on Ca^{2+} efflux (anova, post-hoc dunnett t-test, $*p<0.01$, n=31-45).

Inhibition of ER stress signal transduction rescues dystonin-deficient neurons from death

Finally, to confirm that ER stress was the primary source of neuronal degeneration in *dt*^{27} mice, we attempted to rescue neurons from cell death by intervening in the apoptotic signal cascade identified (Figure 8). We first assessed whether various caspase inhibitors could prevent downstream executioner caspase 3 activation in F11 neuronal cells following loss of dystonin-a2. Pan-caspase inhibition or inhibition of caspase 2 but not caspase 12 prevented downstream caspase 3 activation in F11 neuronal cells (Figure 8A). This was confirmed in primary sensory neurons from *dt*^{27} mice, in which pan-caspase inhibition in addition to inhibition of either caspase 2 or caspase 12 prevented downstream caspase 3 activation (Figure 8B). These data confirmed that ER-associated caspase activation is critical to neurodegeneration in *dt*^{27}. We then sought to block UPR signal transduction directly and evaluate the effect on cell viability. Salubrinal is a selective inhibitor of cellular complexes that dephosphorylate eIF2α, a downstream effector of UPR-mediated protein kinase R–like ER kinase (PERK) activation (Boyce et al., 2005). Western analysis of F11 neuronal cells treated with various concentrations of salubrinal confirmed that it inhibits downstream UPR signaling by preventing dephosphorylation of eIF2α (Figure 8C). Fold change in ethidium homodimer incorporation showed that whereas dystonin-a2 depletion causes a significant increase in death, salubrinal treatment significantly reduces this death (Figure 8, D and E). Finally, we evaluated the effect of salubrinal treatment on viability of *dt*^{27} primary sensory neurons as assessed by ethidium homodimer incorporation. Here we show that UPR blockade with 25 μM salubrinal prevents degeneration in primary *dt*^{27} sensory neurons. In

summary, these data highlight a critical role for dystonin-a2 in mediating normal ER structure and function. Loss of this protein leads to the ER stress and apoptosis that underlie the sensory neurodegeneration observed in *dt*^{27} mice.

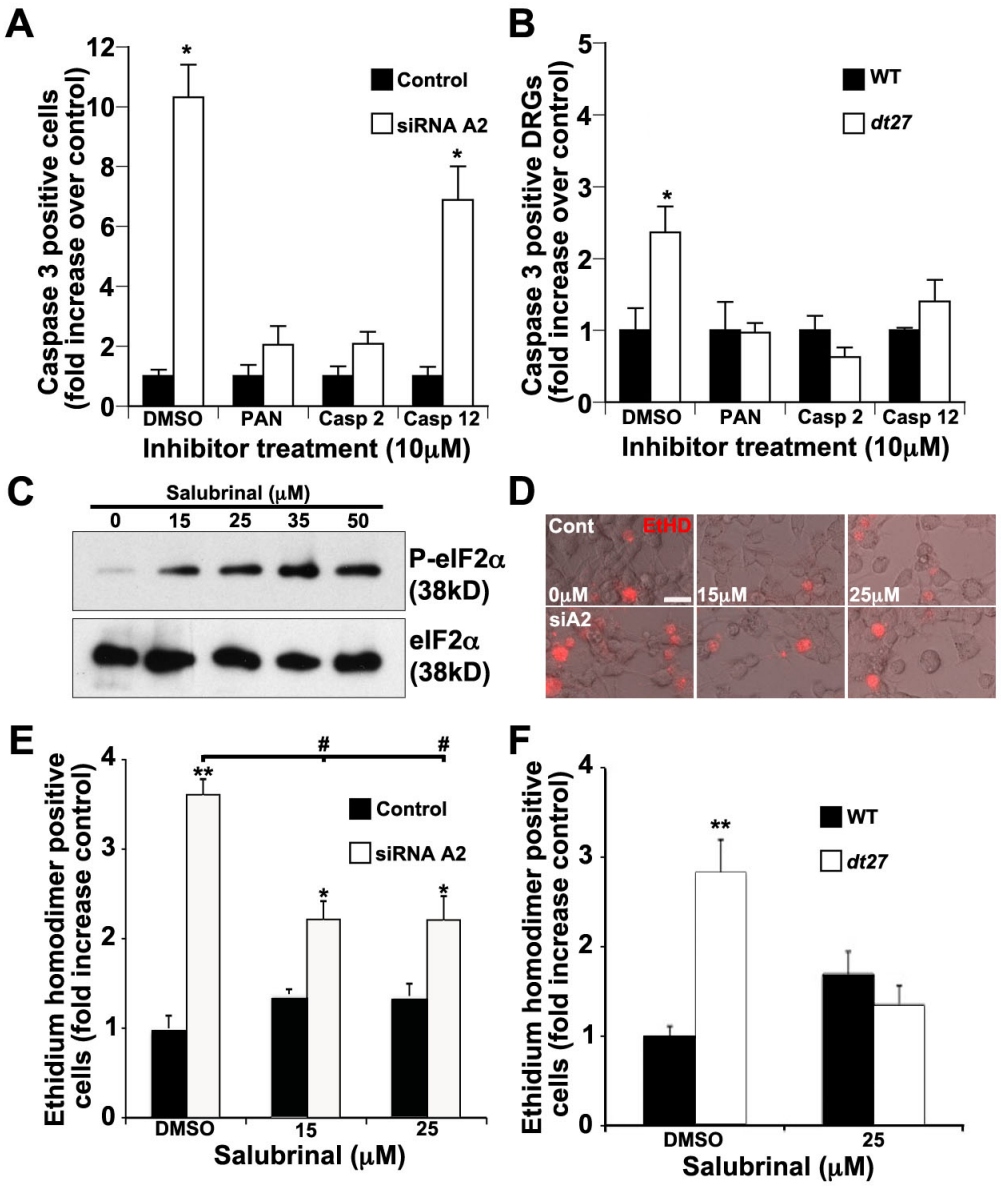

Figure 8: Inhibition of ER stress and the associated caspase cascade rescues dystonin-a2–deficient neurons from death. (A) F11 neuronal cells were screened for caspase 3 activation following knockdown of dystonin-a2 in the presence of various caspase inhibitors using the FLICA assay. Pan-caspase inhibition or inhibition of caspase 2 but not caspase 12 prevented downstream caspase 3 activation in F11 neuronal cells; ANOVA, post hoc Dunnett's t test, *$p < 0.05$. (B) In P15 primary sensory neurons from *dt*^{27} mice subjected to the same assay, pan-caspase inhibition in addition to inhibition of

either caspase 2 or caspase 12 prevented downstream caspase 3 activation; ANOVA, post hoc Dunnett's t test, *$p < 0.05$, $n = 9$. (C) Western analysis of F11 neuronal cells treated with various concentrations of salubrinal confirmed that salubrinal inhibits downstream UPR signaling by preventing dephosphorylation of eIF2α. Fold change in ethidium homodimer incorporation showed that whereas dystonin-a2 depletion causes a significant increase in death (ANOVA, post hoc Tukey, **$p < 0.01$, $n = 9$), salubrinal treatment at 15 and 25 μM significantly reduces death resulting from depletion of dystonin-A2 in F11 neuronal cells relative to vehicle (DMSO)-treated cells (D, E) (scale bars, 10 μm; ANOVA, post hoc Tukey, #$p < 0.05$). (F) Measurements of fold change in ethidium homodimer incorporation indicate that 25 μM salubrinal treatment rescues dt^{27} primary sensory neurons from death; Student's t test, **$p < 0.01$, $n = 18–20$.

Discussion

Mutations in the *Dst* gene that encodes all isoforms of the giant cytoskeletal cross-linking protein dystonin result in sensory neurodegeneration in *dt* mice (Brown et al., 1995). The consensus regarding this degenerative event is that it arises due to loss of structural organization of cytoskeletal elements (Leung et al., n.d.; Yang et al., 1996, 1999). The numerous functions of the cytoskeleton have made elucidation of the mechanism underlying *dt* pathogenesis challenging. Here we identify a signaling cascade resulting from dystonin deficiency in sensory neurons by which loss of organelle integrity that precedes phenotypic onset in dt^{27} mice triggers ER-mediated apoptosis (Figure 9). We observe ultrastructural dilation of the ER that correlates with Ca^{2+} dyshomeostasis and activation of canonical ER stress proteins. This in turn leads to activation of ER stress caspases 2 and 12, culminating in apoptosis. Furthermore, we propose these pathologies to be the consequence of specific loss of dystonin-a2.

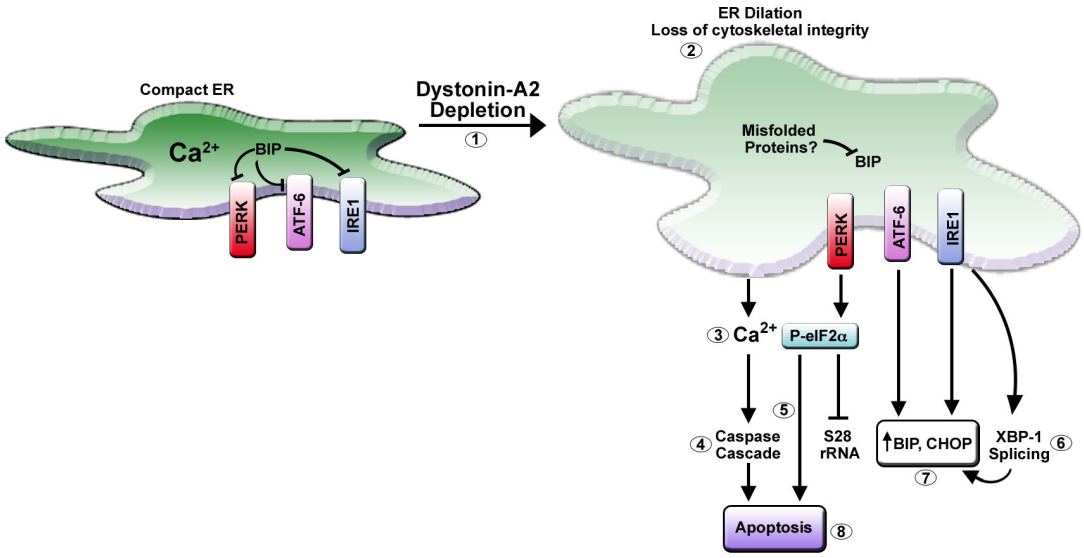

Figure 9: Proposed model of apoptotic signaling initiated by depletion of dystonin-a2 in sensory neurons. 1) Schematic representation of the events that occur following depletion of dystonin-a2 in sensory neurons. 2) Depletion of dystonin-a2 results in a loss of cytoskeletal integrity that culminates in dilation of the ER. 3) Perturbed ER homeostasis leads to a decrease in the steady-state levels of Ca^{2+} in the ER. 4) The associated rise in free intracellular Ca^{2+} likely results in activation of an ER-dependent caspase cascade, inhibition of which can maintain cell viability. 5) Blockade of downstream eIF2α signaling with salubrinal partially rescues neurodegeneration following dystonin-a2 depletion, implicating PERK-mediated eIF2α signal transduction in the apoptotic cascade. 6) Enhanced XBP1 splicing likely coupled with activation of ATF-6 and IRE1 promotes expression of protein chaperones (7) BiP and CHOP in an attempt to maintain ER function. 8) The inability to rescue ER structural integrity culminates in DNA cleavage and programmed cell death.

Dystonin as a regulator of ER stress

The ER is involved in transduction of apoptotic signaling through two pathways—UPR and Ca^{2+} mobilization. UPR is initiated to restore protein folding in the ER and can itself lead to ER dilation through autophagy (Høyer-Hansen and Jäättelä, 2007). Apoptosis is initiated when ER function cannot be restored (Høyer-Hansen and Jäättelä, 2007). Ca^{2+} mobilization from the ER results in activation of the cysteine protease m-calpain (Orrenius et al., 2003). Calpain activation promotes apoptosis through activation of ER-associated caspase 12 (Nakagawa et al., 2000). Alternatively, activation of caspase 2 depends on both cleavage and phosphorylation by Ca^{2+}-dependent CaMKII (Nutt et al., 2005). Caspase 2 propagates apoptosis through activation of executioner caspases and cleavage of cytoskeletal linker protein αII-spectrin. In *dt*, we find a pronounced neuroprotection effected by caspase blockade and a partial rescue of neuronal viability by the UPR inhibitor salubrinal. The dependence of caspase 2 and 12 activation on Ca^{2+} signal transduction implicates ER-Ca^{2+} dyshomeostasis as a primary inducer of neurodegeneration in *dt*.

Molecular interaction studies implicated dystonin in regulation of the dynein motor complex (DMC) through interaction with dynactin and the endosomal vesicle protein retrolinkin (Liu et al., 2003c, 2007a). It is intriguing to speculate how this interaction may implicate cytoskeletal linker proteins as master regulators of ER function. Mutations in the cytoskeletal linker protein βIII-spectrin cause severe cerebrospinal ataxia in murine and Drosophila models (Lorenzo et al., 2010; Perkins et al., 2010). The ataxic phenotype is enhanced by both dynein and dynactin loss-of-function mutations, implicating aberrant intracellular transport as a mediator of pathology (Lorenzo et al.,

2010). The potential role for dystonin as a DMC component, coupled with our findings of a role for dystonin-a2 as mediator of ER integrity, supports the notion that dystonin may regulate components of the endocytic pathway. Indeed, cytoskeletal linkers may have a general role in mediating axonal transport by regulating ER and endosomal organization. As such, their dysfunction may contribute to numerous neurodegenerative conditions whose etiologies are unknown. Aberrations in the signaling events described previously are associated with neurodegenerative disease. For example, mutations in the ER protein presenilin-1 found in familial Alzheimer disease (Sherrington et al., 1995) result in aberrant Aβ processing (Lemere et al., 1996) and increased neuronal susceptibility to ER stress (Katayama et al., 1999). ER stress further promotes Aβ generation, propagating disease pathology (Suh and Checler, 2002). Aβ itself mediates ER collapse by interfering with membrane anchoring to the cytoskeleton (Lai et al., 2009).

Dystonin-a2 and organelle integrity

Initial studies on *dt* mice demonstrated an involvement of the perikaryon of certain sensory neurons in disease. Peripheral displacement of Nissl substance, nuclear eccentricity, and cell enlargement were among defects noted (Duchen et al., 1964; Messer and Strominger, 1980b; Sotelo and Guenet, 1988). More recently, investigation of $dt^{Tg4/Tg4}$ sensory neurons also documented perikaryal defects, suggesting that abnormalities other than those from cytoskeletal disorganization in the axon could initiate or contribute to *dt* pathogenesis (Young and Kothary, 2008). These initial observations of *dt* perikaryon abnormalities fit well with recent data that demonstrated an N-terminal transmembrane domain contained in dystonin-a2 facilitates its localization to perinuclear

membranes (Young et al., 2006). Involvement of dystonin-a2 as a structural component of the ER is further supported by the finding that ectopic overexpression of dystonin-a2 fusion protein alters the subcellular localization of calreticulin (Young and Kothary, 2008). Furthermore, altered protein disulfide isomerase expression in $dt^{Tg4/Tg4}$ sensory neurons suggested that ER dysfunction or impaired protein folding may come as a result of perturbed ER structure in multiple *dt* mutant alleles (Young and Kothary, 2008).

In the present study, we find ER structural integrity to be perturbed in dt^{27} sensory neurons (Figure 7C). Although past studies on *dt* sensory neurons highlighted unexplained changes in ER resident proteins, a mechanistic link between aberrant ER ultrastructure, and activation of ER stress signaling cascades has yet to be resolved. ER dilation and vacuole formation can occur as a component of autophagy and is often induced by ER stress as a neuroprotective mechanism to remove damaged organelles (Koga et al., 2011; Scheper et al., 2011). It is surprising that ER dilation in this instance preceded caspase activation (Figure 4) and UPR induction (data not shown). Considering previous related work on the subject, which described dystonin-a2 as an anchor for perinuclear membranes through its attachment of actin microfilaments, we propose compromised organelle structure to result from loss of cytoskeletal interaction. Indeed, it has been established that organization, movement, and proper function of organelles are highly reliant upon the cytoskeleton (Barr and Egerer, 2005; Starr, 2007; Bola and Allan, 2009). An example of organelle integrity being maintained through cytoskeletal linking proteins is found in the microtubule actin cross-linking factor-1b (MACF1b). As a member of the plakin protein family, MACF1b shares similar domain architecture as dystonin-a. It interacts with microfilaments and microtubules and is critical for Golgi

complex polarization and stability of the microtubule-organizing complex (Leung et al., n.d.; Kodama et al., 2003; Lin et al., 2005). Although the two proteins are expressed in many of the same tissues, DRG neurons express predominantly dystonin (Leung et al., 2001a), which might explain why *dt* degeneration is most prominent in sensory neurons.

Because the functions of organelles are contingent upon organelle structure, the establishment of dystonin-a2 as an ER structural anchor makes it not surprising that Ca^{2+} dyshomeostasis and UPR activation are observed in *dt* sensory neurons. Hallmark pathologies of many neurodegenerative diseases center on elements of ER dysfunction. Future studies should aim to determine whether abnormal ER morphology causes Ca^{2+} dyshomeostasis, whether dystonin-a2 interacts with ER-proteins, or whether cytoskeletal stabilization prevents ER stress in other sensory neuropathies. The partial rescue implied by UPR blockade following dystonin-a2 loss indicates that the mechanisms causing death of *dt* sensory neurons are still active. To further discern the functions of dystonin isoforms, we must target upstream of ER defects. Collectively, data presented here provide compelling evidence that dystonin-a2 is a critical mediator of normal ER structure and function.

Materials and Methods

Reagents

All chemicals were purchased through Sigma-Aldrich (St. Louis, MO), and all cell culture reagents were obtained from Invitrogen (Burlington, Canada), except where indicated.

Animals and cell culture

The dt^{27} and $dt^{Tg4/Tg4}$ mutant mice and control littermates were used at prephenotype (P4 and P10) or phenotype stage (P15). The generation of these lines and characterization of the mutation were described previously (Kothary et al., 1988; Brown et al., 1995; Pool et al., 2005). The onset of phenotype was generally assessed by the appearance of clasping of hind limbs after the mice were picked up by the tails. dt^{27} and $dt^{Tg4/Tg4}$ mice were genotyped by PCR amplification of genomic tail DNA. DRG tissue sections of the lumbar spinal cord region were prepared as previously described (Young and Kothary, 2008). All animal procedures were performed in accordance with institutional guidelines (Animal Care and Veterinary Services and Ethics, University of Ottawa).

Cos-1 cells (an African green monkey kidney fibroblast-like cell line obtained from American Type Culture Collection, Manassas, VA) and F11 cells (a fusion of embryonic rat DRG cells with a mouse neuroblastoma cell line, kindly supplied by Paul Albert, University of Ottawa) were maintained in DMEM + 10% fetal bovine serum (FBS) and 1% penicillin/streptomycin/antimycotic. Cells were passaged at ~70% confluency in 10-cm plastic Petri dishes and plated onto glass coverslips for use in immunofluorescence assays. Cell transfections were performed using Lipofectamine 2000 (Invitrogen), according to the manufacturer's directions.

Primary culture of sensory neurons

Spinal columns were removed from P4, P10, or P15 mice and transferred to a dissection microscope. Approximately 40 DRGs were isolated per mouse and subsequently digested for 15 min each with collagenase A (Roche, Laval, Canada) and papain (Worthington,

Lakewood, NJ) solutions. DRG neurons were dissociated with flame-polished glass Pasteur pipettes and seeded onto 12-mm laminin-2 (Millipore, Billerica, MA)–coated coverslips at a density of 50,000 in DMEM with 10% FBS and 1% penicillin/streptomycin. Cells were placed in a 37°C tissue culture incubator under 8.5% CO2. The following day, the media was changed to neuronal maintenance media (DMEM base, 0.5% FBS, 2% B27, 1% GlutaMax, 16 μg/ml putrescine, 400 μg/ml thyroxine, 400 μg/ml triiodothyronine, 6.2 ng/ml progesterone, 5 ng/ml sodium selenite, 100 μg/ml bovine albumin serum, 5 μg/ml bovine insulin, 50 μg/ml holo-transferrin) supplemented with 200 ng/ml nerve growth factor and 1 μM 5-fluoro-2′-deoxyuridine. A three-fourths media change was carried out every other day, up until day 6 of culture, when calcium-imaging experiments were performed.

Sample preparation for electron microscopy

Samples for electron microscopy were prepared as previously described (De Repentigny et al., 2011). Briefly, dt^{27J} (n = 4) and WT (n = 4) mice were anesthetized at P5, P10, or P15 via intraperitoneal injection of tribromoethanol (Avertin). Mice were perfused transcardially with 3 ml of phosphate-buffered saline (PBS), followed by 10 ml of Karnovsky's fixative (4% paraformaldehyde [PFA], 2% glutaraldehyde, and 0.1 M cacodylate buffer in PBS, pH 7.4). The lumbar region of the spinal cord was dissected and DRGs collected under a stereomicroscope. Ultrathin sections (70 nm) were placed on a 300-mesh copper specimen grid, counterstained in 5% uranyl acetate and Reynold's lead citrate, and then observed by transmission electron microscopy.

siRNA and RT-PCR

Custom siRNAs were developed to target specific dystonin isoforms. To knock down dystonin-a1 and dystonin-a2, isoform-specific nucleotides between 2310 and 2380 (accession number AF396878) for dystonin-a1 and nucleotides between 1 and 661 (accession number: DQ02331) for dystonin-a2 were chosen for the development of siRNAs. The following groups of siRNA sequences were efficacious in knocking down dystonin-a1 and dystonin-a2 expression, respectively: group A (sense 5′–3′) ACAUGUACGUGGAGGAGCAtt; (anti-sense 5′–3′) UGCUCC-UCCACGUACAUGUag, (sense 5′–3′) CCGCCUACAUGUAC-GUGGAtt (antisense 5′–3′) UCCACGUACAUGUAGGCGGcg; group B (sense 5′–3′) CAAGCAUGAGAGAUCCAAAtt; (antisense 5′–3′) UUUGGAUCUCUCAUGCUUGgg; (sense 5′–3′) CUUCCUCUUGUUGCUCCUGtt; (antisense 5′–3′) CAGGAGCAACAAGAGGAAGag. The siRNA target sequences were conserved between mouse and rat. All siRNAs (Silencer Select Custom Designed siRNA) were obtained from Applied Biosystems/Ambion (Austin, TX) and compared with the effects of scrambled controls matched for GC content. F11 and Cos-1 cells were transfected with siRNA using Lipofectamine 2000. Knockdown was assessed at the transcript and protein level. Total RNA was collected from F11 cells using RNeasy Mini Kit (Qiagen, Toronto, Canada) according to manufacturer's protocol. For RT-PCR, QuantiTect Reverse Transcription Kit (Qiagen) was used, following manufacturer's protocol. cDNAs encoding dystonin-a1, dystonin-a2, and actin (control) derived from mouse were PCR amplified as previously described (Pool et al., 2005). For assessment of protein knockdown, Cos-1 cells were cotransfected with siRNA and recombinant

dystonin proteins (dystonin-a2–YFP and Nterm-dystonin-a1–GFP) using Lipofectamine 2000. Fluorescence intensity of recombinant dystonin proteins was used to assess siRNA knockdown efficiency.

Recombinant proteins

The dystonin-a1–GFP construct (GFP-Nterm1) was previously described (Young et al., 2003b). The dystonin-a2–YFP construct was designed and cloned by Kevin Young while a member of the Kothary lab. The 5′ N-terminal region of the dystonin-a2 isoform (a2Nterm-myc/his) (Young and Kothary, 2008) and the 3′ end of an expressed sequence tag clone (GenBank accession AI526522) (Young et al., 2006) were ligated in frame into a pEYFP-N1 vector. The reporter plasmid pHA-XBP1u-GFP was a gift from John Ngsee of the Ottawa Hospital Research Institute and was previously described (Yu et al., 2006). Calreticulin-YFP and Golgi-YFP were gifts from Xiaohui Zha of the Ottawa Hospital Research Institute.

Cell viability

Dead cells were identified by uptake of ethidium homodimer (2 μM) as a result of loss of membrane integrity. Cells were then visualized with a Zeiss Axiovert 200m epifluorescence microscope under 10× objective (Achroplan 0.25) equipped with an AxioCam HRM digital camera and AxioVision 4.6 software (Zeiss, Toronto, Canada).

Fluoro-Jade B staining

Fluoro-Jade B (Millipore) staining was performed according to the method of Schmued et al. (1997). Briefly, 12-µm DRG sections were fixed with 4% PFA dried on a slide warmer at 45°C. The tissue was then subjected to a series of washes (100% ethanol, 3 min; 70% ethanol, 1 min; ddH2O, 1 min; 0.06% potassium permanganate, 15 min; double-distilled water, 1 min; 0.001% Fluoro-Jade in 0.1% acetic acid, 20 min; 3× double-distilled water, 1 min; and xylene, 1 min; and then coverslipped with Permount [Fisher Scientific, Ottawa, Canada]). Sections were analyzed with a Zeiss Axiovert 200m epifluorescence microscope under 10× objective (Achroplan 0.25) equipped with an AxioCam HRM digital camera and AxioVision 4.6 software.

TUNEL

Cells/tissue was washed in PBS and permeabilized in ice-cold 0.1% sodium citrate/0.1% Triton X-100 for 5 min, followed by 2 min in 2:1 ethanol:acetic acid on ice. Samples were rinsed for 2 min in PBS and incubated for 1 h at 37°C with FITC-labeled dUTP in terminal deoxynucleotidyl transferase (TdT) buffer (30 mM Tris-HCl, pH 7.2, 140 mM sodium cacodylate, and 1 mM cobalt chloride) and TdT according to the protocol provided by the manufacturer (Roche). Negative controls included sections incubated with fluorescein isothiocyanate–labeled dUTP in the absence of TdT. Cells were washed in PBS, mounted in fluorescence mounting media (Dako, Burlington, ON), and analyzed with a Zeiss Axiovert 200m epifluorescence microscope under 10× objective (Achroplan 0.25) equipped with an AxioCam HRM digital camera and AxioVision 4.6 software.

Caspase activity assay

Caspase activity in live cells was measured using fluorescein (caspase 12, fluorescein isothiocyanate–ATAD–fluoromethyl ketone [FMK]; Abcam, Cambridge MA) and fluorescence-labeled inhibitor of caspase activity (FLICA; caspase 8, carboxyfluorescein [FAM]–LETD–FMK; caspase 2, FAM-VDVAD-FMK; and caspase 3/7, FAM-DEVD-FMK; ImmunoChemistry Technologies, Bloomington, MN) assays. Fluorescein/FLICA assays were performed using a modified protocol from the manufacturers' instructions. Briefly, 1.67 μl of 30× fluorescein/FLICA reagent (diluted in PBS) was added to each well of a 96-well plate. Cells were incubated for 1 h at 37°C and 5% CO2. Cells were washed twice in PBS and analyzed with a Zeiss Axiovert 200m epifluorescence microscope under 10× objective (Achroplan 0.25) equipped with an AxioCam HRM digital camera and AxioVision 4.6 software. Phase contrast and fluorescence photos were taken of six random fields per well for three of four replicate wells in duplicate or triplicate experiments. The mean number of cells with active caspases at each time point was determined, and data were then standardized against scrambled or WT controls where appropriate to determine fold change in caspase activity attributable to loss of dystonin. Functional dependence of downstream caspase activation on active caspases 2 and 12 or other caspase activation (PAN) was assessed. F11 or primary sensory neurons were treated with either the caspase 2 inhibitor Z-VDVAD-FMK (50 μM), the caspase 12 inhibitor Z-ATAD-FMK (50 μM), or the PAN caspase inhibitor Z-VAD-FMK. Caspase 3 activation was then assessed as described.

Immunocytochemistry

Cultures were fixed in 4% PFA prior to antigenic labeling. Primary antibodies used were rabbit polyclonal anti–cleaved caspase 3 (1:1000; Cell Signaling Technology, Beverly, MA), mouse monoclonal anti–caspase 2 (1:500; EMD Biosciences, San Diego, CA), and mouse monoclonal anti-CHOP (1:1000; Cell Signaling Technologies). Secondary antibodies used were anti–mouse Alexa 488 (1:2000; Molecular Probes, Invitrogen), anti–mouse Alexa 555 (1:2000; Molecular Probes), and anti–rabbit Alexa 488 (1:2000; Molecular Probes). Antibodies were diluted in antibody buffer (PBS, 0.3% Triton X-100, 3% BSA). Where 4′,6-diamidino-2-phenylindole (DAPI) staining is indicated, samples were incubated in DAPI stain (0.2 μg/ml in PBS) for 10 min and washed three times in PBS for 5 min. Samples were mounted in fluorescence mounting media (Dako) and analyzed a Zeiss Axiovert 200m epifluorescence microscope under either a 10× objective (Achroplan 0.25) or a 40× objective (Achroplan 1.3 Oil) equipped with an AxioCam HRM digital camera and AxioVision 4.6 software. Where colocalization studies were performed, F11 neuronal cells treated with either scrambled siRNA or siRNA targeted against dystonin-a2 were analyzed with an LSM 510 meta confocal microscope equipped with an EC Plan-Neofluar 40×/1.30 Oil DIC M27 objective using Zen 8.0 software (Zeiss). Using the colocalization module of Zen 8.0, we compared the total area of caspase 2 staining per the cell with the area of caspase 2 staining that colocalized with either calreticulin-YFP or Golgi-YFP within that same cell. The area of colocalization was then calculated as the percentage colocalized area over the total area of caspase 2. Twelve cells from three different experiments were analyzed per condition.

Western analysis

Proteins were isolated in RIPA buffer (10 mM PBS, 1% NP40, 0.5% sodium deoxycholate, 0.1% SDS, 30 µl/ml aprotinin, 10 mM Na orthovanadate, 100 µl/ml phenylmethylsulfonyl fluoride). Protein samples (30 µg) were separated by SDS–PAGE under reducing conditions. Western analyses were performed using primary mouse monoclonal anti–caspase 2 (1:500; BD Transduction Laboratories, Lexington, KY), mouse monoclonal anti-CHOP (1:1000, Cell Signaling Technology), polyclonal anti–binding protein (BiP, 1:1000; Cell Signaling Technology), rabbit polyclonal anti–phospho-eIF2α (1:1000; Cell Signaling Technology), rabbit polyclonal anti-eIF2α (1:1000; Cell Signaling Technology), rabbit polyclonal anti– glyceraldehyde-3-phosphate dehydrogenase (GAPDH) (1:5000; Abcam), and mouse monoclonal anti–BIII-tubulin (1:2000, E7 clone; Hybridoma Bank, Iowa City, IA). Owing to low protein yields from DRGs, analysis of ER stress (Figure 6 and Supplemental Figure S2) was performed using pooled DRGs from three WT and three *dt*[27] mice per sample. A 40-µg protein sample was loaded thereafter. Secondary antibodies used were horseradish peroxidase (HRP)–conjugated anti-mouse immunoglobulin G (IgG, 1:2000; Bio-Rad, Hercules, CA) and HRP-conjugated anti–rabbit IgG (1:2000; Bio-Rad). Immunoreactive bands were visualized using SuperSignal West Pico (MJS BioLynx, Brockville, Canada). Quantification of protein expression levels was performed by densitometric analysis of individual bands using ImageJ analysis software (National Institutes of Health, Bethesda, MD). At least three Western blots from different experiments were evaluated by densitometry and normalized to a protein standard (actin, tubulin, or GAPDH) for all Western blots depicted.

Ratiometric measurement of intracellular Ca^{2+} using Fura-2AM in primary sensory neurons

The measurement of intracellular Ca^{2+} ($[Ca^{2+}]i$) was performed using the ratiometric dye Fura-2AM based on previously published protocol (Jiang et al., 2005). Briefly, P15 sensory neuron cultures or F11 neuronal cells were grown on 2-mm laminin-2 (Millipore)–coated coverslips (as described) and loaded with 5 μM Fura-2AM (Molecular Probes) and 0.02% pluronic acid in neuronal maintenance media and placed in a 37°C tissue culture incubator under 8.5% CO2 for 30 min. Sensory neuron cultures were then rinsed with PSS Mg2+ buffer (2 mM 4-(2-hydroxyethyl)-1-piperazineethanesulfonic acid [HEPES], pH 7.2, 140 mM NaCl, 5 mM KCl, 2.3 mM CaCl2, and 10 mM glucose) and stabilized in the same buffer for 5 min and then placed in a microperfusion chamber, where Fura-2AM intensities were measured by the Northern Eclipse Digital Ratio Image System (EMPIX, Mississauga, Canada) with an Axiovert 200 camera and light source (Zeiss). After a region was chosen, Fura-2 fluorescence was measured at 510-nm emission with 340/380-nm dual excitation selected by a DG-5 system (Sutter Instrument Company, Novato, CA). $[Ca^{2+}]i$ concentration was determined via the ratio of fluorescence intensity between the two excitation wavelengths of 340/380 nm of Fura-2. The basal level of $[Ca^{2+}]i$ was recorded for 100 s in PSS buffer, followed by a 30-s perfusion of calcium-free Tyrode solution (9 mM NaCl, 12.5 mM KCl, 3 mM MgCl2, 30 mM glucose, 25 mM HEPES, 1 mM ethylene glycol tetraacetic acid, pH 7.4), followed by a 30-s perfusion of Tyrode solution plus caffeine (20 mM). These perfusions were repeated a second time or following 180 s of perfusion with thapsigargin (20 nM) in PSS.

Statistical analysis

Data were analyzed using Student's t test or factorial analysis of variance (ANOVA) as applicable using InStat, version 3.0 (GraphPad Software, La Jolla, CA). Following detection of a statistically significant difference in a given series of treatments by ANOVA, post hoc Dunnett's t tests or Tukey tests were performed where appropriate. $p < 0.05$ was considered statistically significant (shown as either * or #); $p < 0.01$ was considered highly statistically significant (shown as **).

Acknowledgments

We thank Kevin Young for creation of the dystonin-a2–YFP construct, as well as Justin Boyer and the rest of the Kothary laboratory for helpful discussions. We thank Michael Rudnicki for comments on the manuscript, Paul Albert for donation of the F11 cell line, Xiaohui Zha for the calreticulin-YFP and Golgi-YFP constructs, and Johnny Ngsee for the pHA-XBP1u-GFP construct. We also thank Robert Monnette for technical assistance with Ca2+ imaging. This work was supported by a grant from the Canadian Institutes of Health Research, a Multiple Sclerosis Society of Canada Research Fellowship, and a Canadian Institutes of Health Research Fellowship to S.D.R., with the support of the Dystonia Medical Research Foundation of Canada. T.S. is a Research Fellow of the Japan Society for the Promotion of Science. R.K. is a recipient of a University Health Research Chair from the University of Ottawa.

Abbreviations used

DMC dynein motor complex

DRG dorsal root ganglia

DRGN DRG sensory neuron

Dst dystonin gene

Chapter 4

Neuronal dystonin isoform2 expression is essential for the viability of proprioceptive sensory nerves in a mouse model of hereditary sensory autonomic neuropathy

Neuronal dystonin isoform2 expression is essential for the viability of proprioceptive sensory nerves in a mouse model of hereditary sensory autonomic neuropathy

Andrew Ferrier[1,3*], Tadasu Sato[1,2*], Sabrina Gibeault[1], Kunal Bhanot[1], Yves de Repentigny[1], Ryan O'Meara[1,3], Kevin Young[4] and Rashmi Kothary[1,3,5#]

[1]Ottawa Hospital Research Institute, Ottawa, Ontario, Canada K1H 8L6;

[2]Division of Oral and Craniofacial Anatomy, Graduate School of Dentistry, Tohoku University, Sendai 980-8575, Japan;

[3]Department of Cellular and Molecular Medicine, University of Ottawa, Ottawa, Ontario, Canada K1H 8M5;

[4]NRC-Institute for Biological Sciences, University of Ottawa, Ottawa, Ontario, Canada K1A0R6;

[5]Department of Medicine, University of Ottawa, Ottawa, Ontario, Canada K1H 8M5

[*]these authors contributed equally to this work

Running head: Transgenic dystonin-a2 provides partial rescue of *dystonia musculorum* mice

#Correspondence to: Rashmi Kothary; Ottawa Hospital Research Institute; 501 Smyth Road, Ottawa, Ontario, Canada K1H 8L6; Tel: (613) 737-8707; Fax: (613) 737-8803.

Author Contributions

Conceived and designed the experiments: AF TS RK. Performed the experiments: AF (figures 1, 7, 8, 10) TS, YDR, KB, KY. Analyzed the data: YDR AF SDR TS. Contributed reagents/materials/analysis tools: YDR AF SDR TS RK. Wrote the paper: AF YDR RK.

Abstract

Hereditary sensory and autonomic neuropathies (HSANs) are a group of genetically and clinically heterogeneous disorders characterized by profound sensory dysfunction and variable degrees of autonomic disturbance. In approximately two-thirds of HSAN patients, the disease-causing gene is unknown. As such, the underlying pathological mechanisms are incompletely understood. A newly identified lethal form of HSAN, designated HSAN-VI, is caused by a homozygous mutation in the dystonin gene (*DST*). The HSAN-VI mutation impacts all major neuronal dystonin protein isoforms: dystonin-a1, -a2, and -a3. HSAN-VI patients display distal limb contractures, dysautonomia, and early postnatal death. Similar to HSAN-VI, homozygous mutations in the murine *Dst* gene cause a severe sensory neuropathy termed *dystonia musculorum* (*dt*). Phenotypically *dt* mice are similar to HSAN-VI patients, manifesting progressive limb contractures, dystonia, dysautonomia, and early postnatal death. To obtain a better molecular understanding of disease pathogenesis in HSAN-VI patients and the *dt* disorder, we elucidated the causal dystonin isoforms underlying *dt* pathogenesis. In this regard, we generated transgenic mice in which exogenous dystonin-a2 expression was driven by the neuronal Prion Protein Promoter (PrP-dystonin-a2) on the $dt^{Tg4/Tg4}$ background (devoid of dystonin-a1 and -a2). Restoring dystonin-a2 expression in the nervous system, particularly within sensory neurons, attenuates the degeneration of sensory neuron subtypes, and is sufficient to ameliorate the phenotype and increase life span. Despite these improvements, however, both dystonin-a2 and dystonin-a1 are necessary for complete amelioration of *dt* pathogenesis. Taken together, this study provides needed

insight into the molecular basis of the *dt* disorder and other peripheral neuropathies including HSAN-VI.

Introduction

Hereditary sensory and autonomic neuropathies encompass a diverse group of inherited disorders of the peripheral nervous system (PNS), characterized by progressive sensory neuron degeneration and varying degrees of autonomic dysfunction (Rottier, Annelies; Baets, Jonathan; Timmerman, Vincent; Janssens, 2012). The genetic spectrum of HSANs covers both autosomal dominant and autosomal recessive forms. Autosomal dominant traits typically present in the second and third decade of life with marked sensory involvement and little autonomic and variable motor involvement, while autosomal recessive forms typically show an early onset pattern (*i.e.*, congenital or during childhood) with overt sensory and autonomic dysfunction (Rotthier et al., 2009). Based on age of onset, mode of inheritance, and predominant clinical features, a classification system was devised representing HSAN types I-V (Dyck, P.J., Thomas, P.K., Griffin, J.W., Low, P.A., Poduslo, 2005). Over the past 15 years, 12 disease-causing HSAN alleles have been identified, albeit the pathological mechanisms in over two-thirds of HSAN patients remain unresolved. As such, understanding the functional implications of known or novel genetic defects is urgently needed to better understand the molecular basis of these disorders.

A recent study has identified deleterious homozygous mutations in the *DST* gene that impart a frame-shift mutation resulting in a previously undescribed hereditary autonomic sensory neuropathy in four infants (Edvardson et al., 2012). The frame-shift mutation, which reduces dystonin-a transcript expression, starts at Glu4995 and leads to a loss of the C-terminus, which harbors the microtubule-binding domain (MTBD), a domain common to all major dystonin-a isoforms(Ferrier et al., 2013). The patients'

clinical features are reminiscent of Familial Dysautonomia (FD, also known as HSAN-III, or Riley-Day syndrome), although the course and outcome of disease are more severe and is ultimately fatal. This newly reported dystonin-related neuropathy was termed HSAN-VI, and shares clinical features reminiscent of those seen in *dystonia musculorum* (*dt*) mice. Indeed, both human patients and *dt* mice suffer from limb contractures and dysautonomia.

The *dt* phenotype is characterized as a loss of limb coordination beginning between eleven and fourteen days postnatal (Duchen et al., 1964; Duchen, 1976). As the disease progresses, which it does rapidly, limb movement becomes more uncoordinated, while writhing and twisting of the trunk become increasingly prominent features. Among the pathological features displayed by *dt* mice, degeneration is most apparent in large and medium-sized proprioceptive primary sensory afferents of the dorsal root ganglion (DRG) and cranial nerves (Sotelo and Guenet, 1988; al-Ali and al-Zuhair, 1989; Carlsten et al., 2001)

In both humans and rodents, the *DST* gene is characterized as having tissue-specific promoters and an abundance of exons that are alternatively spliced yielding differentially expressed transcripts (Suozzi et al., 2012b). Within the nervous system, three prominently large (> 600 kDa) neuronal dystonin isoforms exist: dystonin-a1, -a2, and -a3, each of which have distinct cellular localizations and are capable of interacting with microtubules (MTs) and actin filaments (Jefferson et al., 2006; Young et al., 2006). Each isoform is endowed with a functional N-terminal actin binding domain, a plakin domain, a spectrin repeat-containing rod domain in the middle of the molecule, and a MTBD at the C-terminus (Sun et al., 2001a). Isoform uniqueness is achieved through

alternative splicing of the first 5' exons. Dystonin-a1 encodes a short N-terminal domain that includes an actin-binding domain, while dystonin-a2 possess a transmembrane domain capable of interacting with various organelle membranes, and dystonin-a3 harbours a myristoylation domain, aiding in anchoring to the plasma membrane (Jefferson et al., 2006; Young et al., 2006).

While the dystonin-a isoforms mediating disease in HSAN-VI remains enigmatic, loss-of-function of dystonin-a1 and -a2 in the murine nervous system is causal in the $dt^{Tg4/Tg4}$ disorder(Pool et al., 2005). As such, numerous studies and speculations have been invested into parsing apart the biological functions of individual dystonin-a isoforms. Initial inspection of dystonin-a transcripts found dystonin-a2 to be the more unique isoform and least likely to be compensated for by any related protein (*e.g.*, microtubule actincrosslinking factor (MACF) and plectin) (Young and Kothary, 2007). Moreover, dystonin-a2 expression predominated in sensory ganglia -- the most severely affected tissue of *dt* mice -- and poorly expressed in non-neuronal tissues (Bernier et al., 1995). These initial descriptions of the dystonin-a2 variant suggested it might be the principle mediator of *dt* pathogenesis (Young and Kothary, 2007, 2008). Support for this notion was later corroborated through isoform-specific loss-of-function analyses. Indeed, depletion of dystonin-a2 perturbs membrane organization (endoplasmic reticulum (ER) and Golgi apparatus) and transport flux through the secretory pathway (Ryan et al., 2012a, 2012c).

In a separate study exploring the individual roles of dystonin-a1 and -a2 isoforms in mediating *dt* sensory neuron degeneration, dystonin-a2 was determined to be the principle initiator of neuronal degeneration (Ryan et al., 2012c). Silencing dystonin-a2 in

neurons elicited distinct neurodegenerative pathologies, including Ca^{2+} dyshomeostasis, unfolded protein response induction, caspase activation, and apoptosis. In addition to these aberrations, ER structural integrity was also compromised, presumably through uncoupling of cytoskeletal filaments, dystonin-a2, and ER membranes. Taken together, these studies demonstrate dystonin-a2 as the chief contributor in the demise of *dt* sensory neurons. Nevertheless, dystonin-a1 is also involved in fundamental neuronal processes, including anterograde and retrograde trafficking (Liu et al., 2003a, 2007b). As disturbance of these processes are well-known to underlie many neurological diseases (Perlson et al., 2010), including HSANs (Rottier, Annelies; Baets, Jonathan; Timmerman, Vincent; Janssens, 2012), dystonin-a1 remains an important contributor in *dt* pathogenesis.

To determine the dystonin-a isoform mediating *dt* pathogenesis, and to gain insight into viable pathogenetic mechanisms underlying HSAN-VI, we generated and characterized transgenic mice expressing dystonin-a2 under the nervous system-specific prion protein promoter (PrP-dystonin-a2). These transgenic mice were subsequently crossed onto the dt^{Tg4} background, producing homozygous (PrP-dystonin-a2/PrP-dystonin-a2; $dt^{Tg4/Tg4}$) transgenic mice. We find restoring dystonin-a2 expression within the nervous system greatly diminishes the severity of the *dt* disorder--due, in part, to prolonged survival of specific sensory neuron subtypes--and significantly extends life span. Albeit, the introduction of dystonin-a2 is not enough to fully rescue the $dt^{Tg4/Tg4}$ disorder, suggesting both dystonin-a1 and -a2 isoforms are necessary for complete rescue.

Results

Generation and Characterization of the PrP-dystonin-a2/PrP-dystonin-a2 transgenic mouse model:

To address whether loss of dystonin-a2 is responsible for the *dt* phenotype, transgenic mice harbouring full-length dystonin-a2 cDNA were generated and used in rescue experiments using $dt^{Tg4/Tg4}$ mice. Full-length dystonin-a2 cDNA was placed under the control of a strong neuronal promoter, the 3.5 kbmouse PrP promoter (Fig. 1A). In addition, a myc/his epitope tag was included in frame at the 3' end of the transgene to facilitate detection of the transgene product. The mouse PrP promoter was previously demonstrated to yield high expression in neuronal tissues of various transgenes (Gavrilina et al., 2008). Although the PrP promoter can exhibit low expression in other cells types (*e.g.*, astrocytes and skeletal muscle), we are mainly concerned with expression within neuronal tissues.

To assess whether the PrP-dystonin-a2 transgene is functional and the myc-tag can be detected via immunocytochemical labeling, immortalized F11 sensory neurons were transfected with the construct. The transgene protein product displays a characteristic perinuclear/cytoplasmic staining pattern aligning with cytoskeletal filaments, particularly MTs (Fig. 1B). Purified PrP-dystonin-a2 cDNA transgene fragment was microinjected into the pronuclei of one-cell mouse embryos and transgenic founder lines were established thereafter. To identify mice harbouring the transgene, a genotyping assay was developed. Amplification of endogenous DNA from non-transgenic mice produces a 318 bp DNA fragment, while amplification of the transgene DNA produces a 220 bp DNA fragment (Fig 1C,D). From five transgenic founder mice

generated, two lines (founder lines F542 and F559) were bred to establish independent strains. These transgenic lines appeared normal and fertile.

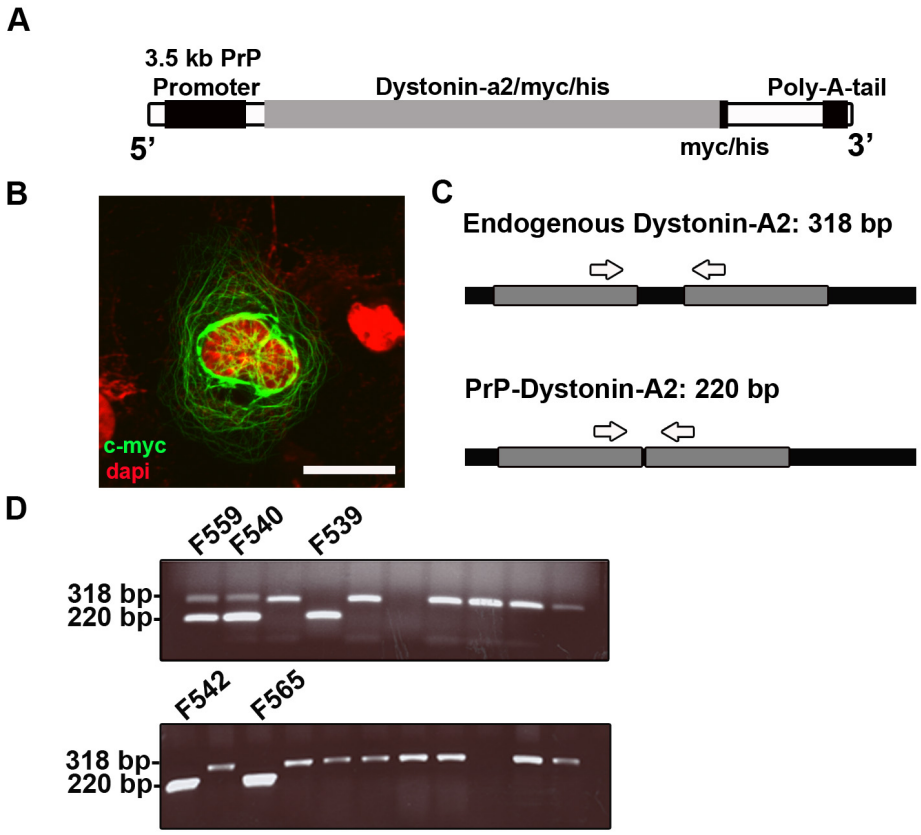

Figure 1: Generation of the PrP-dystonin-a2 transgenic mice. (A) Schematic representation of the PrP-dystonin-a2 cDNA construct used to generate transgenic mice. The construct harbours full-length dystonin-a2 cDNA in frame with a myc/his tag under the regulation of a strong neuronal promoter (prion protein promoter [PrP]). (B) Validation of PrP-dystonin-a2 transgene expression in F11 sensory neurons. Antigenic labeling of the PrP-dystonin-a2 myc/his tag (using anti-c-myc) 48 hours post-transfection in F11 sensory neurons produces a perinuclear/cytoplasmic-staining pattern expected for the dystonin-a2 isoform. Cells were counterstained with dapi to label the nuclei (scale bar = 20 μm). (C) Schematic representation of the location of oligonucleotide primers used to amplify the endogenous *Dst* gene and the PrP-dystonin-a2 transgene. Arrows indicate the position of primers used to amplify between exon 7 and 8 of the *Dst* gene. Amplification

of the endogenous locus yields a 318 bp fragment due to the presence of an intron, whereas amplification of the PrP-dystonin-a2 transgene gives rise to a 220 bp product. (D) PCR screening of the F0 generation indicates five offspring positive for the PrP-dystonin-a2 transgene (220 bp). Founder lines 542 and 559 were bred and established for further analysis.

PrP-dystonin-a2 mice express the transgene in a neuronal specific manner:

Using primers specific to the myc-his tag, transgene expression was assessed in multiple neuronal tissues including DRGs, spinal cord, and brain for both heterozygous PrP-dystonin-a2 transgenic lines (Fig. 2A). At P7 stage, all neuronal tissues exhibited PrP-dystonin-a2 transgene expression, while no expression was evident in tibialis anterior muscle (Fig. 2B-C). PrP-dystonin-a2 transgene expression was also assessed in P7 heterozygous tissues by immunohistochemistry. Using an anti-myc monoclonal antibody to assess protein expression (this tag is placed in frame with the dystonin-a2 isoform), a positive signal was detected in the cerebral cortex and cerebellum of both transgenic lines, however transgene expression in DRG tissue sections was faint and difficult to discern in heterozygous line 542 (data not shown). For this reason, transgenic line 559 was used and bred to homozygosity to increase relative transgene expression levels. Encouragingly, brain (P10) and DRG (P10 and P54) tissue sections of F559 homozygous (PrP-dystonin-a2/PrP-dystonin-a2) mice readily reveal presence of the transgene product (Fig. 3A). Indeed, robust PrP-dystonin-a2 transgene expression was found throughout the sensory neurons of the DRG. In comparison, a dearth of PrP-dystonin-a2 transgene expression was evident in age-matched brain and DRG tissues taken from wild type mice (Fig. 3A).

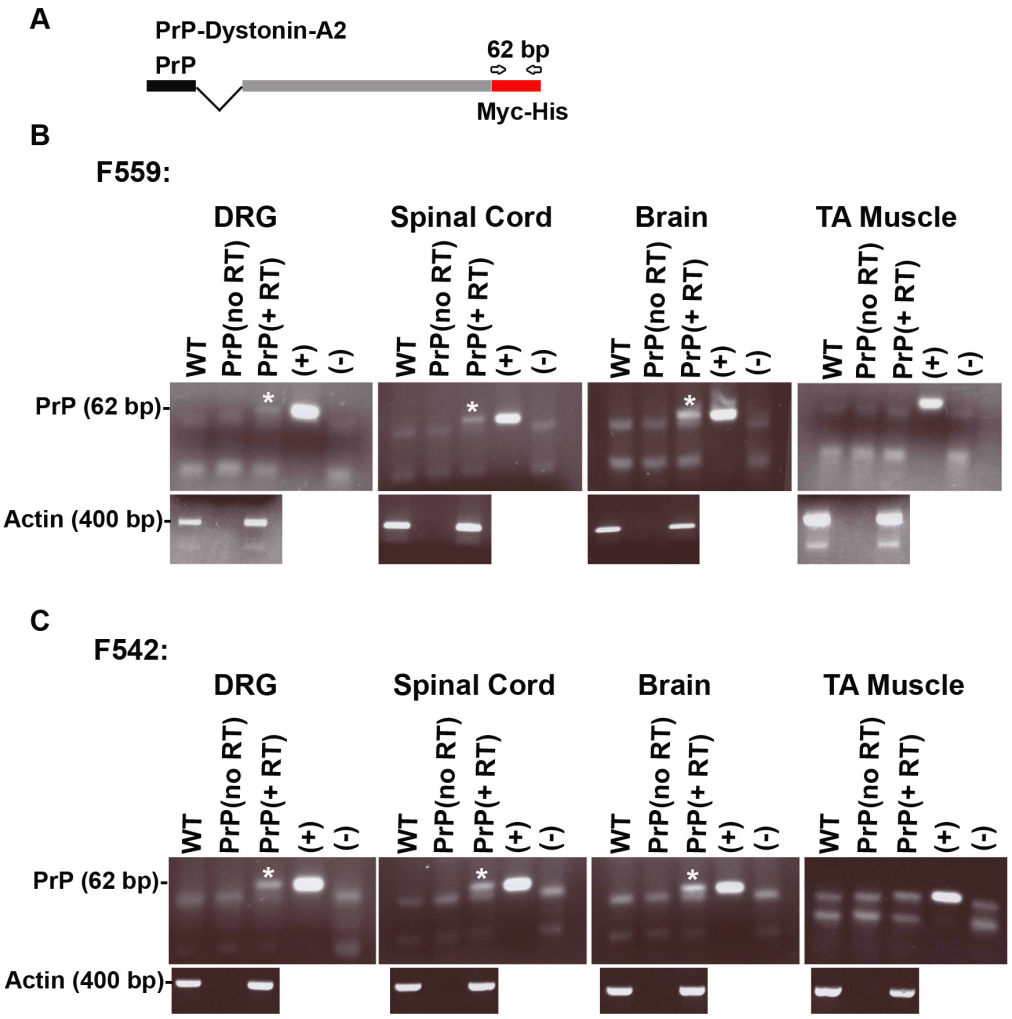

Figure 2: The PrP-dystonin-a2 transgene is expressed in neuronal tissues of transgenic lines 559 and 542. (A) Schematic representation of the location of oligonucleotide primers for the amplification of PrP-dystonin-a2 derived transcripts. Primers amplify a 62 bp fragment that includes the myc/his tag coding sequence. (B, C) RT-PCR analysis of RNA derived from P7 neuronal tissues (DRG, Spinal Cord, and Brain) of heterozygous transgenic mice from lines 559 and 542 indicates PrP-dystonin-a2 transgene expression (PrP, +RT lanes). Transgene expression was not evident in tibialis anterior (TA) muscle of either transgenic line. Controls: P7 wild type (WT) cDNA of neuronal tissues, PrP (no RT, minus reverse transcriptase), (+) and (-) cDNA of F11

sensory neurons transfected or non-transfected with PrP-dystonin-a2 construct, respectively. Actin mRNA amplification served as a positive control.

The DRG contains distinct cell populations including proprioceptive large and medium-sized sensory afferents (muscle sensory) and small-sized (skin and visceral sensory) sensory neurons, each of which has specific physiological properties. Large- and medium-sized sensory neurons innervate muscle tissues and transmit proprioceptive and tactile information, while small-sized sensory neurons innervate and relay information from the skin and viscera. Dystonin-a is expressed throughout the DRG, and not restricted to single subgroup (Bernier et al., 1995).To ensure PrP-dystonin-a2 transgene was expressed in all sensory neuron subtypes, sensory neurons were cultured from P5 PrP-dystonin-a2/PrP-dystonin-a2; $dt^{Tg4/Tg4}$ mice for 5 days *in vitro* and immunolabeled with anti-c-myc. Different sized sensory neurons (small 100 μm - 400 μm, medium 400 μm - 700 μm, and large 700 μm - 1200 μm) were categorized, as previously described (Carlsten et al., 2001), using the Axiovision 4.6 software (Carl Zeiss) circumference-measuring tool. Anti-c-myc staining was replete throughout the PrP-dystonin-a2/PrP-dystonin-a2 sensory neuron subtypes, while no anti-myc labeling was present in $dt^{Tg4/Tg4}$ sensory neurons (Fig. 3B).

These initial observations suggested PrP-dystonin-a2/PrP-dystonin-a2 transgenic mice express the dystonin-a2 transgene throughout the nervous system, most importantly in all sensory neuron subtypes. PrP-dystonin-a2/PrP-dystonin-a2 mice are viable, fertile, and phenotypically similar to wild type mice.

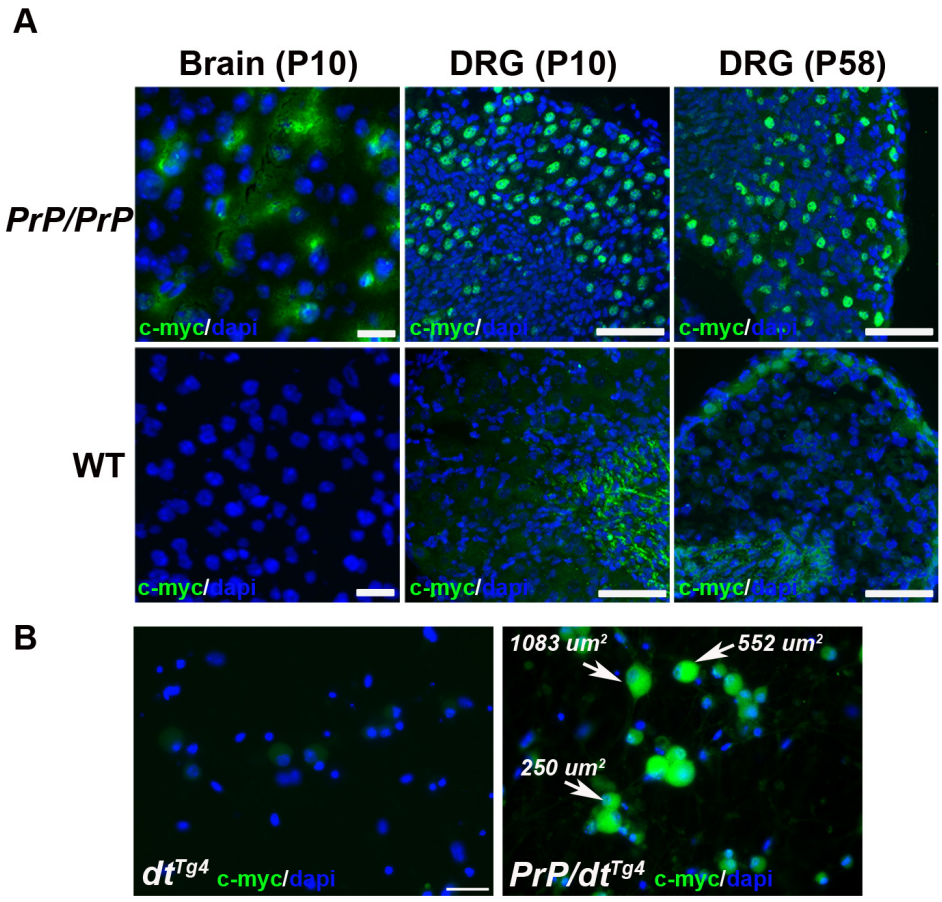

Figure 3: Immunohistochemical staining demonstrating robust PrP-dystonin-a2 transgene expression in neural tissues. (A) Representative tissue sections from brain (P10) and DRGs (P10 and P58) of homozygous PrP-dystonin-a2/PrP-dystonin-a2 (*PrP/PrP*) mice. Immunohistochemical staining with anti-c-myc antibody produced a peri-nuclear/cytoplasmic staining pattern in P10 cortical brain tissue, while a strong peri-nuclear staining pattern was observed in P10 and P58 DRGs. As expected, DRGs from wild type non-transgenic mice stained with anti-c-myc revealed no specific staining (scale bars = 20 μm). (B) Analysis of transgene expression in cultured DRG neurons. Again, as expected, there was no anti-c-myc staining in P10 $dt^{Tg4/Tg4}$ sensory neurons (left panel), whereas staining was present in large, medium, and small-sized sensory neurons

of P10 PrP-dystonin-a2 mice (right panel). Scale bar = 50 μm. Sections or cells were counterstained with dapi to label the nuclei.

Postnatal phenotypic characteristics of PrP-dystonin-a2/PrP-dystonin-a2; $dt^{Tg4/Tg4}$ mice:

To characterize whether PrP-dystonin-a2 confers protection in $dt^{Tg4/Tg4}$ sensory neurons and ameliorates the *dt* phenotype, PrP-dystonin-a2/PrP-dystonin-a2 mice were crossed onto the $dt^{Tg4/Tg4}$ background. While $dt^{Tg4/Tg4}$ mice heterozygous for the PrP-dystonin-a2 transgene mice died at approximately the same age as $dt^{Tg4/Tg4}$ mice (P21) and displayed poor locomotor coordination, unsteady gait and postural instability (data not shown), homozygous PrP-dystonin-a2/PrP-dystonin-a2; $dt^{Tg4/Tg4}$ mice exhibited significant improvements in all these properties, as discussed below. This suggests that differences in dystonin-a2 protein levels likely influence the extent of rescue in *dt* mice.

The life span of $dt^{Tg4/Tg4}$ mice is approximately 2-3 weeks (Kothary et al., 1988). Here we find the life span of PrP-dystonin-a2/PrP-dystonin-a2*;* $dt^{Tg4/Tg4}$ mice was significantly increased (mean age 55 days) compared to $dt^{Tg4/Tg4}$ mice (mean age 22 days, $P < 0.0001$) (Fig. 4A). Indeed, 60% of PrP-dystonin-a2/PrP-dystonin-a2*;* $dt^{Tg4/Tg4}$ mice assessed lived past P50, while 20% survived past 123 days (n = 10). Despite this increase in survival, PrP-dystonin-a2/PrP-dystonin-a2*;* $dt^{Tg4/Tg4}$ life span was compromised compared to control PrP-dystonin-a2/PrP-dystonin-a2 mice. In addition, PrP-dystonin-a2/PrP-dystonin-a2*;* $dt^{Tg4/Tg4}$ mice surviving past 120 days manifested additional phenotypes related to dysautonomia. Two mice (P123 and P126) showed blepharoptosis (drooping of the upper eyelid) and conjungtivitis (an early symptom of dry eye). While these dysautonomic features were not observable amongst the younger PrP-dystonin-a2/PrP-dystonin-a2*;* $dt^{Tg4/Tg4}$ mice, these features are occasionally seen in P20 $dt^{Tg4/Tg4}$ mice. This suggests that it takes a significantly longer period of time for PrP-dystonin-

a2/PrP-dystonin-a2*; $dt^{Tg4/Tg4}$* mice to manifest dysautonomic features compared to $dt^{Tg4/Tg4}$ mice.

From birth to P10, $dt^{Tg4/Tg4}$ mice are indistinguishable in size and phenotype from their wild type littermates. At approximately two weeks of age, however, arrest in weight-gain and ambulating abnormalities are evident. We therefore assessed whether PrP-dystonin-a2/PrP-dystonin-a2*; $dt^{Tg4/Tg4}$* mice show improved growth and ambulation. A progressive gain in weight in PrP-dystonin-a2/PrP-dystonin-a2*; $dt^{Tg4/Tg4}$* mice was observed between postnatal days P16 and P52, albeit this progressive weight-gain was not equivalent to PrP-dystonin-a2/PrP-dystonin-a2 control mice (Fig. 4B). In comparison to $dt^{Tg4/Tg4}$ mice, PrP-dystonin-a2/PrP-dystonin-a2; $dt^{Tg4/Tg4}$ mice showed a normal growth rate between P16 and P22, reminiscent of PrP-dystonin-a2/PrP-dystonin-a2 control mice (Fig. 4C). As $dt^{Tg4/Tg4}$ mice succumb to death at ~ P20, analyses between PrP-dystonin-a2/PrP-dystonin-a2; $dt^{Tg4/Tg4}$and $dt^{Tg4/Tg4}$ mice could not be performed past this time point.

To assess whether the transgenic rescue mice have improved coordination, the mice were subjected to the pen-test -- a test used to measure grip strength and coordination -- and the duration of time the animal was able to stay on the pen was recorded. PrP-dystonin-a2/PrP-dystonin-a2; $dt^{Tg4/Tg4}$ mice had only minor improvements in coordination at early time points compared to $dt^{Tg4/Tg4}$ mice, and were unable to stay on the pen following the P24 time point (Fig. 4D,E). PrP-dystonin-a2/PrP-dystonin-a2 mice, on the other hand, performed normally. Despite poor performance on the pen-test, PrP-dystonin-a2/PrP-dystonin-a2*; $dt^{Tg4/Tg4}$* mice showed a delay in onset of hind limb clasping, a hallmark phenotypic feature of $dt^{Tg4/Tg4}$ mice (Fig. 4F). Indeed, $dt^{Tg4/Tg4}$ mice typically present this pathological reflex at P15, or earlier, whereas PrP-dystonin-a2/PrP-

dystonin-a2; $dt^{Tg4/Tg4}$ mice only begin to show this phenotype at P21. This pathological reflex was non-existent in PrP-dystonin-a2/PrP-dystonin-a2 mice. Gait was assessed by using an in-house gait box as previously described (Bowerman et al., 2012). While P20 $dt^{Tg4/Tg4}$ mice exhibited an aberrant gait, the stride of P20 PrP-dystonin-a2/PrP-dystonin-a2; $dt^{Tg4/Tg4}$mice was indistinguishable from that of P20 PrP-dystonin-a2/PrP-dystonin-a2 control mice (Fig. 4G). Taken together, restoring dystonin-a2 expression on the $dt^{Tg4/Tg4}$ background does improve features of the *dt* phenotype, albeit attenuation of the phenotype is transient, suggesting that both dystonin-a1 and -a2 isoforms are necessary for reversing the phenotype.

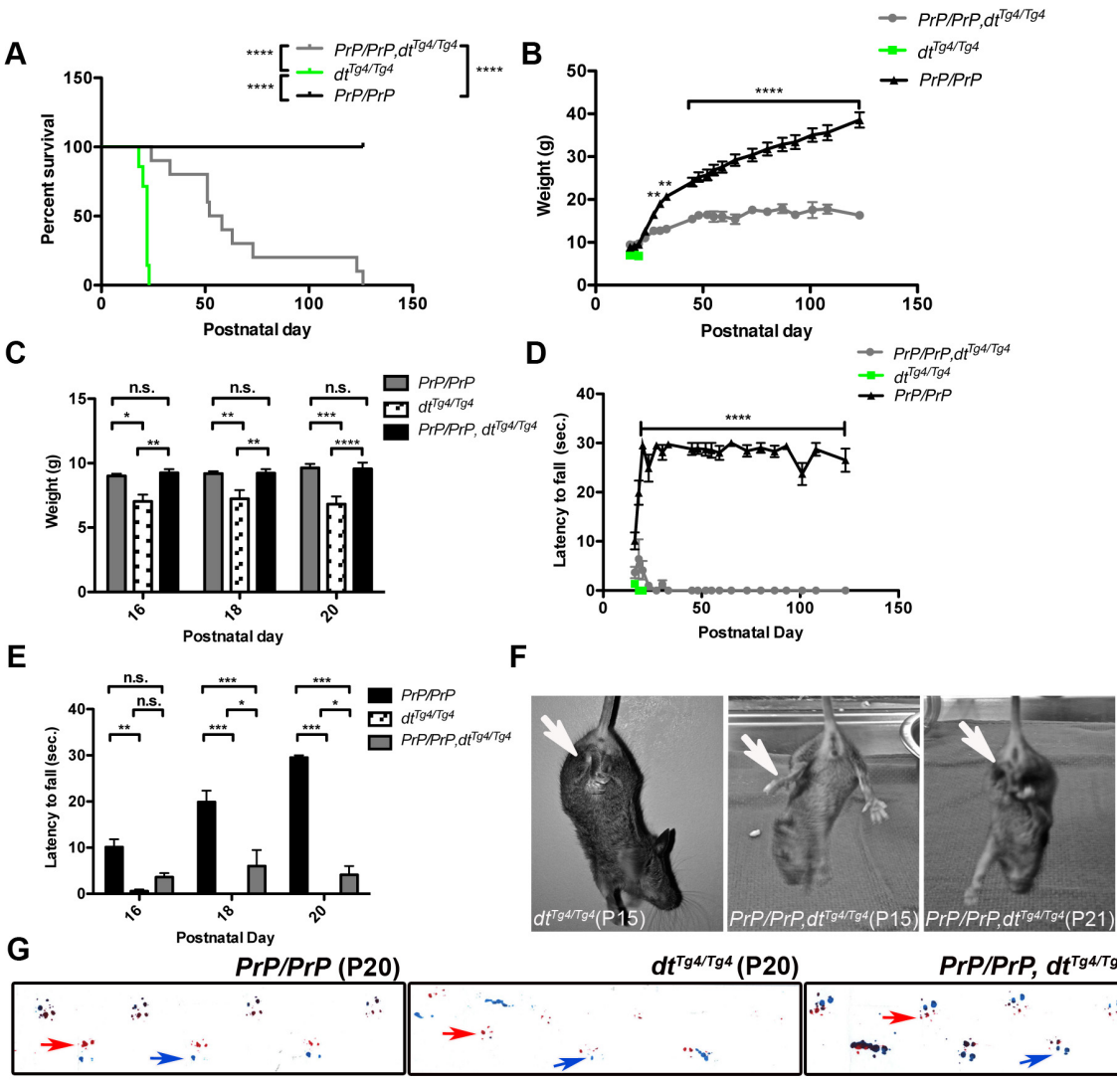

Figure 4: Postnatal characteristics of PrP-dystonin-a2/PrP-dystonin-a2; *dt*$^{Tg4/Tg4}$ transgenic rescue mice. The different groups analyzed were: control (*PrP/PrP*, n=10), mutant (*dt*$^{Tg4/Tg4}$, n=7), and transgenic rescue (*PrP/PrP;dt*$^{Tg4/Tg4}$, n=10). (A) Kaplan-Meier survival curve analysis indicates a significant increase in lifespan of *PrP/PrP;dt*$^{Tg4/Tg4}$ mice (median lifespan, 55 days) when compared to *dt*$^{Tg4/Tg4}$ mice (median lifespan, 21 days) (****P< 0.0001). A significant decrease in lifespan was also observed between *PrP/PrP;dt*$^{Tg4/Tg4}$ mice and *PrP/PrP* mice (****P< 0.0001), indicating that although there was some rescue, it was not complete. (B) Postnatal growth curve

analysis suggests *PrP/PrP;dt*$^{Tg4/Tg4}$ mice have a progressive gain in weight between postnatal days P16 and P52, and plateau thereafter. *PrP/PrP;dt*$^{Tg4/Tg4}$ mice do not show comparable increases in weight to that of control *PrP/PrP* mice between P30 and P123 (***P*< 0.01, *****P*< 0.0001). (C) *PrP/PrP;dt*$^{Tg4/Tg4}$ mice show significant increases in weight compared to *dt*$^{Tg4/Tg4}$ mice at postnatal days P16 (**P < 0.01), P18 (**P < 0.01), and P20 (****P < 0.0001). This increase in weight at early postnatal days is comparable to *PrP/PrP* mice. Further comparative weight analysis was not feasible for *dt*$^{Tg4/Tg4}$ mice as these mice die at ~ P20. Two-way Anova, Bonferroni posttest, data are represented as mean ± SEM. (D) Performance analysis of *PrP/PrP*,*dt*$^{Tg4/Tg4}$, and *PrP/PrP*;*dt*$^{Tg4/Tg4}$ mice in the pen-test at various post-natal days between P23 andP123. *PrP/PrP*;*dt*$^{Tg4/Tg4}$ mice show a decreased latency to fall and as such are unable to effectively balance and/or grip to remain on the suspended pen compared to *PrP/PrP* mice (*****P*< 0.0001). (E) *PrP/PrP*;*dt*$^{Tg4/Tg4}$ mice show improvements in balance and grip at early postnatal days (P18 and P20) compared to *dt*$^{Tg4/Tg4}$ mice (**P*< 0.05). Despite this improvement, *PrP/PrP* mice manifest superior balance and grip at P18 and P20 compared to *PrP/PrP*;*dt*$^{Tg4/Tg4}$ mice (****P*< 0.001). Two-way Anova, Bonferroni posttest, data are represented as mean ± SEM. (F) Representative images of hind-limb clasping during tail suspension, a hallmark *dt* phenotype. P15 *dt*$^{Tg4/Tg4}$ mice consistently displayed limb clasping (arrow) while P15 *PrP/PrP*;*dt*$^{Tg4/Tg4}$ mice manifested splayed hind limbs, reminiscent of wild type or *PrP/PrP* mice. Note that limb clasping was detectable in P21 *PrP/PrP*;*dt*$^{Tg4/Tg4}$ mice. (G) Representative examples of *PrP/PrP* (P20); *dt*$^{Tg4/Tg4}$ (P20), and *PrP/PrP*;*dt*$^{Tg4/Tg4}$ (P20) mouse paw prints used for gait analysis (red = front paws, red arrow; blue = back

paws, blue arrows). Note the similar gait between P20 *PrP/PrP* and P20 *PrP/PrP*;$dt^{Tg4/Tg4}$ mice and the abnormal gait exhibited by P20 $dt^{Tg4/Tg4}$ mice.

The PrP-dystonin-a2 transgene delays sensory neuron degeneration in dt mice:

The degeneration of *dt* sensory neurons is the primary contributor to the overt ataxia and dystonia observed in *dt* mice (Bernier et al., 1995; Dowling et al., 1997). We previously found the demise of $dt^{Tg4/Tg4}$ sensory neurons commences at P15, concomitant with the onset of *dt* pathogenesis and the *dt* phenotype (Ryan et al., 2012c). The PrP-dystonin-a2/PrP-dystonin-a2; $dt^{Tg4/Tg4}$ mouse does not manifest impaired locomotion or dystonia at P15, suggesting delayed sensory neuron degeneration. To address this notion, quantitative TUNEL labeling on lumbar DRG tissue sections was performed.

As expected, P15 PrP-dystonin-a2/PrP-dystonin-a2 DRG tissue sections displayed a dearth of TUNEL labeled neurons, while P15 $dt^{Tg4/Tg4}$ DRGs tissue sections exhibited a significant increase in TUNEL activity (Fig. 5B,C,F $p < 0.001$). In comparison to $dt^{Tg4/Tg4}$ DRGs, P15 PrP-dystonin-a2/PrP-dystonin-a2; $dt^{Tg4/Tg4}$ DRGs showed a significant reduction in the number of TUNEL positive sensory neurons (Fig. 5D,F,$p< 0.001$), suggesting that the PrP-dystonin-a2 transgene confers protection and delays the onset of neurodegeneration. As PrP-dystonin-a2/PrP-dystonin-a2; $dt^{Tg4/Tg4}$ mice eventually present ataxia, sensory neuron viability was assessed at a later time point. At P21, a significant increase in TUNEL positive sensory neurons ($p < 0.05$) was observed compared to the P15 time point (compare Fig. 5D to 5E). Despite this increase, the percentage of dying cells was significantly less than that observed in P15 $dt^{Tg4/Tg4}$ sensory neurons (Fig. 5F, $p < 0.001$). These observations indicate that the aforementioned phenotypic improvements in PrP-dystonin-a2/PrP-dystonin-a2; $dt^{Tg4/Tg4}$ mice are due, in part, to increased viability in $dt^{Tg4/Tg4}$ sensory neurons. Furthermore, while the PrP-dystonin-a2 transgene confers

protection in PrP-dystonin-a2/PrP-dystonin-a2; $dt^{Tg4/Tg4}$ sensory neurons, they still undergo degeneration, albeit at a delayed rate.

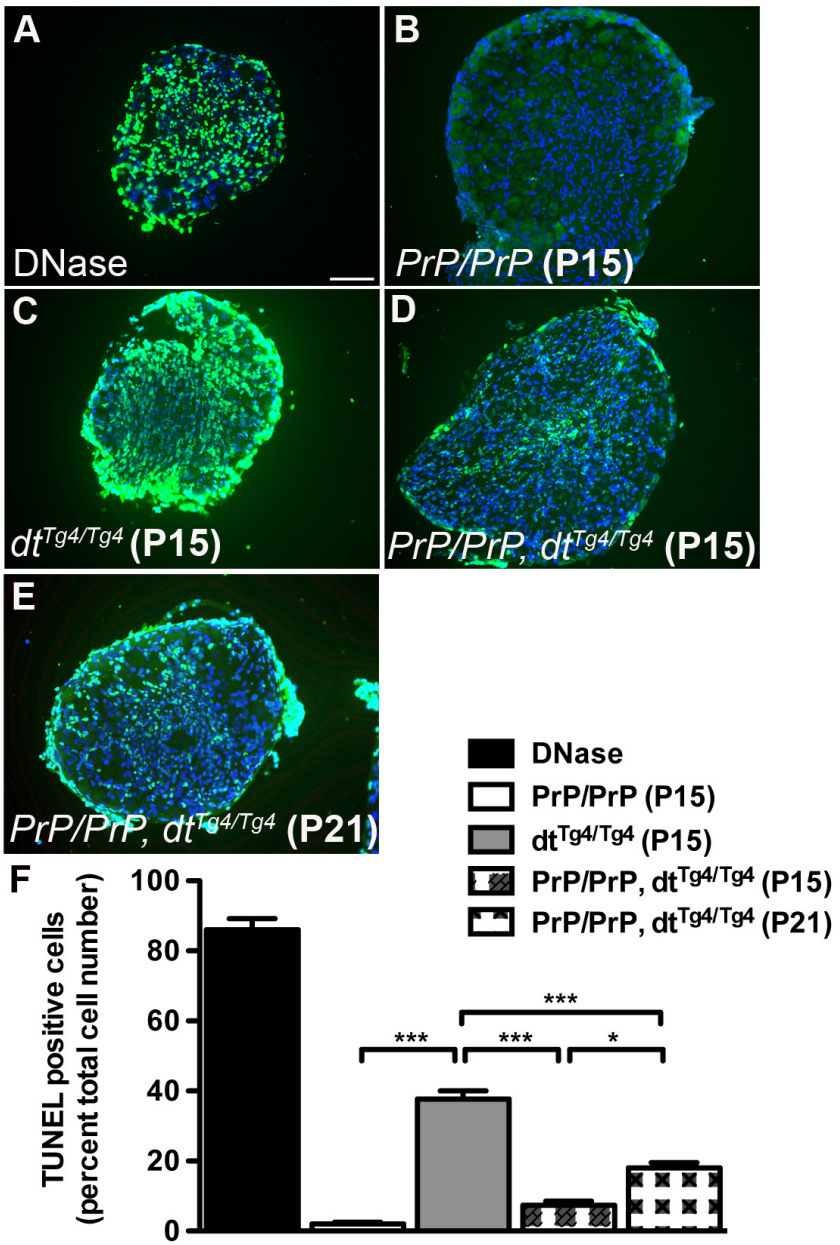

Figure 5: The PrP-dystonin-a2 transgene confers protection in *dt*$^{Tg4/Tg4}$ sensory neurons by delaying cellular demise. (A-E) Representative TUNEL labeling images of lumbar DRG tissue sections. (C) P15 *dt*$^{Tg4/Tg4}$ DRG tissue sections displayed significantly more TUNEL positive cells (mean cell death, 37.6%) then P15 *PrP/PrP;dt*$^{Tg4/Tg4}$ (D)(mean cell death, 7.3%) and P21 *PrP/PrP;dt*$^{Tg4/Tg4}$ cells (E)(mean cell death, 18%). The decrease observed in TUNEL positive cells for P15 *PrP/PrP;dt*$^{Tg4/Tg4}$ DRGs

compared to P15 $dt^{Tg4/Tg4}$ was transient as P21 *PrP/PrP;*$dt^{Tg4/Tg4}$ DRGs showed an increase in cellular death. *PrP/PrP* DRGs showed few TUNEL positive cells, while control DRG tissue sections (DNase treated) were replete with TUNEL positive cells. (F) ANOVA post hoc Tukey, ***$p < 0.001$, *$p < 0.05$, n=3/genotype. Scale bar = 20 μm.

Dystonin-a2 protects proprioceptive sensory afferents and improves MT integrity:

Various HSAN disorders are characterized by the demise of a specific sensory neuron subtype (Axelrod and Gold-von Simson, 2007; Rottier, Annelies; Baets, Jonathan; Timmerman, Vincent; Janssens, 2012). Interestingly, while dystonin-a is expressed throughout different sensory neuron populations, large and medium proprioceptive sensory neurons are most affected by the *dt* disorder (Sotelo and Guenet, 1988; Carlsten et al., 2001). Consequently, movement is severely impaired in *dt* mice. To address which population of sensory afferents the PrP-dystonin-a2 transgene protects, sensory neurons from PrP-dystonin-a2/PrP-dystonin-a2, PrP-dystonin-a2/PrP-dystonin-a2; $dt^{Tg4/Tg4}$, and $dt^{Tg4/Tg4}$ mice we co-labeled with β-III tubulin (a neuronal marker) and caspase-3 (apoptotic marker) (n = 3) (Fig. 6A-C). Furthermore, to differentiate between different sized sensory neurons, soma circumference was measured and grouped by size as discussed above. Primary sensory neurons derived from P5 mice and cultured for five days in vitro (5 D.I.V.) revealed a dearth of caspase-3 labeling for each genetic background (data not shown). As such, sensory neuron cultures were challenged with starvation media (serum-, glucose-, and amino acid-free media) for 24 hours following 5 D.I.V. and cell viability was assessed thereafter. For cells to maintain viability following starvation, cells activate cell-survival mechanisms (*e.g.*, autophagy and robust intracellular transport).

Initial analysis indicated there was no difference in the average number of small and medium sensory neurons between PrP-dystonin-a2/PrP-dystonin-a2, PrP-dystonin-a2/PrP-dystonin-a2; $dt^{Tg4/Tg4}$, and $dt^{Tg4/Tg4}$ cultures following 24 hour serum-free treatment (Fig. 6D). However, a significant increase in caspase-3 labeling was noted in $dt^{Tg4/Tg4}$

small and medium sensory neurons compared to PrP-dystonin-a2/PrP-dystonin-a2 ($p < 0.001$) and PrP-dystonin-a2/PrP-dystonin-a2; $dt^{Tg4/Tg4}$ ($p < 0.01$) sensory neurons (Fig. 6E). Furthermore, no significant difference in capase-3 labeling was observed in small and medium sensory neurons between PrP-dystonin-a2/PrP-dystonin-a2 and PrP-dystonin-a2/PrP-dystonin-a2; $dt^{Tg4/Tg4}$cultures (Fig. 6E). These observations suggest exogenous expression of the PrP-dystonin-a2 transgene on the $dt^{Tg4/Tg4}$ background imparts protection in small and medium sensory neurons.

Unlike small and medium sensory neurons, the average number of large sensory neurons following serum-free treatment was significantly different between genotypes. On average, there were 14 large sensory neurons per PrP-dystonin-a2/PrP-dystonin-a2 culture and significantly fewer in PrP-dystonin-a2/PrP-dystonin-a2; $dt^{Tg4/Tg4}$ (5 large sensory neurons per culture, $p < 0.05$) and in the $dt^{Tg4/Tg4}$culture (1 large sensory neuron per culture, $p < 0.01$) (Fig. 6F). Coupled with this,15% of large PrP-dystonin-a2/PrP-dystonin-a2 sensory neurons were caspase-3 positive, while approximately 52% and 100% of large PrP-dystonin-a2/PrP-dystonin-a2; $dt^{Tg4/Tg4}$and $dt^{Tg4/Tg4}$ sensory neurons were caspase-3 positive, respectively (Fig. 6G). These data indicate that although the PrP-dystonin-a2 transgene imparts slight protection to large sensory neurons, they remain vulnerable to *dt* pathogenesis.

In both HSAN-VI patients and *dt* mice, disorganized MT networks are thought to be a critical driver of disease pathogenesis (Yang et al., 1996; Dalpé et al., 1998; Edvardson et al., 2012). As such, we addressed whether the dystonin-a2 transgene improves MT network integrity. $dt^{Tg4/Tg4}$ cultures exhibited notable accumulations of β-III tubulin throughout axons (arrowheads, Fig. 6C), whereas accumulations of β-III tubulin

were absent from the axons of PrP-dystonin-a2/PrP-dystonin-a2 and PrP-dystonin-a2/PrP-dystonin-a2; $dt^{Tg4/Tg4}$ sensory neurons Fig. 6A,B). Similar accumulations seen herein have been observed in *dt* axons, and likely influence the bi-directional impairment observed in *dt* sensory neurons (De Repentigny et al., 2003). We therefore conclude that the increased viability among small and medium-sized PrP-dystonin-a2/PrP-dystonin-a2; $dt^{Tg4/Tg4}$sensory afferents is associated with, in part, by improved MT organization.

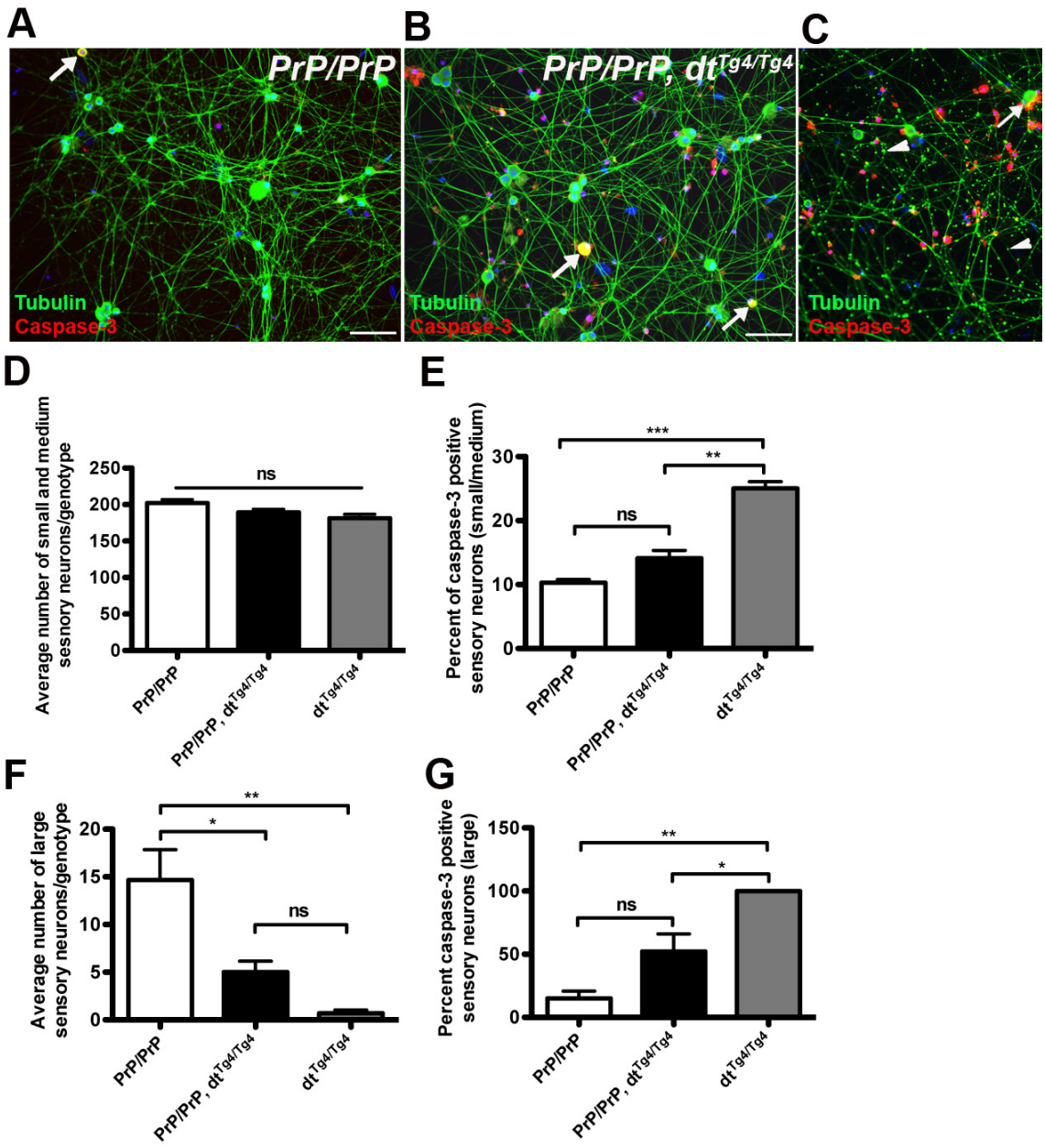

Figure 6: PrP-dystonin-a2 transgene imparts neuro-protection in small and medium caliber sensory neurons but not in large caliber sensory neurons. (A-C) Primary DRG sensory neuron cultures were established from P5 mice of various genetic backgrounds (*PrP/PrP* (A), *PrP/PrP;dt*$^{Tg4/Tg4}$ (B), *dt*$^{Tg4/Tg4}$ (C)), and cultured for 5 days *in vitro*. Cells were challenged with serum-free media for 24 hours and antigenic labeling of β-III tubulin (neuronal marker) and the apoptotic marker caspase-3 was conducted

thereafter. Note the accumulation of β-III tubulin in axons of $dt^{Tg4/Tg4}$ sensory neurons (arrowheads in C). (D) The average number of small (soma area, 100 to 400 μm^2) and medium caliber sensory neurons (400 to 700 μm^2) was not significantly different between genotypes. (E) A significant increase in caspase-3 staining was observed in small and medium-sized $dt^{Tg4/Tg4}$ sensory neurons compared to *PrP/PrP* (***$p < 0.001$) and *PrP/PrP;*$dt^{Tg4/Tg4}$ (**$p < 0.01$), indicating the transgene confers protection in these cell types. (F) The average number of large caliber sensory neurons (700 to1300 μm^2) is significantly different between genotypes *PrP/PrP* and *PrP/PrP;*$dt^{Tg4/Tg4}$ (*$p < 0.05$); *PrP/PrP* and $dt^{Tg4/Tg4}$ (** $p < 0.01$). However, there was no difference between *PrP/PrP;*$dt^{Tg4/Tg4}$ and $dt^{Tg4/Tg4}$. (G) A significant increase in caspase-3 staining was observed in $dt^{Tg4/Tg4}$ large caliber sensory neurons compared to *PrP/PrP* large caliber sensory neurons (*$p < 0.05$). No significant difference in caspase-3 staining was observed between *PrP/PrP* and *PrP/PrP;* $dt^{Tg4/Tg4}$ large caliber sensory neurons. Statistics: ANOVA, post hoc Tukey, n=3/genotype. Scale bar = 20 μm.

Discussion

In this study, we addressed whether restoring dystonin-a2 expression on the $dt^{Tg4/Tg4}$ background is able to partially or completely rescue the *dt* phenotype and the underlying pathophysiology. We successfully generated transgenic mice expressing the PrP-dystonin-a2 transgene on the $dt^{Tg4/Tg4}$ background. Transgene expression was evident throughout neuronal tissues and was, most importantly, expressed throughout all sensory neuron subtypes. Increasing dystonin-a2 expression in neural tissues of $dt^{Tg4/Tg4}$ mice decreased disease severity and increased life span. We find these aforementioned improvements are due in part to improved MT integrity within proprioceptive sensory neurons, and as such, delay the rate at which sensory neurons undergo apoptosis. Collectively, this study proposes dystonin-a2 loss-of-function drives *dt* pathogenesis. Moreover, because dystonin-a2 is incapable of completely rescuing the sensory neuron degeneration in *dt* mice, the dystonin-a1 isoform must also be necessary in maintaining sensory neuron viability.

Dystonin-a2 decreases disease severity and increases life span:

First observed 50 years ago, the *dt* mouse is an autosomal-recessive mutant of the *Dst* gene (Duchen et al., 1964). As mentioned, the *dt* phenotype is characterized by both ataxia and dystonia that commences at 11-14 days postnatal development. Ataxia is most often associated with cerebellar defects, as vividly illustrated by the profound loss of cerebellar Purkinje neurons in human spinocerebellar ataxia type I (Servadio et al., 1995). As well, dystonia is commonly associated with defects in the basal ganglia (Chiken et al., 2008). Alterations in either the cerebellum and/or basal ganglia are not present in *dt* mice

(Dowling et al., 1997). As such, it was deduced that the *dt* phenotype is precipitated through loss of sensory neurons. Specifically, the *dt* mutation provokes a very selective degeneration, mainly affecting large- and medium-sized sensory neurons.

By reintroducing dystonin-a2 expression within the nervous system of $dt^{Tg4/Tg4}$ mice, we extended life span to a mean age of 55 days coupled with a progressive gain in weight between P16 and P52 (Fig. 3). Why some rescue mice show prolonged survival compared to other rescue mice (*e.g.*, 123 days versus 46 days) is unclear. We suspect this variability in survival is due in part to disease modifiers and/or intrinsic genetic background differences. The PrP-dystonin-a2/PrP-dystonin-a2; $dt^{Tg4/Tg4}$ mice also showed a delay in the onset of hind-limb clasping and exhibited a normal gait at P20 reminiscent of PrP-dystonin-a2/PrP-dystonin-a2 control mice. As hind-limb clasping and aberrant gait in *dt* mice are provoked through the degeneration of proprioceptive sensory afferents, improvement in these areas suggests this subgroup of sensory neurons are transiently protected by dystonin-a2 transgenic expression. Qualitatively, PrP-dystonin-a2/PrP-dystonin-a2; $dt^{Tg4/Tg4}$ mice also display a milder form of *dt* phenotype (less limb incoordination, fewer dystonic postures, and little to no writhing). Only later in age -- greater than P100 -- did PrP-dystonin-a2/PrP-dystonin-a2; $dt^{Tg4/Tg4}$ mice produce an overt locomotor ataxia similar to that seen in young $dt^{Tg4/Tg4}$ mice (data not shown).

Dystonin-a2 is protective in subpopulations of sensory neurons:

Although dystonin-a expression is widely distributed throughout DRG sensory afferents, the postnatal consequence of dystonin-a absence varies amongst sensory neuron subpopulations (Sotelo and Guenet, 1988; al-Ali and al-Zuhair, 1989; Carlsten et

al., 2001). As mentioned, the *dt* mutation provokes a very selective degeneration, mainly affecting large- and medium-sized sensory neurons which encompass group Ia and Ib (large), and group II (medium-sized) sensory afferents (Sotelo & Guenet, 1988). These proprioceptive sensory afferents makeup 20% of DRG neurons and innervate specialized sense organs within the musculature, including muscle spindles and Golgi tendon organs (Mu et al., 1993). These sensory organs are critical for posture and stability and goal-directed movements. Multiple studies found the degeneration of muscle spindles is concomitant with phenotypic onset and that aberrations in spindle function are most likely the cause of both the ataxic and dystonic movements seen in *dt* mice (Duchen et al., 1964; Sotelo and Guenet, 1988; Dowling et al., 1997). Delineating which dystonin-a isoform(s) is/are responsible for the demise of these populations is paramount, as it will not only narrow down the principle dystonin-a isoform, but also propose potential pathological mechanisms underlying the *dt* disorder and similar human diseases, like HSAN-VI.

Here, we show dystonin-a2 is necessary in the maintenance of postnatal sensory neurons as it's expression significantly delays the progressive degeneration seen in $dt^{Tg4/Tg4}$ mice (Fig. 5). Moreover, cultured primary sensory neurons from PrP-dystonin-a2/PrP-dystonin-a2; $dt^{Tg4/Tg4}$ mice revealed the dystonin-a2 transgene confers protection among medium-sized sensory neurons (group II sensory afferents), but not large sensory neurons when challenged with serum-free media (Fig. 6). Why large sensory neurons are so vulnerable in the *dt* disorder is unclear. Previous studies have found large sensory neurons are more vulnerable to diseased conditions than small-sized neurons (McIlwain, 1991). Moreover, large and medium sized sensory neurons possess high-energy demands,

and require significant trafficking capacity, and hence may be particularly vulnerable to vesicular and axonal transport defects. As transgene expression was replete throughout all sensory neuron subtypes (Fig. 3), we conclude dystonin-a2 expression is critical for the survival of medium-sized sensory neurons. Although no rescue was seen in large sensory neurons, this does not imply dystonin-a2 expression is dispensable in this population of sensory neurons. It is plausible that a combination of dystonin-a isoforms (dystonin-a1/a2) is necessary for the survival of large sensory afferents.

PrP-dystonin-a2/PrP-dystonin-a2; $dt^{Tg4/Tg4}$ mice show partial, but not complete, improvements in both the pen-test and gait analyses. This would imply that specific sensory nerves--likely large sensory afferents--are already dying or are not functioning optimally. Furthermore, the milder *dt* phenotype indicates that the progressive nature of $dt^{Tg4/Tg4}$ pathogenesis within proprioceptive sensory afferents is delayed.

There are several possibilities as to why PrP-dystonin-a2 transiently rescues medium-sized sensory afferents. One, expression of the dystonin-a2 transgene is not equivalent to that of endogenous dystonin-a2 expression levels. Two, expression of dystonin-a1, or a yet-to-be-determined dystonin-a isoform, is also needed for a complete rescue of medium-sized sensory afferents, or three, the degenerative process of large sensory afferents negatively influences medium sensory afferents.

To address how dystonin-a2 was mediating a partial rescue we investigated the status of MT networks within our primary sensory neuron culture system. Dystonin-a has long been known to be involved in the maintenance of the neuronal cytoskeleton, particularly MTs (Yang et al., 1996; Dalpé et al., 1998). More recently, through interactions with the microtubule-associated protein-1B, dystonin-a2 was found to be

necessary in maintaining the acetylation status of MTs, and as such, preserved optimal protein trafficking (Ryan et al., 2012a). Here, we find the dystonin-a2 transgene is capable of maintaining the integrity of MT networks within $dt^{Tg4/Tg4}$ sensory axons. Indeed, we did not observe axonal accumulations of βIII-tubulin as seen in $dt^{Tg4/Tg4}$ sensory axons (Fig. 6C). In light of the aforementioned studies, improved MT stability is a conceivable explanation as to the delayed degeneration observed herein.

Dystonin-a2 and -a1 underlie dt pathogenesis and share similar pathological mechanisms to various HSANs:

According to the present work as well as recent studies exploring the individual biological functions of dystonin-a isoforms, we conclude the *dt* disorder is a multiple-isoform disease. Dystonin-a2 has been speculated as the primary driver of *dt* pathogenesis(Young and Kothary, 2007, 2008). Support for this notion comes from recent studies where dystonin-a2 was determined as a critical factor in provoking *dt* sensory neuron degeneration (Ryan et al., 2012a, 2012c). In sensory neurons, dystonin-a2 maintains the organization of Golgi membranes and transport flux through the secretory pathway (Ryan et al., 2012a). The organization of Golgi membranes and anterograde transport, which rely upon proper α-tubulin acetylation in MTs, were found to occur through an interaction between dystonin-a2 and microtubule-associated protein 1B. Interestingly, pathological mechanisms mediating HSAN-III (or FD)--an HSAN closely related to HSAN-VI--also implicate the cytoskeleton. Indeed, the disease causing protein, RNA polymerase II elongator complex protein 1 (ELP1), is involved in the maintenance of α-tubulin acetylation (Creppe et al., 2009). As α-tubulin acetylation serves as a

recognition signal for motor protein anchoring, decreased acetylation likely impairs cellular trafficking of various neuronal proteins in both diseases. In addition, HSAN-III neurons also manifest disorganized MTs, which are believed to be caused by an up-regulation of neuron-specific MT-destabilizing protein stahmin-2 (SCG10) (Cheishvili et al., 2011). Intriguingly, dystonin-a expression is robustly increased in cells of HSAN-III patients, suggesting that upregulation of dystonin-a may play a compensatory role and is responsible for the milder course of HSAN-III (Edvardson et al., 2012).

As defects in neuronal MT networks clearly impact cellular trafficking and underlie myriad peripheral neuropathies (Perlson et al., 2010; Rottier, Annelies; Baets, Jonathan; Timmerman, Vincent; Janssens, 2012), disruptions in MT-based motor protein complexes would conceivably impart a similar affect. Dystonin-a1, which has been shown to interact with dynactin, a core component of the dynein/dynactin complex, impairs retrograde transport in *dt* sensory neurons (Liu et al., 2003b). Dystonin-a1 is also essential in the recruitment and retrograde trafficking of endosomes within neurons (Liu et al., 2007b). Similar to dystonin-a1, Rab-7a (Ras-related protein), a protein essential for retrograde vesicular trafficking through recruitment of dynein motor proteins, underlies the sensory/motor neuropathy Charcot Marie Tooth Disease-2B (Meggouh et al., 2006). Moreover, mutations in the cytoplasmic dynein heavy chain 1 gene (Dync1h1) result in a pronounced loss of proprioceptive DRG neurons and muscle spindles in mice (Chen et al., 2007). These studies support the idea that deficiency in motor-based cellular trafficking can provoke neuronal demise, and may very well be the mechanism by which dystonin-a1 invokes *dt* sensory neuron degeneration.

Taken together, both dystonin-a1 and dystonin-a2 are involved in fundamental biological functions within neurons, including vesicular trafficking and maintenance of MTs. As similar biological processes are perturbed in both inherited and acquired peripheral neuropathies, our results should be of clinical interest. Moreover, results herein will provide needed biological insights into the newly identified dystonin-related HSAN-VI.

Materials and Methods

Reagents:

All chemicals were purchased through Sigma-Aldrich (St. Louis, MO USA) and all cell culture reagents were obtained from Invitrogen (Burlington, ON Canada) except where indicated.

Ethics Statement:

All experimental protocols on mice were approved by the Animal Care Committee of the University of Ottawa. Care and use of experimental mice followed the guidelines of the Canadian Council on Animal Care.

Animals and cell culture:

The $dt^{Tg4/Tg4}$, PrP-dystonin-a2/PrP-dystonin-a2; $dt^{Tg4/Tg4}$, and PrP-dystonin-a2/PrP-dystonin-a2 transgenic mice all shared the same mixed genetic background of CD1/C57BL6 and were used at pre-phenotype (P7) and phenotype stages (P15 and P58). The generation of the $dt^{Tg4/Tg4}$ line and characterization of the mutation have been

described previously (Kothary et al., 1988; Brown et al., 1995; Pool et al., 2005). The onset of phenotype was generally assessed by the appearance of clasping of hind limbs after picking the mice up by their tails. $dt^{Tg4/Tg4}$ mice were genotyped by PCR amplification of genomic tail DNA.

The dystonin-a2 cDNA was previously developed in the laboratory. In brief, dystonin-a2 cDNA was amplified from mouse brain RNA and cloned into the pEF1-myc/his vector (Invitrogen) encoding a C-terminal myc/his tag (Young et al., 2006; Young and Kothary, 2008). The dystonin-a2-myc/his cDNA was thereafter cloned into the 3.5kb PrP promoter and the expression vector pEF1myc/hisB (Invitrogen). The resulting transgene construct was microinjected into one-cell mouse embryos. Tail biopsies were obtained from potential founder mice, DNA was extracted and transgenic mice were identified by PCR amplification using sense oligo 5' GTT TGC ACC AAT GCC TTC GC 3' and antisense oligo 5' GCC GGA CCT GAT AGA CAT GA 3'. These primers amplify a 318bp fragment on the wild type *Dst* gene and a 220bp fragment from the PrP-dystonin-a2 transgene. Positive founder mice were bred with wild type mice to establish two independent transgenic lines (founder lines 542 and 559). Heterozygous PrP-dystonin-a2/+ and homozygous PrP-dystonin-a2/PrP-dystonin-a2 mice were subsequently crossed to heterozygous $dt^{Tg4/+}$ mice, and the dt^{Tg4} allele was thereafter bred to homozygosity producing both PrP-dystonin-a2/+; $dt^{Tg4/Tg4}$ mice and PrP-dystonin-a2/PrP-dystonin-a2; $dt^{Tg4/Tg4}$mice. The genotype of offspring mice was confirmed by PCR.

F11 cells (a fusion of embryonic rat DRG cells with a mouse neuroblastoma cell line, kindly supplied by Dr. Paul Albert, University of Ottawa) were maintained in

DMEM + 10% fetal bovine serum (FBS) and 1% penicillin/streptomycin/antimycotic. Cells were passaged at ~70% confluency in 10-cm plastic Petri dishes and plated onto glass coverslips for use in immunofluorescence assays. Cell transfections were performed using Lipofectamine 2000 (Invitrogen), according to manufacturer's directions.

Gait measurements:

Gait assessment was performed using an in-house gait box as previously described (Bowerman et al., 2012). Both front and back paws were marked with red and blue ink, respectively. Mice where situated at the larger end of the gait apparatus with a light shone through to encourage the mice to walk towards the opposite end, leaving their imprints on a piece of white paper. Imprints were thereafter inspected and compared amongst different genotypes.

Pen-test:

Balance and strength were assessed using the pen-test as described (Willmann et al., 2011). Mice were placed on a suspended pen at different time-points. The latency to fall from the pen was measured with a plateau of 30 s. At each time-point, individual mice were placed three consecutive times.

RT-PCR Analysis:

For reverse transcription-polymerase chain reaction (RT-PCR) analysis, RNA was isolated from transgenic P7, P15 and P21 tissues from the two PrP-dystonin-a2 founder lines (F542 and F559). To synthesize cDNA, equal amounts of RNA were reverse-transcribed in a standard reaction with MuLV reverse transcriptase (Invitrogen). PCR

amplification using the sense oligo 5' AAC AAA AAC TCA TCT CAG AAG AG 3', and the antisense oligo 5' ATG GTG ATG GTG ATG ATG AC3' (specific to the Myc/His cDNA), yielded a 62bp fragment. Primers were chosen to flank the intronic region of the construct to selectively amplify the RNA transcript and prevent amplifying any contaminating genomic DNA. The reaction began with a 3 min incubation time at 94°C followed by 30 cycles of 45 sec at 94°C, 45 sec at 55°C, 1 min at 68°C, with a final extension time of 10 min at 68°C. Amplification of actin cDNA served as a control. The PCR products were electrophoresed on a 5% agarose gel containing ethidium bromide, and amplified fragments were visualized under UV transillumination. cDNAs encoding actin (control) derived from mouse were PCR amplified as previously described (Pool et al., 2005).

TUNEL labeling:

10-μm lumbar DRG tissue sections were dissected, washed in PBS and permeabilized in ice cold 0.1% sodium citrate/0.1% Triton-X 100 for 5 min followed by 2 min in 2:1 ethanol:acetic acid on ice. Samples were rinsed for 2 min in PBS and incubated for 1 h at 37°C with FITC-labeled dUTP in terminal deoxynucleotidyltransferase (TdT) buffer (30 mM Tris-HCl, pH 7.2, 140 mM sodium cacodylate, and 1 mM cobalt chloride) and TdT according to the protocol provided by the manufacturer (Roche Laval QC). Negative controls included sections incubated with FITC-labeled dUTP in the absence of TdT. Cells were washed in PBS, mounted in fluorescent mounting media (Dako, Burlington ON) and analyzed with a ZeissAxiovert

200m epifluorescent microscope equipped with an Axiocam HRM digital camera and Axiovision 4.6 software (Zeiss, Toronto ON).

Primary culture of DRG neurons:

Spinal columns were removed from P5 mice and transferred to a dissection microscope. Total DRGs were isolated per mouse, and subsequently digested for 15 minutes each with collagenase A (Roche, Laval QC) and papain (Worthington, Lakewood NJ) solutions. DRG neurons were dissociated with flame polished glass Pasteur pipettes and seeded onto 18mm laminin-2 (Millipore, Billerica MA) coated coverslips at a density of 50,000 per 12-well cell culture vessel. Cells were cultured in DMEM with 10% FBS and 1% Pen/Strep and placed in a 37°C tissue culture incubator, under 8.5% CO2. The following day, media was changed to neuronal maintenance media (DMEM base, 0.5% FBS, 1% Glutamax, 16 µg/mL putrescine, 400 µg/mLthyroxine, 400 µg/mL triiodothyronine, 6.2 ng/mL progesterone, 5 ng/mL sodium selenite, 100 µg/mL bovine albumin serum, 5 µg/mL bovine insulin, 50 µg/mL holo-transferrin) supplemented with 200 ng/mL nerve growth factor, and 1 mM 5-fluoro-2'-deoxyuridine. A ¾ media change was carried out every other day. Cultures were fixed in 4% PFA before antigenic labeling. Primary antibodies used were anti–c-myc (1:800; Santa Cruz Biotechnology, Inc.), mouse polyclonal anti-βIII-tubulin (1:1000; Millipore), rabbit-polyclonal anti-cleaved caspase-3 (1:1000; Cell Signaling Technology, Beverly, MA). Antibodies were diluted in antibody buffer (PBS, 0.3% Triton X-100, and 3% BSA). Where DAPI staining is indicated, samples were incubated in DAPI stain (0.2 µg/ml in PBS) for 10 min and washed three times in PBS for 5 min. Samples were mounted in

fluorescent mounting media (Dako) and analyzed with a confocal microscope (LSM 510 meta) equipped with an EC Plan-Neofluar 40×/1.30 NA oil DIC M27 objective using Zen 8.0 software.

Subpopulations of sensory neurons were visualized with an epifluorescent microscope (Axiovert 200M; Carl Zeiss) under a 20× objective (Achroplan 0.25) equipped with a digital camera (AxioCamHRm; Carl Zeiss). Using Axiovision 4.6 software (Carl Zeiss), the circumference-measuring tool was employed in determining sensory neuron size.

Immunohistochemistry:

Tissues (cortical, cerebellum, DRG, and muscle) were collected from at least three $dt^{Tg4/Tg4}$, PrP-dystonin-a2/PrP-dystonin-a2; $dt^{Tg4/Tg4}$, and PrP-dystonin-a2/PrP-dystonin-a2 mice at multiple time points (P10, P15, P58) as previously described (Young and Kothary, 2008; De Repentigny et al., 2011). Mice were anesthetized with tribromoethanol (Avertin) and perfused transcardially with 3 ml of phosphate buffered saline (PBS) followed by 10 ml of 4% paraformaldehyde (PFA) in PBS. Samples were embedded in OCT compound (Sakura), and frozen in liquid nitrogen. Cryostat sections of 10-µm thickness were stored at -20°C before use. Primary antibodies used were rabbit monoclonal anti-Myc (1:100, Abcam). Secondary antibodies used were anti-rabbit Alexa-488 (1:2000, Molecular Probes). Antibodies were diluted as mentioned above. Samples were mounted in fluorescent mounting media (Dako) and analyzed with a ZeissAxiovert 200m epifluorescent microscope equipped with an Axiocam HRM digital camera and Axiovision 4.6 software (Zeiss, Toronto ON).

Statistical analysis:

Data were analyzed using Student's t-test or factorial ANOVA. Following detection of a statistically significant difference in a given series of treatments by ANOVA, post hoc Dunnett's t-tests or Tukey tests were performed where appropriate. P values under 0.05 were considered statistically significant (shown as *); P values under 0.01, 0.001, or 0.0001 were considered highly statistically significant (shown as **, ***, ****, respectively).

Acknowledgments

We are grateful to the Kothary laboratory for helpful discussions. This project was funded by a grant from the Canadian Institutes of Health Research (CIHR) to R.K. A.F. is supported by an Ontario Graduate Scholarship, R.O'M. is a recipient of a Frederick Banting and Charles Best CIHR Doctoral Research Award, and R.K. is a recipient of a University Health Research Chair from the University of Ottawa.

Chapter 5

A disruption in the autophagic process underlies the sensory neuropathy in *dystonia musculorum* mice

A disruption in the autophagic process underlies the sensory neuropathy in *dystonia musculorum* mice

Andrew Ferrier[1,2], Yves de Repentigny[1], Sabrina Gibeault[1], Daniel Kuo[1], and Rashmi Kothary[1,2,3#]

[1]Ottawa Hospital Research Institute, Ottawa, Ontario, Canada K1H 8L6;

[2]Department of Cellular and Molecular Medicine, University of Ottawa, Ottawa, Ontario, Canada K1H 8M5;

[3]Department of Medicine, University of Ottawa, Ottawa, Ontario, Canada K1H 8M5

Running head: Dystonin is essential for autophagy in sensory neurons

#Correspondence to: Rashmi Kothary

Author Contributions

Conceived and designed the experiments: AF RK. Performed the experiments: AF (figures 1, 2, 3, 4, 5, 6, 7, 8) YDR, DK. Analyzed the data: AF, YDR, RK. Contributed reagents/materials/analysis tools: YDR, AF, RK. Wrote the paper: AF, RK.

Abstract

A newly identified lethal form of hereditary sensory and autonomic neuropathy in humans, designated HSAN-VI, is caused by a homozygous mutation in the dystonin gene (*DST*). Dystonin is a cytoskeletal linker protein involved in microtubule-based motor protein transport and loss of function leads to sensory neuron degeneration and severe ataxia in *dystonia musculorum* (*dt*) mice. Both microtubules and the dynein motor protein are essential to the autophagic pathway. Here, we assessed the influence dystonin imparts on autophagy in the murine nervous system. LC3-II, a marker of autophagy, was significantly increased in pre-and phenotypic stage sensory neurons from multiple *dt* alleles. Electron microscopy revealed authentic autophagosomes and explained the increased LC3-II protein levels. In addition, we observed significant decreases in the autophagosome motor protein dynein-intermediate chain 1 (dynein-IC1). A difference in autophagic flux was detected between *dt* and wild type primary sensory neurons. In accordance with this, *dt* sensory neurons also displayed impaired protein turnover of the autophagosome substrate p62 and of poly-ubiquitinated proteins. As *dt* mice are devoid of two major neuronal dystonin isoforms (dystonin-a1 and -a2), we addressed which isoform was responsible for the autophagic defects. We show that *dt* sensory neurons exogenously expressing dystonin-a2 under the neuronal Prion Protein Promoter have a reduced number of autophagosomes, autolysosomes, and damaged organelles. As well, LC3-II, p62, and poly-ubiquitinated proteins were restored to normal levels. Moreover, autophagic flux in these sensory neurons showed a similar profile to that of wild type. Taken together, our studies show that dysfunctional autophagy underlies *dt* pathogenesis and suggests that the dystonin-a2 isoform is critical for this process to occur normally within sensory neurons.

Introduction

Spectraplakins are a family of giant (>500 kD) multifunctional proteins that are capable of integrating cytoskeletal filaments (*i.e.*, microtubules [MTs], microfilaments [MFs], and intermediate filaments) (Suozzi et al., 2012a). As such, these giant proteins underlie many fundamental cellular processes, including, but not limited to, intracellular trafficking, migration and cellular shape. Dystonin is a member of the spectraplakin family whose loss-of-function in both humans and mice results in lethal peripheral neuropathies, namely Hereditary Sensory Autonomic Neuropathy type VI (HSAN VI) and *dystonia musculorum* (*dt*), respectively (Brown et al., 1995; Edvardson et al., 2012). In mice, homozygous recessive mutations in the *Dst* gene cause a severe sensory neuropathy, characterized by overt ataxic and dystonic movements, and death at approximately 3 weeks postnatal development (Duchen et al., 1964; Duchen, 1976).

The *Dst* gene is remarkably large (~400 kb in mice) and gives rise to three tissue-specific dystonin isoforms, namely dystonin-e (epithelial isoform, ~315 kD), dystonin-b (muscle isoform, ~834 kD), and dystonin-a (neuronal isoform, ~615 kD) (Brown, Dalpe, Mathieu, & Kothary, 1995; Leung, Zheng, Prater, & Liem, 2001; Okumura, Yamakawa, Ohara, & Owaribe, 2002; Sawamura, Li, Chu, & Uitto, 1991). Through alternative splicing of the first 5' exons three major dystonin-a isoforms are produced, including dystonin-a1, -a2, and -a3. While the domain architecture of each dystonin-a isoform is similar, comprising of an N-terminal actin binding domain, an extensive coiled-coil region, and a C-terminal microtubule (MT)-binding domain, it is their unique N-terminal regions that differentiate them and consequently determine their subcellular localization and biological functions (Ferrier et al., 2013). Loss of dystonin-a1 and -a2 is causal of the

dt disorder, as $dt^{Tg4/Tg4}$ mice are devoid of these two isoforms (Pool et al., 2005). While recent studies suggest both dystonin-a1 and -a2 variants contribute to *dt* pathogenesis (Ryan et al., 2012c) (unpublished, Ferrier et al., 2013) the exact pathological mechanisms by which these isoforms precipitate the degeneration of *dt* sensory neurons is unresolved.

Macroautophagy (hereafter referred to as autophagy) in neurons is a constitutive process degrading superfluous long-lived organelles and protein aggregates via the degradative compartments of the endosomal-lysosomal system (Yang and Klionsky, 2010). This process is essential in the maintenance of neuronal homeostasis (Hara et al., 2006; Komatsu et al., 2006), and is implicated in various neurodegenerative diseases (Wong and Cuervo, 2010). Within peripheral nerves, the transport of autophagosomes is highly reliant upon the neuronal cytoskeleton and it's constituent parts, particularly MTs and motor proteins (Jahreiss et al., 2008; Kimura et al., 2008; Monastyrska et al., 2009). Indeed, perturbing the stability of MTs or motor protein function disrupts autophagic flux (Aplin et al., 1992; Ravikumar et al., 2005; Köchl et al., 2006), which in turn can lead to the demise of the cell. Autophagic flux is defined by the formation and trafficking of a mature autophagosome that ultimately fuse with and are degraded by lysosomes and/or endosomes. A number of studies suggest dystonin-a isoforms have the potential to negatively influence autophagy, namely through impairments in motor protein trafficking and/or MT dynamics (Liu et al., 2003b, 2007a; Bhanot et al., 2011; Ryan et al., 2012a). Disruptions to autophagy would conceivably contribute to the degeneration of *dt* sensory neurons.

Initial pathological studies of *dt* sensory neurons indicated dystonin-a loss-of-function resulted in disorganized MTs (Dalpé et al., 1998). More recently, dystonin-a2

was ascribed a role in maintaining MT stability through an interaction with the MT-associated protein 1B (MAP-1B) (Ryan et al., 2012a). The dystonin-a2-MAP1B interaction is critical in maintaining both MT acetylation and intracellular transport within the perinuclear region. Acetylated microtubules in neurons are required for the recruitment of motor proteins and proper trafficking (Reed et al., 2006; Dompierre et al., 2007). Moreover, the biogenesis and fusion of autophagosomes with lysosomes relies upon acetylated MTs (Geeraert et al., 2010; Xie et al., 2010), therefore implicating dystonin-a2 in multiple aspects of autophagy.

Dystonin-a1, on the other hand, is involved in the regulation of retrograde transport of endosomal vesicles in neurons. This occurs through interactions with both p150Glued, a core component of the dynein/dynactin complex, and the neuronal-specific endosomal vesicle protein retrolinkin, respectively (Liu et al., 2003a, 2007a). As the dynein-motor complex is involved in 90% of autophagosome trafficking within sensory neurons (Maday et al., 2012), and the fact that endosomes are a degradative compartment for autophagosomes, dystonin-a1 also becomes a viable contributor to the autophagic mechanism.

To address whether dystonin-a loss-of-function impacts autophagy and underlies *dt* sensory neuron degeneration, we utilized the $dt^{Tg4/Tg4}$ mouse model (devoid of dystonin-a1 and -a2). We find $dt^{Tg4/Tg4}$ sensory neurons are characterized by significant increases in the autophagosome marker LC3-II, coupled with accumulations of authentic autophagosomes, autolysosomes and aberrant mitochondria as assessed by EM. We also find that while autophagic flux proceeds normally in primary $dt^{Tg4/Tg4}$ cortical neurons, flux is impaired in $dt^{Tg4/Tg4}$ sensory neurons, suggesting dystonin-a loss-of-function

imparts a cell-specific impairment on autophagy. In agreement with impaired autophagic flux in $dt^{Tg4/Tg4}$ sensory neurons, we noted significant decreases in the retrograde motor protein dynein-IC1. Defective autophagic flux in $dt^{Tg4/Tg4}$ sensory neurons results in increased expression of the autophagosome substrate p62 and poly-ubiquitinated proteins. Interestingly, sensory neurons from the rescue transgenic mouse *PrP-dystonin-a2/PrP-dystonin-a2;*$dt^{Tg4/Tg4}$ showed reversion of the aforementioned autophagic defects. This work establishes the importance of dystonin in the autophagic process, and further highlights that impairments in autophagic homeostasis underlie the demise of sensory neurons in *dt* mice.

Materials and Methods

Reagents

All chemicals were purchased through Sigma-Aldrich (St. Louis, MO USA) and all cell culture reagents were obtained from Invitrogen (Burlington, ON Canada) except where indicated.

Ethics Statement

All experimental protocols on mice were approved by the Animal Care Committee of the University of Ottawa. Care and use of experimental mice followed the guidelines of the Canadian Council on Animal Care.

Animal models

The dt^{27}, $dt^{Tg4/Tg4}$, and *PrP-dystonin-a2/PrP-dystonin-a2;*$dt^{Tg4/Tg4}$ rescue mice were used at pre-phenotype (P3-5) and phenotype (P15-P17) stages. All mice shared the same mixed genetic background of CD1/C57BL6. The derivation of dt^{27} and $dt^{Tg4/Tg4}$ mutant lines and characterization of the mutation were described previously (Kothary et al., 1988; Brown et al., 1995; Pool et al., 2005). The onset of phenotype was generally assessed by the appearance of clasping of hind limbs after the mice were picked up by the tails. dt^{27} and $dt^{Tg4/Tg4}$ mice were genotyped by PCR amplification of genomic tail DNA as previously described (Pool et al., 2005). *PrP-dystonin-a2/PrP-dystonin-a2;*$dt^{Tg4/Tg4}$ rescue mice were previously described in (Chapter 4).

Primary culture of sensory neurons

Sensory neurons were collected from wild type, $dt^{Tg4/Tg4}$, and *PrP-dystonin-a2/PrP-dystonin-a2;*$dt^{Tg4/Tg4}$ mice at P3-5. Spinal columns were removed and transferred to a dissection microscope. Approximately 40 dorsal root ganglion (DRG) were isolated per mouse and subsequently digested for 15 min with collagenase A (Roche, Laval, Canada) and papain (Worthington, Lakewood, NJ) solutions. DRG neurons were dissociated with flame-polished glass Pasteur pipettes and seeded onto 12-mm laminin-2 (Millipore, Billerica, MA) coated coverslips at a density of 50,000 in DMEM with 10% FBS and 1% penicillin/streptomycin. Cells were placed in a 37°C tissue culture incubator under 8.5% CO2. The following day, the media was changed to neuronal maintenance media (DMEM base, 0.5% FBS, 2% B27, 1% GlutaMax, 16 μg/ml putrescine, 400 μg/ml thyroxine, 400 μg/ml triiodothyronine, 6.2 ng/ml progesterone, 5 ng/ml sodium selenite, 100 μg/ml bovine albumin serum, 5 μg/ml bovine insulin, 50 μg/ml holo-transferrin) supplemented with 200 ng/ml nerve growth factor and 1 μM 5-fluoro-2′-deoxyuridine. A three-fourths media change was carried out every other day, up until day 5 of culture, when autophagy flux, pulse-chase assays, or western blot analyses were performed.

Primary cortical neuron cultures

Cortical brain samples were dissected from P0 wild type and $dt^{Tg4/Tg4}$ mice. Brains were kept in cold HBSS (Gibco), 10 mM HEPES (Gibco), and 1X Penicillin Streptomycin (Gibco) during meninges removal. Post meninges separation, the brain cortices were diced and rinsed with pre-warmed HBSS at 37^{o}C prior to digestion. The digestion of unwanted cortical tissues was done with 0.5 mg/mL trypsin and 0.1 mg/mL

DNaseI (Roche), incubating for 20 minutes with agitation. Further, digested samples were triturated to achieve single-celled suspension with 10% fetal bovine serum in Neurobasal Media (Gibco), centrifuged and resuspended in Neuron Media composed of Neural Basal Media, 1X B27 (Gibco), 1X Sato's supplement, 0.5 mM Glutamax (Gibco), 1X N_2 supplement (Gibco), and 1:1000 Gentamycin. Resuspended cells were allowed to rest for the settling of cell debris, and upper-layer single-celled neurons were seeded on laminin plus 1 mg/ml PDL (Millipore, Billerica, MA) coated cover slips at 5.0 x 10^4 cells/well and 2.5 x 10^5 cells/well in 24 well and 6 well plates, respectively. Gentamycin was removed after 24 hours incubation after sufficient neuronal growth selection.

Cortical neuron cell soma and axonal autophagosome counts

Autophagosomes were visualized and counted with anti-LC3B antibody (Abcam, ab48394) using epifluorescence, and photomicrographs captured using a Zeiss Axiovert 200M microscope equipped with AxiovisionLE V4.8.0.0. Prior to counting, each sample cover slips were individually examined for the minimal signal intensity appropriate to resolve between distinct autophagosomal punctates. The determined minima were set as the standard intensities and remain unchanged for the corresponding coverslip between autophagosome counts of individual cells. Signal intensity differences between cover slips were kept to a range to minimize counting bias due to intensity, and visually ambiguous cells were excluded from the results. Somatic autophagosome counts were counted as average number autophagosomes/cell soma at n = 3 with 40 cells per n. Axonal autophagosomes were counted as average number autophagosomes/μm length of all axons at n = 3 with 40 cells per n. Axonal counts were restricted to linear extensions

of axons for accuracy of length determination. All counts were done blindly by two individuals to compare reproducibility of the counts, and highly differing counts of the same cover slip were discarded to avoid ambiguity and bias.

Autophagy Flux Assay

Primary cortical neurons (P0) or sensory neurons (P5) were cultured (as outlined above) from each genotype in a 6 well culture vessel for 7 or 5 days, respectively. Neurons were washed 3X with PBS and challenged by different flux conditions for 2 h thereafter. Flux conditions included: untreated, (DMEM + 10% FBS), induction of autophagy (DMEM + 10% FBS + 500 nM rapamycin), blockage of autophagy (DMEM + 10% FBS + 30 μM chloroquine), and combination treatment of inducing and blocking autophagy (DMEM + 10% FBS + 500 nM rapamycin + 30 μM chloroquine). Neurons were harvested from each condition and LC3-II protein levels examined thereafter via western blot analysis. A single 6 well vessel represented total sensory neurons from 1 mouse. Each flux assay was conducted n = 2 for each genotype.

Cell preparation for Transmission EM and Morphometric Analysis

P3-5 primary sensory neurons were cultured as described above, washed with PBS (phosphate-buffered saline) and trypsinized (0.25% trypsin/0.53 mM EDTA) for 5 minutes at 37ºC. To obtain a suitable sized pellet of sensory neurons, an n = 3 was collected and combined for each genotype (wild type, $dt^{Tg4/Tg4}$, *PrP-dystonin-a2/PrP-dystonin-a2;*$dt^{Tg4/Tg4}$). Cells were centrifuged at 1000 x g for 5 min and supernatant removed. Neurons were fixed for 1 h at room temperature in Karnovsky's fixative (4%

paraformaldehyde, 2% glutaraldehyde and 0.1 M cacodylate in PBS, pH 7.4) and subsequently washed twice in 0.1 M cacodylate buffer. Neurons were post-fixed with 1% osmium tetroxide in 0.1 M cacodylate buffer for 1 h at RT, followed by 3 x 5 min washes in water. Cells were dehydrated twice for 20 min for each step in a graded series of ethanol from water through 30%, 50%, 70%, 85%, and 95% ethanol, and twice for 30 minutes in 100% ethanol (molecular sieves were used to dehydrate ethanol), followed by two washes for 15 min in 50% ethanol/50% acetone and twice for 15 min in 100% acetone. Neurons were infiltrated in 30% spurr/acetone for 15 h (overnight), then in 50% spurr/acetone for 6 h, and in fresh 100% spurr resin for overnight. Spurr was changed twice a day for three days at room temperature. All infiltration steps were performed on a rotator. Neurons were embedded in fresh liquid spurr epoxy resin and polymerized overnight at 70ºC. Ultrathin sections (80 nm) of cells were collected onto a 200-mesh copper grid and let dry overnight. Grids were stained with 2% aqueous uranyl acetate and with Reynold's lead citrate. Sections were observed under a transmission electron microscope (Hitachi 7100).

Approximately 20 EM micrographs at 20,000X magnification were examined per genotype. For our qualitative analysis, we identified autophagosomes as double membraned compartments of 0.5 μm in diameter or larger, whereas autolysosomes were defined as single membraned vesicles with densely compacted amorphous or multilamellar contents. Mitochondria were considered damaged if they exhibited absent or abnormal cristae.

RT-PCR Analysis

For reverse transcription-polymerase chain reaction (RT-PCR) analysis, RNA was isolated from transgenic P0 cortical tissues of wild type mice (n = 2). To synthesize cDNA, equal amounts of RNA were reverse-transcribed in a standard reaction with MuLV reverse transcriptase (Invitrogen). From these samples, cDNAs encoding dystonin isoforms were PCR amplified using primer pairs targeting dystonin-a1 and -a2 isoforms as previously described (Pool et al., 2005). RT-PCR experiments aimed at determining the relative abundance of dystonin transcripts in brain using cycle parameters that were initially optimized and found to be identical for all samples. The intensity of PCR products visualized on 1.5% ethidium bromide-stained agarose gels was determined using NIH Image software. β-actin served as the internal control for these experiments and all values obtained with the various primer sets were normalized to the respective β-actin values.

Western analysis:

Protein lysates were collected from phenotype or pre-phenotype DRGs, or from primary sensory neuron cultures as previously described (Ryan et al., 2012a). Proteins were isolated in RIPA buffer (10 mM PBS, 1% NP40, 0.5% sodium deoxycholate, 0.1% SDS, 30 μl/ml aprotinin, 10 mM Na orthovanadate, 100 μl/ml phenylmethylsulfonyl fluoride). Protein samples (10 μg) were separated by SDS–PAGE under reducing conditions. Western analyses were performed using the rabbit polyclonal anti-LC3B antibody (Abcam, ab48394), mouse monoclonal anti–BIII-tubulin (1:2000, E7 clone; Hybridoma Bank, Iowa City, IA). Secondary antibodies used were horseradish peroxidase (HRP)-conjugated anti-mouse immunoglobulin G (IgG, 1:2000; Bio-Rad,

Hercules, CA) and HRP-conjugated anti–rabbit IgG (1:2000; Bio-Rad). Immunoreactive bands were visualized using SuperSignal West Pico (MJS BioLynx, Brockville, Canada). Quantification of protein expression levels was performed by densitometric analysis of individual bands using ImageJ analysis software (National Institutes of Health, Bethesda, MD). At least three western blots from different experiments were evaluated by densitometry and normalized to a protein standard (actin, tubulin, or GAPDH) for all western blots depicted.

Statistical analysis

Data were analyzed using Student's t test or factorial analysis of variance (ANOVA) as applicable using InStat, version 3.0 (GraphPad Software, La Jolla, CA). Following detection of a statistically significant difference in a given series of treatments by ANOVA, post hoc Dunnett's t tests or Tukey tests were performed where appropriate. $p < 0.05$ was considered statistically significant (shown as either *); $p < 0.01$ was considered highly statistically significant (shown as **).

Results

As discussed, through interactions with the dynein motor complex (DMC) dystonin-a serves an essential role in retrograde transport in neurons (Liu et al., 2003a). Since autophagosomes are a cargo of the DMC and play a crucial role in the turnover of several organelles and proteins, we hypothesized that disrupting the interaction between dystonin-a and the dynein/dynactin complex would perturb the transport of autophagosomes within neurons and contribute to the degeneration of *dt* sensory neurons. To assess the influence dystonin loss-of-function imparts on the DMC, we assessed the protein levels of cytoplasmic dynein intermediate chain 1 (dynein-IC1), a critical subunit of the DMC involved in binding cellular cargo in particular autophagosomes (Batlevi et al., 2010). While we did not observe a significant change in the levels of dynein-IC1 between P15 WT and $dt^{Tg4/Tg4}$ brains (Fig. 1A), we did find levels to be markedly reduced in P15 $dt^{Tg4/Tg4}$ DRG protein lysates compared to WT controls (Fig. 1B). Given this observation, we next examined the influence of dystonin-loss-of function on autophagic dynamics within *dt* sensory neurons.

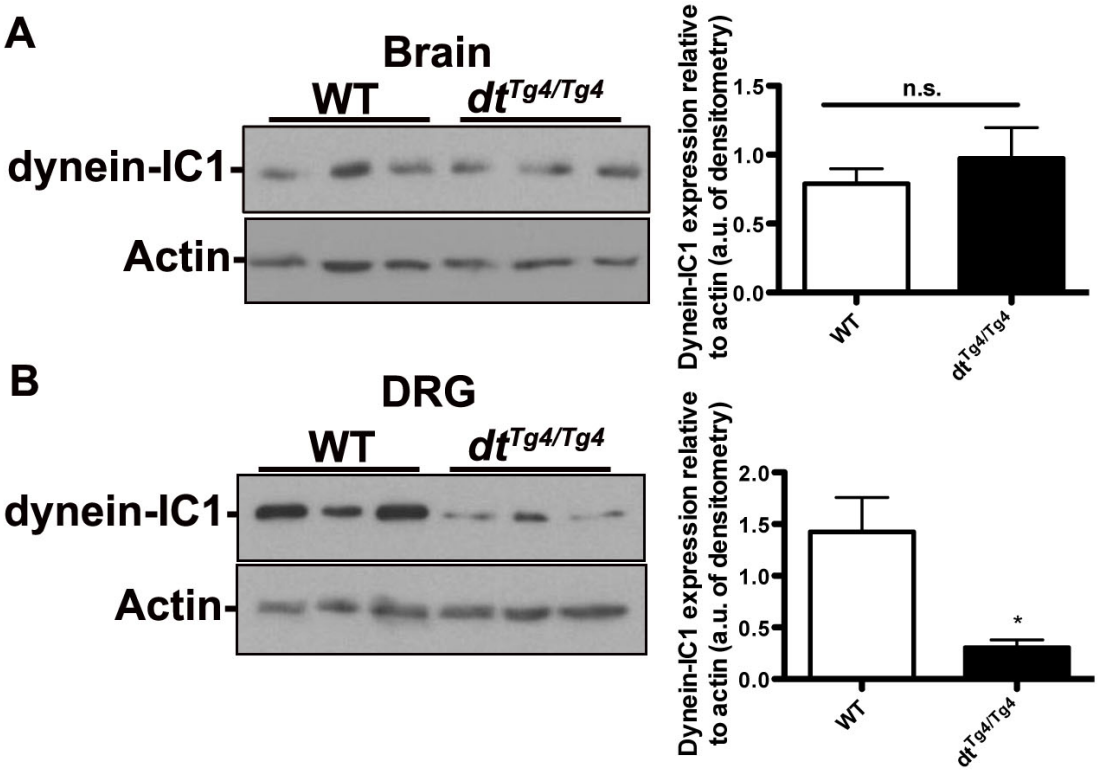

Figure 1: Dystonin loss-of-function has a cell-specific impact on the DMC. A) Immunoblot analyses of wild type (WT) and $dt^{Tg4/Tg4}$ P15 brain (cortical) lysates indicate no significant changes in dynein-IC1 protein levels ($p > 0.05$, $n = 3$). B) P15 $dt^{Tg4/Tg4}$ DRG lysates show a significant decrease in dynein-IC1 protein levels ($p < 0.05$, $n = 3$) compared to P15 WT DRGs. Error bars indicate SEM. Graphs represent arbitrary units (a.u.) of densitometric analysis of membranes in A and B.

dt sensory neurons exhibit autophagosome accumulation

Trafficking of autophagosomes within neurons occurs through the DMC (LaMonte et al., 2002; Ravikumar et al., 2005; Eschbach and Dupuis, 2011). Deficiencies in this complex impede the autophagy pathway and can lead to accumulation of autophagosomes and protein aggregates (Batlevi et al., 2010; Eschbach and Dupuis, 2011). As autophagosomes are transient structures, undergoing rounds of maturation and degradation in lysosomes, impairment in autophagic activity, through diminished trafficking, for instance, could be reflected as a build up of autophagosomes. We sought to address this notion by examining the protein levels of the MT-associated protein light chain 3-II (LC3-II), a component of the inner and outer membrane of double-membraned autophagosomes. Total DRGs were collected from phenotypic (P15) and pre-phenotypic (P10) wild type and $dt^{Tg4/Tg4}$ mice (P15, n = 3; P10, n = 1). Compared to wild type P15 DRGs, $dt^{Tg4/Tg4}$ DRGs displayed a significant increase in LC3-II protein levels (Fig. 2A). P10 $dt^{Tg4/Tg4}$ DRGs also displayed an increase in LC3-II protein levels compared to wild type (Fig. 2B). In addition, DRGs from pre- and phenotypic (P10 and P15) dt^{27} mice (another *dt* allele) also displayed increased LC3-II protein levels, suggesting that this is a common pathological signature of *dt* DRGs (Supplemental Figure S1A-B).

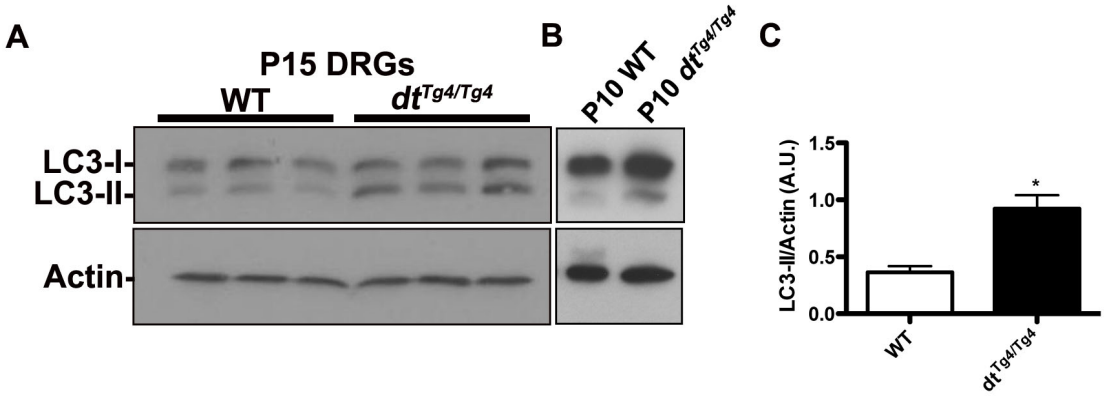

Figure 2: Phenotypic and pre-phenotypic *dt*$^{Tg4/Tg4}$ sensory neuorns display increased LC3-II protein levels. A) P15 wild type (WT) and phenotypic *dt*$^{Tg4/Tg4}$ DRG protein lysates were analyzed by western blot for the induction of LC3-II proteins. A significant induction was of LC3-II was observed in P15 *dt*$^{Tg4/Tg4}$ DRGs. LC3-I represents a soluble form of LC3; LC3-II, membraned-bound form of LC3. Each lane represents total DRGs collected from a single mouse. B) Induction of LC3-II is also evident in pre-phenotypic (P10) *dt*$^{Tg4/Tg4}$ DRGs. C) Quantification of (A) by densitometry and normalized to actin standard; Student's *t* test; error bars represented as SEM (*$p < 0.05$).

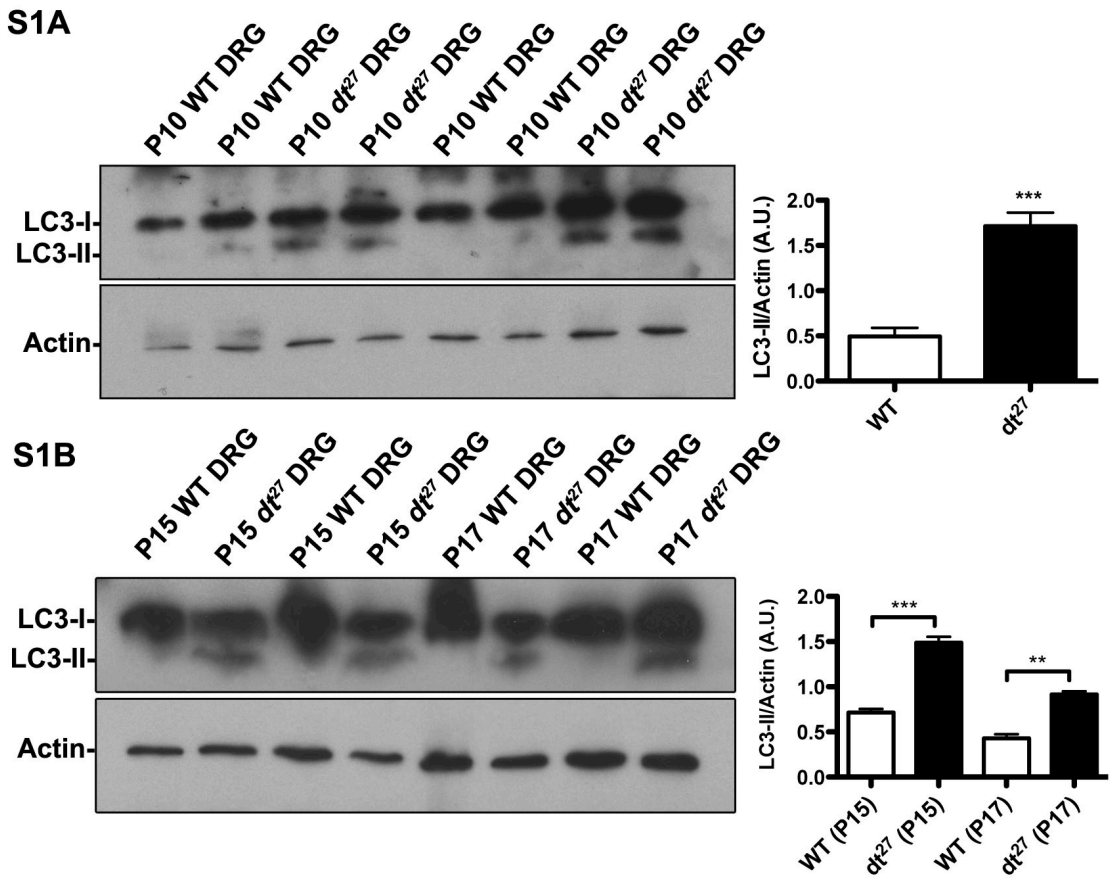

Supplemental Figure S1: **Phenotypic and pre-phenotypic *dt*^{27} sensory neurons display increased LC3-II protein levels**. S1A. Western blot analysis of pre-phenotypic (P10) *dt*^{27} DRG protein lysates antigenically labelled for LC3 display a significant increase in LC3-II ($p < 0.001$, $n = 4$). S1B. LC3-II protein levels are significanlty increased in phenotypic (P15, P17) *dt*^{27} DRGs (P15, $p < 0.001$; P17, $p < 0.01$, $n = 3$). Quantification by densitometry and normalized to actin standard; Student's *t* test; error bars represented as SEM.

To determine if increase in LC3-II protein level was reflective of an increase in authentic autophagasomes and not accumulating LC3-II protein, we conducted trasmission EM on P5 wild type and P5 (pre-phenotypic) $dt^{Tg4/Tg4}$ primary sensory neurons that were cultured in nutrient-rich media for 5 days. Our qualitative analysis suggested that while wild type sensory neuorns were devoid of autophagosomes (Fig. 3A, A'), $dt^{Tg4/Tg4}$ sensory neuorns were replete with double-membraned autophagosomes, damaged mitochondria (Fig. 3B, B'), and autolysosomes (Fig. 3C, C'). We found that wild type sensory neurons when treated with the autophagy inhibitor chloroquine displayed similar cellular pathologies as $dt^{Tg4/Tg4}$ sensory neurons, including accumulating autolysomes (Fig. 3D, D'). As choloroquine disrupts late-stages of the autophagy pathway by blocking the degradative function of autolysosomes, it is possible that, in addition to impairments in trafficking, perturbations in late stages of autophagy occurs in $dt^{Tg4/Tg4}$ sensory neuorns and mediates the increased autophagosomes, autolysosomes and damaged mitochondria.

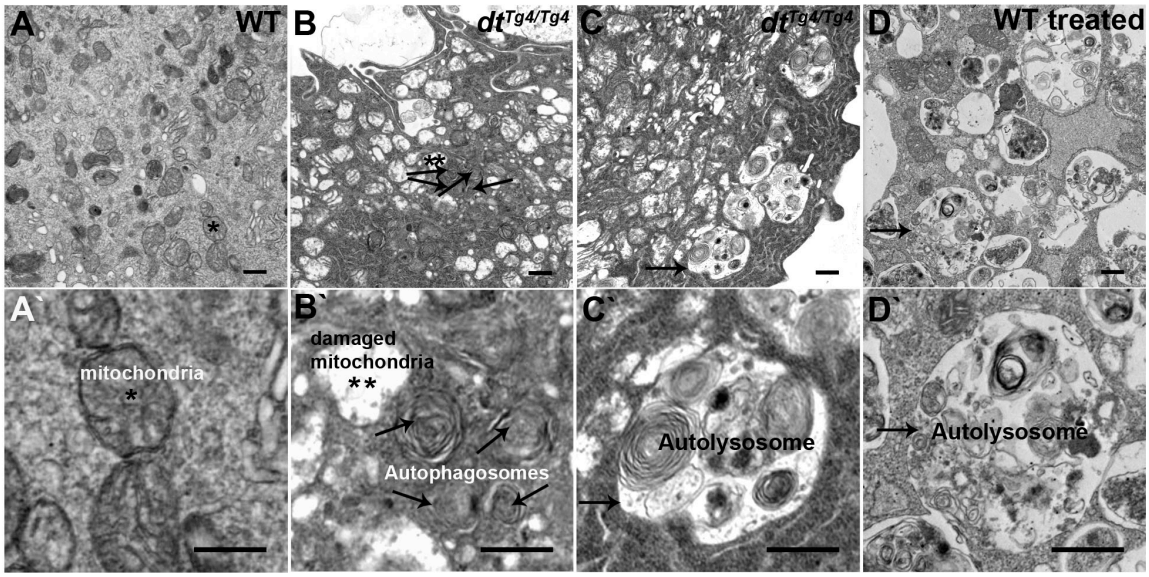

Figure 3: Ultrastructural analysis of P5 wild type and *dt*$^{Tg4/Tg4}$ sensory neurons. A, A') Wild type (WT) P5 sensory neurons cultured for 5 days displayed few autophagosomes, autolysosomes, and damaged mitchondria. B, B') Damaged mitochondria (asterisks) and accumulating double-membraned autophagosomes (arrows) were evident in *dt*$^{Tg4/Tg4}$ sensory neurons. C, C') Single-membraned autolysosome vacuoles with electron-dense sequestered materials (arrows) were also present in *dt*$^{Tg4/Tg4}$ sensory neurons. D, D') P5 WT sensory neurons treated with 30 μM chloroquine for 2 h revealed similar cellular pathologies (*i.e.*, autolysomes with amorphous materials, arrows) as *dt*$^{Tg4/Tg4}$ sensory neurons**.** Scale bars and magnification for A, B, C, D, (6,000X, scale bar 500 nm), and A', B', C', D' (20,000X, scale bar 500 nm).

Autophagic flux is compromised in $dt^{Tg4/Tg4}$ sensory neurons

The increased expression of LC3-II coupled with the pathologies observed in our EM analysis suggests that autophagy is activated in $dt^{Tg4/Tg4}$ sensory neurons, and that deficiencies in autophagic activity may exist. Indeed, increased LC3-II protein levels, accumulating autophagosomes, autolysosomes, and damaged mitochondria are all indicative of impairments in the autophagy pathway (Levine and Kroemer, 2008; Xie et al., 2011). To address whether autophagy proceeds normally in $dt^{Tg4/Tg4}$ neurons, we conducted autophagic flux assays. Autophagic flux encompasses the maturation of autophagosomes to the trafficking, fusion and degradation of autophagosomes in lysosomes (Yang and Klionsky, 2010). We sought to utilize a cortical neuron culture system to assess autophagic flux. This system is amenable to autophagic flux conditions, easy to culture, and like sensory neurons, express dystonin-a (Bernier et al., 1995). Cortices from P0 mice (n = 3) were dissociated and cultured for 7 days in nutrient-rich conditions in the presence of serum supplement B27 and mitotic inhibitors to reduce contaminating cells. As anticipated, prior to assessing autophagic flux, both wild type and $dt^{Tg4/Tg4}$ cortical neurons produced extensive branching, as assessed by anti-β-III tubulin staining (Fig. 4A), and anti-glial fibrillary acidic protein (GFAP) immunostaining showed few, if any, contaminating astrocytes present within the cultures (data not shown). Furthermore, RT-PCR analyses of wild type cortical neurons indicated that both dystonin-a1 and dystonin-a2 transcripts were expressed (Fig. 4B).

Following 7 days in culture, autophagic flux was assessed in wild type and $dt^{Tg4/Tg4}$ cortical neurons. The autophagy flux assay encompassed different flux conditions including untreated control neurons; neurons treated with 500 nM rapamycin

for 2 h to enhance autophagy; neurons treated with 30 μM chloroquine for 2 h to block autophagosome degradation; and neurons treated with both rapamycin/chloroquine for 2h to simultaneously enhance autophagy and block autophagosome degradation. Surprisingly, we found that wild type and $dt^{Tg4/Tg4}$ cortical neurons showed a similar autophagic flux profile (n = 2; Fig. 4C, D). Untreated conditions for both wild type and $dt^{Tg4/Tg4}$ cortical neurons were marked by low basal levels of LC3-II, while neurons pharmacologically treated with the autophagy inducing agent rapamycin showed slight increases in LC3-II protein levels compared to untreated samples. Blocking lysosomal activity with chloroquine produced even greater amounts of LC3-II protein compared to rapamycin and untreated conditions. Similarly, we saw increased LC3-II protein levels when treated with both rapamycin and chloroquine. Coupled with this, we performed immunocytochemistry quantitative analyses of LC3-II punctae in both the cell soma and axons following autophagic induction with 500 nM rapamycin for 2 h (Fig. 4C, D). The average number of LC3-II punctae within cell soma and axons was equivalent between wild type and $dt^{Tg4/Tg4}$ cortical neurons (n = 3). Moreover, neurons displayed a striking punctae LC3-II distribution, consistent with prominent autophagosome formation.

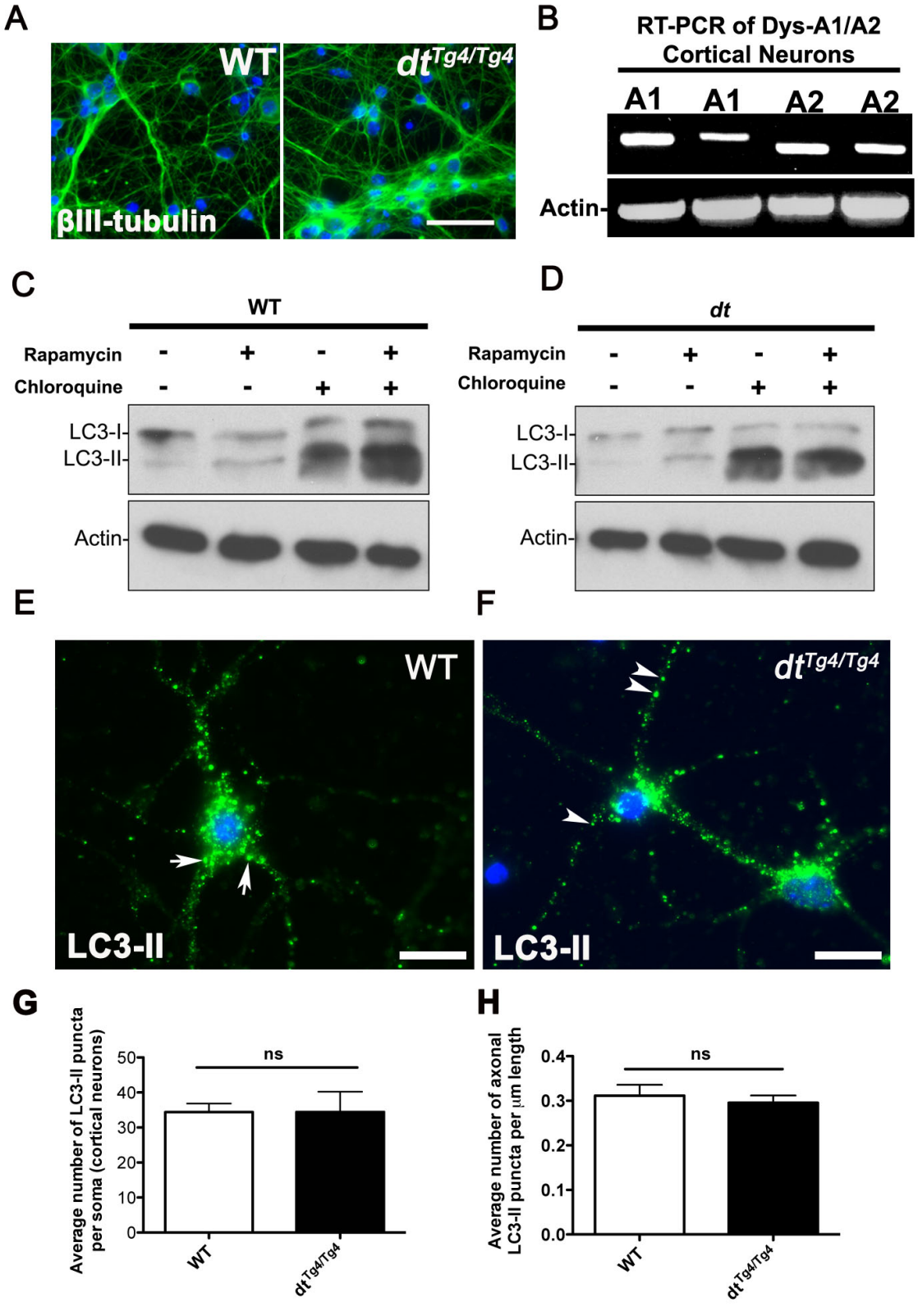
A
WT
dtTg4/Tg4
βIII-tubulin
B
RT-PCR of Dys-A1/A2
Cortical Neurons
A1
A1
A2
A2
Actin
C
WT
Rapamycin
Chloroquine
LC3-I
LC3-II
Actin
D
dt
Rapamycin
Chloroquine
LC3-I
LC3-II
Actin
E
WT
LC3-II
F
dtTg4/Tg4
LC3-II
G
Average number of LC3-II puncta per soma (cortical neurons)
ns
WT
dtTg4/Tg4
H
Average number of axonal LC3-II puncta per μm length
ns
WT
dtTg4/Tg4

Figure 4: Autophagic flux proceeds normally in *dt*$^{Tg4/Tg4}$ cortical neurons. A) P0 primary cortical neurons from wild type (WT) or *dt*$^{Tg4/Tg4}$ mice were cultured for 7 days and antigenically labeled for β-III tubulin. Both culture systems exhibit extensive neurite branching and viability (scale bar, 20 μm). B) Dystonin-a1 and dystonin-a2 transcripts are present in wild type cortical neurons as assessed by RT-PCR. C-D) Both WT (C) and *dt*$^{Tg4/Tg4}$ (D) cortical neurons display similar autophagic flux profiles (n = 2). Where indicated, neurons were treated with autophagy inducing agents (500 nM rapamycin, +), or autophagy blocking agents (30 μM chloroquine, +) for 2 h. Each lane represents a cortical lysate derived from a single mouse. Cultures were lysed, total proteins (10 μg per lane) were separated by SDS-PAGE, and endogenous LC3 in the lysates was recognized by antigenic labeling with anti-LC3 antibody. E-F) Representative immunocytochemistry images of cortical neurons from WT (E) and *dt*$^{Tg4/Tg4}$ (F) mice stained with anti-LC3 (scale bar, 10 μm). Arrows and arrowheads exemplify LC3-II punctae within the neuronal soma or axons, respectively. G) Average number of LC3-II punctae per WT (34.39 ± 2.442) and *dt*$^{Tg4/Tg4}$ (34.45 ± 5.774) soma showed no significant difference (Student's *t* test, p = 0.99; n = 3, with 40 cells per n). H) Average number of axonal LC3-II punctae per μm length showed no significant difference between WT (0.3114 ± 0.02426) and *dt*$^{Tg4/Tg4}$ (0.2955 ± 0.01625) neurons (Student's *t* test, p = 0.71; n = 3 with 40 cells per n).

To assess whether dystonin-a loss-of-function impacts autophagic activity in $dt^{Tg4/Tg4}$ sensory neurons, we performed similar flux assays. Pre-phenotypic (P5) wild type and $dt^{Tg4/Tg4}$ primary sensory neurons were cultured for 5 days in nutrient-rich sensory neuron media and challenged in the aforementioned flux conditions. Due to low yields in cell number, each autophagic flux condition (or, each lane of the western blot) represented sensory neurons from a single mouse. We found that both P5 wild type and $dt^{Tg4/Tg4}$ primary sensory neurons exhibited extensive neurite outgrowth and were devoid of any dying sensory neurons after 5 days in culture as assessed by antigenic labeling of β-III tubulin and caspase-3, respectively (Fig. 5A, B).

As expected, wild type primary sensory neurons displayed a typical autophagic flux profile (n = 2) (Fig. 5C). In contrast to P5 wild type sensory neurons, pre-phenotypic $dt^{Tg4/Tg4}$ sensory neurons did not show a normal flux profile (n = 2) (Fig. 5D). Rather, untreated $dt^{Tg4/Tg4}$ sensory neurons displayed high LC3-II protein levels. Indeed, LC3-II protein levels observed in untreated $dt^{Tg4/Tg4}$ sensory neurons were comparable to that of the other three $dt^{Tg4/Tg4}$ flux conditions, suggesting that autophagy is activated in $dt^{Tg4/Tg4}$ sensory neurons, and that autophagosomes are not being turned over. Taken together, while loss of dystonin-a expression within cortical neurons had no impact, it did disrupt autophagic flux in $dt^{Tg4/Tg4}$ sensory neurons.

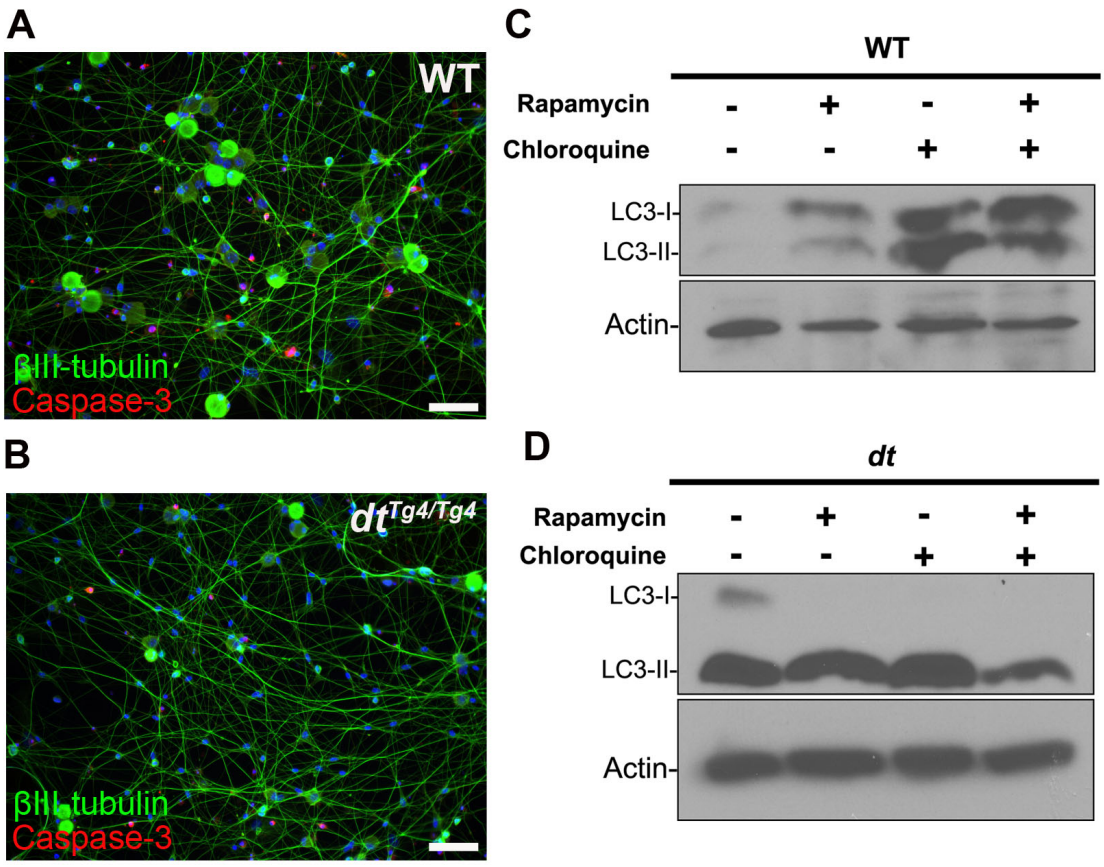

Figure 5: Abnormal autophagic flux in *dt*$^{Tg4/Tg4}$ sensory neurons. A-B) P5 primary sensory neurons from wild type (A, WT) or *dt*$^{Tg4/Tg4}$ (B) mice were cultured for 5 days and antigenically labeled for β-III tubulin and caspase-3. Both culture systems exhibit extensive neurite branching and are devoid of caspase-3 positive neurons (scale bar, 20 μm). C-D) WT (C) and *dt*$^{Tg4/Tg4}$ (D) display dissimilar autophagic flux profiles (n = 2). Where indicated, neurons were treated with autophagy inducing agents (500 nM rapamycin, +), or autophagy blocking agents (30 μM chloroquine, +) for 2 h. Note the increase in LC3-II proteins within each lane of the *dt*$^{Tg4/Tg4}$ sensory neuron flux assay. Each lane represents a sensory lysate derived from a single mouse. Cultures were lysed, total proteins (10 μg per lane) were separated by SDS-PAGE, and endogenous LC3 in the lysates was recognized by antigenic labeling with anti-LC3 antibody.

Restoring Dystonin-a2 expression in *dt*$^{Tg4/Tg4}$ sensory neurons ameliorates defects in autophagic flux

Loss-of-function of dystonin-a1 and -a2 in the murine nervous system is causal in the *dt*$^{Tg4/Tg4}$ disorder (Pool et al., 2005). Recently, dystonin-a2 was determined as the principal initiator of neuronal degeneration (Ryan et al., 2012a, 2012c). To determine if dystonin-a2 underlies the autophagic defects observed in *dt*$^{Tg4/Tg4}$ sensory neurons, we employed the *PrP-dystonin-a2/PrP-dystonin-a2;dt*$^{Tg4/Tg4}$ transgenic mouse model. These transgenic mice, which express exogenous dystonin-a2 under the control of the neuronal Prion Protein Promoter (PrP-dystonin-a2) on the *dt*$^{Tg4/Tg4}$ background. These mice robustly express dystonin-a2 throughout the nervous system, and particularly in sensory neurons (unpublished).

As anticipated, P5 *PrP-dystonin-a2/PrP-dystonin-a2;dt*$^{Tg4/Tg4}$ sensory neurons cultured for 5 days were viable and displayed extensive axonal branching, and were devoid of dying sensory neurons (Fig. 6A). Monitoring LC3-II protein levels, we found that unlike P5 *dt*$^{Tg4/Tg4}$ sensory neurons (Fig. 5D), P5 *PrP-dystonin-a2/PrP-dystonin-a2;dt*$^{Tg4/Tg4}$ sensory neurons exhibited a normal flux profile (Fig. 6B) (n = 2). Furthermore, EM micrographs of P5 *PrP-dystonin-a2/PrP-dystonin-a2;dt*$^{Tg4/Tg4}$ sensory neurons cultured for 5 days also showed a reduction in the number of autophagosomes, autolysosomes and abnormal mitochondria (Fig. 6D) compared to *dt*$^{Tg4/Tg4}$ sensory neurons (Fig. 3B, C, and Fig. 6E).

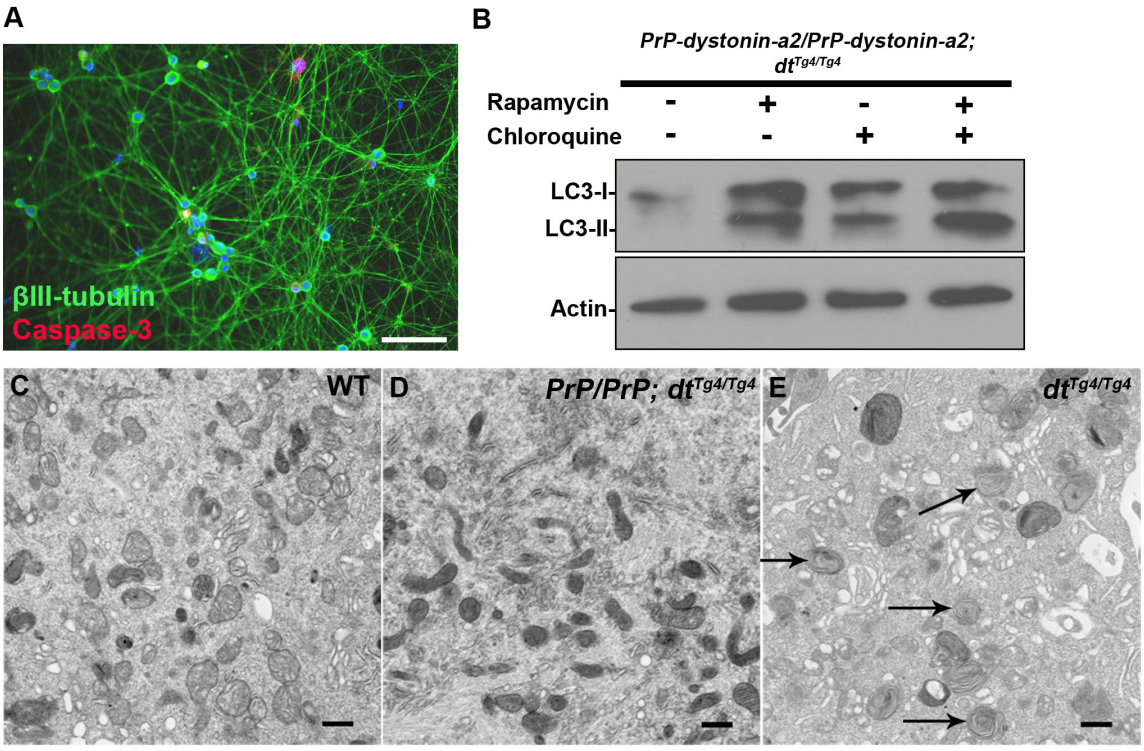

Figure 6. Restoring dystonin-a2 expression in *PrP-dystonin-a2/PrP-dystonin-a2;dt$^{Tg4/Tg4}$* sensory neurons ameliorates autophagic defects. A) Antigenic labeling for βIII-tubulin and caspase-3 indicates pre-phenotypic (P5) *PrP-dystonin-a2/PrP-dystonin-a2;dt$^{Tg4/Tg4}$* sensory neurons are mature, forming extensive neurites, and do not undergo apoptosis (scale bar, 50 μm). B) Autophagic flux in P5 *PrP-dystonin-a2/PrP-dystonin-a2;dt$^{Tg4/Tg4}$* sensory neurons proceeds normally. C) Representative EM micrographs of P5 wild type (WT) (C), *PrP-dystonin-a2/PrP-dystonin-a2;dt$^{Tg4/Tg4}$* (D), and *dt$^{Tg4/Tg4}$* (E) sensory neurons. WT and *PrP-dystonin-a2/PrP-dystonin-a2;dt$^{Tg4/Tg4}$* micrographs are free of accumulating autophagosomes, single-membraned autolysosomes, and damaged mitochondria. *dt$^{Tg4/Tg4}$* sensory neurons are replete with double-membraned autophagosomes (arrows). (Magnification 20,000X, scale bar, 500 nm).

A major substrate for autophagosome-mediated protein degradation is sequestosome p62/(SQSTM) (Pankiv et al., 2007). By binding ubiquitin and polyubiquitin, p62 provides a signal for autophagosomes to degrade superfluous long-lived proteins (Bjørkøy et al., 2005). Impairment in autophagy, in numerous *in vitro* and *in vivo* neurodegenerative models, results in the accumulation of both p62 and ubiquitin-containing aggregates (Bjørkøy et al., 2005; Johansen and Lamark, 2011; Mori et al., 2012). As such, defects in autophagic activity observed within $dt^{Tg4/Tg4}$ sensory neurons may reflect an increase in p62 and poly-ubiquitinated proteins, and this cellular pathology may be reversed in *PrP-dystonin-a2/PrP-dystonin-a2;*$dt^{Tg4/Tg4}$ sensory neurons. In accordance with previous results, protein lysates collected from P5 $dt^{Tg4/Tg4}$ primary sensory neurons cultured for 5 days exhibited significant increases in both LC3-II and p62 protein levels compared to wild type samples (Fig. 7A). In contrast, LC3-II and p62 protein levels were significantly lower in both P5 wild type and P5 *PrP-dystonin-a2/PrP-dystonin-a2;*$dt^{Tg4/Tg4}$ sensory neurons (Fig. 7A). Coupled with these results, wild type and *PrP-dystonin-a2/PrP-dystonin-a2;*$dt^{Tg4/Tg4}$ sensory neurons displayed less poly-ubiquitinated proteins compared to $dt^{Tg4/Tg4}$ sensory neurons (Fig. 7B). Taken together, these results show that dystonin-a2 is necessary for the optimal functioning of autophagy in sensory neurons.

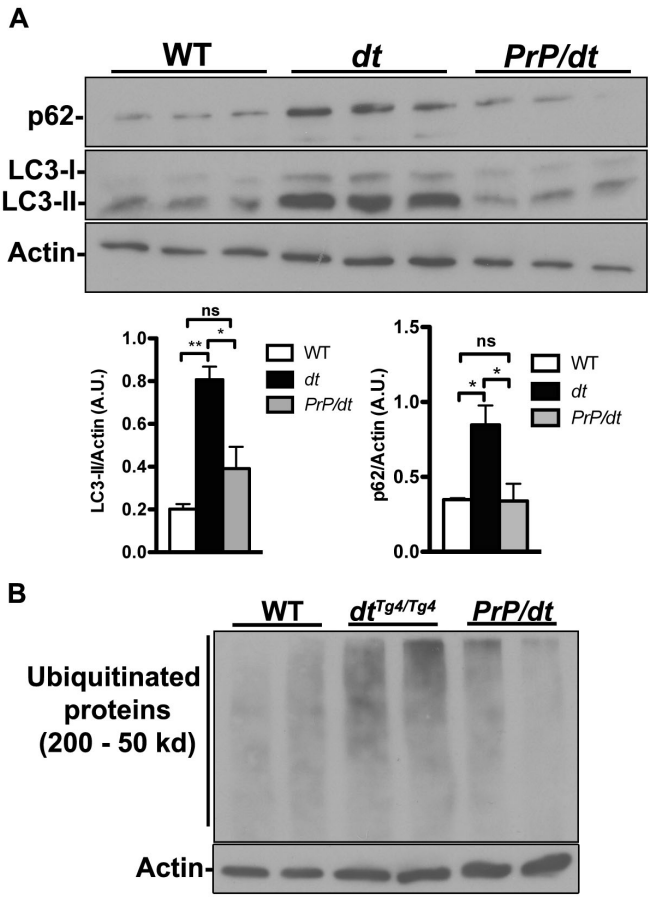

Figure 7: Pre-phenotypic (P5) *PrP-dystonin-a2/PrP-dystonin-a2;dt*$^{Tg4/Tg4}$ sensory neurons efficiently degrade the autophagosome substrate p62 and ubiquitinated proteins. A) P5 wild type (WT), *dt*$^{Tg4/Tg4}$, and *PrP-dystonin-a2/PrP-dystonin-a2;dt*$^{Tg4/Tg4}$ P5 sensory neuron lysates were analyzed by western blot for p62 and LC3-II protein levels. *dt*$^{Tg4/Tg4}$ sensory neurons show significantly increased protein levels of LC3-II compared to WT ($p < 0.01$, $n = 3$) and *PrP-dystonin-a2/PrP-dystonin-a2;dt*$^{Tg4/Tg4}$ sensory neurons ($p < 0.05$, $n = 3$). *dt*$^{Tg4/Tg4}$ sensory neurons also exhibit significant increases in p62 protein levels compared to WT and *PrP-dystonin-a2/PrP-dystonin-a2;dt*$^{Tg4/Tg4}$ sensory neurons ($p < 0.05$, $n = 3$). No significant difference in LC3-II or p62 protein levels was found between WT and *PrP-dystonin-a2/PrP-dystonin-a2;dt*$^{Tg4/Tg4}$ sensory neurons. Quantification by densitometry and normalized to actin standard; Anova, post

hoc Dunnett's *t* test; error bars represented as SEM. B) Qualitative western blot analysis indicates an increase in poly-ubiquinated proteins between 200 – 50 kDa in P5 $dt^{Tg4/Tg4}$ sensory neurons.

Dystonin-a2 does not ameliorate autophagic defects through Dynein-IC1

To address how restoring dystonin-a2 expression in $dt^{Tg4/Tg4}$ sensory neurons improves autophagy dynamics, we sought to investigate dynein-IC1 protein levels, which are reduced in $dt^{Tg4/Tg4}$ sensory neurons (Fig. 1A). Despite the improvement in autophagy functioning within *PrP-dystonin-a2/PrP-dystonin-a2;*$dt^{Tg4/Tg4}$ sensory neurons, this is not mediated through a restoration of dynein-IC1 levels (Fig. 8A). Qualitative western analysis of dynein-IC1 indicated that both P15 $dt^{Tg4/Tg4}$ and *PrP-dystonin-a2/PrP-dystonin-a2;*$dt^{Tg4/Tg4}$ DRG lysates share similar expression profiles, which are less than in wild type controls (Fig. 8A). How exogenous dystonin-a2 expression improves autophagy in $dt^{Tg4/Tg4}$ sensory neurons remains to be demonstrated.

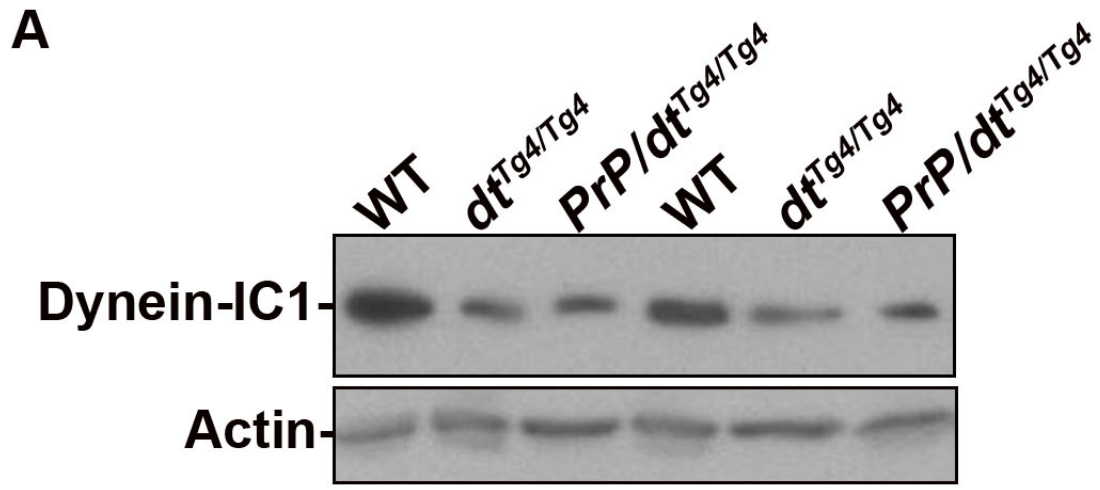

Figure 8: Exogenous dystonin-a2 expression in *PrP-dystonin-a2/PrP-dystonin-a2;dt$^{Tg4/Tg4}$* sensory neurons does not restore dynein-IC1 levels. A) P15 wild type (WT), *PrP-dystonin-a2/PrP-dystonin-a2;dt$^{Tg4/Tg4}$* and *dt$^{Tg4/Tg4}$* DRGs were analyzed by western blot analysis for restoration of dynein-IC1 expression. P15 DRG lysates from both *PrP-dystonin-a2/PrP-dystonin-a2;dt$^{Tg4/Tg4}$* and *dt$^{Tg4/Tg4}$* DRGs revealed reduced dynein-IC1 protein levels in comparison to age-matched WT controls.

Discussion

Autophagy is implicated in several neurodegenerative diseases, including Alzheimer's disease (Nixon et al., 2005; Yu et al., 2005; Boland et al., 2008), Huntington's disease (Ravikumar et al., 2002), Parkinson's disease (Stefanis et al., 2001; Webb et al., 2003), and Amyotrophic Lateral Sclerosis (Morimoto et al., 2007; Li et al., 2008). The importance of autophagy in preventing toxic protein aggregate accumulation and neurodegeneration has been unambiguously established in mice lacking ATG5 and ATG7, both of which are necessary for the activation of autophagy (Hara et al., 2006; Komatsu et al., 2006).

Autophagy is highly reliant upon stable MT filaments and MT-based motor proteins to effectively expel superfluous cytoplasmic materials (Köchl et al., 2006; Monastyrska et al., 2009; Maday et al., 2012; Ikenaka et al., 2013). Disrupting MT-based transport in neurons can lead to the accumulation of both autophagasomes and autolysosomes (Boland et al., 2008). As dystonin-a is well implicated in both these cellular properties we explored the influence dystonin-a loss-of-function imparts on the autophagy pathway.

In this study, we find $dt^{Tg4/Tg4}$ sensory neurons show impairments in the autophagy pathway. Indeed, pre-phenotypic $dt^{Tg4/Tg4}$ sensory neurons exhibit increased LC3-II protein levels coupled with accumulation of autophagosomes, autolysosomes, and damaged organelles. In addition to these pathologies are deficiencies in protein turnover, including the autophagic substrate p62, and poly-ubiquitinated proteins. We attribute these aforementioned abnormalities in $dt^{Tg4/Tg4}$ sensory neurons to compromised autophagic flux. Surprisingly, similar defects in autophagic flux were not observed in

$dt^{Tg4/Tg4}$ cortical neurons, suggesting dystonin-a loss-of-function has a cell-specific influence on the autophagy pathway. Equally surprising, is the rescue in autophagic activity observed in *PrP-dystonin-a2/PrP-dystonin-a2;*$dt^{Tg4/Tg4}$ sensory neurons. The molecular mechanism underlying this improvement remains to be demonstrated, however. Taken together, our study presents autophagy as novel pathway gone awry in the *dt* disorder, and proposes dystonin-a2 as a critical variant underlying this aberration.

How does dystonin affect autophagy?

The complex nature of dystonin-a makes elucidating the cause of autophagy impairments in $dt^{Tg4/Tg4}$ sensory neurons difficult. Indeed, both dystonin-a1 and dystonin-a2 isoforms are absent in $dt^{Tg4/Tg4}$ mice (Pool et al., 2005). As such, loss of both variants can individually influence autophagy. Dystonin-a1 is a suitable candidate for disrupting the autophagy pathway. Dystonin-a1 interacts with $p150^{Glued}$ dynactin, a critical component of the DMC, and regulates retrograde transport in sensory neurons (Liu et al., 2003c). Dynactin loss-of-function alters autophagosome trafficking and induces neurodegeneration (Ikenaka et al., 2013). Coupled with this, dystonin-a1 also recruits and anchors retrolinkin, an endosomal vesicle protein, to the DMC and ensures proper transport of endosomal vesicles (Liu et al., 2007b). Thus, the fusion of endosomes and autophagosomes (forming amphisomes), and subsequent trafficking to lysosomes for degradation could be compromised in $dt^{Tg4/Tg4}$ sensory neurons. As well, newly synthesized precursors of lysosomal hydrolases are transported via endosomes through the trans-Golgi-network to acidic lysosomes for maturation (Mizushima, 2007). It is interesting to note that our EM analyses of $dt^{Tg4/Tg4}$ sensory neurons display

autolysosomes filled with undigested amorphous cytoplasmic material, which are reminiscent of the autolysosomes seen in wild type sensory neurons when treated with the lysosomal deacidifying agent chloroquine. Taken together, dystonin-a1 loss-of-function could in theory disrupt retrograde transport of autophagic and endosomal vesicles, which in turn could disrupt the degradative and maturation capacity of the autophagy-lysosomal system.

Whether or not dystonin-a1 negatively influences autophagy remains to be demonstrated. It is clear, however, that dystonin-a2 contributes to the autophagy pathway. Restoring dystonin-a2 expression in pre-phenotypic primary $dt^{Tg4/Tg4}$ sensory neurons improves autophagic flux, reduced the number of autophagosomes, autolysosomes and damaged organelles, and normalized the protein levels of LC3-II, p62, and poly-ubiquitin. How this benefit is mediated remains enigmatic. Dystonin-a2 loss-of-function was previously shown to alter motor protein expression (Ryan et al., 2012a). As such, we sought to investigate the expression of dynein-IC1, a retrograde motor protein subunit involved in the trafficking of autophagosomes (Batlevi et al., 2010). Decreased dynein-IC1 protein level in P15 $dt^{Tg4/Tg4}$ DRGs was not restored in P15 *PrP-dystonin-a2/PrP-dystonin-a2;*$dt^{Tg4/Tg4}$ DRGs, suggesting that the improvements observed may not be mediated through dynein-IC1.

Dystonin-a2 was recently shown to interact with the microtubule-associated protein-1B (MAP-1B) (Bhanot et al., 2011; Ryan et al., 2012a). MAP1B is well implicated in aspects of autophagy; MAP1B interacts with LC3-II (Wang et al., 2006), mediates the degradation of mitochondria (Xie et al., 2011) and through interactions with the autophagic substrate Nbr1 aids in the degradation of ubiquitinated aggregate proteins

(Marchbank et al., 2012). The dystonin-a2-MAP-1B interaction in neurons maintains perinuclear MT acetylation (Ryan et al., 2012a). MT acetylation is necessary for the fusion between mature autophagosomes and lysosomes, and plays a major role in starvation-induced autophagy. (Geeraert et al., 2010; Xie et al., 2010). Finally, dystonin-a2 was ascribed a role in sustaining and modifying ER morphology (Young and Kothary, 2008; Ryan et al., 2012c). Thus, this puts dystonin-a2 as an important regulator of the endomembrane system (Ryan et al., 2012b) and putative component of the autophagy pathway. Taken together, the loss of both dystonin-a1 and dystonin-a2 likely has server consequences on autophagy.

Impaired Autophagy - a novel pathogenic mechanism of *dt* sensory neurons

Here, we show that unlike wild type or *PrP-dystonin-a2/PrP-dystonin-a2;dt*$^{Tg4/Tg4}$ sensory neurons, protein lysates and EM micrographs of pre-phenotypic *dt*$^{Tg4/Tg4}$ sensory neurons show accumulations in LC3-II proteins, autophagosomes, and autolysosomes, and as such, impaired autophagic flux. Typically, one of the first signs of altered autophagy is often an abnormal number of autophagosomes in affected neurons (Kegel et al., 2000; Nixon et al., 2005; Yang et al., 2007). The accumulation of autophagosomes and autolysosomes in *dt*$^{Tg4/Tg4}$ sensory neurons indicates that autophagosomes are capable of being formed and are able to fuse with lysosomes to form autolysosomes. Whether kinetics of autophagosome maturation and fusion with lysosomes proceeds normally in *dt*$^{Tg4/Tg4}$ sensory neurons is unclear.

There are two possible reasons why autophagosomes accumulate in pre-phenotypic *dt*$^{Tg4/Tg4}$ sensory neurons. First, autophagy is enhanced in order to meet

cellular demands, and, second, autophagosome clearance is impaired (less fusion with and degradation of autophagosomes by lysosomes). The former assertion is conceivable, as increases in p62, poly-ubiquitinated proteins, and damaged mitochondria are all known to enhance autophagy in degenerative settings (Pankiv et al., 2007; Wang and Klionsky, 2011). Furthermore, the ER-stress pathway, a known inducer of the autophagy pathway (Yorimitsu et al., 2006), is activated in *dt* sensory neurons (Young and Kothary, 2008; Ryan et al., 2012c), suggesting *dt* sensory neurons employ a canonical response during pathogenic conditions (Høyer-Hansen and Jäättelä, 2007). The second assertion is likely the reason why these aforementioned pathologies persist. Various studies indicate that changes in the properties of the cellular cytoskeleton (Monastyrska et al., 2009), motor proteins, or degradation compartments (*i.e.*, endosomes and lysosomes) alter autophagosome clearance (He and Klionsky, 2009). As dystonin-a has been ascribed a role in all of these cellular properties (Ferrier et al., 2013), impaired autophagosome clearance becomes a logical explanation for accumulating autophagosomes.

A secondary pathology of *dt* pathogenesis

As mentioned, abolition or impedance of autophagy precipitates neurodegeneration. Apoptosis of $dt^{Tg4/Tg4}$ sensory neurons occurs postnatally at P15 and is concomitant with the onset of the $dt^{Tg4/Tg4}$ phenotype (Ryan et al., 2012c). Murine sensory neurons conditionally deficient for ATG7, an autophagy-specific gene involved in the maturation and completion of autophagosomes, only begin to exhibit apoptotic sensory neurons and impaired mobility 9 months postnatally (Zhou et al., 2010). Therefore, we conclude disrupted autophagy in $dt^{Tg4/Tg4}$ sensory neurons is a secondary pathology and

does not initiate the demise of $dt^{Tg4/Tg4}$ sensory neurons. Nevertheless, accumulating autophagosomes seen in $dt^{Tg4/Tg4}$ sensory neurons may interfere with intracellular trafficking and can become a source of cytotoxic products, as seen in Alzheimer's neurons (Yu et al., 2005). Furthermore, autophagosome compartments that persist longer than usual can become leaky, and if leakage continues after lysosome fusion, the escaping of lysosomal enzymes can induce apoptosis (Yu et al., 2005).

We conclude that depletion of dystonin-a, particularly dystonin-a2, in $dt^{Tg4/Tg4}$ sensory neurons, but not cortical neurons, is responsible for the autophagic pathology. This pathology likely arises through impaired clearance of autophagic vacuoles, and autophagy induction. Therapeutic modulation of autophagy in $dt^{Tg4/Tg4}$ sensory neurons may, therefore, require targeting of late steps in the autophagic pathway.

Chapter 6

General Discussion

6.1 Dystonin and Human Disease

Outside of a single case report, no human disease associated with alterations in the *DST* gene had been reported. In a small Ashkenazi Jewish cohort (4 infants) a new hereditary and lethal sensory and autonomic neuropathy (HSAN) was identified (Edvardson et al., 2012). The disease is characterized by dysautonomic features, distal contractures, myopathic facies, severe cognitive deficits and motor retardation, and shares clinical features with the prominent HSAN, familial dysautonomia (FD), albeit, the disease is more severe and ultimately lethal. This cohort also shares similar phenotypic features to that of *dt* mice, including distal limb contractures, motor deficits and autonomic disturbances, and suggests that insight garnered from *dt* mice should enhance our understanding of this and other rare HSAN disorders.

This dystonin-related HSAN, termed HSAN-VI, arose through a frame-shift mutation in the *DST* gene starting at Glu4955 and was predicted to lead to the loss of the C-terminal 502 amino acids. The dystonin-a/b C-terminus encodes the MT-binding domain, therefore this mutation likely impacts major neuronal and muscle dystonin isoforms, but not the epithelial isoform. As patients transcript levels were not assessed the true nature of this mutation and its influence on major dystonin isoforms remains unresolved. Future studies should explore the aforementioned frame-shift mutation's biological impact on dystonin-a in an *in vitro* model system.

Dystonin expression was also assessed in cultured fibroblasts from two FD patients (Edvardson et al., 2012). FD fibroblasts displayed a six-fold increase in dystonin expression. As MT disorganization is hallmark pathology of FD neurons — and *dt*

neurons — the authors surmised that increased dystonin expression in FD cells was serving a compensatory role.

Prior to the discovery of HSAN-VI, mutations in the *DST* gene have only been reported in one case. A 4-year-old female proband was described as having a chromosomal translocation in the 3' end of the *DST* gene (Giorda et al., 2004). This breakage in the *DST* gene disrupted both the brain- and muscle-specific isoforms, but left the epithelial isoform intact. The patient's clinical features included oesophageal atresia, which was corrected at birth, non-progressive encephalopathy, severe mental and motor retardation, and delayed visual maturity. Similar to *dt* mice, this child manifested hyperreflexia, muscle hypotonia, truncal ataxia, gross motor incoordination and gait ataxia. It was suggested that haploinsufficiency may cause the patient's clinical symptoms, or that a truncated form of dystonin-a/-b could be expressed in tissues and interfere with the activity of the wild type protein, leading to a dominant negative phenotype.

The devastating nature of these mutations reflects why conditions arising through disruptions of the *DST* locus affecting neuronal and muscle isoforms have been rarely reported. As discussed, the large nature of the *DST* gene (~500 kb) should in theory increase its susceptibility to mutations and/or translocations. We attribute the few mutations in the *DST* gene to the fact that null *DST* mutations are incompatible human life. Considering the dynamic nature of the *DST* gene this assertion is conceivable. Indeed, the *DST* gene is typified by multiple-tissue specific promoters, an abundance of coding exons (> 100 exons), and alternatively spliced transcripts yielding diverse protein isoforms, each with the ability to carry out unique biological functions within different

cell types. Thus, disrupting the *DST* gene will affect multiple cellular mechanisms and, as such, have grave biological consequences on multiple tissues, and ultimately, the organism.

6.2 *Dystonia musculorum*: a multiple-isoform disorder

Nearly a decade ago, three major dystonin isoforms (brain [dystonin-a], muscle [dystonin-b], and skin [dystonin-e]) and their basic structures were elucidated (Leung et al., 2001a). Further diversity of the neuronal and muscle transcripts were described through alternative splicing of the first 5' exons producing three alternate dystonin-a/b isoforms, namely dytonin-a1/b1, dystonin-a2/b2, and dystonin-a3/b3 (Jefferson et al., 2006; Young et al., 2006). Each isoform is endowed with a unique N-terminal region, providing distinct cellular localization and unique cellular functions. A summary of the dystonin-a variants, their subcellular localization and function can be found in (Chapter 1, Fig. 1, 2).

Loss of function of neuronal dystonin-a is causal of *dt* sensory neuron degeneration. (Kothary et al., 1988; Brown et al., 1995; Guo et al., 1995; Pool et al., 2005). The disease-causing neuronal isoform(s) and their respective pathological mechanisms, however, are unresolved. As the dystonin-a/b-3 transcript can be amplified normally from $dt^{Tg4/Tg4}$ mice coupled with the fact that dystonin-a/b3 promoter and coding region lie downstream from the $dt^{Tg4/Tg4}$ deletion, it was presumed that dystonin-a/b3 unlikely contributes to the *dt* disorder. The expression of dystonin-a1/a2 isoforms, on the other hand, are affected in various *dt* alleles (Brown et al., 1995; Pool et al., 2005). As such, these isoforms were believed to be primary contributors in the demise of *dt* sensory

neurons. For various reasons dystonin-a2 was speculated as the primary driver of *dt* pathogenesis (Young and Kothary, 2007), although rigorous experimental analysis was necessary to support this claim.

My Ph.D. work addressed this query by two approaches: isoform-specific loss-of-function analyses and transgenic rescue mice that exogenously express dystonin-a2 on the $dt^{Tg4/Tg4}$ background. Our isoform-specific knockdown analyses implicated dystonin-a2 as the chief contributor of sensory neuron degeneration (Chapter 3). Indeed, we found that loss of dystonin-a2 expression disrupted organelle structure and elicited distinct pathological mechanisms, coinciding with those seen in *dt* sensory neurons. Pharmacologically blocking these pathogenic mechanisms provided only partial rescue, indicating that dystonin-a1 also contributes to *dt* pathogenesis. In support of this study, our transgenic rescue mice, which have restored dystonin-a2 expression within the nervous system, showed a partial rescue. Taken together, these studies suggest that dystonin-a2 is involved in the generation of the *dt* phenotype, however, dystonin-a1 or a yet-to-be-identified dystonin-a isoform is/are also involved in the demise of *dt* sensory neurons.

6.3 Dystonin loss-of-function affects multiple cell types and distinct populations of sensory neurons that contribute to the *dt* movement disorder

Dystonin is expressed in numerous cell types and tissues, yet dystonin loss-of-function only exhibits striking pathologies in sensory afferents and in the skin (discussed in Chapter 1). While true, we observed inconspicuous defects, which could contribute to the overt movement disorder in *dt* mice. Our work on the *dt* neuromuscular system

(Chapter 2) indicates that while *dt* motor neurons do not undergo apoptosis at phenotype stage, they do display gross morphological abnormalities distally (*e.g.*, reduced axonal arbors and NF accumulation). In addition, we note immature muscle endplates in various *dt* muscles. Whether immature endplates are the result of abnormal *dt* motor neurons or due to dystonin-b loss-of-function remains to be determined. With this in mind, conditional deletion of dystonin would provide needed insight into the tissue-specific function of dystonin and the influence individual tissues impart on the *dt* disorder. Ultimately, although *dt* sensory neurons are the primary driver of the *dt* phenotype, *dt* motor neurons likely augment the overt movement disorder.

Loss of dystonin-a expression in sensory neurons affects sub-populations of *dt* sensory neurons differently (Carlsten et al., 2001). As discussed (Chapter 5), large and medium sensory neurons are most affected by disease. Not surprisingly, these subtypes encompass proprioceptive sensory neurons, which are critical for motor coordination. Why are certain populations of sensory neurons more susceptible than others in the *dt* disorder? Is dystonin-a only necessary for the viability of certain subpopulations of sensory neurons (*i.e.*, large- and medium-sized sensory neurons), or do these neuronal populations inherently have greater physiological demands (*e.g.* metabolic demands) and, as such, contain a lower sensitivity threshold?

Interestingly, large and medium-sized sensory neurons have been demonstrated to possess exceptionally high energy demands and are therefore believed to be particularly vulnerable to vesicular and trafficking defects (Mu et al., 1993). As well, large motor and sensory neurons are more vulnerable to disease conditions than small-sized peripheral nerves (McIlwain, 1991). As dystonin-a isoforms are well documented in vesicular

trafficking, deficiencies in these pathways may underlie the demise of *dt* proprioceptive neurons. Exactly which dystonin-a isoform(s) mediate the degeneration of medium- and large-sized neurons is not yet resolved. Our work proposes that restoring dystonin-a2 expression in $dt^{Tg4/Tg4}$ sensory neurons can rescue medium-sized sensory neurons, but not large sensory neurons (Chapter 4). It is therefore plausible that dystonin-a1, or a combination of dystonin-a1 and dystonin-a2 expression is necessary for the viability of large sensory neurons. Engineering isoform-specific knockout mice would help elucidate this query.

6.4 Multiple pathways affected in the *dt* disorder converge on the endomembrane system

The vast number of cellular processes associated with cytoskeletal filaments coupled with the numerous protein isoforms generated from the *Dst* gene have made delineation of the causal pathogenic mechanisms in the *dt* disorder arduous. Our work suggests that the demise of *dt* sensory neurons most likely arises through loss-of-function of both dystonin-a1 and dystonin-a2. Exactly what mechanisms are most critical in causing disease remains undetermined. My work has found that the loss of dystonin-a2 expression imparts structural abnormalities on the ER (Chapter 3), which in turn precipitates ER-mediated pathologies (*e.g.*, Ca^{2+} dyshomeostasis and ER-stress induction) and the triggering of specific caspase activity. Previous work from our lab suggested ectopic expression of dystonin-a2 modified ER morphology through the cytoskeleton (Young et al., 2006). As such, we surmise that uncoupling of dystonin-a2,

the cytoskeleton, and the ER, may impair ER structural integrity and causes these aforementioned pathogenic mechanisms.

In a separate study we found interactions between MAP1B and dystonin-a2 maintained α-tubulin acetylation necessary for discrete organization of the Golgi complex (see Appendix). Furthermore, this interaction was essential for transport through the secretory pathway. Like dystonin-a2, dystonin-a1 also has an established role in intracellular transport. Through interactions with dynactin and the endosomal vesicle protein retrolinkin, dystonin-a1 regulates trafficking via the dynein motor complex (Liu et al., 2003b, 2007a). Taken together these studies place dystonin-a1/2 as putative players in the endomembrane system (see Appendix). The endomembrane system which encompasses the ER, Golgi, nuclear envelope (NE) and lysosomes; traffics proteins, lipids, and vesicles among organelles and the plasma membrane along microtubules and actin filaments. Aberrations in components of the endomembrane system have been associated with numerous disorders of the nervous system resulting in both cognitive and sensory-motor deficiencies (Masliah et al., 1995; Tanabe et al., 2009). From this, we believe dystonin-a1/-a2 loss-of-function provokes a complex interplay of pathological mechanisms that emerge from disruptions in the endomembrane system, rather than a single independent mechanism.

6.5 Autophagy -- a novel pathology of *dt* sensory neurons

Autophagy is essential in maintaining neuronal homeostasis. Indeed, conditional deletion of autophagy in murine neurons causes increases in poly-ubiquitinated proteins, damaged organelles and ultimately leads to neurodegeneration (Hara et al., 2006;

Komatsu et al., 2006). Our observations of autophagy indicate the autophagic pathway is not functioning optimally in *dt* sensory neurons (Chapter 5). We find *dt* sensory neurons are fortified with increased LC3-II expression (a marker for autophagosomes), accumulating autophagosomes, autolysosomes, and damaged mitochondria. The fact that autophagosomes and autolysosomes are capable of being formed within *dt* sensory neurons suggests perturbations in the pathway arise through retarded kinetics or impairments in late stages of autophagy, *i.e.*, lysosomal degradation. The former inclination (retarded kinetics) is conceivable. Deficiencies in both MT dynamics and retrograde transport via the dynein motor complex are known to negatively influence autophagy (Köchl et al., 2006; Kimura et al., 2008). Previous studies and work herein find dystonin-a isoforms essential in the maintenance of MT structural integrity (Chapter 4)(Dalpe et al., 1998; Ryan et al., 2012a) and for proper intracellular MT-based motor trafficking (Appendix)(De Repentigny et al., 2003; Liu et al., 2003b; Ryan et al., 2012a).

A second possibility as to how autophagy may be disrupted in *dt* sensory neurons may occur through disruptions in the endomembrane system. It was recently shown in sensory neurons that autophagosomes are formed and fuse with late endosomes and/or immature lysosomes distally, and mature as they progress towards the MTOC (Maday et al., 2012). As the Golgi apparatus manufactures lysosomes, and the fact dystonin-a2 loss-of-function compromises Golgi organization, disruption of the endomembrane system becomes a suitable explanation for the autophagic impairments observed in *dt* sensory neurons.

We found that restoring dystonin-a2 expression in *dt* sensory neurons ameliorates autophagic defects. It remains to be determined, however, how these improvements are

mediated. As exogenous dystonin-a2 expression in *dt* sensory neurons does not restore dynein protein levels, we suspect improved MT structural integrity (Chapter 4) may contribute to improvements in autophagic function.

The influence defective autophagy confers on *dt* pathogenesis is uncertain. We do not imagine perturbations in autophagy to be the primary driver of *dt* sensory neuron degeneration. A recent study noted that mice conditionally deficient of autophagy in sensory neurons only start manifesting abnormal movements and sensory neuron degeneration at 9 months postnatally. This is in contrast to the robust degeneration observed in *dt* sensory neurons at 15 days postnatally. Thus, autophagic defects are a secondary contributor to the *dt* disorder.

Coalescing the data in Chapter 3 and Chapter 5, a cytoprotective mechanism seen in many disease settings emerges in *dt* sensory neurons (Høyer-Hansen and Jäättelä, 2007). In Chapter 3 we propose that dystonin-a2 loss-of-function initiates Ca^{2+} dyshomeostasis and the ER-stress response. In Chapter 5 we suggest that restoration of dystonin-a2 in *dt* sensory neurons rescues autophagic defects. A plethora of studies now indicate that changes in Ca^{2+} dynamics and activation of ER stress are a potent trigger of autophagy (Høyer-Hansen and Jäättelä, 2007). Thus, dystonin-a2 loss-of-function in sensory neurons activates a canonical neuroprotective pathway during pathogenic conditions.

Conclusion and Future Directions

Dystonin-a has emerged as a critical factor in the regulation of cytoskeletal dynamics and consequently has been implicated in a number of cellular processes. Indeed, what seemed

initially a protein essential for the viability of sensory neurons in *dt* mice and capable of interacting with cytoskeletal filaments has now been demonstrated to have roles in multiple nervous system cell types (Chapter 2), anterograde and retrograde transport (Appendix 4.0, 5.0), protein processing through the secretory pathway (Appendix 4.0 , 5.0), maintenance of organelle integrity (Chapter 3, Appendix 4.0, 5.0), and regulation of the autophagy pathway (Chapter 5) (Fig. 1). It has equally been implicated in many protein-protein interactions (Young and Kothary, 2008; Bhanot et al., 2011; Ferrier et al., 2013).

Despite progress made in our understanding of the biological nature of the dystonin-a isoforms and their involvement in *dt* disease pathogenesis, much remains to be understood. For instance, while knowledge has been garnered regarding the biological functions of dystonin-a2 and its role in the *dt* disorder, a dearth of evidence exists for dystonin-a1 and -a3. Moreover, consideration of the diverse tissue expression of dystonin isoforms prompts several questions including whether these non-neuronal dystonin isoforms impart similar biological functions such as maintaining organelle integrity or assisting in cellular trafficking or stabilizing MTs. Work in this thesis suggest dystonin-a2 is not the sole contributor to *dt* pathogenesis and that dystonin-a1 and/or other undiscovered dystonin-a isoforms are pathological mediators of disease. Moreover, the biological role dystonin-a isoforms play in the autophagy pathway remains enigmatic. Further studies on these subjects will certainly provide exciting new insight into the cellular functions of dystonin and its contribution to *dt* and human pathogenesis.

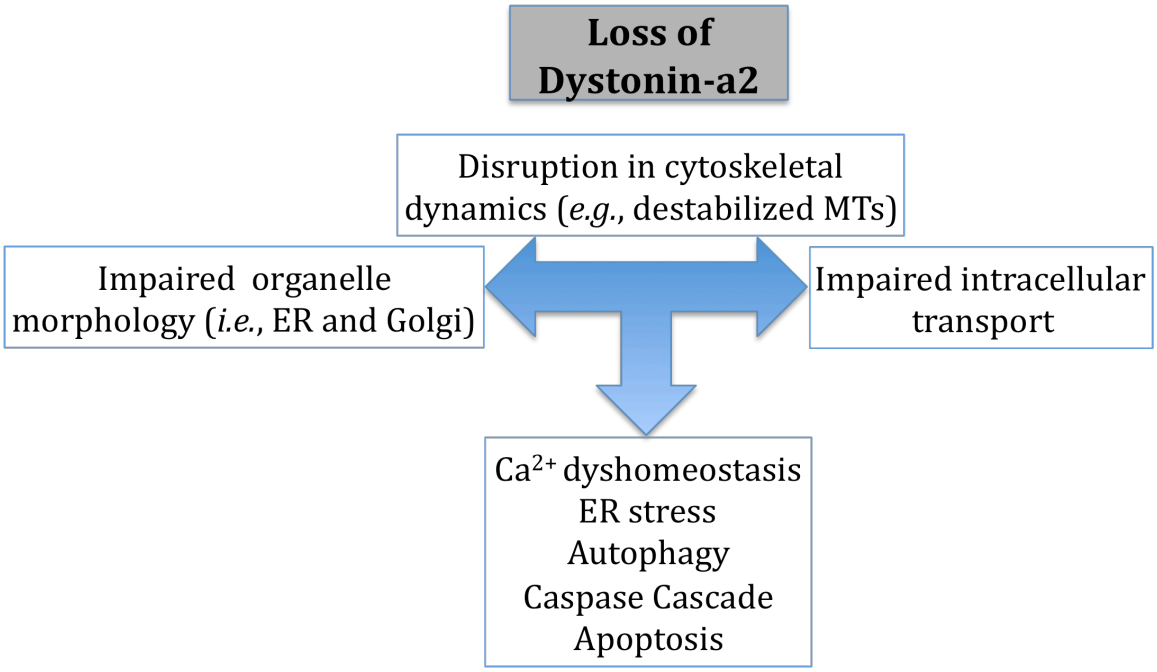

Figure 1: A proposed model as to how dystonin-a2 loss-of-function influences the demise of *dt* sensory neurons. Depletion of dystonin-a2 disrupts the acetylation status of MTs. Deacetylated MTs promote Golgi fragmentation and may also prevent anterograde trafficking of motor proteins. Depletion of dystonin-a2 results in a loss of cytoskeletal integrity that culminates in dilation of the ER. Perturbed ER homeostasis leads to a decrease in the steady-state levels of Ca^{2+} in the ER. The associated rise in free intracellular Ca^{2+} likely results in an ER-stress response and an induction of autophagy. Destabilized MTs could impede intracellular trafficking resulting in the accumulation of autophagosomes and disruption of intracellular processes (*e.g.*, intracellular transport). Perpetuation of Ca^{2+} dyshomeostasis and ER-stress can trigger caspase activation and initiate apoptosis.

Appendix

Appendix

1.0 Structural and Molecular Properties of Dystonin

1.1. Actin-Binding Domain

Several dystonin isoforms harbor an N-terminal ABD (Fig. 1B,C). The ABD is composed of a pair of calponin-homology (CH1 and CH2) domains that are reminiscent of other spectrin family proteins, such as α-actinin and dystrophin (Broderick and Winder, 2005). CH domains were first identified as part of the N-terminus of the muscle protein called calponin and are composed of approximately 100 residues that fold into four linked α-helices (Korenbaum and Rivero, 2002). Dystonin was first demonstrated to bind actin through a series of biochemical experiments (Yang et al., 1996). Subsequent studies dissected the localization of individual CH domains and the ABD (Jefferson et al., 2006; Young et al., 2006). Although a CH1 domain in isolation has the ability to bind actin, a CH1/CH2 tandem represent a functional ABD that can bind actin with greater affinity (Korenbaum and Rivero, 2002; Broderick and Winder, 2005). This holds true for dystonin where the CH1 domain of dystonin can colocalize with stress fibers but not as efficiently as the entire N-terminus composed of both CH1 and CH2 (Jefferson et al., 2006). In contrast, the CH2 domain alone does not appear to associate with actin stress fibers, and therefore, makes it unlikely that dystonin-a3, which is devoid of a CH1 domain, can bind actin stress fibers. The unique residues preceding the ABD of each dystonin-a isoform influences actin organization differently.

To date, N-termini localization studies have been performed in myoblasts or kidney cells, and lack *in vivo* validation. Perhaps performing N-terminus localization experiments in more relevant neuronal cell types or using primary dorsal root ganglion (DRG) neuronal cultures may offer valuable insight into the function of the neuronal dystonin isoforms.

1.2. Plakin Domain

The plakin domain is common to all plakin family members. It consists of two pairs of spectrin repeats separated by a putative Src-homology-3 (SH3) domain, often found in signaling molecules (Jefferson et al., 2007). The spectrin repeats within the plakin domain show weak conservation with those present in the spectrin repeat domain (Jefferson et al., 2007), suggesting that the spectrin repeats within the plakin domain have a different biological function. Simple Modular Architecture Research Tool (SMART) analysis of the dystonin proteins has revealed the presence of a putative histone deacetylase (HDAC) interacting domain that appears to be unique to dystonin (Young and Kothary, 2007). Dystonin localization studies revealed a nuclear staining pattern that led to the identification of a nuclear localization signal (NLS) within the plakin domain (Young et al., 2003a). Site-directed mutagenesis experiments to alter the NLS sequence prevented dystonin fusion proteins from localizing to the nucleus, suggesting that the NLS signal is functional. Non-sensory cells of DRG cultures that were derived from transgenic mice expressing a tagged version of the dystonin-a2 isoform also display a nuclear localization pattern (Fig. 1) (Ferrier et al., unpublished). The nuclear function of dystonin remains to be determined, however.

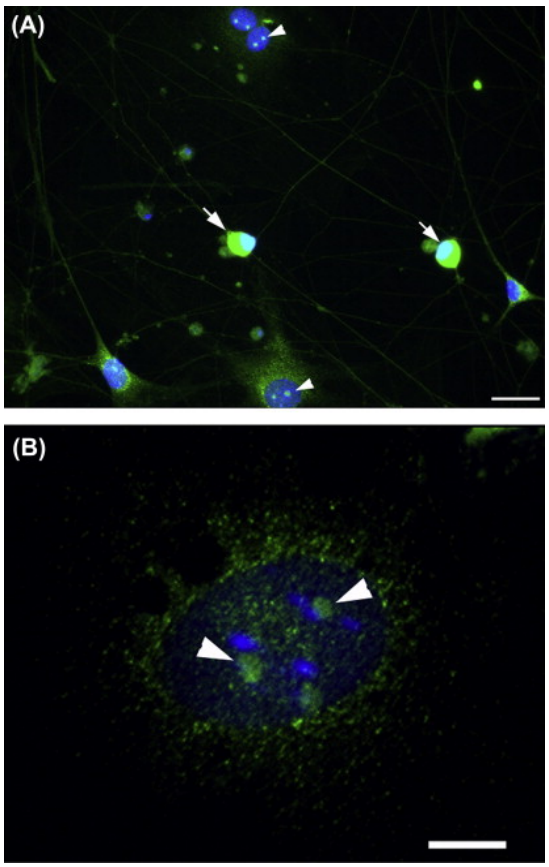

Figure 1. Dystonin-a2 localizes to the nucleus. A, B. Immunofluorescence staining of dystonin-a2-myc/his tagged fusion protein (anti-cMyc, Alexa Fluor 488) in primary DRG cell cultures. DRG cultures were derived from transgenic mice expressing dystonin-a2-myc/his tagged fusion protein under the regulation of the prion protein promoter. A punctate-staining pattern (arrow heads) is observed for dystonin-a2-myc/his fusion protein in the nucleus of nonsensory cells. Sensory cells are indicated by (arrows). Images (A, 20× and B, 40×) were visualized and analyzed with a confocal microscope (LSM 510 meta; Carl Zeiss) equipped with an EC Plan-Neofluar 40×/1.30 NA oil differential interference contrast (DIC) M27 objective using Zen 8.0 software (Carl Zeiss). The c-Myc antibody [(9E10) Antibody: sc-40)] was purchased from Santa Cruz Biotechnology. Scale bars: 20 μm for panel A and 10 μm for panel B.

Extensive association studies of the plakin domain have been performed with epithelial plakins (Jefferson et al., 2004). It is well established that the plakin domain of the dystonin-e isoform binds proteins found at hemidesmosomes (Jefferson et al., 2004). However, until recently, the function(s) of the plakin domain in neuronal isoforms was poorly understood. An interaction screen has identified novel binding partners of dystonin in the context of neuronal cells (Bhanot et al., 2011). This study demonstrated that the plakin domain of dystonin-a directly interacts with clathrin heavy chain and the MT-associated protein 1B (MAP1B). The functional relevance of the dystonin–clathrin interaction is unclear but suggests a possible role for dystonin in endocytosis and Golgi-exocytosis. A functional association has, however, been demonstrated between dystonin and MAP1B. Indeed, dystonin-a2/MAP1B interaction occurs within the centrosomal region where it maintains MT acetylation (Ryan et al., 2012a). Whether MAP2, another putative interactor of the dystonin–plakin domain, in concert with dystonin is also important in modulating MT dynamics remains to be determined. Nevertheless, the MAP1B and MAP2 interactions could put dystonin at the forefront in regulating and stabilizing MT networks.

The plakin domain of dystonin is highly homologous to that of other plakin proteins. For instance, the plakin domains of the spectraplakins dystonin and MACF share over 60% amino acid sequence homology (Bernier et al., 1996a). Therefore, the proteins identified in the dystonin interaction screen could bind other plakin domain-containing proteins such as MACF. The generation of MACF knockout mice led to the identification the protein's involvement in the Wnt signaling pathway (Chen et al., 2006). The plakin domain and the SR portions of MACF associate with β-catenin, which allows

the translocation of β-catenin into the nucleus, and thus the transcriptional activation of genes. We have found that the plakin domain of dystonin also interacts with β-catenin (Bhanot and Kothary, unpublished results). Therefore, it is plausible that dystonin shares a similar function to that of MACF with regards to the Wnt/β-catenin signaling pathway, but likely at a different developmental stage and/or in different cell types.

1.3. Spectrin Repeats

In the past few years, a subset of the plakin family members, which include dystonin and MACF, have been further categorized as spectraplakins (Roper et al., 2002; Sonnenberg and Liem, 2007; Suozzi et al., 2012a). Spectraplakins possess attributes of the plakin protein family; however, it is the addition of SRs that classifies these proteins as members of the spectrin superfamily (Suozzi et al., 2012a). SRs are three-helix bundles that repeat themselves over many times to create very large domains. Indeed, the addition of SRs in dystonin-a isoforms leads to the production of very large proteins (>600 kDa) (Roper et al., 2002; Maatta et al., 2004). In dystonin, SRs make up the coiled-coil region of the protein. The number of SRs can vary among cytolinkers from four repeats in α-actinin to 28 in multiple isoforms of dystonin (Junker et al., 1994). At the moment, the function(s) of SRs in dystonin proteins are not well defined.

Generally, SRs are thought to exert a structural role serving as a spacer domain between the N- and C-termini (Djinovic-Carugo et al., 2002). In the protein α-actinin, the SR region is necessary for dimerization (Djinovic-Carugo et al., 2002). Furthermore, the short SR domain of α-actinin is believed to provide rigidity to the molecule (Le Rumeur et al., 2012). In contrast, the large number of repeats in the dystrophin protein provides

flexibility to the protein within the costamere in muscle fibers (Broderick and Winder, 2005). A flexible structure for the neuronal isoforms of dystonin may also be envisaged given the high number of repeats present in the protein.

The SR domain of dystrophin serves as an interacting platform for structural and signaling molecules (Le Rumeur et al., 2012). The spectrin repeat domain of the neuronal dystonin-a1 (Bpag1n4) binds dynactin p150Glued, an interaction necessary for proper retrograde axonal transport (Liu et al., 2003b). Interaction studies targeting the SR region similar to those performed with the plakin domain would provide needed insight into the possible mechanical and signaling properties of dystonin.

1.4. EF Hands and GAS2 Domain (GAR)

At the carboxyl terminus of dystonin-a/b isoforms, EF hands are oriented side-by-side and can bind Ca^{2+}. The EF hands form a paired helix–loop–helix structure that induces a conformational change from closed to open upon Ca^{2+} binding (Broderick and Winder, 2005). Muscle-specific spectrin isoforms also contain an EF hand motif, however, they do not appear to bind Ca^{2+} suggesting that the EF hands of dystonin-a and dystonin-b have different functions.

Spectraplakins contain a growth arrest-specific 2 (GAS2) protein-related region (GAR) downstream of the EF hands domain. This portion of the protein makes up the MTBD domain (Sun et al., 2001b). In Drosophila, the C-terminal GAR domain of Kakapo/Shot, an invertebrate spectraplakin, interacts with the MT plus end-tracking protein (+TIP) EB1 (Subramanian et al., 2003). In immortalized kidney and myoblast mammalian cell lines, the MTBD domain provides dystonin-a1/2 fusion proteins the

ability to coalign with microtubules throughout the cytoplasm (Young et al., 2006). Cells expressing dystonin-a1 fusion proteins display bundled MTs compared to untransfected controls. Whether dystonin-a1 or -a2 interacts with proteins at the growing end (*i.e.* plus end) of MTs is not known.

2.0. Temporal and Spatial Expression of Dystonin-a in the Nervous System

In situ hybridization and immunohistochemical analyses also demonstrated dystonin-a expression embryonically (from E12.5 to E17.5) and postnatally in various cranial nerves: I (optic), II (olfactory), V (trigeminal), VII (facial), VIII (vestibulocochlear), IX (glossopharyngeal), and X (Vagus). While function in cranial nerves I, II, and VIII is maintained, cranial nerves V, VII, IX, and X all degenerate in the *dt* disorder (Bernier et al., 1995; Dowling et al., 1997). In addition to these embryonic tissues, dystonin-a expression was also present throughout embryogenesis in the neuroepithelium, neural tube, various brain stem nuclei, ventral spinal cord, sympathetic ganglia and the enteric nervous system (for complete list of tissues, see Bernier et al., 1995 and Dowling et al., 1997).

In the young brain (P10), hybridization and immunohistochemical signals of dystonin-a are diffusely observed in the cortex, in the dentate gyrus and hippocampal regions (CA1–CA3), in the thalamic nuclei, and in the granular and Purkinje cell layers of the cerebellum (Bernier et al., 1995; Dalpe et al., 1998). Despite the abnormal movement phenotype in *dt* mice, no expression of dystonin is evident in the basal ganglia, nor are there any pathologies associated with the cerebellum.

Dystonin is also expressed in tissues outside the nervous system. In the lung, dystonin-a3 is the predominant isoform, whereas in the kidney and testis, dystonin-a2 and -a3 are the major isoforms expressed. All of the differentially expressed dystonin-a exons are also expressed in the liver, spleen, and ovary, and in tissues of the embryo (E7.5 and E10.5) (Jefferson et al., 2006). Within the heart, only dystonin-b isoforms are expressed. In summary, through tissue-specific promoters, alternative splicing, and developmentally controlled expression, the *Dst* gene yields tissue-specific isoforms that exert unique biological functions. Finally, considering the number of exons within the *Dst* locus (>100 exons), it is probable that other isoforms exist.

2.1. Subcellualr localization and interactions

Dystonin-a2:

Initial studies exploring the localization pattern of dystonin-a2 N-terminal fusion proteins (unique N-terminal region plus the ABD) identified it localizing with actin stress fibers and bundled actin filaments within the perinuclear region (Young et al., 2003a, 2006; Jefferson et al., 2006). Antisera previously thought specific to dystonin-a2 detected endogenous dystonin-a2 within the nucleus (Young et al., 2003a). This anti-serum can, however, cross-react with other plakin proteins such as MACF and plectin, therefore, caution should be applied to this interpretation. Nonetheless, a functional nuclear localization signal (PVKRRRI) was demonstrated in the plakin domain of dystonin-a2. Similar findings were also found for the plakin protein family member periplakin, although, similar to dystonin, the importance of this localization remains to be determined (Van den Heuvel et al., 2002).

As discussed, dystonin-a2 interacts with the outer NE protein nesprin-3α. This interaction is facilitated through the ABD of dystonin-a2 (Wilhelmsen et al., 2005). Interestingly, nesprin-3α can recruit dystonin-a2 to the NE even if dystonin-a2 is devoid of its TM domain although loss of dystonin-a2 does not influence the localization of nesprin-3α in *dt* sensory neurons. Unlike the other nesprin family members (nesprin-1, -2, or -4), nesprin-3α connects the nucleus with the IF cytoskeleton (Ketema and Sonnenberg, 2011). The interaction between nesprin-3α and IFs is mediated through another plakin family member, plectin (Wilhelmsen et al., 2005). It is therefore conceivable that nesprin-3α can connect both IFs and MTs to the nucleus through interactions with plectin and dystonin-a, respectively. Future studies should explore whether a functional interaction between dystonin-a2 and nesprin-3α occurs in neurons.

Dystonin-a3:

As previously described, the N-terminal domain of dystonin-a3 is endowed with a single CH2 domain. As a direct consequence of its differing N-terminal domain, dystonin-a3 has weaker interactions with actin filaments than dystonin-a1/2, which carry both CH domains (Leung et al., n.d.; Yang et al., 1999; Karakesisoglou et al., 2000). N-terminal to its single-CH2 domain, dystonin-a3 harbors residues that can be potentially myristoylated (addition of a myristoyl group at N-terminal amino acids) and/or palmitoylated (attachment of fatty acids to cysteine residues). These co- and posttranslational modifications enable proteins to localize to the plasma membrane (Bologna et al., 2004; Resh, 2004; Martin et al., 2011). Indeed, truncated N-terminal dystonin-a3 fusion proteins exhibit a strong cortical localization in immortalized kidney cells (Jefferson et al., 2006). Moreover, point mutations in these putative myristoylation

or palmitoylation residues of dystonin-a3 reduce cortical localization. Unlike other dystonin-a isoforms, however, dystonin-a3 has not been demonstrated to have high-affinity interactions with cytoskeletal elements. That said, to date, there have been no studies investigating full-length dystonin-a3 localization and function in neuronal and nonneuronal cells. At the C-terminal region, dystonin-a3 encodes both a GAR domain and a glycine–serine–arginine domain, which are capable of binding MTs (Sun et al., 2001b). The latter domain has been demonstrated to interact with the +TIP protein EB1 (Slep et al., 2005). Future studies should explore the biological role of full-length dystonin-a3 at the plasma membrane in neuronal cells.

Coupled with the above studies on the various dystonin-a isoforms was the finding that the plakin domain of dystonin-a interacts with the protein clathrin in brain tissues (Bhanot et al., 2011). Clathrin is a protein involved in the coating of newly developed vesicles during both endocytosis and Golgi-exocytosis, and utilizes the actin cytoskeleton in these processes (Yarar et al., 2005; Galletta et al., 2010). This suggests that dystonin may play a role in linking clathrin-coated vesicles with the cytoskeleton. Moreover, the fact that clathrin-coated vesicles eventually shed their coat, fuse with endosomes (a compartment dystonin-a1 has been shown to associate with) and proceed down the endocytic pathway raises interesting possibilities. Namely, because all dystonin-a isoforms share the plakin domain and localize differently throughout the cell, it seems possible they may all participate at different points in both the endocytic and secretory pathways (Chapter 1, Fig. 3). For example, dystonin-a3 or dystonin-a1, both of which localize to the plasma membrane, may assist clathrin in the invagination process of immature vesicles, and subsequently the trafficking and fusion with endosomes. In

contrast, dystonin-a2, which localizes to both the ER and Golgi membranes, may serve a role in the development and transport of membrane compartments in the secretory pathway. This could occur through an interaction with clathrin at the Golgi apparatus or with neurobeachin, a putative interactor with the dystonin-a plakin domain and a protein believed to modulate post-Golgi membrane targeting, vesicle biogenesis and trafficking, and exocytosis (Wang et al., 2000; Su et al., 2004; Bhanot et al., 2011).

3.0 *dt* mouse strains:

Although all the aforementioned mutant strains share similar phenotypic and pathological features, differences do exist, particularly at the genetic level. Notably, the dt^{Alb} strain results from a deletion–insertion that disrupts exons 12 through 46 (Fig. 1A) (Goryunov et al., 2007). This deletion impacts the coding sequence of the plakin domain, the CC rod, both IFBD domains (or PRD domains), and portions of the SRs (Pool et al., 2005; Goryunov et al., 2007). As the plakin domain is common among all dystonin isoforms, the dt^{Alb} mutation results in a null mutation for all dystonin isoforms in both neural and muscle tissues.

Other differences existing between *dt* strains, albeit subtle, are severity and survival. For instance, the initial *dt* strain discovered in Edinburgh (Duchen et al., 1964) survived longer—weeks, in fact—than that of the initial Jackson laboratory dt^{J} mutant (Duchen, 1976). Our work with the $dt^{Tg4/Tg4}$ and dt^{27J} strains shows the dt^{27J} strain to exhibit a more severe phenotype (*i.e.* more overt locomotor deficits) and to succumb to lethality days earlier (unpublished observation). Work on several *dt* alleles has produced conflicting results (Tseng et al., 2006; Young et al., 2007), and it remains possible that

discrepancies between *dt* strains may arise through differing genetic backgrounds and/or through the varied impact of mutations on dystonin-a isoforms. Indeed, the dt^{27J} mutation is known to disrupt expression of all three dystonin-a isoforms, whereas $dt^{Tg4/Tg4}$ interferes only with the expression of dystonin-a1/2.

3.1. Cell types affected in the *dt* disorder:

Myelination defects are another well-documented pathology of *dt* mice and were initially considered responsible for the noted peripheral neuropathy (Moss, 1981-a, 1981-b). Abnormal myelination is present in both peripheral and central nerves, however, defects are more pronounced in peripheral nerves (Bernier et al., 1998; Saulnier et al., 2002). The peripheral nerve myelination abnormalities in *dt* mice are autonomous to Schwann cells, and are not instigated via degenerating axons. Indeed, loss of dystonin expression in Schwann cells results in disorganized cytoskeletal elements, and likely underlies abnormal Schwann cell myelination. As Schwann cells undergo extensive cytoskeletal rearrangements before and during axon ensheathment (Mirsky and Jessen, 1999), and given that dystonin-a is involved in cytoarchitecture maintenance, it is possible that loss of dystonin perturbs cytoskeletal-driven axon ensheathment. Speculation aside, Schwann cells can ultimately be only contributors to the *dt* disorder as sensory neuron degeneration commences before the Schwann cell myelination process (Campbell and Peterson, 1992; Bernier and Kothary, 1998).

4.0. A novel role for the cytoskeletal linker protein dystonin in the maintenance of microtubule stability and the regulation of ER-Golgi transport

Andrew Ferrier, 1, 2, † Scott D. Ryan, 1, † and Rashmi Kothary 1, 2, 3, *

[1]Ottawa Hospital Research Institute; Ottawa, ON Canada

[2]Department of Cellular and Molecular Medicine; University of Ottawa; Ottawa, ON Canada

[3]Department of Medicine; University of Ottawa; Ottawa, ON Canada

[†]These authors contributed equally to this work.

[*]Correspondence to: Rashmi Kothary

Keywords: Golgi, cytoskeleton, dystonin, endoplasmic reticulum, neuron, transport

This work was published in the Journal *Bioarchitecture*. 2012 January 1; 2(1): 2–5.

Author Contributions

Conceived and designed the experiments: AF, SR, RK. Performed the experiments: AF (figures 1) SR (figure 1). Analyzed the data: SR, RK. Contributed reagents/materials/analysis tools: AF, SR, RK. Wrote the paper: AF, SR, RK.

Abstract

Crosslinking proteins maintain organelle structure and facilitate their function through the crosslinking of cytoskeletal elements. We recently found an interaction between the giant crosslinking protein dystonin-a2 and the microtubule-associated protein-1B (MAP1B), occurring in the centrosomal region of the cell. In addition, we showed that this interaction is necessary to maintain microtubule acetylation. Loss of dystonin-a2 disrupts MT stability, Golgi organization, and flux through the secretory pathway. This, coupled to our recent finding that dystonin-a2 is critical in maintaining endoplasmic reticulum (ER) structure and function, provides novel insight into the importance of dystonin in maintenance of organelle structure and in facilitating intracellular transport. These results highlight the importance of cytoskeletal dynamics in communicating signals between organelle membranes and the cytoskeleton. Importantly, they demonstrate how defects in cytoskeletal dynamics can translate into a failure of vesicular trafficking associated with neurodegenerative disease.

Keywords: Golgi, cytoskeleton, dystonin, endoplasmic reticulum, neuron, transport

Introduction

Cytoskeletal cross-linker proteins have been the focus of much attention in disorders of the sensory-motor system. While much investigation has focused on understanding the role of the giant cytoskeletal linker protein dystonin, the daunting size of the protein coupled to the numerous protein isoforms generated from the dystonin (*Dst*) gene have made elucidation of divergent isoform functions arduous. In the recent article Microtubule stability, Golgi organization, and transport flux require dystonin-a2/MAP1B interaction (Ryan et al., 2012a), we highlight a novel function of the dystonin-a2 isoform in mediating Golgi organization and flux through the secretory pathway. We have previously determined that the dystonin-a2 isoform is anchored at the nuclear envelope, and is involved in organization of membranous structures of the ER (Young et al., 2003a, 2006; Young and Kothary, 2008; Ryan et al., 2012c). We have now performed expression profiling of pre-phenotype stage dystonin null dorsal root ganglia and isoform-specific loss of function analysis to evaluate the role of dystonin in flux through the secretory pathway. We find defects in anterograde transport and secretion coincident with ultrastructural dilation of the Golgi complex and loss of MT acetylation resulting from depletion of the dystonin-a2 isoform. Through interaction with MAP1B, dystonin-a2 maintains perinuclear acetylation of α-tubulin necessary for discrete organization of the Golgi complex. Maintenance of MT acetylation status through chemical inhibition of deacetylation or MAP1B overexpression, maintains Golgi structure following dystonin-a2 loss, normalizing flux through the secretory pathway. Moreover, dystonin-a2 was found to be critical for MAP1B localization at the centrosome. Collectively, our recent

work identifies dystonin-a2 as a novel regulator of ER-Golgi transport through structural organization of the endomembrane system.

Dystonin as a regulator of ER-Golgi transport

The endomembrane system (consisting of the ER, Golgi, nuclear envelope (NE) and lysosomes) traffics proteins and lipids among organelles and the plasma membrane along microtubules and actin filaments. Aberrations in components of the endomembrane system have been associated with numerous disorders of the nervous system resulting in both cognitive and sensory-motor deficiencies (Tanabe et al., 2009; Shore et al., 2011). Our recent findings offer an improved understanding of the bridge connecting newly formed transport vesicles and the cytoskeleton that may offer important insight into the underlying cause of sensory-motor pathologies. We find dystonin-a2 critical to maintenance of transport flux by maintaining the structural organization of both the ER and Golgi (Ryan et al., 2012a, 2012c) We further find this effect to be conserved across multiple dystonia musculorum (*dt*) mutant alleles.

dt is an inherited homozygous recessive sensory neuropathy, which results in a severe form of ataxia in mice. Mutations in the *Dst* gene underlie the *dt* disorder. There exist several *dt* alleles, including those induced through spontaneous mutations (*e.g.*, dt^{27J}) or through transgene insertion (*e.g.*, dt^{Tg4}) (Pool et al., 2005). As both dt^{Tg4} and dt^{27J} alleles are allelic and do not complement, the nature of their mutations impacts the expression of dystonin isoforms differently (Kothary et al., 1988; Pool et al., 2005) The dt^{Tg4} mutation prevents the expression of two dystonin isoforms, dystonin-a1 and -a2;

while the dt^{27J} mutation disrupts the expression of all three dystonin isoforms, dystonin-a1, -a2 and -a3 (Kothary et al., 1988; Pool et al., 2005).

We report here, consistent with our findings in dt^{27J} spontaneous mutant mice, that a second *dt* allele, the transgenic dt^{Tg4} mouse, displays similar deficits in secretion and Golgi organization (Fig. 1). A failure in transport flux results from defective ER-Golgi transport emanating from aberrant organization of the endomembrane system. Dystonin-a2 is a giant cytoskeletal linker protein flanked by an N-terminal transmembrane domain and a C-terminal microtubule binding domain. The transmembrane domain of dystonin-a2 positions the protein in the perinuclear membranes of the ER, Golgi and NE. The microtubule binding domain of dystonin anchors these membranes to the microtubular cytoskeleton. This maintains the organization of the Golgi around the microtubule organizing complex (MTOC) and centrosome (Fig. 2). Ultrastructural and macrostructural evaluation of the Golgi revealed both the dispersal of Golgi ribbons in addition to the dilation of Golgi vesicles in the absence of dystonin-a2. We also observed ultrastructural defects in the ER of dt^{27J} sensory neurons (Ryan et al., 2012c), which preceded phenotype onset. We believe these structural abnormalities arise through impaired cytoskeletal dynamics. Support for this notion comes from previous studies wherein ectopic expression of dystonin-a2 localizes with both ER and Golgi protein markers, and re-organizes the ER via cytoskeletal filaments (Young and Kothary, 2008). At the NE, the dystonin-a2 isoform associates with the NE protein nesprin 3α. However, ultrastructural analysis of the NE has not revealed any gross changes in NE structure (data not shown). As such, the cellular role of dystonin-a2 at the NE does not appear to involve structural maintenance. Rather, dystonin-a2 recruits various

cytoskeletal elements to the NE (Young et al., 2003a, 2006). Perturbation of this connection between the NE and cytoskeleton may underlie the eccentric nuclei observed in dystonin deficient sensory neurons (Duchen et al., 1964; Sotelo and Guenet, 1988) and may yet prove to be essential to intracellular communication via the endomembrane system. We propose a novel function for dystonin-a2 in the regulation of ER-Golgi transport though binding and sequestration, or in some instances activation, of multiple proteins required for normal transport flux. We find dystonin-a2 to functionally interact with multiple proteins critical to ER-Golgi transport (Bhanot et al., 2011). Through interaction with MAP1B (centrosome), clathrin (Golgi), nesprin 3α (NE), neurobeachin (lysosomes) and CLIP-170 (polymerizing microtubules) (Ryan et al., 2012a), or direct anchoring of membranes via the N-terminal transmembrane domain, dystonin modulates activity of proteins critical to proper vesicular transport between every organelle of the endomembrane system. The full extent of this protein interaction network and its importance to cellular communication in both neuronal and non-neuronal systems remains to be elucidated.

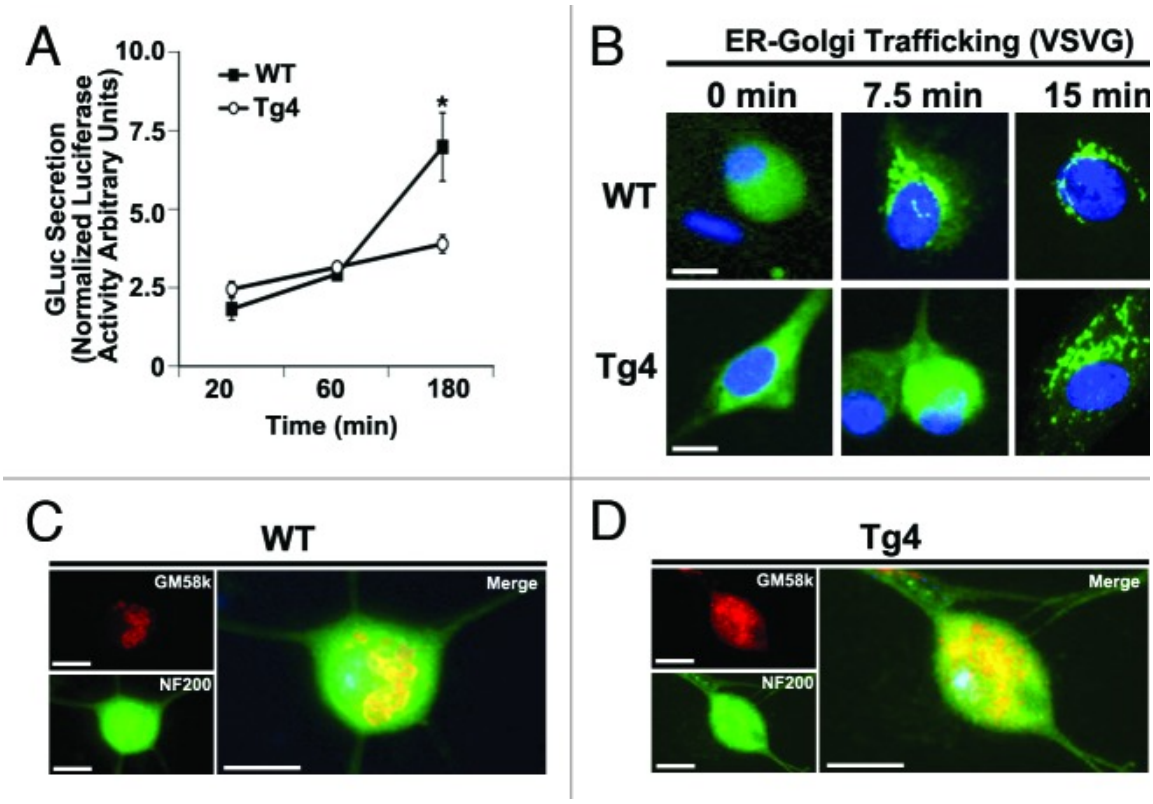

Figure 1. Transport flux in *dt*^{Tg4} sensory neurons is impeded. (A) Flux through the secretory pathway was assessed in primary sensory neurons. Secreted gaussia luciferase (GLuc) was delivered to WT and *dt*^{Tg4} sensory neurons, and its secretion was monitored by measuring luciferase activity in the medium over time. Data were normalized to non-secreted firefly luciferase. *dt*^{Tg4} neurons show a decrease in flux through the secretory pathway relative to WT sensory neurons, (anova post hoc Tukey, *$p < 0.05$, $n = 3$). (B) Defective trafficking of VSVGts0–45 (VSVG) from the ER to the Golgi was observed in *dt*^{Tg4} sensory neurons relative to WT. (C) WT sensory neurons labeled with the Golgi marker GM58K show a discrete perinuclear organization of the Golgi. *dt*^{Tg4} neurons show fragmented Golgi through the cytoplasm. Scale bars are 10 μm.

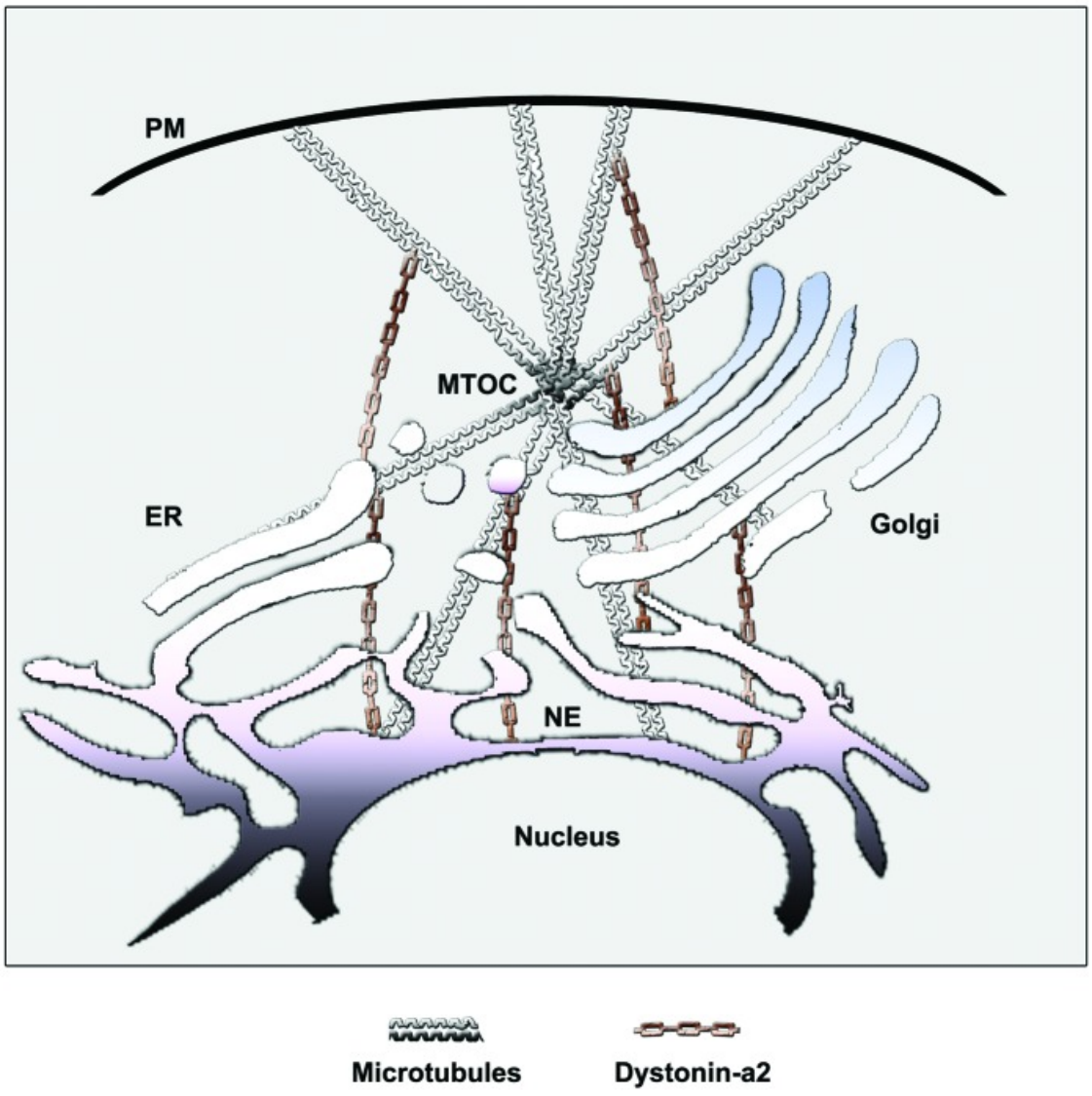

Figure 2. The role of dystonin-a2 in organization of ER-Golgi membranes.

Schematic illustration of dystonin-a2 as an anchor of the endomembrane system. Dystonin-a2 links the perinuclear membrane of the ER, Golgi and NE to the microtubular cytoskeleton. This maintains the organization of the Golgi around the microtubule organizing complex (MTOC) and facilitates transport flux from the ER to the Golgi.

Dystonin-a2: A transducer of second messenger signaling?

Our analyses of dystonin-a2 focused on the neuronal cell soma, where we find dystonin-a2 critically associates with the ER, Golgi and NE. Within the soma, rough ER sheets and cis-Golgi elements are most prominent, and are involved in protein synthesis, trafficking, quality control, and post-translational modification (Renvoise and Blackstone, 2010). Through modulation of organelle structure, we find dystonin-a2 to be critically linked to second messenger signal transduction. Ultrastructural aberrations in ER morphology following dystonin loss were evaluated for their impact on ER function. We found that primary sensory neurons derived from dt^{27J} mice show perturbations in both Ca^{2+} homeostasis (*i.e.*, defective efflux of Ca^{2+} from the ER) and protein quality-control (*i.e.*, activation of the unfolded protein response) (Ryan et al., 2012a). While this study provided important insight into the cellular functions of dystonin-a2, it suggests dystonin-a2 may act as a link between endomembrane system function and apoptosis. Maintenance of transport flux between the ER and Golgi is critical to neuronal function. As transport defects are associated with numerous neurodegenerative diseases, these processes must be tightly regulated and mechanisms must exist to translate defects in orthograde transport into apoptotic messages. Maintenance of ER Ca^{2+} homeostasis may represent one avenue through which these signals are transduced. It remains to be determined, however, whether aberrant ER morphology is causal of Ca^{2+} dyshomeostasis or whether dystonin-a2 interacts with other ER-proteins capable of regulating calcium mobilization.

Conclusion

Dystonin proteins have been implicated in a variety of cellular processes, including processing of proteins through secretory pathways, transport of organelles along neuronal processes, and maintaining cytoskeletal integrity. Their broad involvement in cellular mechanisms can be explained by the importance of cytoskeletal dynamics and the role these proteins have in communicating signals between membranes and the cytoskeleton. While the role we highlight herein for dystonin-a2 in ER-Golgi transport is novel, it is also intuitive given the integral role the cytoskeleton plays in maintaining the structure and function of membrane organelles. Dystonin-a2 is primarily expressed in sensory neurons of the peripheral nervous system. A majority of our work has focused on the role of dystonin isoforms in post-mitotic neurons. The diverse expression of dystonin isoforms in dividing cells of the skeletal muscle and epithelial cell lineages prompts intriguing questions on the role of dystonin in endomembrane organelles at multiple stages of the cell cycle. It would be interesting to assess the impact loss of dystonin has on the integrity of organelles (*i.e.*, ER, Golgi and NE) in dividing cells. Understanding the common functions of dystonin proteins in multiple cell systems will provide critical insight into the role of ER/Golgi/NE cytoskeletal interactions in maintaining cell integrity.

Acknowledgments

We thank Kunal Bhanot for technical assistance with experiments depicted herein. This work was supported by a grant from the Canadian Institutes of Health Research (CIHR), and a Multiple Sclerosis Society of Canada Research Fellowship and a CIHR Fellowship

to S.D.R. with the support of the Dystonia Medical Research Foundation of Canada. A.F. is supported by an Ontario Graduate Scholarship (OGS). R.K. is a recipient of a University Health Research Chair from the University of Ottawa.

Abbreviations: *dt* dystonia musculorum**,** ER endoplasmic reticulum**,** MAP1B microtubule-associated protein-1B**,** MTOC microtubule organizing complex**,** NE nuclear envelope, UPR, unfolded protein response

5.0. Microtubule stability, Golgi organization, and transport flux require dystonin-a2/MAP1B interaction

Scott D. Ryan[1], Kunal Bhanot[1], Andrew Ferrier[1,3], Yves De Repentigny[1], Alphonse Chu[2], Alexandre Blais[2], and Rashmi Kothary[1,3,4#]

[1]Ottawa Hospital Research Institute, Ottawa, Ontario, Canada K1H 8L6;

[2]Department of Biochemistry, Microbiology, and Immunology, University of Ottawa, Ottawa, Ontario, Canada K1H 8M5; [3]Department of Cellular and Molecular Medicine, University of Ottawa, Ottawa, Ontario, Canada K1H 8M5;

[4]Department of Medicine, University of Ottawa, Ottawa, Ontario, Canada K1H 8M5

Running head: Dystonin-a2 facilitates anterograde transport

eTOC summary statement: "Loss of interaction between the dystonin-a2 isoform and the microtubule-associated protein MAP1B induces microtubule instability and trafficking defects that may underlie certain neuropathies."

Characters: 38278

Ms. No. 201107096, Submission Jan 20th 2012.

#Correspondence to: Rashmi Kothary

Key words: dystonin, golgi, transport, sensory neuron, MAP1B

Author Contributions

Conceived and designed the experiments: AF RK. Performed the experiments: SR, KB, AF (figures 2D-F, S3, 9). Analyzed the data: SR, KB, AF, AC, AB, RK. Contributed reagents/materials/analysis tools: YDR, AC, AB. Wrote the paper: SR, RK.

Abstract

Loss of function of dystonin cytoskeletal linker proteins causes neurodegeneration in dystonia musculorum (*dt*) mutant mice. Although much investigation has focused on understanding *dt* pathology, the diverse cellular functions of dystonin isoforms remain poorly characterized. Here, we highlight novel functions of the dystonin-a2 isoform in mediating microtubule (MT) stability, Golgi organization, and flux through the secretory pathway. Using dystonin mutant mice combined with isoform-specific loss-of-function analysis, we found dystonin-a2 bound to MT-associated protein 1B (MAP1B) in the centrosomal region where it maintained MT acetylation. In *dt* neurons, absence of MAP1B-dystonin-a2 interaction resulted in altered MAP1B perikaryal localization, leading to MT deacetylation and instability. Deacetylated MT accumulation resulted in Golgi fragmentation and prevented anterograde trafficking via motor proteins. Maintenance of MT acetylation through trichostatin A (TSA) administration or MAP1B overexpression mitigated the observed defect. These cellular aberrations are apparent in pre-phenotype dorsal root ganglia (DRG) and primary sensory neurons from *dt* mice, suggesting they are causal in the disorder.

Introduction

Dystonia musculorum (*dt*) is an inherited homozygous recessive sensory neuropathy in mice caused by mutations in the dystonin (*Dst*) gene (Duchen et al., 1964; Brown et al., 1995). In early postnatal development, *dt* mice lose control of the fore limbs, hind limbs, and trunk, and subsequently die of unknown causes (Duchen, 1976). The *Dst* gene is remarkably large (~400 kb in mice) and gives rise to three tissue-specific dystonin isoforms, namely dystonin-e (epithelial isoform, ~315 kDa), dystonin-b (muscle isoform, ~834 kDa), and dystonin-a (neuronal isoform, ~615 kDa) (Sawamura et al., 1991; Brown et al., 1995; Leung et al., 2001c; Okumura et al., 2002). While dystonin-e serves as an auto-antigen in the skin blistering disease Bullous Pemphigoid, loss of function of a dystonin-a isoform or isoforms is believed to be causal in the *dt* disorder (Kothary et al., 1988; Sawamura et al., 1991; Brown et al., 1995; Pool et al., 2005). Three neuronal isoforms are derived through alternative splicing, namely dystonin-a1, dystonin-a2, and dystonin-a3 (Young and Kothary, 2007). These isoforms share an N-terminal actin binding domain, an extensive coiled-coil region, and a C-terminal MT-binding domain, allowing for interactions with cytoskeletal filaments and facilitating their function as cytoskeletal linkers (Leung et al., 2001b). While the dystonin-a isoforms share similar domain architecture, it is their unique N-terminal regions that differentiate them and dictate their sub-cellular localization. Specifically, dystonin-a1 encodes a short N-terminal domain that includes an actin-binding domain localizing it to actin filaments, while dystonin-a2 possesses a transmembrane domain localizing it to the nuclear envelope and perinuclear membranes, and dystonin-a3 possesses a putative myristoylation domain, aiding in anchoring to the plasma membrane (Jefferson et al.,

2006; Young et al., 2006). Loss of the neuronal dystonin isoforms has been attributed to degeneration of both sensory and motor neurons (Brown et al., 1995; Guo et al., 1995; De Repentigny et al., 2011).

Several *dt* alleles exist through spontaneous mutations (dt^{27J}, dt^{Alb}), chemically induced mutations (dt^{37J}, dt^{33J}), targeted alleles (dt^{tm1Efu}), and transgenic insertions (dt^{Tg4}) (Pool et al., 2005). While only three *dt* mutations (dt^{Tg4}, dt^{tm1Efu}, and dt^{Alb}) have been characterized at the DNA level, dt^{Tg4} and dt^{27J} are allelic and do not complement (Kothary et al., 1988; Guo et al., 1995; Bernier et al., 1998). To date, *dt* pathologies have been recorded in motor neurons, skeletal muscle, and Schwann cells, but degeneration is most prominent in DRG sensory neurons (Dowling et al., 1997; Bernier et al., 1998; Dalpe et al., 1999; De Repentigny et al., 2011). While *dt* pathology has been thoroughly examined, evidence explaining the mechanisms of *dt* pathogenesis remain elusive. Moreover, it is unresolved as to whether loss of a single isoform or combination of isoforms is responsible for the neurodegeneration.

The consensus regarding this degenerative event is that it arises due to loss of structural organization of cytoskeletal elements (Yang et al., 1996, 1999). The numerous functions of the cytoskeleton have made elucidating the mechanism underlying *dt* pathogenesis challenging. The present study therefore aims to elucidate the mechanism of sensory neuron degeneration underlying *dt* pathogenesis to further our understanding of the diverging functions of dystonin isoforms. We have previously determined that the dystonin-a2 isoform is involved in nuclear envelope structuring, nuclear tethering, and organization of membranous structures surrounding the nucleus (Young et al., 2003a, 2006; Young and Kothary, 2008). Here, we employ expression profiling of pre-

phenotype DRGs to identify early aberrations in biological processes. We find defects in anterograde transport and secretion coupled with ultrastructural dilation of the Golgi complex and loss of MT acetylation that precede phenotype onset. Through isoform-specific loss of function analysis, we identify a novel role for the dystonin-a2 isoform in mediating MT acetylation and stability. Through interaction with the MT associated protein MAP1B, dystonin-a2 maintains perinuclear acetylation of α-tubulin necessary for discrete organization of the Golgi complex. Maintenance of MT acetylation status through chemical inhibition of deacetylation or MAP1B overexpression, maintains Golgi structure following dystonin-a2 loss, normalizing flux through the secretory pathway. Moreover, dystonin-a2 is critical for MAP1B localization at the centrosome. Taken together, these findings provide needed insight into how aberrant cytoskeletal linkage may participate in dysfunctional neuronal signalling in multiple neurodegenerative pathologies and identify a novel function for the dystonin-a2 protein.

Results

To gain a better understanding of the mechanism underlying the specific pathological decline of *dt* sensory neurons, we first conducted expression profiling of DRGs from pre-phenotype WT and dt^{27J} mice. Differentially expressed genes were clustered based on Gene Ontology (GO) and enrichment analysis of those biological processes among up-regulated (1580 genes) or down regulated (1809 genes) genes was preformed to identify early changes in cellular processes that may predict mechanistic functions of dystonin proteins (Fig 1). Not surprisingly, several processes associated with cytoskeletal organization were aberrant, including MT polymerization and axon guidance. In addition, there was indication of early apoptotic signal transduction coupled with enhanced cell cycle and differentiation, likely to compensate for cyto-degeneration. The most significantly down-regulated biological process in pre-phenotype dt^{27J} DRGs, however, was transport (Fig 1). We thus sought to determine whether this expression profile translated into impairment of intracellular transport and a role for dystonin isoforms in mediating vesicle trafficking.

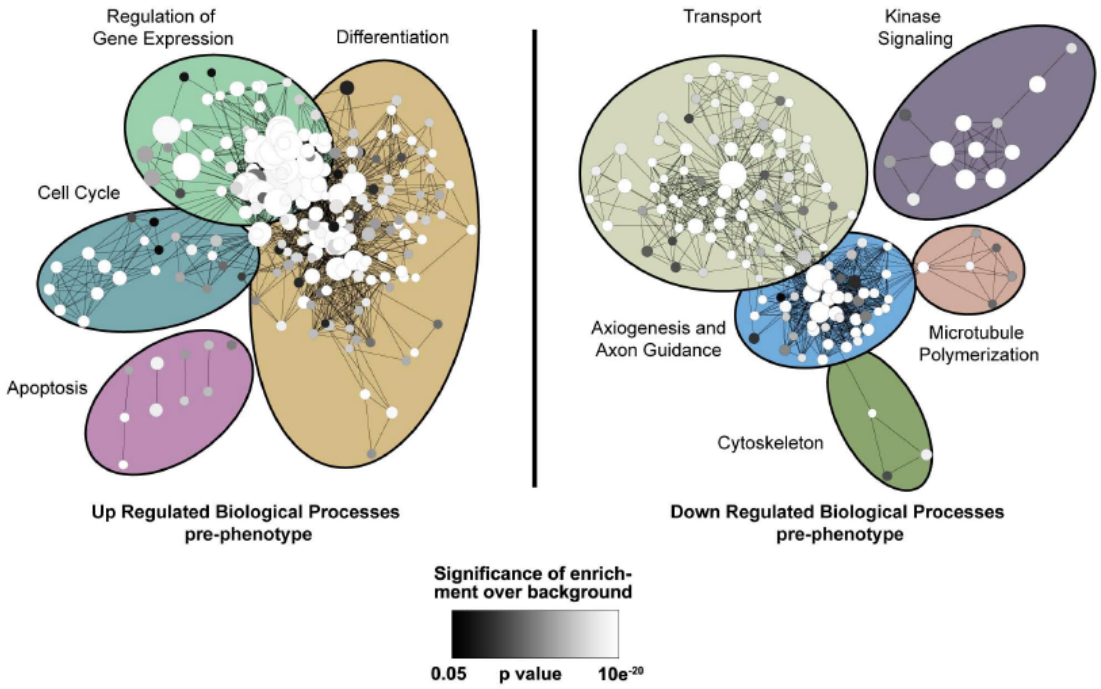

Figure 1: Gene Ontology enrichment map of biological processes altered in pre-phenotype *dt*^{27J} mice. mRNA expression profiling P4 WT (n=3) and *dt*^{27J} (n=3) DRGs. Genes were clustered based on GO term and an enrichment map of those biological processes up-regulated (left panel) or down regulated (right panel) in pre-phenotype *dt*^{27J} DRGs relative to WT littermates is depicted. Each node represents one GO term. The node size represents the number of genes clustered to each GO term, node color reflects the significance of the enrichment above the background of the entire mouse genome (white most significant, black least significant, significance cut is $p<0.05$, Fisher's exact test) and edge length reflects the similarity between GO terms. Clusters of functionally related gene-sets were manually circled and assigned a label representative of the overall biological process. The most significantly down regulated biological process in pre-phenotype *dt*^{27J} *DRGs* is transport.

Analysis of the specific biological processes (Table 1) altered within the enriched transport cluster lead us to focus on anterograde transport and components of the secretory pathway. Indeed, protein validation of down regulated target genes indicated that expression of components of the kinesin motor complex (Fig S1) were in fact, decreased in dt^{27J} DRGs. We thus assessed flux through the secretory pathway in primary sensory neurons from pre-phenotype (P4) and phenotype (P15) stage dt^{27J} mice (Fig 2A-C). Lentiviral vector encoding the secreted YFP-Gaussia luciferase (GLuc) was delivered to cells, and GLuc secretion was monitored by measuring luciferase activity in the medium over time. P4 and P15 dt^{27J} neurons show a decrease in flux through the secretory pathway relative to WT sensory neurons (Fig 2B-C), indicating that an impairment of protein transport exists in *dt* sensory neurons prior to phenotype onset in mice.

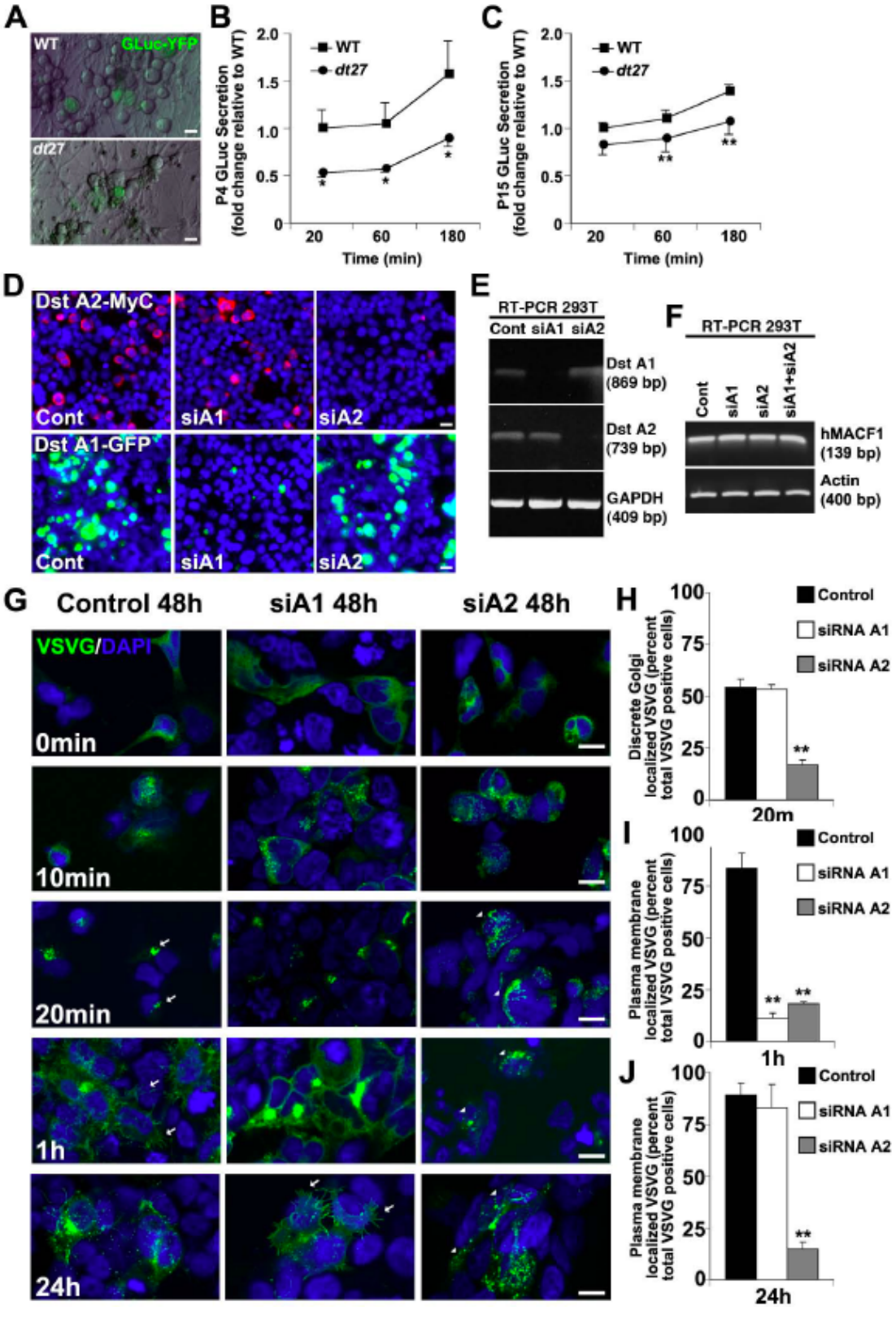
A
WT
GLuc-YFP
dt27
B
P4 GLuc Secretion (fold change relative to WT)
WT
dt27
Time (min)
C
P15 GLuc Secretion (fold change relative to WT)
WT
dt27
Time (min)
D
Dst A2-MyC
Cont
siA1
siA2
Dst A1-GFP
Cont
siA1
siA2
E
RT-PCR 293T
Cont siA1 siA2
Dst A1 (869 bp)
Dst A2 (739 bp)
GAPDH (409 bp)
F
RT-PCR 293T
Cont
siA1
siA2
siA1+siA2
hMACF1 (139 bp)
Actin (400 bp)
G
Control 48h
siA1 48h
siA2 48h
VSVG/DAPI
0min
10min
20min
1h
24h
H
Discrete Golgi localized VSVG (percent total VSVG positive cells)
Control
siRNA A1
siRNA A2
20m
I
Plasma membrane localized VSVG (percent total VSVG positive cells)
Control
siRNA A1
siRNA A2
1h
J
Plasma membrane localized VSVG (percent total VSVG positive cells)
Control
siRNA A1
siRNA A2
24h

Figure 2: Loss of dystonin impedes flux through the secretory pathway. Flux through the secretory pathway was assessed in primary sensory neurons (A) GLuc was delivered to cells, and its secretion was monitored by measuring luciferase activity in the medium over time. (B) P4 and (C) P15 dt^{27J} neurons show a decrease in flux through the secretory pathway relative to WT sensory neurons, data are expressed as fold change relative to WT 20 min (anova post hoc Tukey, *$p<0.05$, n=4-8). Isoform-specific silencing of dystonin-a1 and -a2 isoforms in 293T cells was confirmed on a protein (D) and mRNA (E) level. (F) Isoform-specific silencing of dystonin-a1 and -a2 isoforms or combined silencing in 293T cells has no impact on *MACF1* mRNA levels. (G) Defective trafficking of VSVG from the ER to the Golgi following loss of dystonin-a2. Arrows depict Golgi associated VSVG at 20 min and PM associated VSVG at 1 h while arrowheads depict aberrant VSVG localization (H). While trafficking to the PM was retarded in both dystonin-a1 and dystonin-a2 knockdown cells at 1 h (G, I), only loss of dystonin-a2 showed a persisting defect at 24 h (G arrows, J). (scale bars = 10 μm, anova post hoc dunett t-test, **$p<0.01$, n=6)

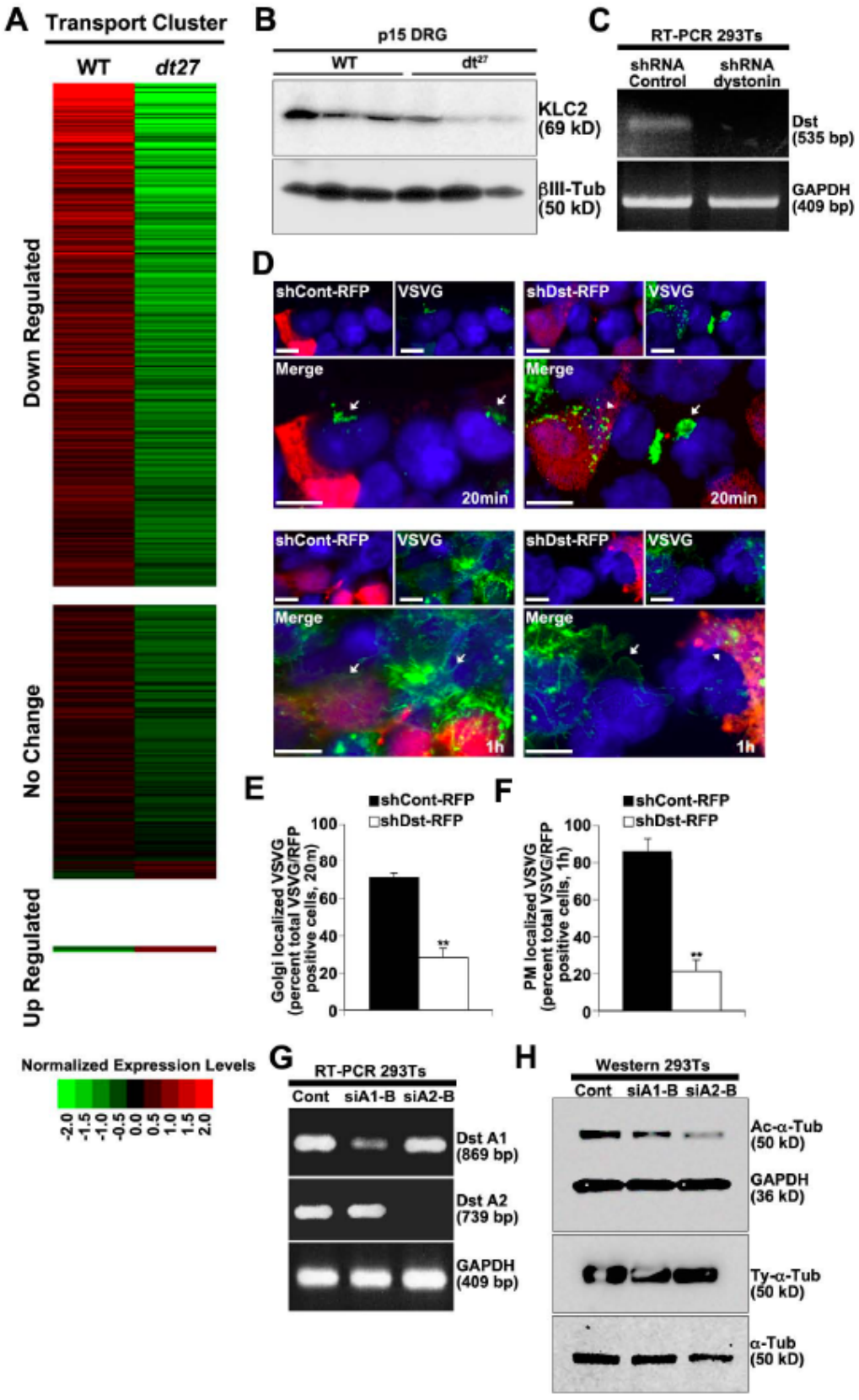
A
Transport Cluster
WT
dt27
Down Regulated
No Change
Up Regulated
Normalized Expression Levels
-2.0 -1.5 -1.0 -0.5 0.0 0.5 1.0 1.5 2.0
B
p15 DRG
WT
dt27
KLC2 (69 kD)
βIII-Tub (50 kD)
C
RT-PCR 293Ts
shRNA Control
shRNA dystonin
Dst (535 bp)
GAPDH (409 bp)
D
shCont-RFP
VSVG
Merge
20min
shDst-RFP
VSVG
Merge
20min
shCont-RFP
VSVG
Merge
1h
shDst-RFP
VSVG
Merge
1h
E
shCont-RFP
shDst-RFP
Golgi localized VSVG (percent total VSVG/RFP positive cells, 20m)
100
80
60
40
20
0
**
F
shCont-RFP
shDst-RFP
PM localized VSVG (percent total VSVG/RFP positive cells, 1h)
100
80
60
40
20
0
**
G
RT-PCR 293Ts
Cont
siA1-B
siA2-B
Dst A1 (869 bp)
Dst A2 (739 bp)
GAPDH (409 bp)
H
Western 293Ts
Cont
siA1-B
siA2-B
Ac-α-Tub (50 kD)
GAPDH (36 kD)
Ty-α-Tub (50 kD)
α-Tub (50 kD)

Figure S1. Dystonin depletion impedes flux through the secretory pathway by impairing MT stability. (A) Heat map representing the expression of genes that participate in transport (i.e. 561 genes annotated with the GO term transport) from P4 WT and *dt*^{27J} DRG tissue. (B) Western blot analysis confirms that KLC2 protein is down-regulated in *dt*^{27J} *DRGs* relative to WT. (C) RT-PCR of total dystonin following RFP tagged shRNA mediated knock down. (D) Defective trafficking of VSVG from the Golgi following total dystonin depletion. Arrows depict Golgi associated VSVG at 20 min and PM associated VSVG at 1 h while arrow heads depict aberrant VSVG localization in RFP positive dystonin depleted cells. Quantification of aberrant VSVG localization at the Golgi (E) and the PM (F) following dystonin depletion (scale bars = 10 μm, student t-test, **p<0.01, n=3). (G) Isoform-specific dystonin silencing via alternative siRNA sequences (siRNA-B) was performed to control for off-target effects. (H) siRNA-B mediated silencing of dystonin-a2 resulted in a decrease in the ratio of Ac-α-tubulin to total α-tubulin.

Null mutation in dt^{27J} precludes expression of all dystonin isoforms. The diverging cellular localization of the three neuronal isoforms of dystonin implicates each protein at different stages of secretion. Characterization of other allelic mutations (dt^{Tg4}) resulting in *dt* have shown that expression of dystonin-a3 is insufficient to rescue phenotype (Young and Kothary, 2007). The known expression profile of dystonin-a1 and dystonin-a2 proteins in DRG tissue lead us to focus on these proteins for mechanistic analysis (Pool et al., 2005; Young and Kothary, 2007). To identify the role of each dystonin isoform in intracellular transport we employed loss of function analysis in 293T cells. Microarray and proteomic analysis of 293T cells has revealed that these cells express a number of cytoskeletal components characteristic of neurons (Shaw et al., 2002). As such, we find that 293T cells endogenously express dystonin-a1 and dystonin-a2 (Fig 2E and Fig S1C, G). Isoform-specific silencing of dystonin-a1 and dystonin-a2 was confirmed on a protein (Fig 2D) and mRNA (Fig 2E and Fig S1G) level. To determine if dystonin knock down had an impact on the expression of a closely related spectraplakin, microtubule-actin crosslinking factor 1 (MACF1), we monitored the level of *MACF1* transcripts in 293T cells silenced for dystonin-a1, dystonin-a2, or both. There was no compensatory increase in MACF1 levels under any of the experimental conditions (Fig 2F). To evaluate anterograde transport in a compartmentalized fashion we traced the movement of YFP tagged VSV-$G^{ts0\text{-}45}$ (VSVG) through the secretory pathway. By regulating cellular temperature, unfolded VSVG can be loaded into ER, and then visualized as it traffics to the Golgi where the protein temporarily accumulates while undergoing N-glycosylation. Trafficking continues to the plasma membrane (PM), where the protein ultimately deposits. VSVG packaged into an adenoviral vector was

administered to 293T cells following isoform-specific silencing of dystonin. Kinetic visualization of VSVG trafficking from the ER to the Golgi (Fig 2G, H) showed a defect in transport following loss of dystonin-a2. We confirmed these defects were specific to cells in which dystonin had been depleted using RFP-tagged shRNAs to total dystonin (Fig S1D-F). Subsequently, we confirmed that this effect was not due to impaired protein folding or ER exit as folded VSVG protein was readily detectable (Fig S2). While trafficking to the PM was retarded in both dystonin-a1 and dystonin-a2 knockdown at 1 h (Fig 2G, I), only loss of dystonin-a2 showed a persistent defect (Fig 2G, J). Collectively, these data indicate a defect in flux through the secretory pathway in *dt* sensory neurons may exist pre-phenotype and is likely the combined result of loss of multiple dystonin isoforms.

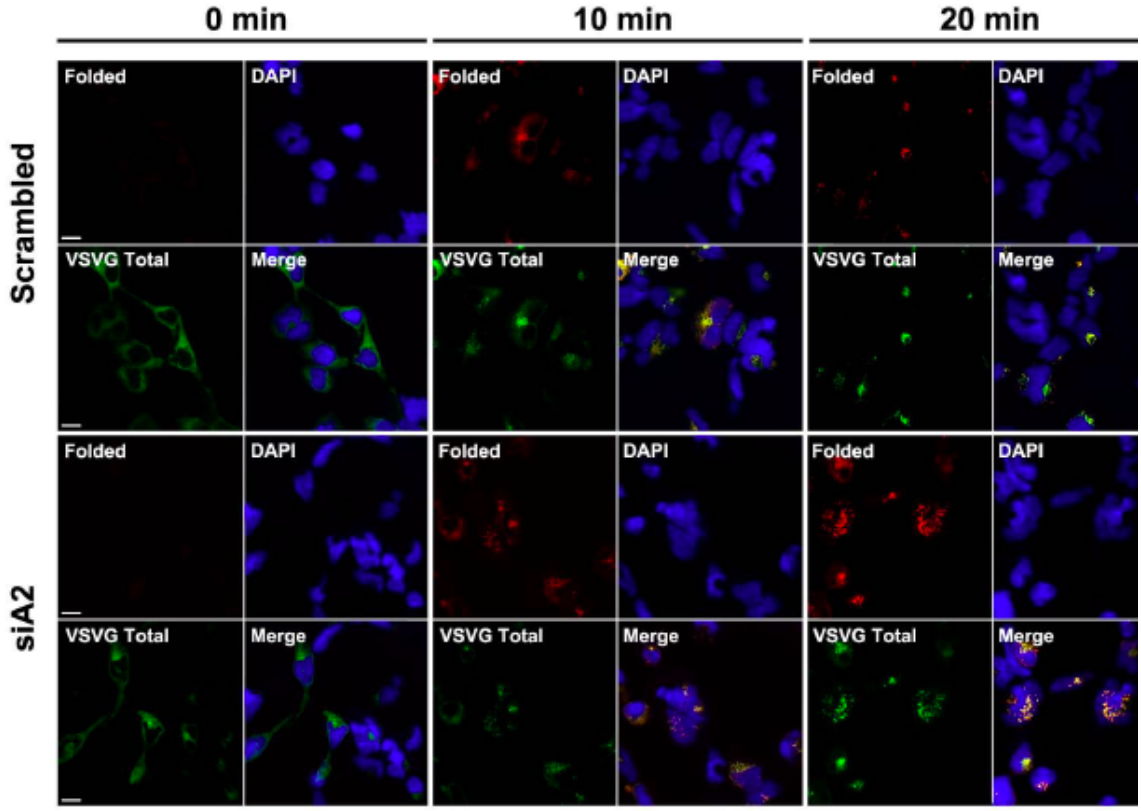

Figure S2. Protein folding occurs normally following dystonin-a2 depletion. (A) 293T cells infected with VSVG expressing adenovirus were incubated at 40.5°C to block protein folding and allow VSVG to accumulate in the ER. Cells were rapidly cooled to 32°C to permit protein folding and antigenically labeled with a VSVG antibody specific to the folded form of VSVG. Both control and siA2 treated cells display positive labeling for folded protein within 10 min of incubation at 32°C suggesting that protein folding occurs normally. All scale bars are 10 μm.

To address the varying degree to which loss of each isoform contributed to the transport defect and whether either isoform is functional in the normal transport process, we attempted to differentiate the cytoskeletal aberrations resulting from loss of each isoform. In a healthy cell, the MT network should distribute uniformly from the cell center to the cortex of the cell. Following either dystonin-a1 or dystonin-a2 silencing, the MT network of cells appeared abnormal, with compact and dense packs of MTs in the center and significantly decreased density in the periphery (Fig 3A). Furthermore, peripheral MTs failed to reach the cell cortex, with the greatest deficiency evident following dystonin-a2 loss (Fig 3B). Full-length epitope-tagged dystonin-a2 (Dst-a2-myc) co-localizes with α-tubulin in the perinuclear region of the cell (Fig 3C). This suggests that the observed defect is not a failure of MT anchoring to the cell cortex but rather compromised MT stability and organization. We confirmed that dystonin-a2 mediated MT stability by challenging 293T cells with nocodazole. Cells overexpressing Dst-a2-myc maintain polymerized MTs relative to non-transfected cells in the presence of nocodazole (Fig 3D). We thus examined the acetylation status of α-tubulin as a marker of MT stability and found a significant reduction in acetylated (Ac) α-tubulin following specific loss of dystonin-a2 (Fig 3E-G). This decrease in Ac-α-tubulin was most prominent in the perinuclear region of the cell where dystonin-a2 localization was observed (Fig 3G). We confirmed MT acetylation status was decreased in the perinuclear region of primary sensory neurons from pre-phenotype (Fig 4A) and phenotype (Fig 4B) stage mice as well as in tissue (Fig 4C-F). We expanded this analysis to include assessment of tubulin tyrosination (ty). While minor dynamic changes in ty-α-tubulin expression were observed, no significant change in the ratio of ty-α-tubulin to total α-

tubulin could be detected (Fig 3E and Fig S1H). MT acetylation has previously been shown to promote anterograde transport via the kinesin motor complex (Reed et al., 2006). We thus sought to determine the impact of MT acetylation on transport in *dt.* The prominence of defects resulting from loss of dystonin-a2 led us to focus on this isoform as a mediator of cytoskeletal organization critical to anterograde transport.

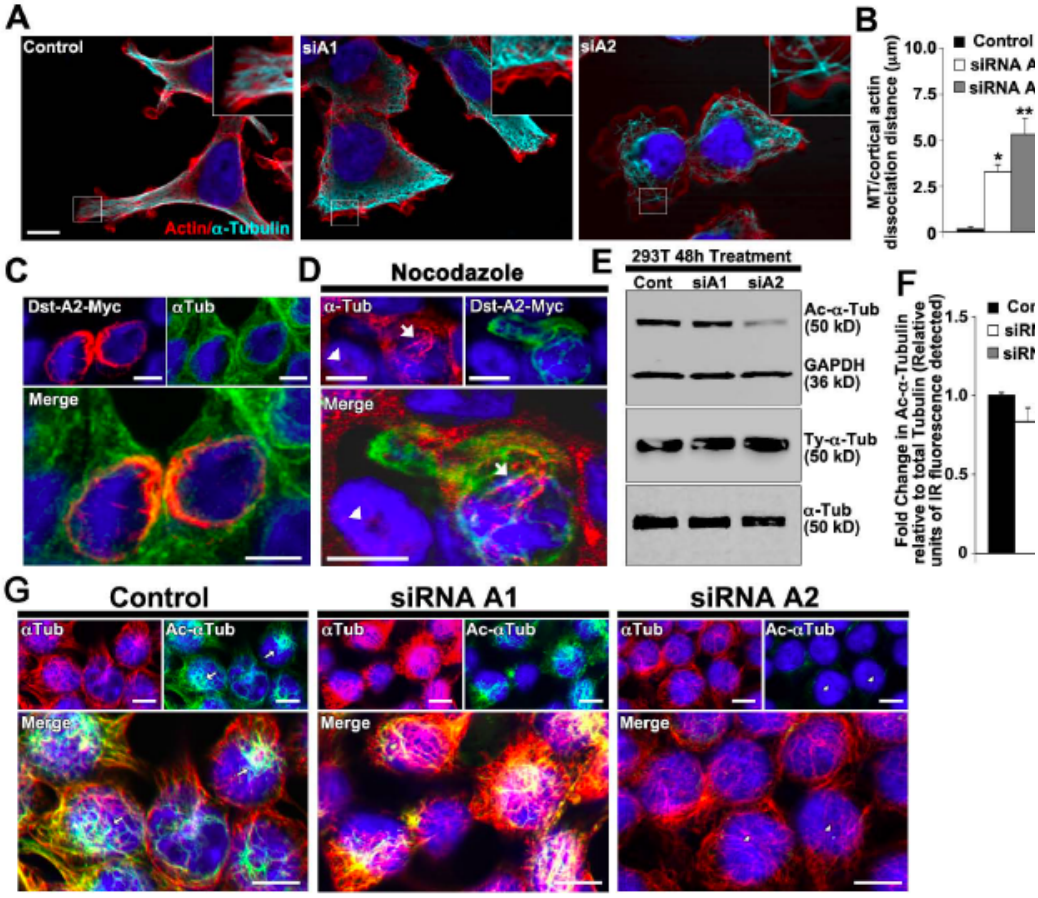

Figure 3: Loss of dystonin-a2 reduces α-tubulin acetylation status. (A-B) Loss of either dystonin-a1 or dystonin-a2 in 293T cells results in disorganization of the MTs relative to the actin cortex (anova post hoc dunett t-test, *p<0.05, **p<0.01, n=9-12). Insets show that MTs do not extend to the actin cortex following dystonin silencing (A, Instet). (C) Dystonin-a2 co-localizes with α-tubulin in the perinuclear region. (D) Overexpression of dystonin-a2-myc stabilizes MTs in 293T cells as indicated by conferring resistance to nocodazole-mediated depolymerization of α-tubulin (compare the protected cell depicted by arrow vs. the susceptible cell depicted by an arrow head). (E-F) 293T western and (G) immunofluorescent analysis of Ac-α-tubulin following

dystonin depletion. (F) Quantification of the normalized ratio of Ac-α-tubulin to total α-tubulin showed a significant decrease in Ac-α-tubulin following dystonin-a2 depletion (anova post hoc dunett t-test, *$p<0.05$, $n=4$). (G) Note the decrease in Ac-α-tubulin in the perinuclear region of the cell following dystonin-a2 silencing (G, arrows vs. arrow heads). All scale bars = 10 μm.

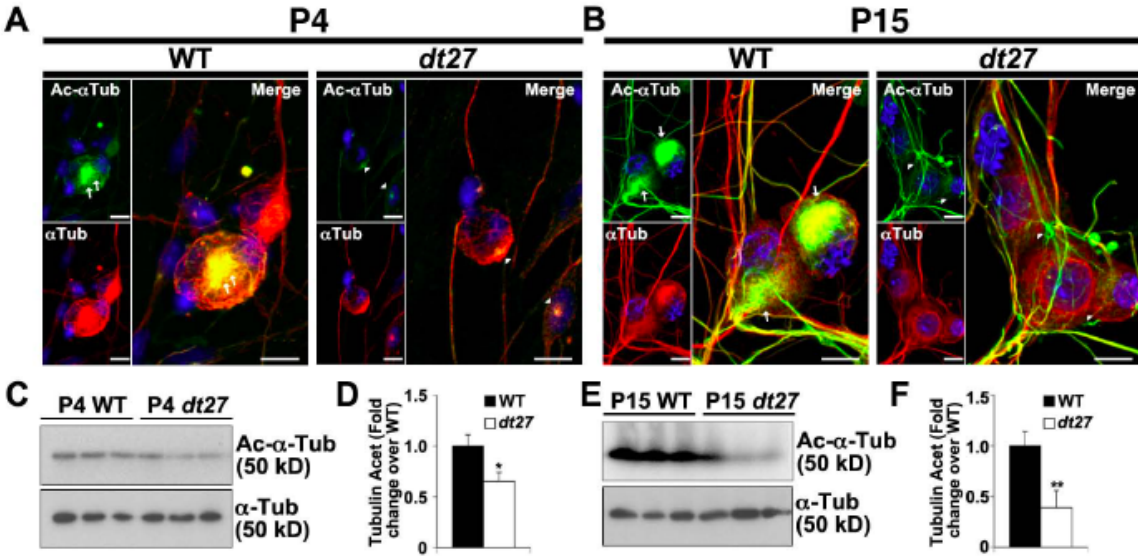

Figure 4: MT acetylation is reduced in DRGs and primary sensory neurons of *dt*^{27J} mice. (A) P4 and (B) P15 analysis of tubulin acetylation state. Decreased Ac-α-tubulin is evident in *dt*^{27J} sensory neurons relative to WT in the perinuclear region (arrows vs. arrow heads). Western analysis of DRG tissue at P4 (C-D) and P15 (E-F) also show decreased Ac-α-tubulin in *dt*^{27J} relative to WT samples. Each lane represents DRGs from one animal. (t-test, *$p<0.05$, **$p<0.01$, n=3). All scale bars = 10 μm.

TSA inhibits class II histone deacetylases and in this respect has been shown to promote MT acetylation (Matsuyama et al., 2002). We used TSA to maintain MT acetylation status following dystonin-a2 silencing. Western analysis of 293T lysate shows that TSA treatment maintains α-tubulin acetylation state following depletion of dystonin-a2 (Fig 5A). Subsequent evaluation of anterograde transport showed that TSA promotes VSVG trafficking to the Golgi (Fig 5B, C) and PM (Fig 5B, D) following dystonin-a2 depletion. To evaluate whether MT acetylation status could impact on anterograde transport in *dt,* primary DRG neurons from pre-phenotype and phenotype stage mice were treated for 24 h with TSA and GLuc secretion into culture media was assessed. TSA returned GLuc flux through the secretory pathway to WT levels in both P4 (Fig 5E) and P15 (Fig 5F) dt^{27J} sensory neurons.

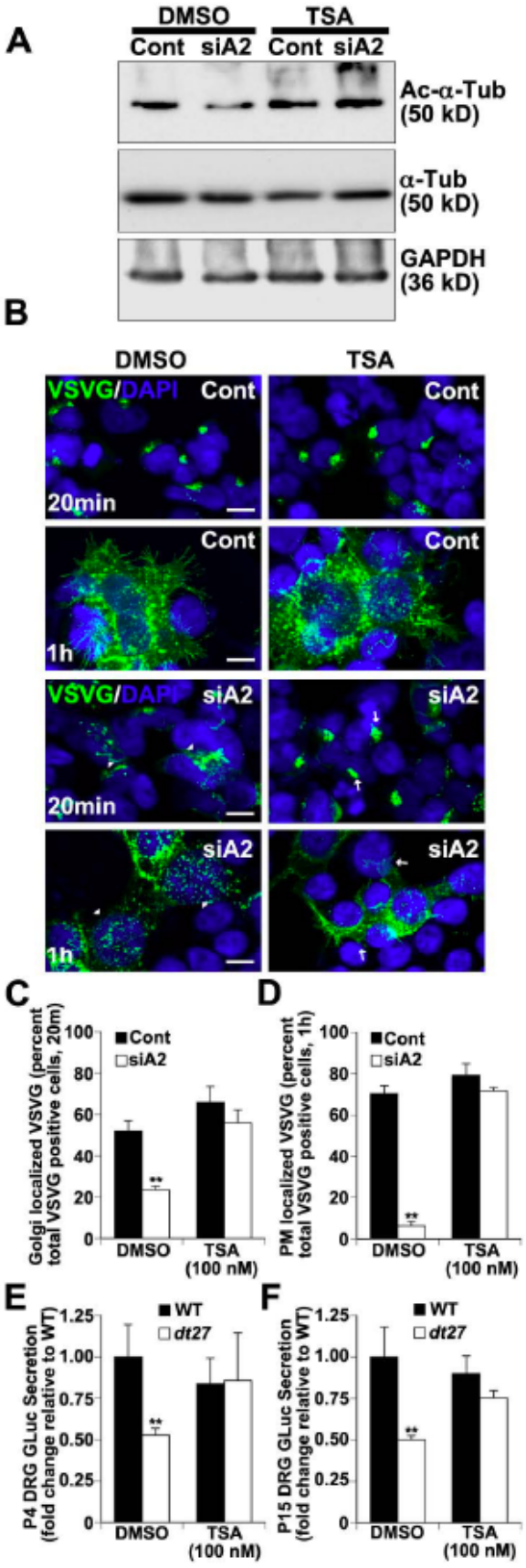
A
DMSO
TSA
Cont siA2 Cont siA2
Ac-α-Tub (50 kD)
α-Tub (50 kD)
GAPDH (36 kD)
B
DMSO
TSA
VSVG/DAPI Cont
Cont
20min
Cont
Cont
1h
VSVG/DAPI siA2
siA2
20min
siA2
siA2
1h
C
Golgi localized VSVG (percent total VSVG positive cells, 20m)
Cont
siA2
DMSO
TSA (100 nM)
D
PM localized VSVG (percent total VSVG positive cells, 1h)
Cont
siA2
DMSO
TSA (100 nM)
E
P4 DRG GLuc Secretion (fold change relative to WT)
WT
dt27
DMSO
TSA (100 nM)
F
P15 DRG GLuc Secretion (fold change relative to WT)
WT
dt27
DMSO
TSA (100 nM)

Figure 5: Maintaining Ac-α-tubulin status permits flux through the secretory pathway following dystonin depletion. (A) Western analysis of 293T cell lysate shows that TSA treatment maintains Ac-α-tubulin following depletion of dystonin-a2. (B) TSA promotes VSVG trafficking to the Golgi and PM following dystonin-a2 depletion relative to DMSO treated control. Arrowheads identify aberrantly localized VSVG molecules while arrows identify normal VSVG localization. Quantification of TSA impact on VSVG accumulation in the Golgi (C) and at the PM (D) (anova post hoc tukey, **p<0.01, n=3). TSA promotes GLuc flux through the secretory pathway (time=1 hr) in (E) P4 and (F) P15 *dt*^{27J} sensory neurons (anova post hoc tukey, **p<0.01, n=6). All scale bars are 10 μm.

In characterizing the defect in VSVG trafficking following dystonin-a2 silencing in 293T cells, we found that while VSVG protein never organized into a discrete Golgi pattern, co-localization with the *cis*-Golgi marker GM130, was observed nonetheless (Fig 6A). Further analysis of Golgi morphology indicated that loss of dystonin-a2 in 293T cells promotes Golgi fragmentation (Fig 6B, C). We have previously reported that the transmembrane domain of dystonin-a2 positions the protein in perinuclear membranes including the *cis*-Golgi (Young and Kothary, 2008). We thus sought to evaluate the ultra-structure of Golgi in WT and dt^{27J} DRGs. Electron micrographs of P4 and P15 WT and dt^{27J} DRG sections show dilated Golgi in sensory neurons of dt^{27J} mice prior to phenotype onset (Fig 6D-G). Furthermore, while Golgi stacking appears normal, laterally adjacent Golgi vesicles are disconnected, suggesting Golgi ribboning may be impeded. These data suggest a role for dystonin in organization of Golgi membranes. A close spatial temporal association is known to exist between acetylated Ac-α-tubulin and *cis*-Golgi (Skoufias et al., 1990; Thyberg and Moskalewski, 1993). We thus sought to determine whether a change in MT acetylation status following dystonin loss was related to Golgi fragmentation in *dt*.

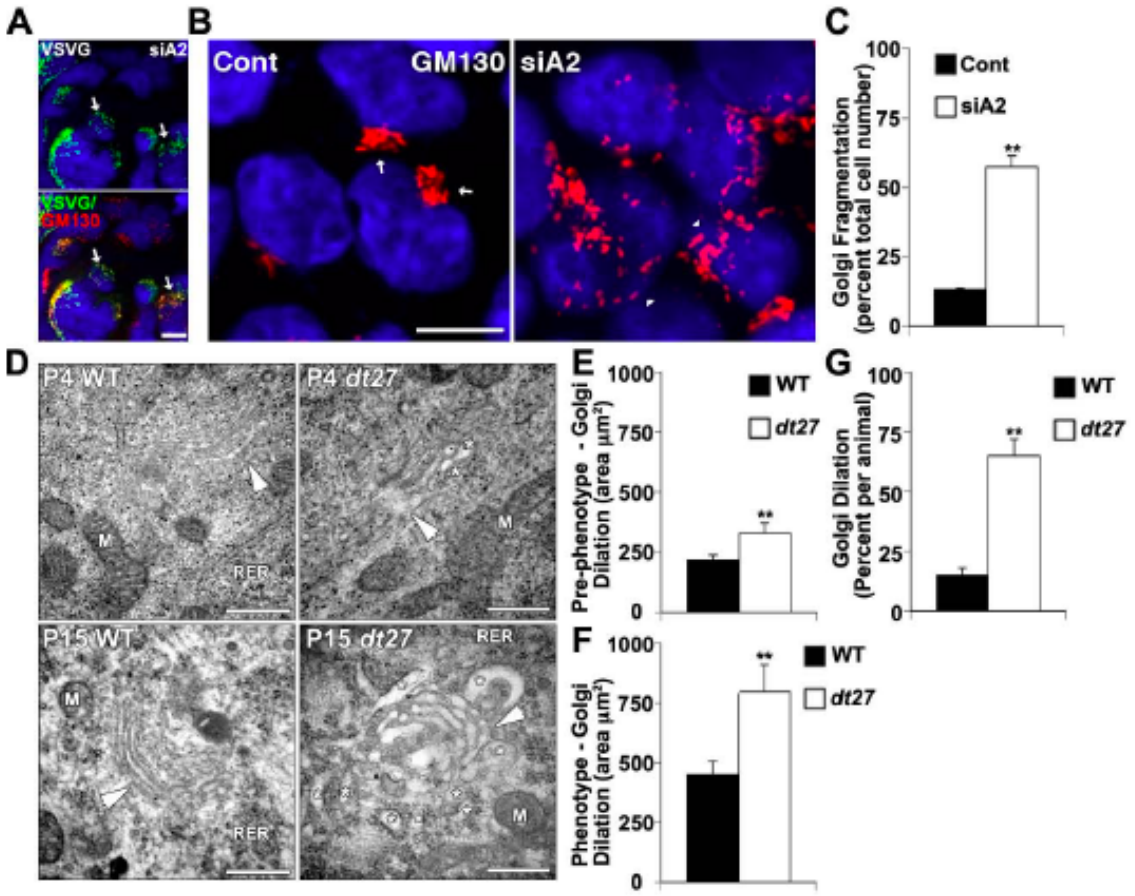

Figure 6: Loss of dystonin-a2 alters Golgi morphology. (A) VSVG localizes with *cis*-Golgi marker GM130 despite inability to traffic in 293T cells deficient in dystonin-a2. (B-C) Loss of dystonin-a2 in 293T cells promotes Golgi fragmentation, arrows depict compact Golgi while arrowheads depict dispersed Golgi (student t-test, **p<0.01, n=3). Scale bars are 10 µm. (D) Electron micrograph of P4 and P15 WT and dt^{27J} *DRG* sections show dilated Golgi in sensory neurons of dt^{27J} mice. Arrowheads depict the cis-Golgi face while asterisks depict dilated Golgi vesicles (scale bars are 500 nm). (E-G) Ultrastructural analysis of dt^{27J} Golgi showed increased area at P4 and P15 relative to WT littermates and an increase in the number of dilated Golgi per animal (M=Mitochondria, RER=Rough ER) (student t-test, **p<0.01, n=4).

Silencing of dystonin-a2 in 293T cells results in decreased MT acetylation coupled with reorganization of the *cis*-Golgi (Fig 7A). This phenomenon also occurs in cultured sensory neurons from dt^{27J} mice (Fig 7B). 3D-rendering shows reduced Ac-α-tubulin coupled to a decrease in GM130 antigenic labeling in the cell soma of P15 primary sensory neurons from dt^{27J} mice compared to WT. To determine whether loss of Golgi organization was impacted upon by MT acetylation status, we treated cells with TSA prior to dystonin-a2 depletion. Maintenance of MT acetylation status with TSA decreased Golgi fragmentation following dystonin-a2 silencing (Fig 7C, D). Ac-α-tubulin, is often found in MTs polymerized via the Golgi complex (Chabin-Brion et al., 2001) and is implicated in Golgi-mediated MT nucleation. This coupled with pre-phenotype gene expression data from *dt* DRGs implicate impaired MT nucleation/polymerization as a component of *dt* pathology. Nocodazole wash out of 293T cells following dystonin-a2 depletion, however, showed that non-centrosomal MT nucleation proceeds, albeit from dispersed cellular locations following dystonin-a2 depletion [Fig 7E (siA2 30s, arrow)]. Centrosomal MT nucleation, however, is moderately delayed following dystonin-a2 loss relative to dystonin-a1 depleted or control cells, normalizing soon after nocodazole is removed (Fig 7E). Centrosomal positioning and MT polymerization toward the leading edge of the cell requires Golgi components to proceed normally (Bisel et al., 2008; Lowe, 2011). While non-centrosomal nucleation was observed, chronically fragmented Golgi due to dystonin loss would have a net negative impact on centrosomal MT polymerization. This coupled with MT instability due to deacetylation may explain defective anterograde transport processes. No direct role for dystonin in post-translational modification of MTs has previously been reported.

We recently conducted a proteomic screen of dystonin binding partners and identified a strong interaction between the MT associated protein MAP1B and the plakin domain of dystonin (Bhanot et al., 2011). Interestingly, a functional role in maintaining Ac-α-tubulin has been attributed to MAP1B (Takemura et al., 1992). MAP1B overexpression in the presence and absence of nocodazole demonstrated that MAP1B could maintain tubulin acetylation status in the face of nocodazole treatment, indicating an increase in MT stability (Fig S3C). We therefore set out to verify whether loss of this interaction has a causal implication to *dt* pathology.

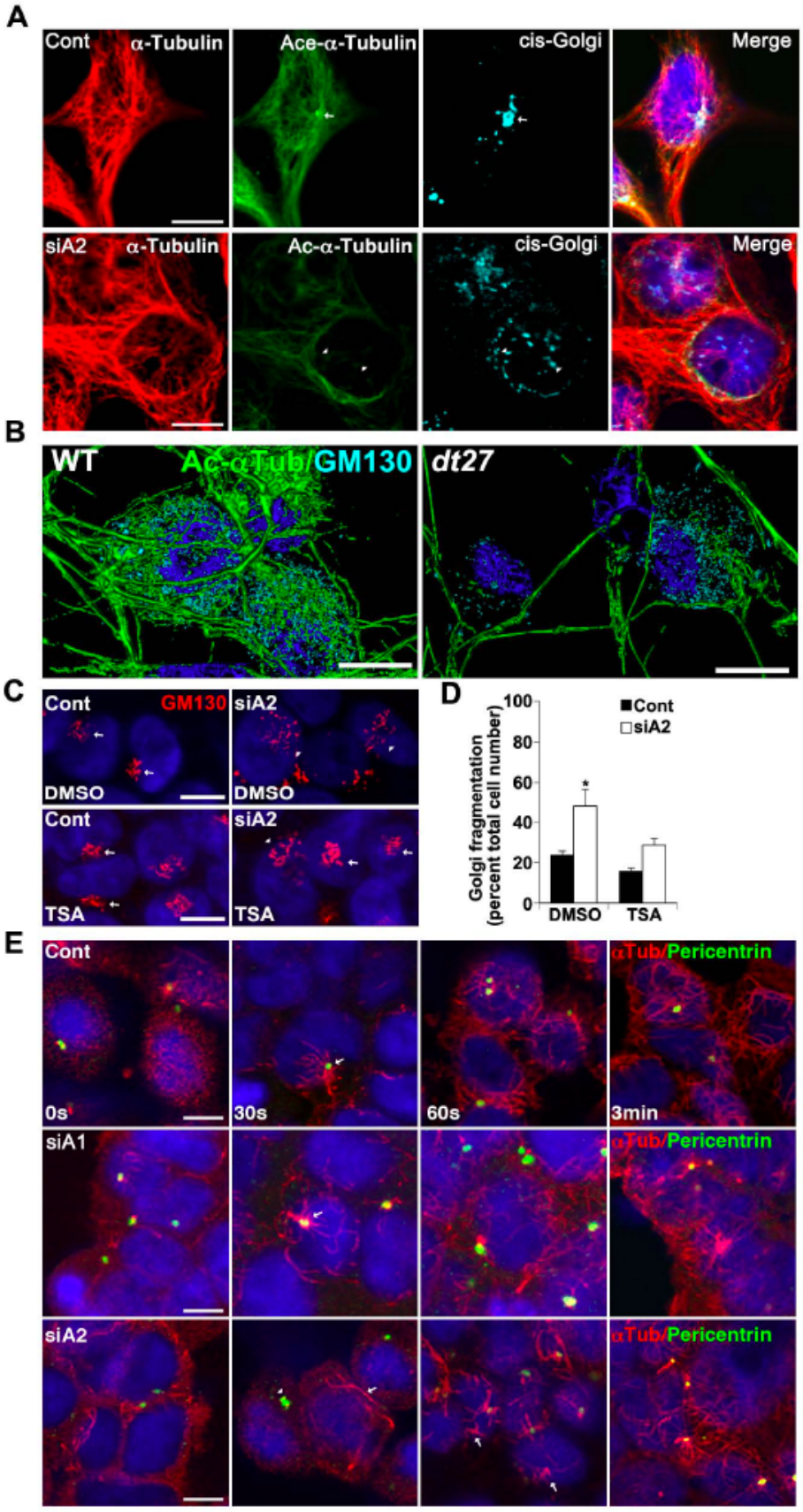
A
Cont
α-Tubulin
Ace-α-Tubulin
cis-Golgi
Merge
siA2
α-Tubulin
Ac-α-Tubulin
cis-Golgi
Merge
B
WT
Ac-αTub/GM130
dt27
C
Cont
GM130
siA2
DMSO
DMSO
Cont
siA2
TSA
TSA
D
Golgi fragmentation (percent total cell number)
100
80
60
40
20
0
Cont
siA2
*
DMSO
TSA
E
Cont
αTub/Pericentrin
0s
30s
60s
3min
siA1
αTub/Pericentrin
siA2
αTub/Pericentrin

Figure 7: Impaired MT acetylation results in Golgi fragmentation following loss of dystonin-a2. (A) Silencing of dystonin-a2 in 293T cells results in decreased MT acetylation coupled with reorganization of the Golgi complex. *cis*-Golgi (GM130) tightly associates with Ac-α-tubulin (arrows vs. arrowheads). (B) 3D rendering of P15 primary sensory neurons from WT and dt^{27J} mice. dt^{27J} sensory neurons show reduced Ac-α-tubulin coupled to a decrease GM130 antigenic labeling in the cell soma. (C-D) Maintenance of MT acetylation status with TSA prevents Golgi fragmentation following depletion of dystonin-a2, arrows depict compact Golgi while arrowheads depict dispersed Golgi (anova post hoc tukey, *$p<0.05$, $n=6$). (E) Nocodazole wash out of 293T cells following dystonin-a2 depletion shows that MT nucleation from the centrosome is moderately delayed following dystonin-a2 depletion but not dystonin-a1 silencing. Arrows identify sites of MT polymerization. Following dystonin-a2 silencing centrosomal MT polymerization is impeded (arrowhead). All scale bars are 10 μm.

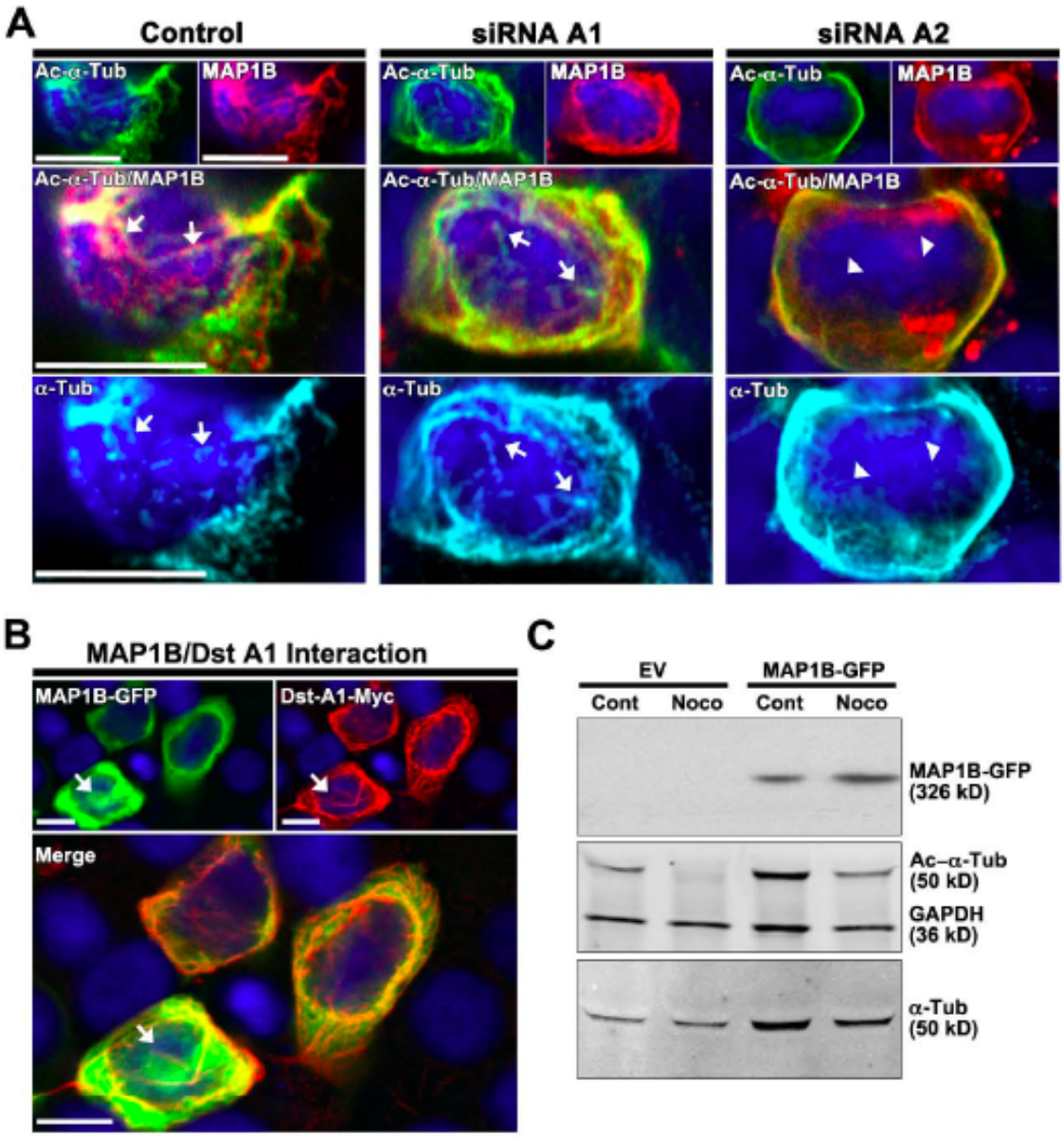

Figure S3. MAP1B stabilizes MTs via dystonin interaction. (A) Following Dystonin-a2 silencing, the decrease in centrosomal Ac-α-Tub corresponds with a decrease in MAP1B association with α-Tub in this region. Arrows identify regions of Ac-α-Tub while arrowheads identify regions where α-Tub is not acetylated. (B) Confocal microscopy of ectopically expressed MAP1B-GFP and dystonin-a1-myc show colocalization indicating that MAP1B is able to interact with multiple dystonin isoforms.

Arrows identify regions of colocalization between MAP1B and dystonin-a1. All scale bars are 10 μm. (C) Western analysis of nocodazole treated cells expressing MAP1B-GFP or empty vector (EV). MAP1B-GFP expression stabilizes microtubules by maintaining Ac-α-Tub status.

We first characterized the interaction between MAP1B and dystonin-a2 in our system. Confocal microscopy of recombinant dystonin-a2 and MAP1B-GFP shows colocalization at the perinuclear cytoskeleton (Fig 8A). We confirmed the proximity of these proteins using the proximity ligation assay. Recombinant dystonin-a2 and MAP1B-GFP molecules within 3 Å of each other fluoresce red when excited with a 543 nm laser (Fig 8B). Reciprocal pull down assays of MAP1B and the plakin domain of dystonin confirmed that MAP1B and dystonin interact via the plakin domain (Fig 8C). We then confirmed that ectopic Dst-a2-myc colocalized with endogenous MAP1B (Fig 8D). The observed defect at centrosomal MTs coupled with the loss of *cis*-Golgi organization at the centrosome lead us to investigate the location of this interaction. Co-labeling with pericentrin shows that dystonin-a2 and MAP1B interact in the area surrounding the centrosome (Fig 8E). We further examined the ability of dystonin a1-myc to interact with MAP1B-GFP by confocal microscopy (Fig S3B). This experiment revealed that MAP1B is capable of interacting with the plakin domain of multiple dystonin isoforms. Our subsequent experiments sought to determine whether MAP1B mediated acetylation of MTs prevents deficiency associated with dystonin loss.

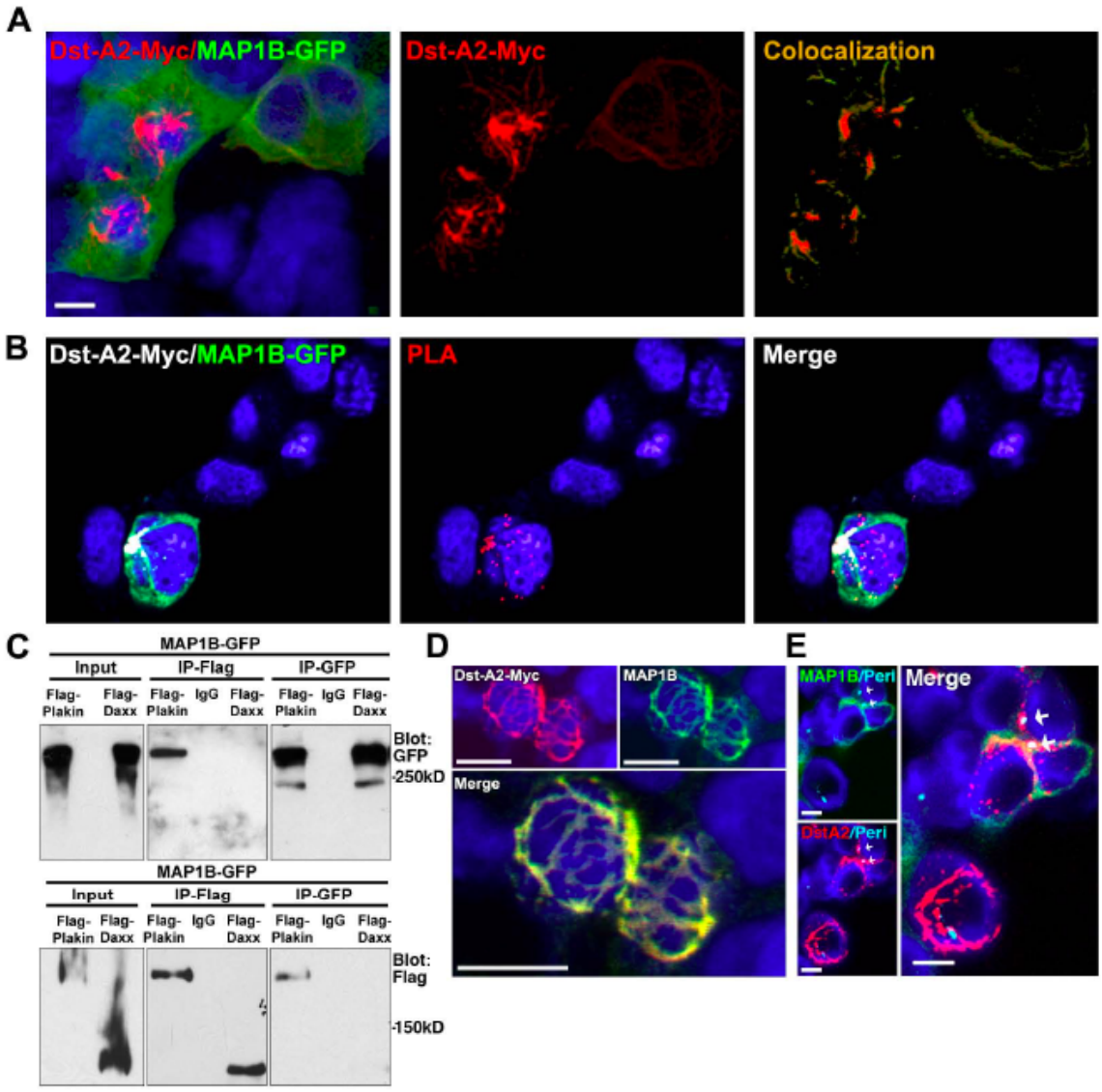

Figure 8: Dystonin-a2 interacts with MT stabilizing protein MAP1B. (A) Colocalization of recombinant dystonin-a2-myc and MAP1B-GFP in 293T cells as assessed by confocal microscopy. Vector mask of colocalization shows the region of colocalization is at the perinuclear cytoskeleton. (B) Proximity ligation assay (PLA) of recombinant dystonin-a2 and MAP1B-GFP shows that the two proteins are within 3 Å of each other. (C) Reciprocal GFP/FLAG pull down of MAP1B and the plakin domain of dystonin shows that MAP1B and dystonin interact via the plakin domain. (D) Confocal microscopy of dst-a2-myc and endogenous MAP1B show colocalization in perinuclear

regions of the cell. (E) Colocalization analysis of recombinant dst-a2-myc and MAP1B-GFP combined with antigenic labeling of percentrin by confocal microscopy shows that the interaction occurs in a sub-cellular region surrounding the centrosome (arrows). All scale bars are 10 μm.

Western analysis of 293T lysate shows that MAP1B overexpression maintains Ac-α-tubulin following dystonin-a2 depletion (Fig 9A). Furthermore, this change in acetylation state appears sufficient to overcome Golgi fragmentation following dystonin-a2 depletion (Fig 9B). We thus evaluated whether MAP1B overexpression influences the ability of VSVG to traffic out of the Golgi following dystonin-a2 silencing. Kinetic visualization of VSVG trafficking showed that MAP1B promoted VSVG accumulation in discreetly organized Golgi (Fig 9C, D). Furthermore, MAP1B facilitates Golgi exit of VSVG and trafficking to the PM (Fig 9C, E). This confirmed that MT stabilization rescues transport defects resulting from dystonin-a2 loss and suggested that MAP1B-dystonin interaction is critical to anterograde transport. Antigenic labeling of WT primary sensory neurons shows a perinuclear accumulation of MAP1B that is lost in dt^{27J} neurons (Fig 9F, arrows) indicating a requirement of dystonin for MAP1B subcellular localization and supporting the notion that disruption of MAP1B-dystonin interaction is causal in *dt* pathogenesis. This was confirmed using isoform-specific dystonin silencing. Isoform-specific dystonin-a2 depletion resulted in a change in MAP1B localization whereby the decrease in Ac-α-tubulin in the centrosomal region of the cell corresponded with a decrease in MAP1B association with α-tubulin in this region (Fig S3A). This further suggests that MAP1B mediated maintenance of MT acetylation at the centrosome requires dystonin-a2. Finally, we examined whether overexpression of MAP1B promoted GLuc flux through the secretory pathway in primary sensory neurons of dt^{27J} mice (Fig 9G). We find that MAP1B ectopic expression normalizes flux through the secretory pathway in *dt* neurons. Collectively these data suggest that dystonin-a2 maintains the acetylation status of MTs in the sub-cellular compartments surrounding the

Golgi through interaction with MAP1B and that stabilized MTs in turn maintain the organization of *cis*-Golgi compartments and facilitate flux through the secretory pathway.

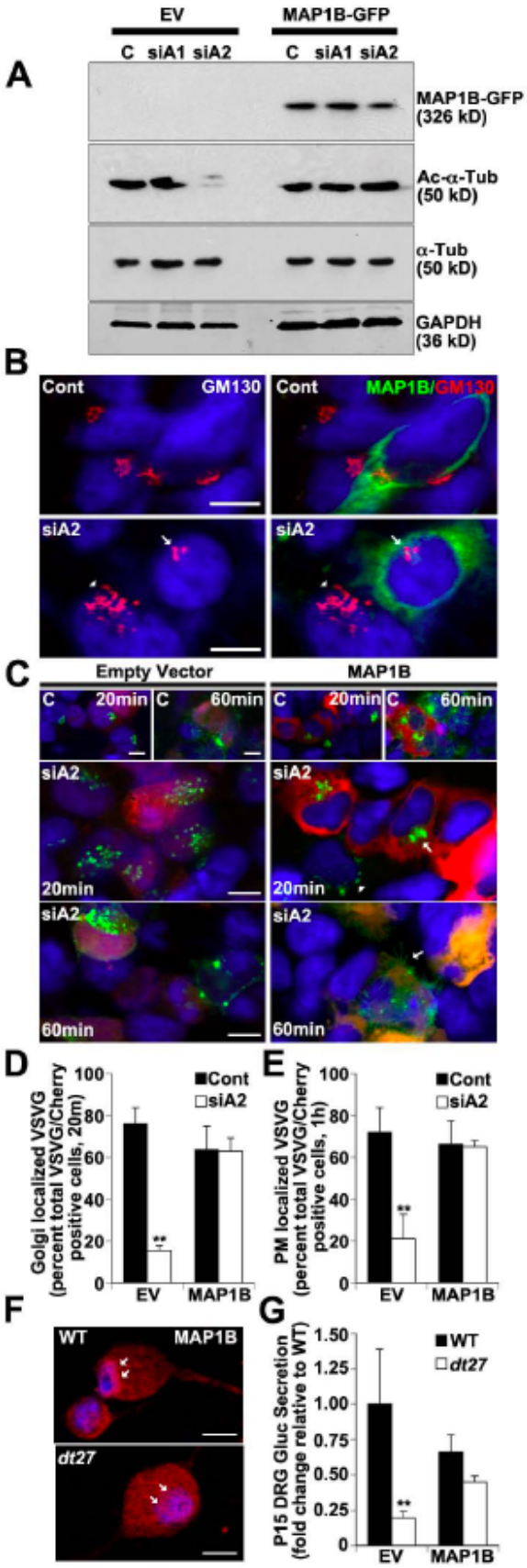
A
EV
MAP1B-GFP
C siA1 siA2
C siA1 siA2
MAP1B-GFP (326 kD)
Ac-α-Tub (50 kD)
α-Tub (50 kD)
GAPDH (36 kD)
B
Cont
GM130
Cont
MAP1B/GM130
siA2
siA2
C
Empty Vector
MAP1B
C 20min
C 60min
C 20min
C 60min
siA2
20min
siA2
20min
siA2
60min
siA2
60min
D
Golgi localized VSVG (percent total VSVG/Cherry positive cells, 20m)
100
80
60
40
20
0
Cont
siA2
**
EV
MAP1B
E
PM localized VSVG (percent total VSVG/Cherry positive cells, 1h)
100
80
60
40
20
0
Cont
siA2
**
EV
MAP1B
F
WT
MAP1B
dt27
G
P15 DRG Gluc Secretion (fold change relative to WT)
1.50
1.25
1.00
0.75
0.50
0.25
0
WT
dt27
**
EV
MAP1B

Figure 9: Dystonin-a2-MAP1B interaction maintains Ac-α-tubulin and promotes flux through the secretory pathway. (A) Western analysis of 293T cell lysate shows that MAP1B overexpression maintains Ac-α-tubulin following dystonin-a2 depletion relative to EV control. (B) MAP1B overexpression prevents Golgi fragmentation following dystonin-a2 depletion in 293Ts. Arrow points to intact Golgi in siA2 treated cell that is positive for MAP1B-GFP expression. Arrowhead points to fragmented Golgi in a neighboring cell that was not transfected with the MAP1B-GFP construct. (C) MAP1B overexpression promotes VSVG trafficking to the Golgi and PM following dystonin-a2 depletion relative to EV control. Scramble siRNA treated cells (top panel) are labeled "C". Arrowheads identify aberrantly localized VSVG molecules while in while arrows identify normal VSVG localization. Quantification of MAP1B impact on VSVG accumulation in the Golgi (D) and at the PM (E) (anova post hoc tukey, **p<0.01, n=3). (F) MAP1B antigenic labeling of WT primary sensory neurons shows a perinuclear accumulation that is lost in dt^{27J} neurons (arrows). (G) MAP1B expression restores GLuc flux through the secretory pathway (time=1 hr) in P15 dt^{27J} sensory neurons (anova post hoc tukey, **p<0.01, n=6). All scale bars are 10 μm.

Discussion

Dst mutations have been attributed a casual role in degeneration of sensory neurons in the neurological mouse mutant *dt*. While much investigation has focused on understanding *dt* pathology, the daunting size of the *Dst* gene coupled to the numerous protein isoforms generated from the gene have made elucidation of divergent isoform functions arduous. Here, we highlight a novel function of the dystonin-a2 isoform in mediating Golgi organization and flux through the secretory pathway (Fig 10). We find under normal conditions dystonin-a2 associates with MAP1B in the area surrounding the centrosome, maintaining the acetylation status of MTs in this sub-cellular compartment. Stabilized MTs maintain the organization of the *cis*-Golgi and promote anterograde trafficking of motor proteins. In *dt*, the absence of the MAP1B-dystonin-a2 interaction results in a loss of MAP1B perinuclear localization, promoting MT instability through loss of MT acetylation. Deacetylated MT leads to Golgi fragmentation and prevent anterograde trafficking of motor proteins. These aberrations are apparent in pre-phenotype DRG tissue and primary sensory neurons of pre-phenotype *dt* mice, suggesting that they are causal in the *dt* disorder. Moreover, we report major changes in gene expression that precede the *dt* phenotype. While MT stability in and of itself can lead to the changes in gene expression observed in *dt* DRGs, there may be direct effects of dystonin depletion on gene expression. Given the complexity of dystonin function, in particular its localization in the nuclear envelope and its known interaction with nesprin 3α (Young and Kothary, 2008), it is possible that the transcription changes observed may also be a direct result of dystonin depletion at the nuclear envelope.

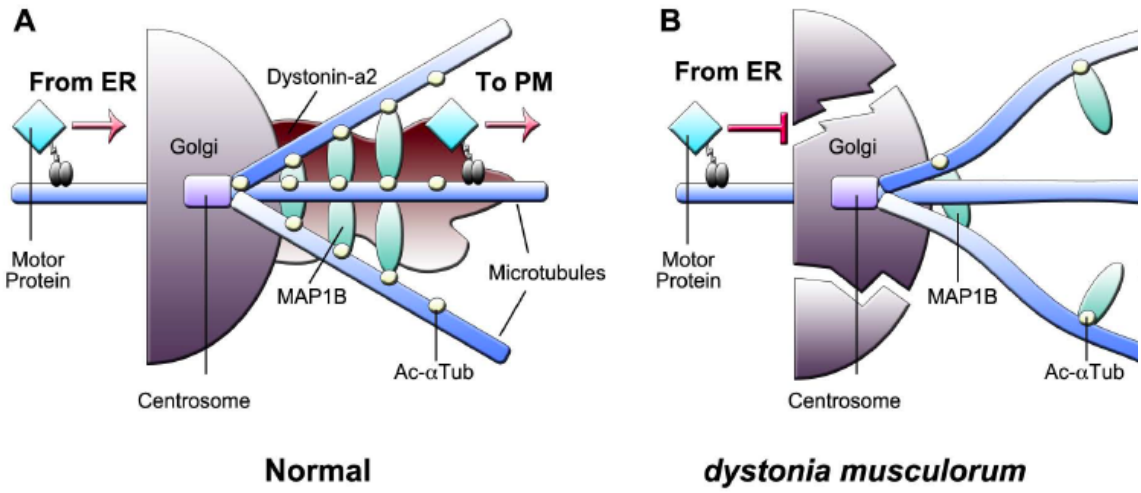

Figure 10. Schematic representation of the mechanism underlying transport defects in *dystonia musculorum*. (A) Under normal conditions, dystonin-a2 is present at Golgi membranes maintaining the acetylation status of MTs in the sub-cellular compartments surrounding the centrosome. Stabilized MTs maintain the organization of the *cis*-Golgi and promote anterograde trafficking of motor proteins. (B) In *dystonia musculorum* mice, the absence of MAP1B-dystonin-a2 interaction promotes MT instability through loss of MT acetylation. Deacetylated MT promotes Golgi fragmentation and prevents anterograde trafficking of motor proteins.

Dystonin in MT stabilization: MTs radiate from the MT-organizing complex forming a scaffold network for organelles mediating their dispersal throughout the cell (Thyberg and Moskalewski, 1999; Lowe, 2011). Stabilized MTs form rigid, rod-like structures that collapse toward the MT-organizing complex, resulting in perinuclear rings where organelles aggregate (Kreitzer et al., 1999; Rios and Bornens, 2003). Loss of MT stability promotes organelle dispersal and Golgi fragmentation (Burkhardt, 1998). MT stability is regulated by MT-associated proteins such as MAP1S and MAP1B that bind and stabilize both organelles and MTs and by MT motor complexes (dynein and kinesin) involved in transporting Golgi vesicles to MT ends (Takemura et al., 1992; Thyberg and Moskalewski, 1993; Burkhardt, 1998; Liu et al., 2005; Bondallaz et al., 2006). The stabilizing effect of MAP1B is mediated in part through posttranslational modification of α-tubulin (Takemura et al., 1992; Bouquet et al., 2004). MAP1B maintains the acetylation status of α-tubulin making MTs resistant to nocodazole-mediated depolymerization. MAP1B and MAP2 synergistically regulate multiple aspects of brain development (Teng et al., 2001; González-Billault et al., 2005). Mice with a complete MAP1B null allele show developmental defects in the brain and peripheral nervous system with reduction in large caliber axons in the sciatic nerve, a similar result to what we have observed in *dt* mice (Bernier and Kothary, 1998; Meixner et al., 2000; De Repentigny et al., 2003). MT stability is associated with post-translational acetylation of α-tubulin that closely associates with the *cis*-Golgi and is critical to Golgi organization (Thyberg and Moskalewski, 1993; Lowe, 2011). Deficiency of the histone acetyltransferase complex, elongator, results in a defect in neuronal migration and axon branching through loss of Ac-α-tubulin (Creppe et al., 2009). This suggests that tubulin

acetylation status underlies neuronal deficits related to cytoskeletal instability. Our demonstration of functional interaction between MAP1B and the plakin domain of dystonin-a2 may explain why phenotypic similarities exist among neuronal deficits resulting from mutations in MT associated proteins. Indeed, developmental expression patterns of MAP1B show a decrease in expression with maturation of most nervous tissues with the exception of DRG sensory neurons (Ma et al., 1997). As the MAP1B phenotype has been interpreted as resulting from changes in MT stabilization in addition to effects on axonal transport, the prominent expression of MAP1B and dystonin in sensory neurons suggests loss of this interaction may significantly contribute to MT instability. Interestingly, while aberrant MAP1B localization can be seen in dt^{27J} sensory neurons, silencing of dystonin-a2 in 293T cells does not alter localization of ectopically overexpressed MAP1B. While many differences, no doubt, exist between these two systems, we have observed an increased MAP1B phosphorylation status in phenotypic dt^{27J} DRG tissue relative to WT littermates (data not shown). This change in phosphorylation may be the result of altered kinase activity associated with the neurodegenerative process that is not represented by transient knockdown of dystonin-a2 *in vitro*. This may explain why we see altered MAP1B localization specifically in *dt* sensory neurons. The requirement of the dystonin-a2/MAP1B interaction for maintenance of MT acetylation status suggests that mutual expression of dystonin and MAP1B is critical in sensory neurons. Moreover, these data propose a role for MAP1B in other neurodegenerative conditions associated with mutations of plakin family members such as MACF1.

Plakins as regulator of MT polymerization: Mammalian and Drosophila plakin family members (mammalian MACF1 and dystonin, *Drosophila* Short stop) associate with MTs using two conserved domains: the Gas2 related domain and its adjacent carboxy terminal tail region (Leung et al., n.d.; Sun et al., 2001b; Lee and Kolodziej, 2002). While Gas2 related domains associate along MT shafts and promote MT stabilization (Sun et al., 2001b; Lee and Kolodziej, 2002) the carboxy terminus of MACF1 and Short stop have recently been shown to bind EB1 and localize at growing MT ends (Kodama et al., 2003; Slep et al., 2005; Applewhite et al., 2010), establishing plakins as putative +tip interacting proteins. Here, we show that dystonin/MAP1B interaction is critical to Golgi organization around the centrosome and supports MT polymerization. Plus-end polymerization from the Golgi toward the leading edge of the cell supports cell migration (Bisel et al., 2008; Miller et al., 2009). MAP1B has previously been shown to localize to the centrosome where it promotes MT nucleation (Domínguez et al., 1994) and numerous mutations of MT associated proteins including MAP1B and MACF1 are causal in defects of neuronal migration and cortical development (Meixner et al., 2000; Teng et al., 2001; Goryunov et al., 2010). Furthermore, migration defects have been noted in mice with mutations in the smaller epithelial isoform of dystonin (dystonin-e) (Guo et al., 1995). These data implicate dystonin in guidance of +end MTs to the leading edge of the cell and may offer insight into the role of cytoskeletal linker proteins in both axon guidance and neuronal migration.

Dystonin-a2 and organelle integrity: It has been established that organization, movement, and proper function of organelles is highly reliant upon the cytoskeleton (Barr and Egerer, 2005; Starr, 2007; Bola and Allan, 2009). The MACF1b isoform demonstrates

the dependency of organelle integrity on cytoskeletal linking proteins. MACF1b shares similar domain architecture to neuronal dystonin, and is critical for organization of the Golgi complex (Leung et al., 1999; Lin, Chen, Leung, Parry, & Liem, 2005). Chemical dispersion of the Golgi results in reorganization of MACF1b to the ER while silencing of MACF1b induces Golgi fragmentation. Furthermore, MACF1b localization to the Golgi is dictated by the protein's N-terminal plakin domain (Lin et al., 2005). We have previously demonstrated an N-terminal transmembrane domain adjacent to the plakin domain in dystonin-a2 that facilitates its localization to the outer membrane of the nuclear envelope and peri-nuclear membranes of the ER and Golgi (Young et al., 2006). Indeed, ectopic dystonin-a2 protein colocalizes with the *cis*-Golgi protein GM130 that has been attributed a functional role in MT nucleation from the Golgi (Young et al., 2006; Rivero et al., 2009). While the two proteins are expressed in many of the same tissues, DRG neurons predominantly express dystonin while MACF1 is highly expressed in brain (Leung et al., 2001b). Contrasting localization may explain why *dt* degeneration is most prominent in sensory neurons. Indeed, the similarities in domain architecture and subcellular localization make it interesting to speculate if there are compensating functions between these two plakin family members, with dystonin/MAP1B facilitating MT stability in sensory neurons and hypothetical MACF1b/MAP1B complex facilitating MT stability in brain. Thus, implicating differential expression patterns in the divergent susceptibility of various neuronal tissues to mutation of each respective protein.

Cytoskeletal cross-linker proteins as mediators of axon transport: Cytoskeletal cross-linker proteins have been the focus of much attention in disorders of the sensory motor system. Mutations in the cytoskeletal linker protein βIII-spectrin cause severe

cerebrospinal ataxia in murine and drosophila models (Clarkson et al., 2010; Lorenzo et al., 2010; Perkins et al., 2010). The ataxic phenotype is enhanced by both dynein and dynactin loss of function mutations implicating aberrant intracellular transport as a mediator of pathology (Lorenzo et al., 2010). Molecular interaction studies have implicated dystonin in regulation of the dynein motor complex through interaction with dynactin and the endosomal vesicle protein retrolinkin (Liu et al., 2003b, 2007b). The potential role for dystonin as a dynein motor complex component coupled with our findings of a role for dystonin-a2 as mediator of anterograde transport supports the notion that improper functioning of the secretory pathway causes degeneration of neurons in the sensory motor system. We have previously reported defective fast axonal transport in the sciatic nerves of phenotypic dt^{27J} mice in both orthograde and retrograde directions (De Repentigny et al., 2003). The present study elucidates the mechanism underlying aberrant transport and attributes this defect to phenotypic onset. Indeed, cytoskeletal linkers may have a general role in mediating axonal transport by regulating organelle organization. As such, their dysfunction may contribute to numerous neurodegenerative conditions whose etiologies are as yet unknown.

Materials and Methods

Reagents: *All chemicals were purchased through Sigma-Aldrich (St. Louis, MO) and all cell culture reagents were obtained from Invitrogen (Burlington, ON) except where indicated.*

Animals and cell culture: The dt^{27J} mutant mice arose from a spontaneous recessive mutation in the *Dst* allele, first identified at The Jackson Laboratory. Characterization of the mutation revealed no large rearrangements or deletions in the alleles but a drastic reduction in neuronal transcript levels (Pool et al., 2005). dt^{27J} and control littermates were sacrificed at pre-phenotype (P4 or P10) and phenotype (P15) stage. The onset of phenotype was generally assessed by the appearance of clasping of hind limbs after picking the mice up by the tails. dt^{27J} mice were genotyped by PCR amplification of genomic tail DNA. All animal procedures were performed in accordance with institutional guidelines (Animal Care and Veterinary Services and Ethics, University of Ottawa).

For primary culture of sensory neurons, spinal columns were removed from P4 or P15 mice and transferred to a dissection microscope. Approximately 40 DRGs were isolated per mouse, and subsequently digested for 15 minutes each with collagenase A (Roche, Laval QC) and papain (Worthington, Lakewood NJ) solutions. DRG neurons were dissociated with flame polished glass Pasteur pipettes and seeded onto 12 mm laminin-2 (Millipore, Billerica MA) coated coverslips at a density of 50,000 in DME with 10% FBS and 1% penicillin/streptomycin. Cells were placed in a 37^{o}C tissue culture incubator, under 8.5% CO_2. The following day, the media was changed to neuronal

maintenance media (DME base, 0.5% FBS, 2% B27, 1% glutamax, 16 μg/mL putrescine, 400 μg/mL thyroxine, 400 μg/mL triiodothyronine, 6.2 ng/mL progesterone, 5 ng/mL sodium selenite, 100 μg/mL bovine albumin serum, 5 μg/mL bovine insulin, 50 μg/mL holo-transferrin) supplemented with 200 ng/mL nerve growth factor, and 1 μM 5-fluoro-2'-deoxyuridine. A ¾ media change was carried out every other day, up until day 6 of culture, when neurons were analyzed. Where TSA treatment was performed, cells were incubated with 100 nM TSA or 0.1% DMSO for 24 h prior to analysis.

Human embryonic kidney 293T cells were maintained in DME + 10% FBS and 1% penicillin/streptomycin at 37°C and 8.5% CO_2. Cells were passaged at ~70% confluency in 10 cm plastic Petri dishes, and plated onto glass coverslips for use in immunofluorescence assays. Cell transfections were performed using either lipofectamine 2000 (Invitrogen, Burlington ON) or X-Treme Gene (Roche, Laval QC), according to the manufacturer's directions. Where TSA treatment was performed, cells were incubated with 100 nM TSA or 0.1% DMSO for 24 h prior to analysis. Where nocodazole treatment was performed, 293T cells were treated with 10 μM nocodazole for 4 h at 37°C and 8.5% CO_2. Cells were then either fixed immediately or placed on ice, and ice-cold nocodazole free maintenance media added for wash out experiments. Cells were subsequently fixed in 4% PFA at various time points for antigenic analysis.

mRNA microarray analysis: RNA was harvested from P4 WT (n=3) and dt^{27J} (n=3) DRGs using the RNeasy® Mini Kit (Qiagen, Toronto ON) according to manufacturer's protocol. Each n represents an individual animal, sacrificed from at least 2 separate litters. Expression profiling was performed using the One-Color Microarray Gene

Expression Platform and the 4x44k Whole Mouse Genome Oligo microarray (Design ID #014868) from Agilent Technologies as previously described and according to the manufacturer's protocol (Liu et al., 2010). Briefly, 300 ng of RNA was labeled and used for each microarray. The slides were hybridized at 65ºC for at least 17 hours. The slides were subsequently washed and scanned with the Agilent DNA Microarray Scanner. After scanning, the intensities of the spots were extracted using Feature Extraction Version 10.1.1. For each sample, raw median probe intensity data was normalized, using GeneSpring GX Version 10.0 (Agilent Technologies), first by scaling probe signals within each microarray by the quantiles method, then by eliminating probes with no or marginal signal in all samples, and finally by averaging the normalized signal among replicate samples. Microarray data can be downloaded from the Gene Expression Omnibus under accession number GSE30960. The k-means clustering of expression profiling microarray data was performed with the Cluster 3 program using Euclidean metrics (De Hoon et al., 2004). After clustering, only genes associated with transport were retained (561 genes) and fold changes visualized using Java Treeview (Saldanha, 2004). For cluster enrichment, all genes with a fold change greater than 1-fold or less than minus 1-fold relative to WT DRGs were clustered for GO terms using the Database for Annotation, Visualization and Integrated Discovery (DAVID) v6.7 (Dennis et al., 2003) and visualized using Cytoscape 2.8.1 (Cline et al., 2007). The significance cut off for enrichment over background was $p<0.05$ using Fisher's exact test with correction for multiple hypothesis testing by the algorithm of Benjamini and Hochberg (Benjamini and Hochberg, 1995). The background set of genes used was the entire mouse genome.

Sample preparation for electron microscopy: Samples were prepared as previously described (De Repentigny et al., 2011). Briefly, dt^{27J} (n=4) and wt (n=4) mice were anesthetized at P4 and P15 via intraperitoneal injection of tribromoethanol (Avertin). Mice were perfused transcardially with 3 ml of PBS followed by 10 ml of Karnovsky's fixative (4% PFA, 2% glutaraldehyde, and 0.1 M cacodylate buffer in PBS, pH7.4). The lumbar region of the spinal cord was dissected and DRGs collected under a Leica MZ6 stereomicroscope (Leica, Wetzlar Germany). Ultrathin sections (70 nm) were placed on a 300 mesh copper specimen grid and counterstained in 5% uranyl acetate and Reynold's lead citrate, and then observed by transmission electron microscopy. Area calibrated electron micrographs from both P4 and P15 mice were then analyzed and Golgi area measured recorded using the advances measurements module of Photoshop CS4 Extended version 11. The number of dilated Golgi per DRG was then counted relative to total Golgi resent using Image J 1.42Q in P15 dt^{27J} and WT ganglion.

Recombinant protein construct: Full-length MAP1B fused to the green fluorescent protein at the N-terminus (MAP1B-GFP) was produced by PCR amplification of mouse *MAP1B* cDNA cloned into the pSVsport vector and subcloned into pEGFP-C1 (Dr. Phillip Gordon Weeks, University of London, London, UK) (Scales et al., 2009). Dystonin-a1-myc/his, Dystonin-a2-myc/his, Nterm-dystonin-a2-MYC/HIS and FLAG-Bpag1a2ΔTM (from here on referred to as Plakin-FLAG) were developed by Dr. Kevin Young (National Research Council, Ottawa, ON, Canada). Briefly, dystonin cDNA were amplified from mouse brain RNA and cloned into either the pCMV-TAG2 vector (Stratagene) encoding an N-terminal FLAG tag, or the pEF1-myc/his vector (Invitrogen)

encoding a C-terminal myc/his tag (Young et al., 2006; Young and Kothary, 2008). The N-terminal region of dystonin-a1 was generated by RT-PCR and subcloned into the pEGFP-C1 vector (Clontech) (Young et al., 2003b). Full-length Daxx protein (Daxx-FLAG) (Dr. David Picketts, Ottawa Hospital Research Institute, Ottawa, ON Canada) was developed by fusing Daxx cDNA to an N-terminal FLAG tag in the pRK5 vector. MAP1B-Cherry was produced by PCR amplification of mouse MAP1B from a pSVsport MAP1B plasmid (Dr. Nicholas Cowan, New York University). The PCR product was ligated in frame into an m-cherry-C1 vector (Dr. Laura Trinkle-Mulcahy, University of Ottawa, Ottawa, ON Canada).

Transfection and RT-PCR: Custom siRNAs were developed to target specific dystonin isoforms. To knockdown dystonin-a1 and dystonin-a2, isoform specific nucleotides between 2310-2380 (accession number AF396878) for dystonin-a1 and nucleotides between 1-661 (accession number: DQ023311.2) for dystonin-a2 were chosen for the development of siRNAs. These regions were chosen, as they are isoform specific and share 90% identity between mouse and human dystonin/BPAG1n targets. The following siRNA sequences were efficacious in knocking down dystonin-a1 and dystonin-a2 expression, respectively: Group A (sense 5'-3') ACAUGUACGUGGAGGAGCAtt; (antisense 5'-3') UGCUCCUCCACGUACAUGUag; (sense 5'-3') CAAGCAUGAGAGAUCCAAAtt; (antisense 5'-3') UUUGGAUCUCUCAUGCUUGgg. Group B (sense 5'-3') CAAGCAUGAGAGAUCCAAAtt; (antisense 5'-3') UUUGGAUCUCUCAUGCUUGgg; (sense 5'-3') CUUCCUCUUGUUGCUCCUGtt; (antisense 5'-3') CAGGAGCAACAAGAGGAAGag. All siRNAs (Silencer® Select

Custom Designed siRNA) were obtained from Applied Biosystems and compared to the effects of scrambled controls matched for guanine/cytosine content, Ambion (Austin, TX). For shRNA-RFP (Sigma MISSION shRNA, pLKO.1-puro-CMV-TagRFP) mediated knock down, the following sequence was efficacious in knocking down dystonin expression:

5'CCGGCCCTTGTCAAACTCTACGAAACTCGAGTTTCGTAGAGTTTGACAAGG GTTTTTG3'. As a control, Sigma non-target shRNA custom clones (pLKO.1-puro-CMV-TagRFP) were used. Knockdown was assessed at the transcript and protein level following 48 h of treatment. Total RNA was collected from 293T cells using RNeasy® Mini Kit (Qiagen, Toronto ON) according to manufacturer's protocol. For RT-PCR QuantiTect® Reverse Transcription Kit was used following manufacturer's protocol. cDNAs encoding MACF1, dystonin-a1, dystonin-a2, or total dystonin and GAPDH or actin (control) were PCR amplified as previously described (Bernier et al., 1996b; Pool et al., 2005). For assessment of protein knockdown, 293T cells were co-transfected with siRNA and recombinant dystonin proteins [Nterm-dystonin-a2-MYC/HIS described in (Young and Kothary, 2008) and Nterm-dystonin-a1-GFP described in (Young et al., 2003b)] using X-Treme Gene. Cells were then visualized with a Zeiss Axiovert 200m epifluorescent microscope under 10X objective (Achroplan 0.25) equipped with an Axiocam HRM digital camera and Axiovision 4.6 software (Zeiss, Toronto ON). Fluorescence intensity of recombinant dystonin proteins was used to assess siRNA knockdown efficiency. Where the influence of MAP1B on dystonin deficient systems was evaluated, MAP1B-GFP, MAP1B-Cherry or N1-GFP, N1-Cherry empty vector was co-transfected with siRNA.

Viral Infection and Trafficking: 293T cells were infected with an adenoviral vector expressing YFP-VSVG$_{ts045}$ [VSVG (Dr. Xiaohui Zha and Dr Robin Parks, Ottawa Hospital Research Institute, Ottawa, ON Candada)] and incubated at 40.5°C for 16-20 h to permit VSVG accumulation in the ER. Where TSA treatment was performed, cells were incubated in the presence of either 100 nM TSA or 0.1% DMSO. Cells were then transferred to 32°C and incubated for time periods ranging from 10 min 24 h to allow VSVG to move to the Golgi/plasma-membrane and were fixed at the end of the 32°C incubation with 4% PFA. Cells were subsequently visualized and analyzed with an LSM 510 meta confocal microscope equipped with an EC Plan-Neofluar 40x/1.30 Oil DIC M27 objective using Zen 8.0 software (Zeiss, Toronto ON).). VSVG was considered ER associated if any residual VSVG could be visualized within ER compartments, while VSVG was considered Golgi associated once all VSVG was deposited within Golgi. Data were expressed as a percent of total cell number in each condition. Lentiviral infection of RFP-firefly luciferase [FLuc, control (Dr. Xandra Breakefield, Harvard Medical School)] and the secreted GLuc (Dr. Bakhos Tannous, Harvard Medical School) was conducted according to the method of (Badr et al., 2007). Briefly, primary sensory neurons from either P4 or P15 mice were co-infected with GLuc/FLuc lentivirus following 72 h in culture. Efficiency of infection was comparable between WT and *dt*^{27J} neuronal cultures as established by counting YFP and RFP or Cherry positive cells prior to subsequent treatment. 48 h following infection, media was changed and 50 µl media samples were harvested at various time points for analyses for GLuc activity to determine the rate of secretion. At the end of the time course cells were lysed and FLuc activity measured for standardization across samples. Luciferase activity was measured using the

Stop and Glo substrate (Promega, Madison WI) and luminescence recoded using a LUMIstar Optima luminometer from DMG labtech and analysed using Optima Version 2.10 R2.

Calcium phosphate transfection: MAP1B-Cherry was transfected into WT or *dt*^{27J} sensory neurons by calcium phosphate transfection after 72 h in culture. Maximal Cherry expression was observed 72 h after transfection. Control transfections were with N1-Cherry (Dr. Laura Trinkle-Mulcahy, University of Ottawa, Ottawa, ON Canada) empty vector plasmid. Cells were then visualized with a Zeiss Axiovert 200m epifluorescent microscope under 10X objective (Achroplan 0.25) equipped with an Axiocam HRM digital camera and Axiovision 4.6 software (Zeiss, Toronto ON). Efficiency of transfection was comparable between WT and *dt*^{27J} neuronal cultures as established by counting Cherry positive cells prior to subsequent treatment. For Gluc/Fluc analysis cells were infected 24 h following calcium phosphate transfection.

Immunocytochemistry: Cultures were fixed in 4% PFA prior to antigenic labeling. Primary antibodies used were rabbit polyclonal α-Tubulin (1:2000, Sigma), MAP1B (1:500, Sigma) mouse monoclonal anti-α-Tubulin (IgG1, 1:2000, oncogene), anti-Ac-α-Tubulin (IgG2B, 1:2000, Sigma), anti-GM130 (1:500, BD Transduction Laboratories), anti-pericentrin (1:1000, Abcam), anti-c-myc (1:800, Santa Cruz) and anti-VSVG (1:100, Dr. Xiaohui Zha, Ottawa Hospital Research Institute, Ottawa, ON Candada). Secondary antibodies used were, anti-mouse IgG1 DyeLight-549 (1:2000, Jackson ImmunoResearch) anti-mouse IgG2B DyeLight-488 (1:2000, Jackson ImmunoResearch) anti-mouse Alexa-555 (1:2000, Molecular Probes) anti-mouse Alexa-647 (1:2000,

Molecular Probes) and anti-rabbit Alexa-488 (1:2000, Molecular Probes). Antibodies were diluted in antibody buffer (PBS, 0.3% Triton X-100, 3% BSA). Where DAPI staining is indicated, samples were incubated in DAPI stain (0.2 μg/mL in PBS) for 10 min and washed 3 times in PBS for 5 min. Samples were mounted in fluorescent mounting media (Dako) and analyzed with an LSM 510 meta confocal microscope equipped with an EC Plan-Neofluar 40x/1.30 Oil DIC M27 objective using Zen 8.0 software (Zeiss, Toronto ON).

Protein interactions: For pull down assays, protein lysate from 293T cells expressing either MAP1B-GFP and Plakin-FLAG or MAP1B-GFP and Daxx-FLAG was pre-cleared overnight. Samples were subsequently incubated with either dynal protein G magnetic beads (Invitrogen) and 5 μg of FLAG antibody (M2, Sigma, mouse) or GFP conjugated magnetic beads (Abcam). IgG controls were performed by incubation of dynal protein G magnetic beads (Invitrogen) and 5 μg of rabbit or mouse IgG was used as appropriate. Samples were subsequently centrifuged or placed on a magnetic rack where appropriate. Proteins were eluted in elution buffer (60 mM Tris pH 6.8, 2% SDS, 10% glycerol) and subjected to SDS-PAGE. Proximity ligation assay was performed as previously described (Shafey et al., 2010). Briefly, HEK 293 cells were co-transfected with dystonin-a2 and MAP1B-GFP fixed with 4% PFA and antigenically labelled for myc or MAP1B. Proximity ligation assay detection was performed according to the manufacturer's specifications and analyzed with an LSM 510 meta confocal microscope equipped with an EC Plan-Neofluar 40x/1.30 Oil DIC M27 objective using Zen 8.0 software (Zeiss, Toronto ON).

Western analysis: Proteins were isolated in RIPA buffer (10 mM PBS, 1% NP40, 0.5% sodium deoxycholate, 0.1% SDS, 30 µl/ml aprotinin, 10 mM Na orthovanadate, 100 µl/ml PMSF). Protein samples (30 µg) were separated by SDS-PAGE under reducing conditions. Western analyses were performed using primary rat anti ty-α-Tubulin (1:1000, Abcam), mouse monoclonal anti-α-Tubulin (IgG1, 1:2000, Oncogene), anti-Ac-α-Tubulin (IgG2B, 1:2000, Sigma), anti-KLC2 (1:1000, Abcam), anti-BIII-tubulin (1:2000, E7 clone Hybridoma Bank), anti-MAP1B (1:5000, Sigma), FLAG (1:15000, Sigma), rabbit polyclonal anti-GAPDH (1:5000, AbCam) and GFP (1:1000, Invitrogen). Secondary antibodies used were biotin conjugated anti-rat (1:2000, Jackson ImmunoResearch), HRP-conjugated anti-mouse IgG (1:2000, BioRad) or HRP-conjugated anti-rabbit IgG (1:2000, BioRad). Tertiary amplification was performed using HRP-conjugated neutravidin (1:2000, Fisher Scientific). Immunoreactive bands were visualized using enhanced chemiluminescent substrate (Fisher Scientific). Quantification of protein levels was performed using either the Odyssey infrared fluorescence detection system or by densitometric analysis of individual bands using ImageJ analysis software (NIH). For infrared analysis, mouse anti-Ac-α-Tub and anti-GAPDH were probed simultaneously in combination with rabbit anti-α-Tub (total). Appropriate infrared secondary antibodies allowed for direct quantification of the ratio of Ac-α-Tub to total α-Tub normalized to GAPDH on each membrane. Four experiments were conducted and the resulting blots and quantification are depicted.

Statistical analysis: All error bars reflect standard error of the mean. Data were analyzed using Student's *t*-test or factorial ANOVA as applicable using Instat v3.0. Following detection of a statistically significant difference in a given series of treatments by ANOVA, *post hoc* Dunnett's *t*-tests or Tukey tests were performed where appropriate. P values under 0.05 were considered statistically significant (shown as *); P values under 0.01 were considered highly statistically significant (shown as **).

Online Supplemental Material

Figure S1 shows that the defect in secretion and MT stability observed following isoform-specific dystonin-a2 depletion is consistently observed across multiple siRNA and shRNA sequences. Figure S2 shows that the defect in transport is not due to aberrant protein folding. Figure S3 shows that dystonin-a2 silencing results in loss of MAP1B localization at the centrosome. In addition, this figure shows that MAP1B alone promotes MT stabilization by maintaining α-tubulin acetylation status.

Acknowledgements

We thank Justin Boyer for comments on the manuscript and the rest of the Kothary laboratory for helpful discussions. We also thank Drs. Xandra Breakefield and Bakhos Tannous for donation of Gluc/Fluc lentivirus, Xiaohui Zha and Robin Parks for the VSVG adenovirus and David Picketts for the Daxx construct. MAP1B-GFP was kindly provided by Dr. Phillip Gordon Weeks, pSVsport-MAP1B was kindly provided by Dr. Nicholas Cowan and m-cherry-C1 was a gift from Dr. Laura Trinkle-Mulcahy. This work was supported by a grant from the Canadian Institutes of Health Research (CIHR), and a

Multiple Sclerosis Society of Canada Research Fellowship and a CIHR Fellowship to SDR with the support of the Dystonia Medical Research Foundation of Canada. AF is supported by an Ontario Graduate Scholarship (OGS). RK is a recipient of a University Health Research Chair from the University of Ottawa.

Abbreviations

acetylated	Ac
clathrin, light chain B	CLTB
dorsal root ganglia	DRG
dystonia musculorum	*dt*
dystonin gene	*dst*
gene ontology	GO
huntingtin	HTT
microtubule	MT
microtubule–actin crosslinking factor	MACF
microtubule associated protein 1B	MAP1B
microtubule-associated protein tau	MAPT
plasma membrane	PM
RFP-firefly luciferase	FLuc
spastin	SPAST
trichostatin A	TSA
tubulin polymerization promoting protein	TPPP
YFP-Gaussia luciferase	GLuc
YFP tagged VSV-$G^{ts0\text{-}45}$	VSVG

References

al-Ali SY, al-Zuhair AG (1989) Fine structural study of the spinal cord and spinal ganglia in mice afflicted with a hereditary sensory neuropathy, dystonia musculorum. Journal of submicroscopic cytology and pathology 21:737–748.

Antolik C, Catino DH, O'Neill AM, Resneck WG, Ursitti JA, Bloch RJ (2007) The actin binding domain of ACF7 binds directly to the tetratricopeptide repeat domains of rapsyn. Neuroscience 145:56–65.

Aplin A, Jasionowski T, Tuttle DL, Lenk SE, Dunn WA (1992) Cytoskeletal elements are required for the formation and maturation of autophagic vacuoles. Journal of cellular physiology 152:458–466.

Applewhite DA, Grode KD, Keller D, Zadeh AD, Zadeh A, Slep KC, Rogers SL (2010) The spectraplakin Short stop is an actin-microtubule cross-linker that contributes to organization of the microtubule network. Molecular biology of the cell 21:1714–1724.

Axelrod FB, Gold-von Simson G (2007) Hereditary sensory and autonomic neuropathies: types II, III, and IV. Orphanet journal of rare diseases 2:39.

Badr CE, Hewett JW, Breakefield XO, Tannous BA (2007) A highly sensitive assay for monitoring the secretory pathway and ER stress. PloS one 2:e571.

Barr FA, Egerer J (2005) Golgi positioning: are we looking at the right MAP? The Journal of cell biology 168:993–998.

Batlevi Y, Martin DN, Pandey UB, Simon CR, Powers CM, Taylor JP, Baehrecke EH (2010) Dynein light chain 1 is required for autophagy, protein clearance, and cell death in Drosophila. Proceedings of the National Academy of Sciences of the United States of America 107:742–747.

Bekoff A, Betz WJ (1977) Physiological properties of dissociated muscle fibres obtained from innervated and denervated adult rat muscle. The Journal of physiology 271:25–40.

Bernier G, Brown A, Dalpé G, De Repentigny Y, Mathieu M, Kothary R (1995) Dystonin expression in the developing nervous system predominates in the neurons that degenerate in dystonia musculorum mutant mice. Molecular and cellular neurosciences 6:509–520.

Bernier G, De Repentigny Y, Mathieu M, David S, Kothary R (1998) Dystonin is an essential component of the Schwann cell cytoskeleton at the time of myelination. Development 125:2135–2148.

Bernier G, Kothary R (1998) Prenatal onset of axonopathy in Dystonia musculorum mice. Dev Genet 22:160–168.

Bernier G, Mathieu M, De Repentigny Y, Vidal SM, Kothary R (1996a) Cloning and characterization of mouse ACF7, a novel member of the dystonin subfamily of actin binding proteins. Genomics 38:19–29.

Bernier G, Mathieu M, De Repentigny Y, Vidal SM, Kothary R (1996b) Cloning and characterization of mouse ACF7, a novel member of the dystonin subfamily of actin binding proteins. Genomics 38:19–29.

Bhanot K, Young KG, Kothary R (2011) MAP1B and clathrin are novel interacting partners of the giant cyto-linker dystonin. J Proteome Res 10:5118–5127.

Bisel B, Wang Y, Wei J-H, Xiang Y, Tang D, Miron-Mendoza M, Yoshimura S, Nakamura N, Seemann J (2008) ERK regulates Golgi and centrosome orientation towards the leading edge through GRASP65. The Journal of cell biology 182:837–843.

Bjørkøy G, Lamark T, Brech A, Outzen H, Perander M, Overvatn A, Stenmark H, Johansen T (2005) p62/SQSTM1 forms protein aggregates degraded by autophagy and has a protective effect on huntingtin-induced cell death. The Journal of cell biology 171:603–614.

Bola B, Allan V (2009) How and why does the endoplasmic reticulum move? Biochemical Society transactions 37:961–965.

Boland B, Kumar A, Lee S, Platt FM, Wegiel J, Yu WH, Nixon RA (2008) Autophagy induction and autophagosome clearance in neurons: relationship to autophagic pathology in Alzheimer's disease. J Neurosci 28:6926–6937.

Bologna G, Yvon C, Duvaud S, Veuthey AL (2004) N-Terminal myristoylation predictions by ensembles of neural networks. Proteomics 4:1626–1632.

Bondallaz P, Barbier A, Soehrman S, Grenningloh G, Riederer BM (2006) The control of microtubule stability in vitro and in transfected cells by MAP1B and SCG10. Cell motility and the cytoskeleton 63:681–695.

Bouquet C, Soares S, Von Boxberg Y, Ravaille-Veron M, Propst F, Nothias F (2004) Microtubule-associated protein 1B controls directionality of growth cone migration and axonal branching in regeneration of adult dorsal root ganglia neurons. The Journal of neuroscience : the official journal of the Society for Neuroscience 24:7204–7213.

Bowerman M, Murray LM, Beauvais A, Pinheiro B, Kothary R (2012) A critical smn threshold in mice dictates onset of an intermediate spinal muscular atrophy

phenotype associated with a distinct neuromuscular junction pathology. Neuromuscular disorders : NMD 22:263–276.

Boyce M, Bryant KF, Jousse C, Long K, Harding HP, Scheuner D, Kaufman RJ, Ma D, Coen DM, Ron D, Yuan J (2005) A selective inhibitor of eIF2alpha dephosphorylation protects cells from ER stress. Science (New York, NY) 307:935–939.

Boyer JG, Bernstein MA, Boudreau-Lariviere C (2009) Plakins in striated muscle. Muscle Nerve 41:299–308.

Broderick MJ, Winder SJ (2005) Spectrin, alpha-actinin, and dystrophin. Adv Protein Chem 70:203–246.

Brown A, Bernier G, Mathieu M, Rossant J, Kothary R (1995) The mouse dystonia musculorum gene is a neural isoform of bullous pemphigoid antigen 1. Nature genetics 10:301–306.

Brown A, Dalpe G, Mathieu M, Kothary R (n.d.) Cloning and characterization of the neural isoforms of human dystonin. Genomics 29:777–780.

Burkhardt JK (1998) The role of microtubule-based motor proteins in maintaining the structure and function of the Golgi complex. Biochimica et biophysica acta 1404:113–126.

Campbell RM, Peterson AC (1992) An intrinsic neuronal defect operates in dystonia musculorum: a study of dt/dt<==>+/+ chimeras. Neuron 9:693–703.

Carlsten JA, Kothary R, Wright DE (2001) Glial cell line-derived neurotrophic factor-responsive and neurotrophin- 3-responsive neurons require the cytoskeletal linker protein dystonin for postnatal survival. Journal of Comparative Neurology 432:155–68. ST – Glial cell line–derived neurotrophic.

Chabin-Brion K, Marceiller J, Perez F, Settegrana C, Drechou A, Durand G, Poüs C (2001) The Golgi complex is a microtubule-organizing organelle. Molecular biology of the cell 12:2047–2060.

Cheishvili D, Maayan C, Cohen-Kupiec R, Lefler S, Weil M, Ast G, Razin A (2011) IKAP/Elp1 involvement in cytoskeleton regulation and implication for familial dysautonomia. Human molecular genetics 20:1585–1594.

Chen HJ, Lin CM, Lin CS, Perez-Olle R, Leung CL, Liem RK (2006) The role of microtubule actin cross-linking factor 1 (MACF1) in the Wnt signaling pathway. Genes Dev 20:1933–1945.

Chen X-J, Levedakou EN, Millen KJ, Wollmann RL, Soliven B, Popko B (2007) Proprioceptive sensory neuropathy in mice with a mutation in the cytoplasmic Dynein heavy chain 1 gene. The Journal of neuroscience : the official journal of the Society for Neuroscience 27:14515–14524.

Cheung HH, Lynn Kelly N, Liston P, Korneluk RG (2006) Involvement of caspase-2 and caspase-9 in endoplasmic reticulum stress-induced apoptosis: a role for the IAPs. Experimental cell research 312:2347–2357.

Chhabra ES, Higgs HN (2007) The many faces of actin: matching assembly factors with cellular structures. Nat Cell Biol 9:1110–1121.

Chiken S, Shashidharan P, Nambu A (2008) Cortically evoked long-lasting inhibition of pallidal neurons in a transgenic mouse model of dystonia. The Journal of neuroscience : the official journal of the Society for Neuroscience 28:13967–13977.

Cifuentes-Diaz C, Nicole S, Velasco ME, Borra-Cebrian C, Panozzo C, Frugier T, Millet G, Roblot N, Joshi V, Melki J (2002) Neurofilament accumulation at the motor endplate and lack of axonal sprouting in a spinal muscular atrophy mouse model. Human molecular genetics 11:1439–1447.

Clarkson YL, Gillespie T, Perkins EM, Lyndon AR, Jackson M (2010) Beta-III spectrin mutation L253P associated with spinocerebellar ataxia type 5 interferes with binding to Arp1 and protein trafficking from the Golgi. Human molecular genetics 19:3634–3641.

Cline MS et al. (2007) Integration of biological networks and gene expression data using Cytoscape. Nature protocols 2:2366–2382.

Creppe C, Malinouskaya L, Volvert M-L, Gillard M, Close P, Malaise O, Laguesse S, Cornez I, Rahmouni S, Ormenese S, Belachew S, Malgrange B, Chapelle J-P, Siebenlist U, Moonen G, Chariot A, Nguyen L (2009) Elongator controls the migration and differentiation of cortical neurons through acetylation of alpha-tubulin. Cell 136:551–564.

Dalpe G, Leclerc N, Vallee A, Messer A, Mathieu M, De Repentigny Y, Kothary R (1998) Dystonin Is Essential for Maintaining Neuronal Cytoskeleton Organization. Mol Cell Neurosci 10:243–257.

Dalpe G, Mathieu M, Comtois A, Zhu E, Wasiak S, De Repentigny Y, Leclerc N, Kothary R (1999) Dystonin-deficient mice exhibit an intrinsic muscle weakness and an instability of skeletal muscle cytoarchitecture. Dev Biol 210:367–380.

Dalpé G, Leclerc N, Vallée A, Messer A, Mathieu M, De Repentigny Y, Kothary R (1998) Dystonin is essential for maintaining neuronal cytoskeleton organization. Molecular And Cellular Neurosciences 10:243–257.

De Hoon MJL, Imoto S, Nolan J, Miyano S (2004) Open source clustering software. Bioinformatics (Oxford, England) 20:1453–1454.

De Repentigny Y, Deschenes-Furry J, Jasmin BJ, Kothary R (2003) Impaired fast axonal transport in neurons of the sciatic nerves from dystonia musculorum mice. J Neurochem 86:564–571.

De Repentigny Y, Ferrier A, Ryan SD, Sato T, Kothary R (2011) Motor Unit Abnormalities in Dystonia musculorum Mice Feany MB, ed. PLoS ONE 6:14.

De Waegh SM, Lee VM, Brady ST (1992) Local modulation of neurofilament phosphorylation, axonal caliber, and slow axonal transport by myelinating Schwann cells. Cell 68:451–463.

Dennis G, Sherman BT, Hosack DA, Yang J, Gao W, Lane HC, Lempicki RA (2003) DAVID: Database for Annotation, Visualization, and Integrated Discovery. Genome biology 4:P3.

Di Zenzo G, Della Torre R, Zambruno G, Borradori L (2012) Bullous pemphigoid: from the clinic to the bench. Clin Dermatol 30:3–16.

Djinovic-Carugo K, Gautel M, Ylanne J, Young P (2002) The spectrin repeat: a structural platform for cytoskeletal protein assemblies. FEBS Lett 513:119–123.

Dompierre JP, Godin JD, Charrin BC, Cordelières FP, King SJ, Humbert S, Saudou F (2007) Histone deacetylase 6 inhibition compensates for the transport deficit in Huntington's disease by increasing tubulin acetylation. The Journal of neuroscience : the official journal of the Society for Neuroscience 27:3571–3583.

Domínguez JE, Buendia B, López-Otín C, Antony C, Karsenti E, Avila J (1994) A protein related to brain microtubule-associated protein MAP1B is a component of the mammalian centrosome. Journal of cell science 107 (Pt 2:601–611.

Dowling J, Yang Y, Wollmann R, Reichardt LF, Fuchs E (1997) Developmental expression of BPAG1-n: insights into the spastic ataxia and gross neurologic degeneration in dystonia musculorum mice. Dev Biol 187:131–142.

Duchen LW (1976) Dystonia musculorum--an inherited disease of the nervous system in the mouse. Advances in neurology 14:353–365.

Duchen LW, Strich SJ, Falconer DS (1964) CLINICAL AND PATHOLOGICAL STUDIES OF AN HEREDITARY NEUROPATHY IN MICE (DYSTONIA MUSCULORUM). Brain : a journal of neurology 87:367–378.

Dyck, P.J., Thomas, P.K., Griffin, J.W., Low, P.A., Poduslo JF (2005) (Eds) Peripherial Neuropathy. (WB Saunders, Philadelphia).

Edvardson S, Cinnamon Y, Jalas C, Shaag A, Maayan C, Axelrod FB, Elpeleg O (2012) Hereditary sensory autonomic neuropathy caused by a mutation in dystonin. Annals of neurology 71:569–572.

Ehrlich BE, Kaftan E, Bezprozvannaya S, Bezprozvanny I (1994) The pharmacology of intracellular Ca(2+)-release channels. Trends in pharmacological sciences 15:145–149.

Elliott DA, Kim WS, Gorissen S, Halliday GM, Kwok JB (2012) Leucine-rich repeat kinase 2 and alternative splicing in Parkinson's disease. Mov Disord.

Eschbach J, Dupuis L (2011) Cytoplasmic dynein in neurodegeneration. Pharmacol Ther 130:348–363.

Eyer J, Cleveland DW, Wong PC, Peterson AC (1998) Pathogenesis of two axonopathies does not require axonal neurofilaments. Nature 391:584–587.

Ferri KF, Kroemer G (2001) Organelle-specific initiation of cell death pathways. Nature cell biology 3:E255–63.

Ferrier A, Boyer JG, Kothary R (2013) Cellular and Molecular Biology of Neuronal Dystonin. International review of cell and molecular biology 300:85–120.

Fuchs E, Karakesisoglou I (2001) Bridging cytoskeletal intersections. Genes Dev 15:1–14.

Galletta BJ, Mooren OL, Cooper JA (2010) Actin dynamics and endocytosis in yeast and mammals. Curr Opin Biotechnol 21:604–610.

Gavrilina TO, McGovern VL, Workman E, Crawford TO, Gogliotti RG, DiDonato CJ, Monani UR, Morris GE, Burghes AHM (2008) Neuronal SMN expression corrects spinal muscular atrophy in severe SMA mice while muscle-specific SMN expression has no phenotypic effect. Human molecular genetics 17:1063–1075.

Geeraert C, Ratier A, Pfisterer SG, Perdiz D, Cantaloube I, Rouault A, Pattingre S, Proikas-Cezanne T, Codogno P, Poüs C (2010) Starvation-induced hyperacetylation of tubulin is required for the stimulation of autophagy by nutrient deprivation. The Journal of biological chemistry 285:24184–24194.

Giorda R, Cerritello A, Bonaglia MC, Bova S, Lanzi G, Repetti E, Giglio S, Baschirotto C, Pramparo T, Avolio L, Bragheri R, Maraschio P, Zuffardi O (2004) Selective disruption of muscle and brain-specific BPAG1 isoforms in a girl with a 6;15 translocation, cognitive and motor delay, and tracheo-oesophageal atresia. Journal of medical genetics 41:e71.

González-Billault C, Del Río JA, Ureña JM, Jiménez-Mateos EM, Barallobre MJ, Pascual M, Pujadas L, Simó S, Torre A La, Gavin R, Wandosell F, Soriano E, Avila J (2005) A role of MAP1B in Reelin-dependent neuronal migration. Cerebral cortex (New York, NY : 1991) 15:1134–1145.

Goryunov D, Adebola A, Jefferson JJ, Leung CL, Messer A, Liem RK (2007) Molecular characterization of the genetic lesion in Dystonia musculorum (dt-Alb) mice. Brain Res 1140:179–187.

Goryunov D, He CZ, Lin CS, Leung CL, Liem RK (2010) Nervous-tissue-specific elimination of microtubule-actin crosslinking factor 1a results in multiple developmental defects in the mouse brain. Mol Cell Neurosci 44:1–14.

Guillery RW, August BK (2002) Doubt and certainty in counting. Progress in brain research 135:25–42.

Guo L, Degenstein L, Dowling J, Yu QC, Wollmann R, Perman B, Fuchs E (1995) Gene targeting of BPAG1: abnormalities in mechanical strength and cell migration in stratified epithelia and neurologic degeneration. Cell 81:233–243.

Gülow K, Bienert D, Haas IG (2002) BiP is feed-back regulated by control of protein translation efficiency. Journal of cell science 115:2443–2452.

Hara T, Nakamura K, Matsui M, Yamamoto A, Nakahara Y, Suzuki-Migishima R, Yokoyama M, Mishima K, Saito I, Okano H, Mizushima N (2006) Suppression of basal autophagy in neural cells causes neurodegenerative disease in mice. Nature 441:885–889.

He C, Klionsky DJ (2009) Regulation mechanisms and signaling pathways of autophagy. Annual review of genetics 43:67–93.

Hitomi J, Katayama T, Eguchi Y, Kudo T, Taniguchi M, Koyama Y, Manabe T, Yamagishi S, Bando Y, Imaizumi K, Tsujimoto Y, Tohyama M (2004) Involvement of caspase-4 in endoplasmic reticulum stress-induced apoptosis and Abeta-induced cell death. The Journal of cell biology 165:347–356.

Ho WC, Allan VJ, Van Meer G, Berger EG, Kreis TE (1989) Reclustering of scattered Golgi elements occurs along microtubules. Eur J Cell Biol 48:250–263.

Howard J, Hyman AA (2003) Dynamics and mechanics of the microtubule plus end. Nature 422:753–758.

Høyer-Hansen M, Jäättelä M (2007) Connecting endoplasmic reticulum stress to autophagy by unfolded protein response and calcium. Cell death and differentiation 14:1576–1582.

Ikenaka K, Kawai K, Katsuno M, Huang Z, Jiang Y-M, Iguchi Y, Kobayashi K, Kimata T, Waza M, Tanaka F, Mori I, Sobue G (2013) dnc-1/dynactin 1 Knockdown Disrupts Transport of Autophagosomes and Induces Motor Neuron Degeneration. PloS one 8:e54511.

Jahreiss L, Menzies FM, Rubinsztein DC (2008) The itinerary of autophagosomes: from peripheral formation to kiss-and-run fusion with lysosomes. Traffic (Copenhagen, Denmark) 9:574–587.

Janota I (1972) Ultrastructural studies of an hereditary sensory neuropathy in mice (dystonia musculorum). Brain 95:529–536.

Jefferson JJ, Ciatto C, Shapiro L, Liem RK (2007) Structural analysis of the plakin domain of bullous pemphigoid antigen1 (BPAG1) suggests that plakins are members of the spectrin superfamily. J Mol Biol 366:244–257.

Jefferson JJ, Leung CL, Liem RK (2004) Plakins: goliaths that link cell junctions and the cytoskeleton. Nat Rev Mol Cell Biol 5:542–553.

Jefferson JJ, Leung CL, Liem RKH (2006) Dissecting the sequence specific functions of alternative N-terminal isoforms of mouse bullous pemphigoid antigen 1. Experimental cell research 312:2712–2725.

Jiang SX, Lertvorachon J, Hou ST, Konishi Y, Webster J, Mealing G, Brunette E, Tauskela J, Preston E (2005) Chlortetracycline and demeclocycline inhibit calpains and protect mouse neurons against glutamate toxicity and cerebral ischemia. The Journal of biological chemistry 280:33811–33818.

Johansen T, Lamark T (2011) Selective autophagy mediated by autophagic adapter proteins. Autophagy 7:279–296.

Junker U, Rittner K, Homann M, Bevec D, Bohnlein E, Sczakiel G (1994) Reduction in replication of the human immunodeficiency virus type 1 in human T cell lines by polymerase III-driven transcription of chimeric tRNA-antisense RNA genes. Antisense Res Dev 4:165–172.

Karakesisoglou I, Yang Y, Fuchs E (2000) An epidermal plakin that integrates actin and microtubule networks at cellular junctions. J Cell Biol 149:195–208.

Kariya S, Park G-H, Maeno-Hikichi Y, Leykekhman O, Lutz C, Arkovitz MS, Landmesser LT, Monani UR (2008) Reduced SMN protein impairs maturation of the neuromuscular junctions in mouse models of spinal muscular atrophy. Human molecular genetics 17:2552–2569.

Katayama T, Imaizumi K, Sato N, Miyoshi K, Kudo T, Hitomi J, Morihara T, Yoneda T, Gomi F, Mori Y, Nakano Y, Takeda J, Tsuda T, Itoyama Y, Murayama O,

Takashima A, St George-Hyslop P, Takeda M, Tohyama M (1999) Presenilin-1 mutations downregulate the signalling pathway of the unfolded-protein response. Nature cell biology 1:479–485.

Kegel KB, Kim M, Sapp E, McIntyre C, Castaño JG, Aronin N, DiFiglia M (2000) Huntingtin expression stimulates endosomal-lysosomal activity, endosome tubulation, and autophagy. The Journal of neuroscience : the official journal of the Society for Neuroscience 20:7268–7278.

Keire P, Shearer A, Shefer G, Yablonka-Reuveni Z (2013) Isolation and culture of skeletal muscle myofibers as a means to analyze satellite cells. Methods in molecular biology (Clifton, NJ) 946:431–468.

Ketema M, Sonnenberg A (2011) Nesprin-3: a versatile connector between the nucleus and the cytoskeleton. Biochem Soc Trans 39:1719–1724.

Kimura S, Noda T, Yoshimori T (2008) Dynein-dependent movement of autophagosomes mediates efficient encounters with lysosomes. Cell structure and function 33:109–122.

Kodama A, Karakesisoglou I, Wong E, Vaezi A, Fuchs E (2003) ACF7: an essential integrator of microtubule dynamics. Cell 115:343–354.

Koga H, Kaushik S, Cuervo AM (2011) Protein homeostasis and aging: The importance of exquisite quality control. Ageing research reviews 10:205–215.

Komatsu M, Waguri S, Chiba T, Murata S, Iwata J, Tanida I, Ueno T, Koike M, Uchiyama Y, Kominami E, Tanaka K (2006) Loss of autophagy in the central nervous system causes neurodegeneration in mice. Nature 441:880–884.

Korenbaum E, Rivero F (2002) Calponin homology domains at a glance. J Cell Sci 115:3543–3545.

Kothary R, Clapoff S, Brown A, Campbell R, Peterson A, Rossant J (1988) A transgene containing lacZ inserted into the dystonia locus is expressed in neural tube. Nature 335:435–437.

Kreitzer G, Liao G, Gundersen GG (1999) Detyrosination of tubulin regulates the interaction of intermediate filaments with microtubules in vivo via a kinesin-dependent mechanism. Molecular biology of the cell 10:1105–1118.

Köchl R, Hu XW, Chan EYW, Tooze SA (2006) Microtubules facilitate autophagosome formation and fusion of autophagosomes with endosomes. Traffic (Copenhagen, Denmark) 7:129–145.

Lai CS-W, Preisler J, Baum L, Lee DH-S, Ng H-K, Hugon J, So K-F, Chang RC-C (2009) Low molecular weight Abeta induces collapse of endoplasmic reticulum. Molecular and cellular neurosciences 41:32–43.

Lalonde R, Marchetti N, Strazielle C (2005) Primary neurologic screening and motor coordination of Dstdt-J mutant mice (dystonia musculorum) with spinocerebellar atrophy. Physiology & behavior 86:46–51.

LaMonte BH, Wallace KE, Holloway BA, Shelly SS, Ascaño J, Tokito M, Van Winkle T, Howland DS, Holzbaur ELF (2002) Disruption of dynein/dynactin inhibits axonal transport in motor neurons causing late-onset progressive degeneration. Neuron 34:715–727.

Lance-Jones C (1982) Motoneuron cell death in the developing lumbar spinal cord of the mouse. Brain research 256:473–479.

Le Rumeur E, Hubert JF, Winder SJ (2012) A new twist to coiled coil. FEBS Lett.

Lee A-H, Iwakoshi NN, Glimcher LH (2003) XBP-1 regulates a subset of endoplasmic reticulum resident chaperone genes in the unfolded protein response. Molecular and cellular biology 23:7448–7459.

Lee MK, Cleveland DW (1996) Neuronal intermediate filaments. Annu Rev Neurosci 19:187–217

Lee S, Kolodziej PA (2002) Short Stop provides an essential link between F-actin and microtubules during axon extension. Development (Cambridge, England) 129:1195–1204.

Lemere CA, Lopera F, Kosik KS, Lendon CL, Ossa J, Saido TC, Yamaguchi H, Ruiz A, Martinez A, Madrigal L, Hincapie L, Arango JC, Anthony DC, Koo EH, Goate AM, Selkoe DJ (1996) The E280A presenilin 1 Alzheimer mutation produces increased A beta 42 deposition and severe cerebellar pathology. Nature medicine 2:1146–1150.

Leung CL, Green KJ, Liem RK (2002) Plakins: a family of versatile cytolinker proteins. Trends Cell Biol 12:37–45.

Leung CL, Sun D, Liem RK (n.d.) The intermediate filament protein peripherin is the specific interaction partner of mouse BPAG1-n (dystonin) in neurons. J Cell Biol 144:435–446.

Leung CL, Sun D, Zheng M, Knowles DR, Liem RK (n.d.) Microtubule actin cross-linking factor (MACF): a hybrid of dystonin and dystrophin that can interact with the actin and microtubule cytoskeletons. J Cell Biol 147:1275–1286.

Leung CL, Zheng M, Prater SM, Liem RK (2001a) The BPAG1 locus: Alternative splicing produces multiple isoforms with distinct cytoskeletal linker domains, including predominant isoforms in neurons and muscles. J Cell Biol 154:691–697.

Leung CL, Zheng M, Prater SM, Liem RK (2001b) The BPAG1 locus: Alternative splicing produces multiple isoforms with distinct cytoskeletal linker domains, including predominant isoforms in neurons and muscles. The Journal of cell biology 154:691–697.

Leung CL, Zheng M, Prater SM, Liem RK (2001c) The BPAG1 locus: Alternative splicing produces multiple isoforms with distinct cytoskeletal linker domains, including predominant isoforms in neurons and muscles. J Cell Biol 154:691–697.

Levine B, Kroemer G (2008) Autophagy in the pathogenesis of disease. Cell 132:27–42.

Li L, Zhang X, Le W (2008) Altered macroautophagy in the spinal cord of SOD1 mutant mice. Autophagy 4:290–293.

Lin CM, Chen HJ, Leung CL, Parry DA, Liem RK (2005) Microtubule actin crosslinking factor 1b: a novel plakin that localizes to the Golgi complex. J Cell Sci 118:3727–3738.

Liu J-J, Ding J, Kowal AS, Nardine T, Allen E, Delcroix J-D, Wu C, Mobley W, Fuchs E, Yang Y (2003a) BPAG1n4 is essential for retrograde axonal transport in sensory neurons. The Journal of cell biology 163:223–229.

Liu J-J, Ding J, Wu C, Bhagavatula P, Cui B, Chu S, Mobley WC, Yang Y (2007a) Retrolinkin, a membrane protein, plays an important role in retrograde axonal transport. Proceedings of the National Academy of Sciences of the United States of America 104:2223–2228.

Liu JJ, Ding J, Kowal AS, Nardine T, Allen E, Delcroix JD, Wu C, Mobley W, Fuchs E, Yang Y (2003b) BPAG1n4 is essential for retrograde axonal transport in sensory neurons. J Cell Biol 163:223–229.

Liu JJ, Ding J, Kowal AS, Nardine T, Allen E, Delcroix JD, Wu C, Mobley W, Fuchs E, Yang Y (2003c) BPAG1n4 is essential for retrograde axonal transport in sensory neurons. J Cell Biol 163:223–229.

Liu JJ, Ding J, Wu C, Bhagavatula P, Cui B, Chu S, Mobley WC, Yang Y (2007b) Retrolinkin, a membrane protein, plays an important role in retrograde axonal transport. Proc Natl Acad Sci U S A 104:2223–2228.

Liu L, Vo A, Liu G, McKeehan WL (2005) Distinct structural domains within C19ORF5 support association with stabilized microtubules and mitochondrial aggregation and genome destruction. Cancer research 65:4191–4201.

Liu Y, Chu A, Chakroun I, Islam U, Blais A (2010) Cooperation between myogenic regulatory factors and SIX family transcription factors is important for myoblast differentiation. Nucleic acids research 38:6857–6871.

Lorenzo DN, Li M, Mische SE, Armbrust KR, Ranum LPW, Hays TS (2010) Spectrin mutations that cause spinocerebellar ataxia type 5 impair axonal transport and induce neurodegeneration in Drosophila. The Journal of cell biology 189:143–158.

Lowe M (2011) Structural organization of the Golgi apparatus. Current opinion in cell biology 23:85–93.

Lytton J, Westlin M, Hanley MR (1991) Thapsigargin inhibits the sarcoplasmic or endoplasmic reticulum Ca-ATPase family of calcium pumps. The Journal of biological chemistry 266:17067–17071.

Ma D, Nothias F, Boyne LJ, Fischer I (1997) Differential regulation of microtubule-associated protein 1B (MAP1B) in rat CNS and PNS during development. J Neurosci Res 49:319–332.

Maatta A, Hutchison CJ, Watson MD (2004) Spectraplakins and nesprins, giant spectrin repeat proteins participating in the organization of the cytoskeleton and the nuclear envelope. Symp Soc Exp Biol:265–277.

Maday S, Wallace KE, Holzbaur ELF (2012) Autophagosomes initiate distally and mature during transport toward the cell soma in primary neurons. The Journal of cell biology 196:407–417

Mancini M, Machamer CE, Roy S, Nicholson DW, Thornberry NA, Casciola-Rosen LA, Rosen A (2000) Caspase-2 is localized at the Golgi complex and cleaves golgin-160 during apoptosis. The Journal of cell biology 149:603–612.

Marchbank K, Waters S, Roberts RG, Solomon E, Whitehouse CA (2012) MAP1B Interaction with the FW Domain of the Autophagic Receptor Nbr1 Facilitates Its Association to the Microtubule Network. International journal of cell biology 2012:208014.

Martin DD, Beauchamp E, Berthiaume LG (2011) Post-translational myristoylation: Fat matters in cellular life and death. Biochimie 93:18–31.

Martini R (2001) The effect of myelinating Schwann cells on axons. Muscle & nerve 24:456–466.

Masliah E, Mallory M, Ge N, Alford M, Veinbergs I, Roses AD (1995) Neurodegeneration in the central nervous system of apoE-deficient mice. Experimental neurology 136:107–122.

McHanwell S, Biscoe TJ (1981) The localization of motoneurons supplying the hindlimb muscles of the mouse. Philosophical transactions of the Royal Society of London Series B, Biological sciences 293:477–508.

McIlwain DL (1991) Nuclear and cell body size in spinal motor neurons. Advances in neurology 56:67–74.

Meggouh F, Bienfait HME, Weterman MAJ, De Visser M, Baas F (2006) Charcot-Marie-Tooth disease due to a de novo mutation of the RAB7 gene. Neurology 67:1476–1478.

Meixner A, Haverkamp S, Wässle H, Führer S, Thalhammer J, Kropf N, Bittner RE, Lassmann H, Wiche G, Propst F (2000) MAP1B is required for axon guidance and Is involved in the development of the central and peripheral nervous system. The Journal of cell biology 151:1169–1178.

Messer A, Strominger NL (1980a) An allele of the mouse mutant dystonia musculorum exhibits lesions in red nucleus and striatum. Neuroscience 5:543–549.

Messer A, Strominger NL (1980b) An allele of the mouse mutant dystonia musculorum exhibits lesions in red nucleus and striatum. Neuroscience 5:543–549.

Michelot A, Drubin DG (2011) Building distinct actin filament networks in a common cytoplasm. Curr Biol 21:R560–9.

Miller PM, Folkmann AW, Maia ARR, Efimova N, Efimov A, Kaverina I (2009) Golgi-derived CLASP-dependent microtubules control Golgi organization and polarized trafficking in motile cells. Nature cell biology 11:1069–1080.

Minin AA (1997) Dispersal of Golgi apparatus in nocodazole-treated fibroblasts is a kinesin-driven process. J Cell Sci 110 (Pt 1:2495–2505.

Mirsky R, Jessen KR (1999) The neurobiology of Schwann cells. Brain Pathol 9:293–311.

Mizushima N (2007) Autophagy: process and function. Genes & development 21:2861–2873.

Monastyrska I, Rieter E, Klionsky DJ, Reggiori F (2009) Multiple roles of the cytoskeleton in autophagy. Biological reviews of the Cambridge Philosophical Society 84:431–448.

Mori F, Tanji K, Odagiri S, Toyoshima Y, Yoshida M, Kakita A, Takahashi H, Wakabayashi K (2012) Autophagy-related proteins (p62, NBR1 and LC3) in intranuclear inclusions in neurodegenerative diseases. Neuroscience letters 522:134–138.

Morimoto N, Nagai M, Ohta Y, Miyazaki K, Kurata T, Morimoto M, Murakami T, Takehisa Y, Ikeda Y, Kamiya T, Abe K (2007) Increased autophagy in transgenic mice with a G93A mutant SOD1 gene. Brain research 1167:112–117.

Moss TH (n.d.) Schwann cell involvement in the neurological lesion of the dystonic mutant mouse. A nerve grafting study. J Neurol Sci 49:207–222.

Moss TH (n.d.) Segmental demyelination in the peripheral nerves of mice affected by a hereditary neuropathy (dystonia musculorum). Acta Neuropathol 53:51–56.

Mu X, Silos-Santiago I, Carroll SL, Snider WD (1993) Neurotrophin receptor genes are expressed in distinct patterns in developing dorsal root ganglia. The Journal of neuroscience : the official journal of the Society for Neuroscience 13:4029–4041.

Munro S, Pelham HR (1986) An Hsp70-like protein in the ER: identity with the 78 kd glucose-regulated protein and immunoglobulin heavy chain binding protein. Cell 46:291–300.

Murakami Y, Aizu-Yokota E, Sonoda Y, Ohta S, Kasahara T (2007) Suppression of endoplasmic reticulum stress-induced caspase activation and cell death by the overexpression of Bcl-xL or Bcl-2. Journal of biochemistry 141:401–410.

Nakagawa T, Zhu H, Morishima N, Li E, Xu J, Yankner BA, Yuan J (2000) Caspase-12 mediates endoplasmic-reticulum-specific apoptosis and cytotoxicity by amyloid-beta. Nature 403:98–103.

Narver HL, Kong L, Burnett BG, Choe DW, Bosch-Marcé M, Taye AA, Eckhaus MA, Sumner CJ (2008) Sustained improvement of spinal muscular atrophy mice treated with trichostatin A plus nutrition. Annals of neurology 64:465–470.

Nixon RA, Wegiel J, Kumar A, Yu WH, Peterhoff C, Cataldo A, Cuervo AM (2005) Extensive involvement of autophagy in Alzheimer disease: an immuno-electron microscopy study. Journal of neuropathology and experimental neurology 64:113–122.

Nutt LK, Margolis SS, Jensen M, Herman CE, Dunphy WG, Rathmell JC, Kornbluth S (2005) Metabolic regulation of oocyte cell death through the CaMKII-mediated phosphorylation of caspase-2. Cell 123:89–103.

Okumura M, Yamakawa H, Ohara O, Owaribe K (2002) Novel alternative splicings of BPAG1 (bullous pemphigoid antigen 1) including the domain structure closely related to MACF (microtubule actin cross-linking factor). The Journal of biological chemistry 277:6682–6687.

Oppenheim RW, Yin QW, Prevette D, Yan Q (n.d.) Brain-derived neurotrophic factor rescues developing avian motoneurons from cell death. Nature 360:755–757.

Orrenius S, Zhivotovsky B, Nicotera P (2003) Regulation of cell death: the calcium-apoptosis link. Nature reviews Molecular cell biology 4:552–565.

Ouasti S, Matarrese P, Paddon R, Khosravi-Far R, Sorice M, Tinari A, Malorni W, Degli Esposti M (2007) Death receptor ligation triggers membrane scrambling between Golgi and mitochondria. Cell death and differentiation 14:453–461.

Pankiv S, Clausen TH, Lamark T, Brech A, Bruun J-A, Outzen H, Øvervatn A, Bjørkøy G, Johansen T (2007) p62/SQSTM1 binds directly to Atg8/LC3 to facilitate degradation of ubiquitinated protein aggregates by autophagy. The Journal of biological chemistry 282:24131–24145.

Perkins EM, Clarkson YL, Sabatier N, Longhurst DM, Millward CP, Jack J, Toraiwa J, Watanabe M, Rothstein JD, Lyndon AR, Wyllie DJA, Dutia MB, Jackson M (2010) Loss of beta-III spectrin leads to Purkinje cell dysfunction recapitulating the behavior and neuropathology of spinocerebellar ataxia type 5 in humans. The Journal of neuroscience : the official journal of the Society for Neuroscience 30:4857–4867.

Perlson E, Maday S, Fu M-M, Moughamian AJ, Holzbaur ELF (2010) Retrograde axonal transport: pathways to cell death? Trends in neurosciences 33:335–344.

Platika D, Boulos MH, Baizer L, Fishman MC (1985) Neuronal traits of clonal cell lines derived by fusion of dorsal root ganglia neurons with neuroblastoma cells. Proceedings of the National Academy of Sciences of the United States of America 82:3499–3503.

Pool M, Boudreau Larivière C, Bernier G, Young KG, Kothary R (2005) Genetic alterations at the Bpag1 locus in dt mice and their impact on transcript expression. Mammalian genome : official journal of the International Mammalian Genome Society 16:909–917.

Popko B (2010) Myelin maintenance: axonal support required. Nature neuroscience 13:275–277.

Prokop A, Uhler J, Roote J, Bate M (1998) The kakapo mutation affects terminal arborization and central dendritic sprouting of Drosophila motorneurons. The Journal of cell biology 143:1283–1294.

Ravikumar B, Acevedo-Arozena A, Imarisio S, Berger Z, Vacher C, O'Kane CJ, Brown SDM, Rubinsztein DC (2005) Dynein mutations impair autophagic clearance of aggregate-prone proteins. Nature genetics 37:771–776.

Ravikumar B, Duden R, Rubinsztein DC (2002) Aggregate-prone proteins with polyglutamine and polyalanine expansions are degraded by autophagy. Human molecular genetics 11:1107–1117.

Reed NA, Cai D, Blasius TL, Jih GT, Meyhofer E, Gaertig J, Verhey KJ (2006) Microtubule acetylation promotes kinesin-1 binding and transport. Current biology : CB 16:2166–2172.

Renvoise B, Blackstone C (2010) Emerging themes of ER organization in the development and maintenance of axons. Curr Opin Neurobiol 20:531–537.

Resh MD (2004) Membrane targeting of lipid modified signal transduction proteins. Subcell Biochem 37:217–232.

REXED B (1952) The cytoarchitectonic organization of the spinal cord in the cat. The Journal of comparative neurology 96:414–495.

Rios RM, Bornens M (2003) The Golgi apparatus at the cell centre. Current opinion in cell biology 15:60–66.

Rivero S, Cardenas J, Bornens M, Rios RM (2009) Microtubule nucleation at the cis-side of the Golgi apparatus requires AKAP450 and GM130. The EMBO journal 28:1016–1028.

Rodriguez OC, Schaefer AW, Mandato CA, Forscher P, Bement WM, Waterman-Storer CM (2003) Conserved microtubule-actin interactions in cell movement and morphogenesis. Nat Cell Biol 5:599–609.

Rogalski AA, Singer SJ (1984) Associations of elements of the Golgi apparatus with microtubules. J Cell Biol 99:1092–1100.

Roper K, Gregory SL, Brown NH (2002) The “spectraplakins”: cytoskeletal giants with characteristics of both spectrin and plakin families. J Cell Sci 115:4215–4225.

Rosenblatt JD, Lunt AI, Parry DJ, Partridge TA (1995) Culturing satellite cells from living single muscle fiber explants. In vitro cellular & developmental biology Animal 31:773–779.

Rotthier A, Baets J, Vriendt E De, Jacobs A, Auer-Grumbach M, Lévy N, Bonello-Palot N, Kilic SS, Weis J, Nascimento A, Swinkels M, Kruyt MC, Jordanova A, De Jonghe P, Timmerman V (2009) Genes for hereditary sensory and autonomic neuropathies: a genotype–phenotype correlation. Brain: A journal of neurology 132:2699–2711.

Rottier, Annelies; Baets, Jonathan; Timmerman, Vincent; Janssens K (2012) Mechanisms of disease in hereditary sensory and autonomic neuropathies. Nature reviews, Neurology Volume 8:73–85.

Ruegg MA, Bixby JL (1998) Agrin orchestrates synaptic differentiation at the vertebrate neuromuscular junction. Trends in neurosciences 21:22–27.

Ruhrberg C, Watt FM (1997) The plakin family: versatile organizers of cytoskeletal architecture. Curr Opin Genet Dev 7:392–397.

Ryan SD, Bhanot K, Ferrier A, De Repentigny Y, Chu A, Blais A, Kothary R (2012a) Microtubule stability, Golgi organization, and transport flux require dystonin-a2-MAP1B interaction. The Journal of Cell Biology 196:727–742.

Ryan SD, Ferrier A, Kothary R (2012b) A novel role for the cytoskeletal linker protein dystonin in the maintenance of microtubule stability and the regulation of ER-Golgi transport. BioArchitecture 2:2–5.

Ryan SD, Ferrier A, Sato T, O'Meara RW, De Repentigny Y, Jiang SX, Hou ST, Kothary R (2012c) Neuronal dystonin isoform 2 is a mediator of endoplasmic reticulum structure and function. Molecular Biology of the Cell 23:553–566.

Saldanha AJ (2004) Java Treeview--extensible visualization of microarray data. Bioinformatics (Oxford, England) 20:3246–3248.

Sanchez-Soriano N, Travis M, Dajas-Bailador F, Goncalves-Pimentel C, Whitmarsh AJ, Prokop A (2009) Mouse ACF7 and drosophila short stop modulate filopodia formation and microtubule organisation during neuronal growth. J Cell Sci 122:2534–2542.

Sanes JR, Lichtman JW (1999) Development of the vertebrate neuromuscular junction. Annual review of neuroscience 22:389–442.

Sanes JR, Lichtman JW (2001) Induction, assembly, maturation and maintenance of a postsynaptic apparatus. Nature reviews Neuroscience 2:791–805.

Saulnier R, De Repentigny Y, Yong VW, Kothary R (2002) Alterations in myelination in the central nervous system of dystonia musculorum mice. J Neurosci Res 69:233–242.

Sawamura D, Li K, Chu ML, Uitto J (1991) Human bullous pemphigoid antigen (BPAG1). Amino acid sequences deduced from cloned cDNAs predict biologically important peptide segments and protein domains. The Journal of biological chemistry 266:17784–17790.

Scales TME, Lin S, Kraus M, Goold RG, Gordon-Weeks PR (2009) Nonprimed and DYRK1A-primed GSK3 beta-phosphorylation sites on MAP1B regulate microtubule dynamics in growing axons. Journal of cell science 122:2424–2435.

Scheper W, Nijholt DAT, Hoozemans JJM (2011) The unfolded protein response and proteostasis in Alzheimer disease: preferential activation of autophagy by endoplasmic reticulum stress. Autophagy 7:910–911.

Schlager G, Dickie MM (1967) Spontaneous mutations and mutation rates in the house mouse. Genetics 57:319–330.

Schmued LC, Hopkins KJ (n.d.) Fluoro-Jade: novel fluorochromes for detecting toxicant-induced neuronal degeneration. Toxicologic pathology 28:91–99.

Servadio A, Koshy B, Armstrong D, Antalffy B, Orr HT, Zoghbi HY (1995) Expression analysis of the ataxin-1 protein in tissues from normal and spinocerebellar ataxia type 1 individuals. Nature genetics 10:94–98.

Shaw G, Morse S, Ararat M, Graham FL (2002) Preferential transformation of human neuronal cells by human adenoviruses and the origin of HEK 293 cells. FASEB journal : official publication of the Federation of American Societies for Experimental Biology 16:869–871.

Sherrington R et al. (1995) Cloning of a gene bearing missense mutations in early-onset familial Alzheimer's disease. Nature 375:754–760.

Shore GC, Papa FR, Oakes SA (2011) Signaling cell death from the endoplasmic reticulum stress response. Current opinion in cell biology 23:143–149.

Skoufias DA, Burgess TL, Wilson L (1990) Spatial and temporal colocalization of the Golgi apparatus and microtubules rich in detyrosinated tubulin. The Journal of cell biology 111:1929–1937.

Slep KC, Rogers SL, Elliott SL, Ohkura H, Kolodziej PA, Vale RD (2005) Structural determinants for EB1-mediated recruitment of APC and spectraplakins to the microtubule plus end. J Cell Biol 168:587–598.

Sonnenberg A, Liem RK (2007) Plakins in development and disease. Exp Cell Res 313:2189–2203.

Sotelo C, Guenet JL (1988) Pathologic changes in the CNS of dystonia musculorum mutant mouse: an animal model for human spinocerebellar ataxia. Neuroscience 27:403–424.

Stanley JR (1993) Cell adhesion molecules as targets of autoantibodies in pemphigus and pemphigoid, bullous diseases due to defective epidermal cell adhesion. Adv Immunol 53:291–325.

Starr DA (2007) Communication between the cytoskeleton and the nuclear envelope to position the nucleus. Molecular bioSystems 3:583–589.

Stefanis L, Larsen KE, Rideout HJ, Sulzer D, Greene LA (2001) Expression of A53T mutant but not wild-type alpha-synuclein in PC12 cells induces alterations of the ubiquitin-dependent degradation system, loss of dopamine release, and autophagic

cell death. The Journal of neuroscience : the official journal of the Society for Neuroscience 21:9549–9560.

Su Y, Balice-Gordon RJ, Hess DM, Landsman DS, Minarcik J, Golden J, Hurwitz I, Liebhaber SA, Cooke NE (2004) Neurobeachin is essential for neuromuscular synaptic transmission. J Neurosci 24:3627–3636.

Subramanian A, Prokop A, Yamamoto M, Sugimura K, Uemura T, Betschinger J, Knoblich JA, Volk T (2003) Shortstop recruits EB1/APC1 and promotes microtubule assembly at the muscle-tendon junction. Curr Biol 13:1086–1095.

Suh Y-H, Checler F (2002) Amyloid precursor protein, presenilins, and alpha-synuclein: molecular pathogenesis and pharmacological applications in Alzheimer's disease. Pharmacological reviews 54:469–525.

Sun D, Leung CL, Liem RK (2001a) Characterization of the microtubule binding domain of microtubule actin crosslinking factor (MACF): identification of a novel group of microtubule associated proteins. J Cell Sci 114:161–172.

Sun D, Leung CL, Liem RK (2001b) Characterization of the microtubule binding domain of microtubule actin crosslinking factor (MACF): identification of a novel group of microtubule associated proteins. J Cell Sci 114:161–172.

Suozzi KC, Wu X, Fuchs E (2012a) Spectraplakins: Master orchestrators of cytoskeletal dynamics. J Cell Biol 197:465–475.

Suozzi KC, Wu X, Fuchs E (2012b) Spectraplakins: master orchestrators of cytoskeletal dynamics. The Journal of cell biology 197:465–475.

Takemura R, Okabe S, Umeyama T, Kanai Y, Cowan NJ, Hirokawa N (1992) Increased microtubule stability and alpha tubulin acetylation in cells transfected with microtubule-associated proteins MAP1B, MAP2 or tau. Journal of cell science 103 (Pt 4:953–964.

Tanabe LM, Kim CE, Alagem N, Dauer WT (2009) Primary dystonia: molecules and mechanisms. Nature reviews Neurology 5:598–609.

Teng J, Takei Y, Harada A, Nakata T, Chen J, Hirokawa N (2001) Synergistic effects of MAP2 and MAP1B knockout in neuronal migration, dendritic outgrowth, and microtubule organization. The Journal of cell biology 155:65–76.

Thornburg LP, Hanker JS (1975) Lysosomal hydrolases in the trigeminal ganglion of mice afflicted with an hereditary sensory neuropathy (dystonia musculorum). Acta Neuropathol 32:91–101.

Thyberg J, Moskalewski S (1993) Relationship between the Golgi complex and microtubules enriched in detyrosinated or acetylated alpha-tubulin: studies on cells recovering from nocodazole and cells in the terminal phase of cytokinesis. Cell and tissue research 273:457–466.

Thyberg J, Moskalewski S (1999) Role of microtubules in the organization of the Golgi complex. Exp Cell Res 246:263–279.

Tseng K-W, Chau Y-P, Yang M-F, Lu K-S, Chien C-L (2008) Abnormal cellular translocation of alpha-internexin in spinal motor neurons of Dystonia musculorum mice. The Journal of comparative neurology 507:1053–1064

Tseng KW, Lu KS, Chien CL (2006) A possible cellular mechanism of neuronal loss in the dorsal root ganglia of Dystonia musculorum (dt) mice. J Neuropathol Exp Neurol 65:336–347.

Van den Heuvel AP, De Vries-Smits AM, Van Weeren PC, Dijkers PF, De Bruyn KM, Riedl JA, Burgering BM (2002) Binding of protein kinase B to the plakin family member periplakin. J Cell Sci 115:3957–3966.

Vincent JB, Choufani S, Horike S, Stachowiak B, Li M, Dill FJ, Marshall C, Hrynchak M, Pewsey E, Ukadike KC, Friedman JM, Srivastava AK, Scherer SW (2008) A translocation t(6;7)(p11-p12;q22) associated with autism and mental retardation: localization and identification of candidate genes at the breakpoints. Psychiatr Genet 18:101–109.

Wang K, Klionsky DJ (2011) Mitochondria removal by autophagy. Autophagy 7:297–300.

Wang QJ, Ding Y, Kohtz DS, Kohtz S, Mizushima N, Cristea IM, Rout MP, Chait BT, Zhong Y, Heintz N, Yue Z (2006) Induction of autophagy in axonal dystrophy and degeneration. The Journal of neuroscience : the official journal of the Society for Neuroscience 26:8057–8068.

Wang X, Herberg FW, Laue MM, Wullner C, Hu B, Petrasch-Parwez E, Kilimann MW (2000) Neurobeachin: A protein kinase A-anchoring, beige/Chediak-higashi protein homolog implicated in neuronal membrane traffic. J Neurosci 20:8551–8565.

Webb JL, Ravikumar B, Atkins J, Skepper JN, Rubinsztein DC (2003) Alpha-Synuclein is degraded by both autophagy and the proteasome. The Journal of biological chemistry 278:25009–25013.

Wilhelmsen K, Litjens SH, Kuikman I, Tshimbalanga N, Janssen H, Van den Bout I, Raymond K, Sonnenberg A (2005) Nesprin-3, a novel outer nuclear membrane protein, associates with the cytoskeletal linker protein plectin. J Cell Biol 171:799–810.

Willmann R, Dubach J, Chen K (2011) Developing standard procedures for pre-clinical efficacy studies in mouse models of spinal muscular atrophy: report of the expert workshop “Pre-clinical testing for SMA”, Zürich, March 29-30th 2010. Neuromuscular disorders : NMD 21:74–77.

Witzemann V (2006) Development of the neuromuscular junction. Cell and tissue research 326:263–271.

Wong E, Cuervo AM (2010) Autophagy gone awry in neurodegenerative diseases. Nature neuroscience 13:805–811.

Xie R, Nguyen S, McKeehan K, Wang F, McKeehan WL, Liu L (2011) Microtubule-associated protein 1S (MAP1S) bridges autophagic components with microtubules and mitochondria to affect autophagosomal biogenesis and degradation. The Journal of biological chemistry 286:10367–10377.

Xie R, Nguyen S, McKeehan WL, Liu L (2010) Acetylated microtubules are required for fusion of autophagosomes with lysosomes. BMC cell biology 11:89.

Yang Y, Bauer C, Strasser G, Wollman R, Julien JP, Fuchs E (1999) Integrators of the cytoskeleton that stabilize microtubules. Cell 98:229–238.

Yang Y, Dowling J, Yu QC, Kouklis P, Cleveland DW, Fuchs E (1996) An essential cytoskeletal linker protein connecting actin microfilaments to intermediate filaments. Cell 86:655–665.

Yang Y, Fukui K, Koike T, Zheng X (2007) Induction of autophagy in neurite degeneration of mouse superior cervical ganglion neurons. The European journal of neuroscience 26:2979–2988.

Yang Z, Klionsky DJ (2010) Eaten alive: a history of macroautophagy. Nature cell biology 12:814–822.

Yarar D, Waterman-Storer CM, Schmid SL (2005) A dynamic actin cytoskeleton functions at multiple stages of clathrin-mediated endocytosis. Mol Biol Cell 16:964–975.

Yorimitsu T, Nair U, Yang Z, Klionsky DJ (2006) Endoplasmic reticulum stress triggers autophagy. The Journal of biological chemistry 281:30299–30304.

Yoshida H, Matsui T, Yamamoto A, Okada T, Mori K (2001) XBP1 mRNA is induced by ATF6 and spliced by IRE1 in response to ER stress to produce a highly active transcription factor. Cell 107:881–891.

Young KG, De Repentigny Y, Kothary R (2007) Re: “A possible cellular mechanism of neuronal loss in the dorsal root ganglia of dystonia musculorum (dt) mice”. J Neuropathol Exp Neurol 66:248–9; author reply 249.

Young KG, Kothary R (2007) Dystonin/Bpag1--a link to what? Cell Motility and the Cytoskeleton 64:897–905.

Young KG, Kothary R (2008) Dystonin/Bpag1 is a necessary endoplasmic reticulum/nuclear envelope protein in sensory neurons. Experimental Cell Research 314:2750–2761.

Young KG, Pinheiro B, Kothary R (2006) A Bpag1 isoform involved in cytoskeletal organization surrounding the nucleus. Experimental cell research 312:121–134.

Young KG, Pool M, Kothary R (2003a) Bpag1 localization to actin filaments and to the nucleus is regulated by its N-terminus. J Cell Sci 116:4543–4555.

Young KG, Pool M, Kothary R (2003b) Bpag1 localization to actin filaments and to the nucleus is regulated by its N-terminus. J Cell Sci 116:4543–4555.

Yu C-Y, Hsu Y-W, Liao C-L, Lin Y-L (2006) Flavivirus infection activates the XBP1 pathway of the unfolded protein response to cope with endoplasmic reticulum stress. Journal of virology 80:11868–11880.

Yu WH, Cuervo AM, Kumar A, Peterhoff CM, Schmidt SD, Lee J-H, Mohan PS, Mercken M, Farmery MR, Tjernberg LO, Jiang Y, Duff K, Uchiyama Y, Näslund J, Mathews PM, Cataldo AM, Nixon RA (2005) Macroautophagy--a novel Beta-amyloid peptide-generating pathway activated in Alzheimer’s disease. The Journal of cell biology 171:87–98.

Zhou X, Wang L, Hasegawa H, Amin P, Han B-X, Kaneko S, He Y, Wang F (2010) Deletion of PIK3C3/Vps34 in sensory neurons causes rapid neurodegeneration by disrupting the endosomal but not the autophagic pathway. Proceedings of the National Academy of Sciences of the United States of America 107:9424–9429.